Title
Microfluidic Immunoblotting using Multi-Purposed Soft Materials

Author
Hughes, Alex James

Publication Date
2013

Peer reviewed|Thesis/dissertation

Microfluidic Immunoblotting using Multi-Purposed Soft Materials

by

Alex James Hughes

A dissertation submitted in partial satisfaction of the
requirements for the degree of
Joint Doctor of Philosophy
with University of California, San Francisco

in

Bioengineering

in the

Graduate Division

of the

University of California, Berkeley

Committee in charge:

Professor Amy Herr, Chair
Professor Ming Wu,
Professor Adam Abate

Spring 2013

Microfluidic Immunoblotting using Multi-Purposed Soft Materials

Abstract

Microfluidic Immunoblotting using Multi-Purposed Soft Materials

by

Alex James Hughes

Joint Doctor of Philosophy
with University of California, San Francisco in Bioengineering

University of California, Berkeley

Professor Amy Herr, Chair

The miniaturization of biological assays for basic science and clinical diagnostics is a strong focus of the microfluidics field. Substantial impacts on assay time, throughput, and sample requirement, for example, can be achieved through integrating process workflows for the detection of protein analytes. Yet to permeate the broader scientific community, a strong focus on simplified device architectures, modularity, and adaptability should be at the forefront of endeavors in the microfluidics field.

Here, I describe thesis contributions covering a number of embodiments of a microfluidic immunoblotting toolbox. Central to the themes of each facet of the toolbox are the integration of assay stages from separations to quantitative protein analyte detection using microfabricated polymer structures. These structures immobilize proteins after weight or charge-based separations from complex clinical samples or cell lysates, preserving separation resolution for often protracted immunoprobing or activity-based detection stages.

After describing methods to separate, immobilize, and assay for enzyme activity within polyacrylamide gradient gels, I describe the development of photoactive polyacrylamide matrices that yield rapid, highly efficient capture of separated protein bands upon the application of UV light with performance that is robust to a wide range of assay conditions.

These materials form the basis of microfluidic immunoblotting methods based on charge and size separations, culminating in microfluidic western blotting architectures that support

analysis of low-zeptomole quantities of target proteins from cell lysates, blood sera, and single cells in integrated, automated assay workflows complete in tens of minutes.

Among specific contributions of this thesis are, firstly, the discovery and characterization of an isoelectric point photoswitching phenomenon in green fluorescent protein variants from the jellyfish *Aequorea victoria* in response to different wavelengths of light that may have applications in the engineering of biomimetic smart materials with light-actuated transitions in zeta potential, hydrophilicity / wetting behavior, and adhesion properties.

Secondly, I describe an immunoprobed isoelectric focusing technology that quantifies the isoforms of the prostate cancer biomarker prostate specific antigen in less than 120 min with detection limits in the low pg.

Finally, I describe two variants of an integrated microfluidic western blotting assay that reduce 6–12 hr analysis times of traditional techniques to as little as 10 min, with detection sensitivities as low as 10^4–10^5 molecules. The first is applied to the confirmatory testing of HIV+ status in clinical patient serum, addressing the traditional western blotting bottleneck in infectious disease diagnostics. The second is a single-cell western blotting technique in a standard microscope slide format that has the hallmarks of design for application and uptake in a range of life science fields. This microarray-like tool leverages timescale separation at the microscale to link lysis, separation, capture, and immunoblotting of the protein contents of more than 10^3 single cells per assay. I detail the nascent application of this exciting addition to the rather limited single-cell proteomics pipeline to neural stem cells in a case study of cell-to-cell heterogeneity over signaling and differentiation timescales.

To my family.

Acknowledgments

These pages are filled with hard-fought, minuscule advances that are the sparkly varnish on the emotional journey of success and failure in graduate school. The 5 years that have culminated in this document are long enough to have seeded life-long friendships, and there are several people that deserve mention.

Thanks go to my brother and parents for hearing out frustrations, offering soothing words, and for putting my efforts in the perspective of a broader human experience. Lukasz Bugaj, Oscar Westesson, and Tim Downing were allies and confidants. We shared the hikes, skiing, drinking, and gambling that are necessary to counteract the precision and restraint of science. I will look back fondly on the various varminting projects that Oscar and I undertook together.

Some allies in the lab included Augusto Tentori, Sam Tia, Kwasi Apori, Monica Kapil, and several others along the way. The mutual respect and cohesion that we developed helped us through the minor disputes, challenges, and disappointments that inevitably come with such a highly charged intellectual environment. Sharp minds come with sharp senses of humor, and we certainly laughed together.

Without rebellion there cannot be progress in science, so thanks must go to my patient advisor, Amy Herr, for corralling my scientific efforts and making room for my rebellious spirit. Thanks also to our patient collaborators, Donna Peehl, David Schaffer, and Dawn Spelke, for enthusiastically supporting our technology development efforts. I have also had the benefit of drawing upon the experiences and advice of seasoned undergraduate mentors at the University of Auckland, New Zealand; special thanks are due to Dr. Mark Titchener, Dr. Robert Kirkpatrick, and Professor John J.J. Chen.

Some funding sources that I have been fortunate enough to take advantage of include the National Defense Science and Engineering Graduate Fellowship through the U.S. Department of Defense, the F.W.W. Rhodes memorial fellowship through Auckland Grammar School, UC Berkeley Start-Up and NIH New Innovator funding to Amy Herr, and the Siebel Scholarship; many thanks to these organizations for supporting and investing in my work.

Contents

List of Figures

List of Tables

Chapter 1

Introduction

1.1 Thesis Overview

Microfluidics is the study of fluid and material transport at the microscale. The application of microfabricated systems to the integration and automation of biological assays to improve analytical performance has been a strong emphasis in the microfluidics field, which has seen an increase in the number of publications relating to it from tens in the mid-1990's to approximately 1,700 in 2008 [1]. Shrinking material manipulation to the microscale can bring broad benefits in performance metrics relating to portability (e.g. the emergence of point-of-care diagnostic devices), cost per assay readout, time to result, parallelization (number of readouts per assay), and integration of disparate assay stages; and further enables the controlled perturbation and analysis of biological systems at length scales on the order of a single cell.

The microfluidics field has taken advantage of several aspects of the physics of energy, fields, and materials at the microscale to achieve these analytical advances [2]. The dominance of viscous over inertial forces at the microscale, for example, allows stable laminar interfaces to be maintained between adjacent, homogeneous fluids, allowing researchers to design devices both leveraging and fighting the influence of diffusion to implement unit operations achieving mixing, separations, and reactions.

The ability to fabricate large-scale microscale structures in layers of hard and soft engineered materials has also seen the rise of large-scale integration, in which many unit operations can be parallelized and integrated to achieve high-throughput biological assays in the spirit of electronic integrated circuits [3]. Although paradigm-shifting, this valved microchamber approach necessitates complex off-chip control and actuation infrastructure and limits community-wide adoption of microfluidic techniques (although commercialization of high-throughput genetic amplification and sequencing technologies has certainly thrived since its inception).

In an effort to make the benefits of microfluidic assays more broadly accessible to life science and medical diagnostic communities, a microfluidics "counterculture" has emerged that focuses on simpler device architectures, often aiming to achieve quantitative readouts of biological activity with minimal off-chip infrastructure [4, 5]. These devices typically make use of passive control systems, and focus heavily on the engineering of often multi-purposed polymer materials including hydrogels and paper. In the context of these two paradigms in the microfluidics community, the contributions of this thesis balance the need for community accessibility of engineered tools with the fundamental tenets of control and quantitation by leveraging soft polymer materials for multiple mass transport and reaction functions.

Chapter 2 explores microfluidic methods for enzyme separations and assays (known as zymography), integrating pore limit electrophoresis, in which protein analytes are sieved and "pseudo-immobilized" in a polyacrylamide pore-gradient gel with the *in situ* assay of en-

zymes using electrophoresable, fluorogenic substrates. This integrated assay is operated solely under electrophoretic control in single glass microchannels, letting the polyacrylamide material passively control the dimensions and kinetics operating within a virtual microreactor created by its sieving properties. In comparison to 2–12 hr workflows in conventional PAGE zymography, the microfluidic assay takes 40 min and retrieves quantitative kinetic information from as little as 3,000 enzyme molecules for a calf intestinal alkaline phosphatase model system.

Extending the integrative potential of sieving and scaffolding polyacrylamide matrices in biological assays, we develop a more controlled and widely applicable protein analyte immobilization technique in Chapter 3. Here, isoelectric focusing (IEF) assays that separate proteins by according to differences in their electrostatic charge are integrated with downstream immunoprobing using a polyacrylamide gel engineered for photocapture duty. UV light converts a light-activated, volume accessible "LAVAgel" into a scaffold support for immobilized protein analytes that then become targets for fluorescent antibody-based detection, complex kinetic processes that are rigorously analyzed in Chapter 4. We apply this immunoblotting platform to the analysis of prostate specific antigen isoforms from clinical samples with detection limits of 1.1 pg in assay times of less than 120 min, achieving a proof-of-concept, validated workflow for high-throughput biomarker validation with a view towards clinical implementation.

Besides clinically-oriented assays with practical advances over gold-standard techniques, we were interested in using the isoelectric focusing immunoblotting assay to study a focused question of biophysical relevance. Chance observations of unusual peak migration behaviors for the wild-type green fluorescent protein (GFP) from the jellyfish *Aequorea victoria* in the IEF assay led to the discovery and quantitative study of "isoelectric photoswitching", in which the electrostatic charge of GFPs are found to change dynamically upon the application of different wavelengths of light (Chapter 5).

Intrigued by the ability of photoactive polyacrylamide materials to link short and long-timescale assay stages in the context of the immunoblotting toolbox, we tackle the widely used western blotting assay to explore the prospect that an integrated microfluidic approach would yield benefits in analysis time, sample and reagent consumption, automation, and assay repeatability in Chapter 6. Indeed, denaturing sodium dodecyl sulfate-polyacrylamide gel electrophoresis (SDS-PAGE) separations are successfully executed in single microchannels by relying on optimized but standard buffer conditions to achieve transient isotachophoretic stacking of protein samples from diffuse initial injection aliquots. SDS-PAGE is also found to be fully compatible with PACTgel (a photopatternable version of the LAVAgel)-mediated analyte capture and immunoprobing, constituting a fully integrated microfluidic alternative to traditional western blotting that reduces analysis times from 6–12 hrs to 10–60 min with 50 pM detection limits and 3.6-log linear dynamic range. Using this new assay framework, we demonstrate 48-plex parallelized assays of raw cell lysate and develop a microfluidic

confirmatory HIV diagnostic that captures anti-HIV antibodies in HIV+ patient sera using blotted HIV antigens to determine infection status.

Finally, we describe recent efforts to push the limits of separation scale and mass sensitivity by innovating a generic high-throughput single-cell western blotting assay capable of sieving and capturing single cell contents extracted from microwells fabricated in the photoactive PACTgel matrix (Chapter 7). We detail parallel analysis of $> 10^3$ single cells per $1'' \times 3''$ microscope slide, detecting protein bands with sensitivities on the order of $10^4 - 10^5$ molecules even without enzymatic amplification of assay readout. We apply this new technology to the analysis of signaling and differentiation in neural stem cells, revealing exciting insights into cell-to-cell heterogeneity.

1.2 Electrophoretic Protein Separations

Separation of proteins in complex samples plays a variety of roles in analytical assays, including reduction of sample complexity, purification of targets, and extraction of physicochemical properties such as weight or charge [6]. Here, we review isoelectric focusing and SDS-PAGE separation modes with a view towards integrative assay design.

1.2.1 Transport Principles & Characterization of Performance

1.2.1.1 Equilibrium Separations — Isoelectric Focusing

Isoelectric focusing (IEF, Figure 1.1) is a widely applied technique in which a heterogeneous mixture of proteins is separated in an anti-convective medium (such as a polyacrylamide gel) subjected to an imposed pH gradient towards a steady-state in which protein constituents focus into bands at their isoelectric points, pI (i.e. where the net charge of each species is zero) [7]. The velocity of each protein is governed by its charge state, such that the migration rate decreases with the net charge on a protein as it approaches its pI. The pH gradient is commonly imposed through the use of a set of "carrier" ampholytes (CA) in the gel buffer having good buffer capacity and conductance at their respective pI values, which are scattered over the pH range to generate a steady background ramp in pH across the length of the gel (see Figure 1.2) [8, 9]. Alternatively, immobilized pH gradients (IPGs) can be generated in polyacrylamide gels through the use of "immobiline" acrylamide derivatives. In the simplest case, one immobiline species having a single ionizable group is titrated around its pK_a using a gradient in a second fully dissociated immobiline species to create the spatial pH gradient [10, 11]. Both IEF classes have been recently demonstrated in microfluidic chips functionalized with crosslinked polyacrylamide gels or modified for suppression of electroosmotic flow in free-solution focusing [12–14].

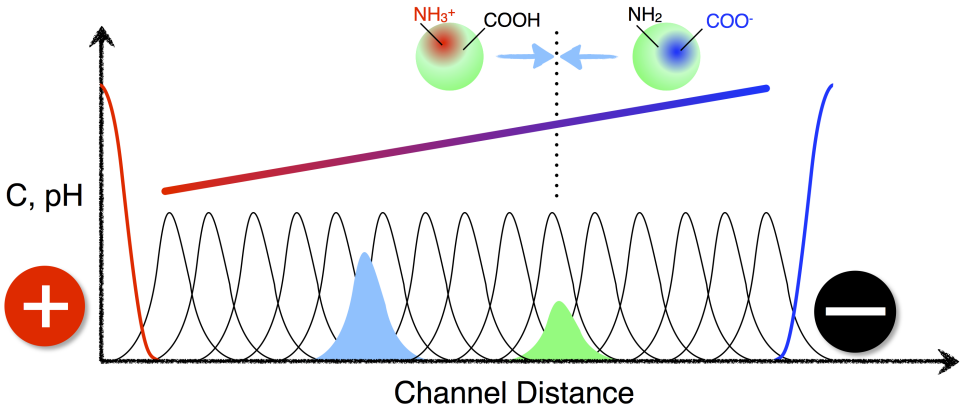

Figure 1.1: A sketch of ampholyte, protein, and pH distributions in isoelectric focusing. Black lines depict concentration profiles of carrier ampholytes centered at their isoelectric points. The spatial arrangement of the ampholytes ensures uniform current and creates a pH gradient upon the application of electric field. Proteins (green spheres) focus at their isoelectric points according to titration of surface residues such that their net charges are zero. Red and blue lines depict the concentrations of anolyte and catholyte, respectively.

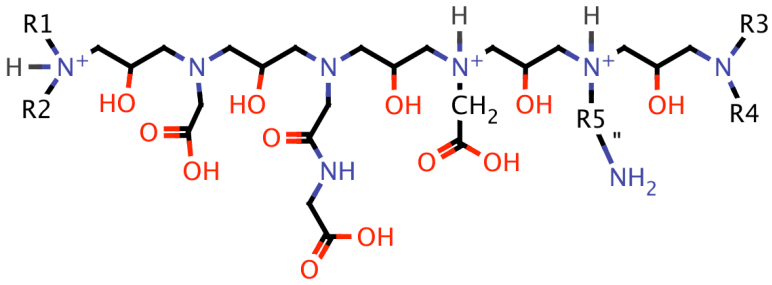

Figure 1.2: The generalized structure of a carrier ampholyte, reflecting the presence of multiple titratable groups in a polyaminopolycarboxylic acid structure [7].

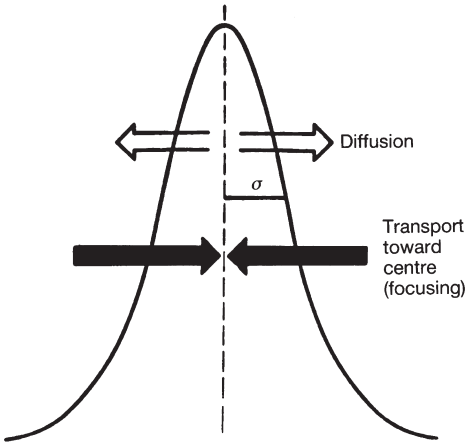

Figure 1.3: A schematic of the opposing actions of focusing and diffusive band broadening in IEF, which together generate a Gaussian protein distribution centered around the pI (reproduced from [9]).

The following sections examine IEF theory relevant to the design of a probed isoelectric focusing device coupling the separation process to covalent immobilization of focused species.

Derivation of IEF Peak Resolution at Steady-State. The balance between electrophoretic transport of a protein towards its pI and diffusional transport acting to broaden the resulting zone (see Figure 1.3) is readily formulated as follows [8, 15]:

$$C\mu_{\mathrm{EP}}E = D\frac{dC}{dx} \tag{1.1}$$

Where E is the applied electric field, D is the analyte diffusivity and μ_{EP} is the analyte electrophoretic mobility. The protein concentration C is in units of mass per unit time and channel crossectional area, and the pH gradient through the protein zone is assumed to be linear, i.e.:

$$p = -\frac{d\mu_{\mathrm{EP}}}{dx} = -\frac{d\mu_{\mathrm{EP}}}{d(pH)}\frac{d(pH)}{dx} = \text{constant} \tag{1.2}$$

$$\Rightarrow \mu = -px \tag{1.3}$$

Substituting into Equation 1.1 and integrating gives:

$$\frac{1}{C}dC = \frac{Ep}{D}xdx \tag{1.4}$$

$$\Rightarrow C = C_0 e^{\frac{-pEx^2}{2D}} \tag{1.5}$$

Thus, the protein adopts a Gaussian distribution in the channel centered around its pI, with a standard deviation of:

$$\sigma = \sqrt{\frac{D}{pE}} = \sqrt{\frac{D}{-\frac{d\mu_{\mathrm{EP}}}{d(pH)}\frac{d(pH)}{dx}E}} \tag{1.6}$$

The resolution between two protein bands in a channel is often evaluated using the separation resolution R_s, where x here denotes the distance between the center of each Gaussian band:

$$R_s = \frac{\Delta x}{4\sigma} \tag{1.7}$$

By substituting for $\Delta x = \Delta(pI)\frac{dx}{d(pH)}$ and σ (from Equation 1.6) [12]:

$$R_s = \frac{\Delta(pI)}{4}\sqrt{\frac{-E\frac{d\mu_{\mathrm{EP}}}{d(pH)}}{D\frac{d(pH)}{dx}}} \tag{1.8}$$

Thus, the separation resolution between a given pair of analytes in an IEF device can be improved by increasing the applied electric field and/or by decreasing the range of pH exercised in the device ($\frac{d(pH)}{dx}$). In practical application, CA-IEF separations readily achieve resolution of proteins with pI differences of as little as 0.02 pH units [7], with restriction of the pH range of separation to only 0.25 pH units yielding an impressive resolution limit of $\Delta(pI) \approx 0.001$ in an IPG system [12, 16].

Rearranging for a minimum acceptable resolution of $R_s = 1$:

$$\Delta(pI)_{\min} = 4\sqrt{\frac{D\Delta(pH)}{-V\frac{d\mu_{\mathrm{EP}}}{d(pH)}}} \tag{1.9}$$

Cathodic Drift and Mobilization of Focused Protein Zones. In practice, IEF is not a purely equilibrium separation. Changes in the slope and channel position of the ampholyte-imposed pH gradient have been almost universally described [7]. Typically, a phenomenon known as "cathodic drift" is observed, in which focused species move towards the cathode at a rate dependent on the applied electric field (see Section 3.4.2). This phenomenon is most likely caused by the presence of trace quantities of acrylic acid in commercial acrylamide monomer preparations, which imbues a slight negative charge to polyacrylamide gel matrices commonly used for IEF [7]. The resulting effect on the electrical double layer is to induce electroosmotic flow (EOF) according to the Helmholtz-Smoluchowski equation $u_{\mathrm{EO}} = -\frac{\epsilon\zeta E_x}{\eta}$, which predicts a linear dependence on the EOF velocity u_{EO} on the applied electric field E_x, with the constant of proportionality (the electroosmotic mobility, μ_{EO}) comprising the electrical permittivity ϵ and dynamic viscosity η of the fluid medium, and the zeta potential ζ of the gel surface (see [17] for details).

To test the hypothesis of gel charge affecting the drift direction and velocity in microscale IEF, we introduced negative charge into polyacrylamide separation gels prior to IEF via an acrylamide derivative known as immobiline, having a pK_a of 3.6. Thus, under focusing conditions over a pH range of 4–9, the added immobiline monomers will largely be negatively charged. We measured the cathodic/anodic drift velocity for GFP isoforms in a set of gels ranging in immobiline concentration from 0–1000 nM (Figure 1.4). A clear trend shows that increasing concentrations of immobiline cause a reduction in the velocity of anodic drift (the prevailing drift direction in this particular IEF experiment), and eventually reversal of the drift direction such that protein species were driven rapidly towards the cathode under focusing conditions. This experiment lends weight to the hypothesis that even incremental changes to the electrostatic charge of polyacrylamide gels can produce EOF-generated focusing instabilities in IEF, an otherwise equilibrium separation regime.

Drift and disruption of the pH gradient can be a useful phenomenon from the perspective of linking isoelectric focusing with downstream detection or analysis. "Chemical mobilization" processes are widely used in capillary electrophoresis to shift focused bands past a single-point detector, or to elute components of the separation from the capillary for further fractionation or analysis. Mobilization can be induced in several ways, e.g. by adding catholyte to the anode chamber, or vice versa; or by adding salts or zwitterionic buffers to either chamber. The movement of the pH gradient in response to such changes in boundary

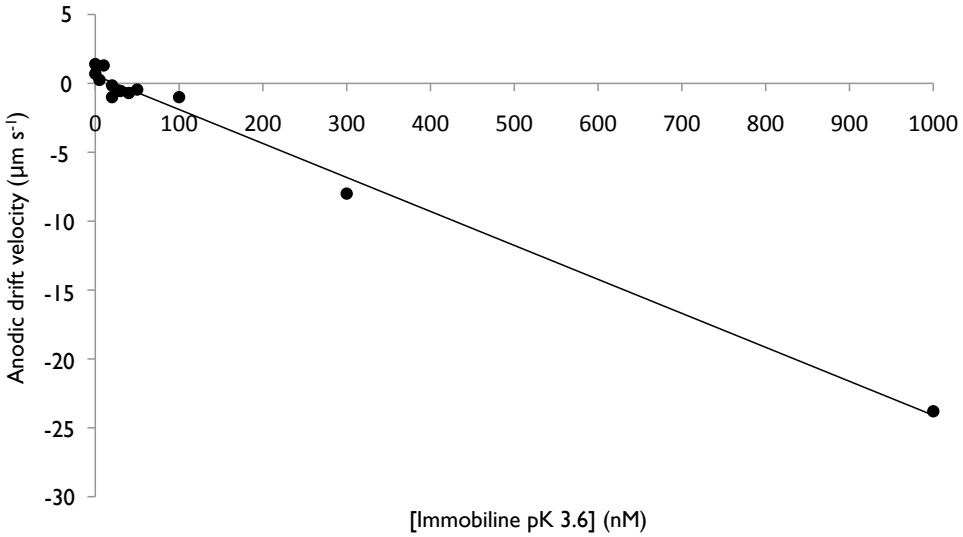

Figure 1.4: Arbitrary drift velocity of GFP isoforms against immobiline addition in a set of 3.5%T, 20% v/v Polybuffers 74 + 96, 4% w/v CHAPS devices polymerized using APS/TEMED shows increased cathodic drift with increasing additions of immobiline pK_a 3.6.

condition compositions stems from an electroneutrality argument as follows:

$$[\mathrm{H}^+] + \sum[\mathrm{NH}_3^+] = [\mathrm{OH}^-] + \sum[\mathrm{COO}^-] \tag{1.10}$$

Where square brackets denote concentrations, and the NH_3^+ and COO^- terms refer to charged chemical groups on the focused ampholytes. To achieve anodic mobilization (in which the pH gradient is induced to shift towards the anode), we require $\sum[\mathrm{NH}_3^+] < \sum[\mathrm{COO}^-]$ across the pH range, such that all ampholytes have a net negative charge. This condition could be achieved upon an increase in pH, however this thought experiment would violate equality of Equation 1.10. If, instead, a second carrier of positive charge, $\mathrm{X}^{\mathrm{n}+}$, is introduced to the system, such a change in pH occurs, given:

$$[\mathrm{X}^{\mathrm{n}+}] + [\mathrm{H}^+] + \sum[\mathrm{NH}_3^+] = [\mathrm{OH}^-] + \sum[\mathrm{COO}^-] \tag{1.11}$$

Thus, the addition of any cation other than H^+ to the anodic chamber will cause net negative charge in the ampholytes, causing mobilization of the pH gradient towards the anode. In Chapter 3, anodic mobilization is achieved by addition of glycine to the anodic chamber, allowing "washout" of the pH gradient within a microchannel, allowing further analysis of

captured protein analytes using fluorescent antibody probing. Thus, the "quasi-equilibrium" nature of IEF, including the ability to rationally perturb the pH gradient by chemical means at its boundaries only, provides convenient access to integrative multi-stage assays within enclosed microfluidic devices.

1.2.1.2 Non-equilibrium Separations — SDS-PAGE

Sodium dodecyl sulfate (SDS) polyacrylamide gel electrophoresis (PAGE) is a weight-based separation methods comprising the separation of a denatured protein sample upon the application of an applied electric field in a porous polyacrylamide separation matrix. The sample is typically denatured using SDS, a reducing agent such as dithiothreitol (DTT), and heat; although many sample treatments have been applied to retain native function of the protein targets of interest [18].

Transient Isotachophoresis. Many SDS-PAGE protocols make use of an electrochemical stacking phenomenon known as transient isotachophoresis (tITP) to compact protein samples in the separation axis at the start of the separation process. This phenomenon stems from the use of discontinuities in buffer composition and pH between the sample and the polyacrylamide gel. In addition to a pH change between stacking and sieving gels, a porosity discontinuity is used to trigger a transition between isotachophoretic and zone electrophoresis stages.

To understand tITP, we begin with a simple mathematical treatment of discontinuous buffer systems attributed to Kohlrausch [19, 20]. The electrical conductivity of any ionic solution can be written as:

$$\sigma = e \sum c_i \mu_{i,\mathrm{EP}} z_i \tag{1.12}$$

Where e is the charge of an electron; and c_i, $\mu_{i,\mathrm{EP}}$, and z_i are the concentration, mobility, and elementary charge, respectively, of the i^{th} ion in the solution. In zone electrophoresis, ionic mobility is the distance moved, d, per unit time t by a particle for a given applied electric field E:

$$\mu_{\mathrm{EP}} = \frac{d}{tE} = \frac{u_{\mathrm{EP}}}{E} \tag{1.13}$$

More formally, this mobility stems from the balance of an electrophoretic force qE and a drag force fu_{EP}, such that $\mu_{\mathrm{EP}} = \frac{q}{f}$, where q is the effective charge of the ion, having a complex dependence on the size of the ion and its environment [17, 20].

Monoprotic buffer molecules generally have an elementary charge z that is determined by solution pH according to the Henderson-Hasselbalch equation:

$$\mathrm{p}H = \mathrm{p}K_a + \log\left(\frac{[\mathrm{A}]^-}{[\mathrm{HA}]}\right) \tag{1.14}$$

Where [HA] and [A^-] are the concentrations of the conjugate acid and base of species A, and $\mathrm{p}K_a = -\log(K_a)$, K_a being the acid dissociation constant of the species. Setting $x_i = \frac{[\mathrm{A}]^-}{[\mathrm{A}]^- + [\mathrm{HA}]}$, the fraction of dissociation, we can readily write the *average* velocity of a charged titratable particle as:

$$s_i = E\mu_{i,\mathrm{EP}}x_i \tag{1.15}$$

We consider a discontinuity in buffer composition for separations run from top to bottom in a gel or capillary, such that the lower (L) buffer contains a "fast" ion γ and the upper (U) buffer contains a "slow" ion α ($\mu_{\gamma,\mathrm{EP}}x_\gamma > \mu_{\alpha,\mathrm{EP}}x_\alpha$). Upon the application of electric field, the discontinuity between upper and lower buffers will be maintained, since if a molecule of γ were placed in the upper buffer, it would outrun the α molecules; and likewise, if a molecule of α were placed in the lower buffer, it would fall behind γ molecules. This thought experiment implies that given continuity of mass and electrical current, the velocity of each buffer zone should be the same:

$$s_\alpha = E_U\mu_{\alpha,\mathrm{EP}}x_\alpha = s_\gamma = E_L\mu_{\gamma,\mathrm{EP}}x_\gamma \tag{1.16}$$

Since the two buffers are electrically in series, the current (I) through them should be the same, and from Ohm's law $E_L = \frac{I}{\sigma_L A_s}$ and $E_U = \frac{I}{\sigma_U A_s}$, where A_s is the cross-sectional area of the separation medium. From Equations 1.12 and 1.15, for a counter-ion β that is common between the two buffer zones:

$$\frac{\mu_{\alpha,\mathrm{EP}}x_\alpha}{c_\alpha\mu_{\alpha,\mathrm{EP}}z_\alpha + c_{\beta_U}\mu_{\beta,\mathrm{EP}}z_\beta} = \frac{\mu_{\gamma,\mathrm{EP}}x_\gamma}{c_\gamma\mu_{\gamma,\mathrm{EP}}z_\gamma + c_{\beta_L}\mu_{\beta,\mathrm{EP}}z_\beta} \tag{1.17}$$

Electroneutrality in each solution prescribes that $c_\alpha z_\alpha = -c_{\beta_U}z_\beta$ and $c_\gamma z_\gamma = -c_{\beta_L}z_\beta$, so:

$$\frac{C_\alpha}{C_\gamma} = \frac{x_\gamma c_\alpha}{x_\alpha c_\gamma} = \frac{\mu_{\alpha,\mathrm{EP}}z_\gamma(\mu_{\gamma,\mathrm{EP}} - \mu_{\beta,\mathrm{EP}})}{\mu_{\gamma,\mathrm{EP}}z_\alpha(\mu_{\alpha,\mathrm{EP}} - \mu_{\beta,\mathrm{EP}})} \tag{1.18}$$

For total species concentrations $C_i = \frac{c_i}{x_i}$. This "regulating function" reveals a fascinating behavior of discontinuous buffer systems, namely that the concentrations of the α and γ ions on either side of the discontinuity are continuously prescribed (regulated) by their mobilities. The power of this phenomenon in terms of the ability to concentrate protein samples prior to zone electrophoresis is best conveyed using a specific example.

Consider the case in which the slow ion α is glycinate (Gly^-), the fast ion γ is chloride (Cl^-), and the counter-ion β is potassium (K^+). The parameters for this system are $z_\alpha = z_\gamma = -1$, $\mu_{\alpha,\mathrm{EP}} = -15$ (in units of 10^{-5} $\frac{\mathrm{cm}^2}{\mathrm{Vs}}$), $\mu_{\gamma,\mathrm{EP}} = -37$, $\mu_{\beta,\mathrm{EP}} = +37$. In order to concentrate proteins at the interface between the α and γ zones, we require protein mobilities to fall within the range of the effective mobilities $\mu_{i,\mathrm{EP}} x_i$ of glycinate and chloride. Above pH 8, serum proteins typically have free solution mobilities in the range of -0.6 to -7.5. Since the fraction of glycinate, x_α, can be adjusted via pH given Equation 1.14, choosing the pH of the system to be approximately 8.1 for $\mathrm{p}K_{a,Gly} \approx 9.6$ yields $x_\alpha \approx \frac{1}{30}$, and thus $\mu_{\alpha,\mathrm{EP}} x_\alpha \approx -0.5$. This effective mobility for the slow trailing ion Gly^- falls below that of a typical protein, meaning that isotachophoretic stacking of proteins should occur in this system at pH 8.1.

We now consider stacking of serum albumin in this Cl^-/Gly^- system, where we set the slow ion α to be albumin itself. Further parameters that are necessary to solve Equation 1.16 are $z_\alpha \approx -30$ (the approximate number charges on an albumin molecule at pH 8.1), and $\mu_{\alpha,\mathrm{EP}} = -6$. Solving Equation 1.16 yields $\frac{[\mathrm{Albumin}]}{[\mathrm{Chloride}]} \approx 10 \times 10^{-3}$. So for a chloride concentration of 60 mM in the leading electrolyte zone, the albumin concentration in its stack between the Cl^- and Gly^- zones is set by the parameters of the discontinuous system to be 600 μM (an enormous concentration, given typical samples concentrations in the nM range).

In separation systems of fixed cross-sectional area, the length of a protein zone should thus scale linearly with the total amount of that protein originally present within the system, given that the *concentration* of protein within the zone is the parameter that is regulated. This facet of transient ITP is an important consideration for microscale stacking processes, since the width of the protein stack (which affects the average spatial standard deviation of protein zones in the stack, σ_o) can be considerable for large injected protein masses. Thus, a tradeoff can exist between separation resolution in downstream zone electrophoresis, $R_s \approx \frac{d}{4(\sigma_o + \sqrt{2Dt})}$ (where d is the distance between neighboring Gaussian protein zones, D is average diffusivity and t is time), and the ability to assay samples of large mass in microfluidic channels of small cross-sectional area.

In the specific example, if a 20 μl sample of albumin at 1.5 μM were stacked in a system of 1 cm^2 cross-sectional area, the resulting albumin zone would be roughly 0.5 μm long. However, if the system were 100 $\mu\mathrm{m}^2$ in cross-section (a typical dimension for a microfluidic channel), the zone would be 50 cm long; completely impractical as a starting zone for electrophoresis

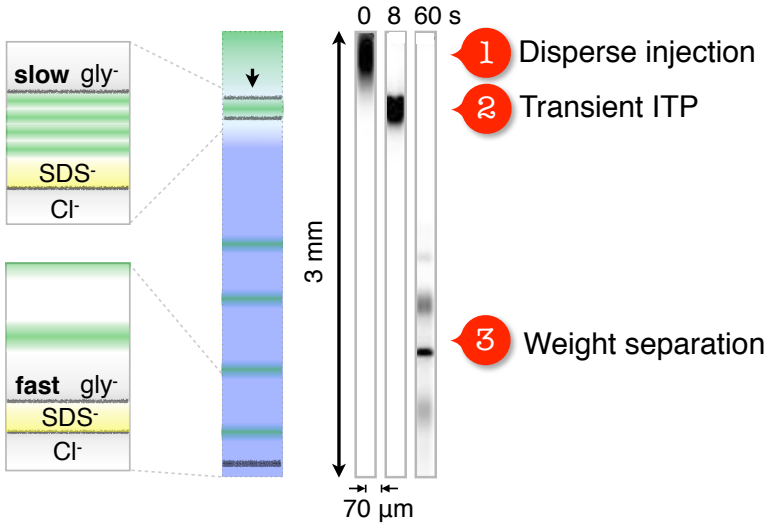

Figure 1.5: A schematic of transient ITP stacking and transition to zone electrophoresis in microfluidic SDS-PAGE. At top left, proteins are stacked between chloride and glycine buffers following injection into the microchannel. At bottom left, a transition in gel pore size leads to reduced mobility of protein species, which fall behind the buffer discontinuity and separate according to their molecular weights. At right, inverted fluorescence micrograph data show stacking and separation phases for a 4-protein mixture.

in mm-lengthscale separation channels. The inverse relationship between zone length and channel cross-sectional area clearly places strong geometrical limitations on the starting sample volume for microfluidic separations of proteins in the typical pM–μM concentration range.

Zone Electrophoresis. After transient ITP, stacked protein zones must be separated to complete SDS-PAGE. The transition between these phases is typically instigated by building a pH and/or pore size discontinuity into the separation gel to manipulate the relative mobilities of the trailing ion (typically glycine) and the protein analytes. The integration of denatured sample stacking and separation was pioneered by Laemmli for the study of bacteriophage assembly [21], see Figure 1.5. Here, a pH change from 6.8 in a 3%T stacking gel, to 8.8 in a 8-10%T separation gel increases the effective mobility $\mu_{\mathrm{Gly}^-,\mathrm{EP}} x_{\mathrm{Gly}^-}$ of the glycinate trailing ion by around 100-fold, in concert with a substantial drop in the mobility of protein analytes, causing the thin starting zones present in the ITP stack to fall behind the buffer discontinuity into a region of homogeneous buffer composition.

The governing equation for the reduced protein mobility in polymer gels is due to Ferguson

[22, 23]:

$$\log(\mu_{i,\mathrm{EP}}) = \log(\mu_{i,\mathrm{EP},0}) - K_r T \tag{1.19}$$

Where K_r is known as the retardation coefficient, and T is the weight fraction of monomers in the gel. Here, the denatured proteins hold approximately equivalent charge:mass ratios (and thus free solution mobilities, $\mu_{i,\mathrm{EP},0}$) due to the stoichiometric addition of SDS molecules to protein chains at a ratio of around one SDS molecule for every two amino acid residues [18]. Migration proceeds in such a way as to produce a log-linear relationship between protein molecular weight and separation distance, as extensively verified for on-chip SDS-PAGE (Figure 6.6 and [23]). This phenomenological migration pattern allows molecular weight to be predicted from migration distance of a given target of interest when SDS-PAGE is coupled with a downstream band identification procedure such as western blotting.

1.3 Reactive Processes in Porous Media

1.3.1 Enzyme Reactions

Enzyme catalysts convert reactants to products by forming a bound complex with substrate and initiating a biochemical change to produce the product. It is often of interest to perform enzyme reactions in porous media such as polymer beads, since such systems are amenable to scale-up in continuous reactors that do not require extra provisions for separating the enzyme from reaction products. In our hands, enzyme immobilization (at least on the timescale of the activity assay) is an important facet of the integration of multiple-readout assays.

Several kinetic effects are often observed following immobilization of enzymes in polymer networks, including [24]:

- *Conformational/steric effects:* Immobilization of enzymes can change their native conformations, or cause steric interactions between polymer chains and enzyme active sites (i.e. physical blockage of substrate access to the enzyme).
- *Partitioning effects:* If the polymer is at equilibrium with bulk solution containing a known concentration of substrate, the actual substrate concentration within the polymer can be biased due to physical exclusion, hydrophobic, or electrostatic interaction of the substrate with the polymer.
- *Mass transfer effects:* Substrate may distribute by convective and diffusive transport modes to immobilized enzyme sites. Thus, mass transfer resistances relating to substrate penetration through the polymer volume can lead to non-linear spatial concen-

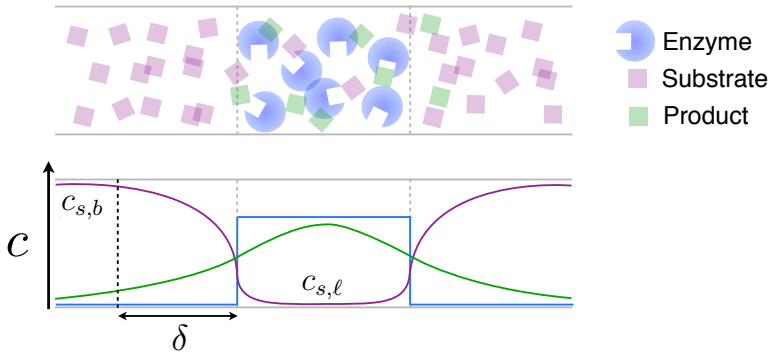

Figure 1.6: A schematic of mass transport around an immobilized enzyme plug in a microchannel without electrophoretic delivery of substrate. Substrate diffuses into the enzyme zone and is converted to product, causing spatial non-uniformity in substrate and product concentration profiles. Note especially the formation of a boundary layer of thickness δ in which substrate concentration transitions form a bulk concentration $c_{s,b}$ to a local concentration $c_{s,\ell}$.

trations of substrate with complex effects on kinetics that depend on the interplay between enzyme turnover rates and mass transfer rates.

The effect of mass transfer limitations in such systems is readily determined and well-studied in the chemical engineering field. In order to justify the interplay between diffusional ("internal") mass transfer and substrate turnover, consider a band of enzyme (with arbitrary length) immobilized in a polyacrylamide gel within a microchannel of height h and width w. Further, we take the substrate to be initially evenly distributed throughout the pores of the gel in the vicinity of the enzyme band at a bulk concentration $c_{s,b}$. If substrate is not electrophoretically delivered to the enzyme over time, a depletion region forms as the enzyme converts substrate to product that extends away from the enzyme band in either direction. At a particular snapshot in time, the depletion region will have a characteristic length δ, and we can consider the effect of the growth of the region on the local substrate concentration $c_{s,\ell}$ available to the enzyme. Firstly, the diffusive flux J_D of substrate through the depletion zone can be written as [25]:

$$J_D = \frac{D(c_{s,b} - c_{s,\ell})hw}{\delta} \tag{1.20}$$

The reactive flux J_R for Michaelis-Menten kinetics, which prescribes a shift in reaction order from one to zero as the substrate concentration increases (i.e. saturating enzyme turnover

rate with substrate concentration), is likewise:

$$J_R = \frac{V_{\max} c_{s,\ell} h w}{c_{s,\ell} + K_m} \tag{1.21}$$

Where $V_{\max}$ is the maximum reaction rate in mol m^{-2} s^{-1} (for an enzyme concentration per unit of channel cross-section) and K_m is known as the Michaelis constant, the substrate concentration at which a rate of $\frac{1}{2}V_{\max}$ is achieved. We consider the first-order range in the enzyme's behavior within which it responds linearly to changes in the substrate concentration, i.e. when $c_{s,\ell} \ll K_m$,

$$J_R \approx \frac{V_{\max} c_{s,\ell} h w}{K_m} \tag{1.22}$$

In this system, diffusion and reaction are coupled, such that we can equate the two fluxes, yielding an expression for the ratio of the substrate concentration in the depletion zone to that in the bulk of the microchannel:

$$\frac{c_{s,\ell}}{c_{s,b}} = \frac{1}{\frac{V_{\max}\delta}{K_m D} + 1} = \frac{1}{Da + 1} \tag{1.23}$$

Where the Damköhler number $Da = \frac{V_{\max}\delta}{K_m D} = \frac{\text{Diffusion time}}{\text{Reaction time}}$, a convenient dimensionless parameter that evaluates the interplay between diffusion and reaction rates. As time goes on, δ becomes larger due to depletion of substrate, causing a drop in the local substrate concentration $c_{s,\ell}$, and a corresponding drop in J_R. Thus, in practice, we choose the bulk substrate concentration $c_{s,b}$ to be much larger than K_m such that the enzyme operates with zero-order kinetics (i.e. with a rate insensitive to substrate concentration), and/or take measurements of enzyme activity from *initial* substrate conversion rates in order to minimize the effect of diffusional limitation on enzyme activity.

Alternatively, the width of the depletion zone can be reduced or even completely eliminated with respect to the characteristic channel width by applying electric field to deliver a charged substrate by electrophoresis with flux:

$$J_{EP} = c_{s,b} u_{EP} h w \tag{1.24}$$

Such that the thickness of the depletion zone upstream of the enzyme band can be roughly determined from Equations 1.20 and 1.24 to be $\delta \sim \frac{D}{u_{EP}}$ for the small $c_{s,\ell}$ regime. Thus,

electrophoretic delivery of substrate can ensure that the maximum substrate concentration $c_{s,b}$ is available to the immobilized enzyme by reducing δ such that $Da \ll 1$ and $c_{s,b} \approx c_{s,\ell}$, known as "reaction-limited" conditions. Conversely, if the δ is allowed to grow in the absence of electrophoretic substrate delivery, eventually $Da \gg 1$ and $c_{s,\ell} \ll c_{s,b}$; a condition in which the enzyme is starved of substrate and the system is referred to as being in a "mass transfer-limited" regime.

Less readily analyzed is the effect of conformational and/or steric effects of enzyme immobilization in closed microfluidic systems. The act of chemically immobilizing enzymes within polymer networks has been found to produce 2–3 order of magnitude reductions in k_{cat} [26]. In Chapter 2, however, we show that physical immobilization of enzymes by trapping within dense polyacrylamide networks does not reduce k_{cat}, perhaps because of the lack of the permanent inhibition of enzyme activity generally caused by chemical immobilization approaches. Further, partitioning effects are accounted for using direct measurement of substrate concentration within polyacrylamide matrices.

1.3.2 Antibody-Antigen Reactions

The determination of binding kinetics by intrinsic reaction or transport rates (or a mixture of the two), is equally applicable in the case of antibody binding to immobilized ligand within polymer materials. The same analytical framework as in Section 1.3.1 applies, in fact, since antibody binding to antigen follows first order kinetics, at least for low antigen "occupancy" by antibody. Here, we are interested in the relative benefits of probing for antigen via electrophoretic delivery of antibodies throughout polyacrylamide pores, as opposed to diffusive delivery of antibody to plane surfaces patterned with antigen. An in depth discussion of this subject is carried out in Chapter 4, but the concept of boundary layer diffusional transport resistance plays a large role in the intuition underlying expected benefits for "through-pore" electrophoretic probing (Figure 1.7).

In cases in which relatively large binding partners (with respect to the gel pore size) such as antibodies are delivered to polymer surfaces, the effect of partitioning on the expected reaction kinetics becomes an important concern. Even at equilibrium, the exclusion of antibody from the polymer causes its concentration to be lower within the polymer matrix than within the bulk solution, as expressed by Ogston for rigid spheres of radius a in a matrix of long cylindrical fibers of radius a_f [27]:

$$K = \frac{c_{\text{Ab},\ell}}{c_{\text{Ab},b}} = e^{-\phi\left(1+\frac{a}{a_f}\right)^2} \tag{1.25}$$

Where K is the partition coefficient; a ratio of $c_{\text{Ab},\ell}$ and $c_{\text{Ab},b}$, the local gel and bulk solution

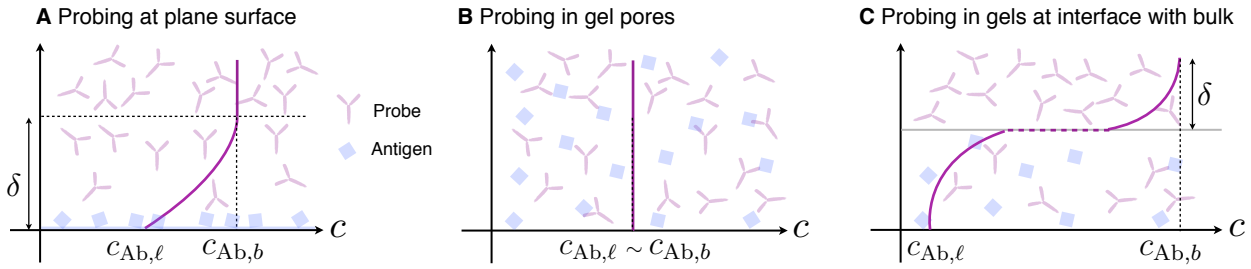

Figure 1.7: Schematics of mass transport regimes in (A) antibody probing at plane surfaces, (B) within gel pores (middle), and (C) within thick gel layers in contact with bulk solution. At surfaces, external diffusive mass transfer resistance generally arises in thin boundary layers (thickness δ) due to local probe depletion caused by reaction at and/or beneath the surface. Internal competition between reaction and diffusion also produces non-linear probe concentration gradients in (C). Within gel pores, however, electrophoretic delivery of probe eliminates diffusive boundary layers and spatial non-uniformities in probe concentration. Note the discontinuity in probe concentration at the solution-gel interface in (C) due to probe partitioning effects.

concentrations of antibody probe; and ϕ is the volume fraction of the polymer network. For proteins, the radius a can be taken to be the Stokes-Einstein radius $a = \frac{k_B T}{6\pi\eta D}$, where k_B is the Boltzmann constant, T is temperature, and D is the diffusivity of the protein in free solution.

Experimental measurements of K for proteins diffusing into pieces of polyacrylamide gel confirm a strong log-linear effect of ϕ on K. For bovine serum albumin (66 kDa, $a \sim 3.8$ nm [20]), partition coefficients on the order of 10^{-2} were measured for ϕ in the 8-10% range [27]. Even for reaction-limited antibody-antigen kinetics, for which the characteristic reaction time is $\tau_R = \frac{1}{k_{off}+k_{on}c_{Ab,\ell}}$ and the equilibrium antigen occupancy is $\frac{c_{Ab-Ag,\ell}}{c_{Ag,\ell}} = \frac{c_{Ab,\ell}/K_D}{1+c_{Ab,\ell}/K_D}$ (see Section 4.2.2) [25], the exclusion of antibodies from dense gel networks can have strong detrimental effects on both assay time (through τ_R) and sensitivity (through antigen occupancy at equilibrium). This exclusion effect is directly relevant to probing of polyacrylamide sheets as in Section 7.2.1, where it is counteracted by raising $c_{Ab,b}$, albeit at a cost in the usage of relatively expensive antibody probe reagents.

1.4 Principles of Integrative Assay Design

1.4.1 Design Challenges for Multi-Stage Assays at the Microscale

Though integrating multiple assay readouts brings advantages in assay quantitation, reproducibility, and automation, the design of material transport and analysis inherent in multiplexing poses difficult engineering problems, including:

- *Small diffusion-length regimes operating within microfluidic devices:* Separation processes, especially non-equilibrium separations such as SDS-PAGE, are pitted against diffusion. Retaining separation resolution between protein bands thus places considerable emphasis on carrying out downstream analysis within the diffusion timescale, since the separation resolution $R_s \propto \frac{1}{\sqrt{t}}$ (see Figure 3.6). For downstream analyses requiring longer timescales, e.g. antibody probing, immobilization of the separated protein constituents is a viable option for circumventing rapid diffusion kinetics operating on the microscale. In such cases, the immobilization timescale $\tau_{\text{react}} = \frac{1}{k_{\text{react}}}$ (for a first order capture reaction) should also be at least as small as e.g. the time for the separation resolution between a given pair of peaks to halve under the diffusion-only conditions following completion of a separation, $t_{\frac{1}{2}R_{s,0}} \sim \frac{\sigma_0^2}{2D}$, where σ_0^2 is the initial average peak variance at the end of the separation phase, and D is the average diffusivity of the peaks. The tradeoff between these timescales makes the race between diffusion and capture clear, an especially demanding one on τ_{react} for high quality separations with low σ_0^2.

- *Compatibility of buffer systems:* Tradeoffs almost always exists between the demands of integrated assay stages in terms of optimal buffer composition for closed microfluidic systems. Electrophoretic separation processes, in general, require low conductivity, alkaline, aqueous, and dispersive (i.e. detergent-containing) conditions. Antibody binding processes, on the other hand, are typically optimized at high salt concentrations, and low concentrations of denaturing detergents. Immobilization processes can be prone to cross-reactivity with buffer constituents, calling for low concentrations of e.g. detergents. Optimizing such a multi-dimensional parameter space is not a trivial task, because the number of "successful" independent experiments required to quantify assay performance scales as $n \sim v^p$ where v is the number of values (e.g. concentrations) taken by p different parameters (e.g. buffer constituents). Even for a modest 5 parameters with only 3 possible values each, the number of experiments (243) quickly becomes implausible for low-throughput, prototype assays, unless an arbitrary walk through the space is conducted based on experience or prior knowledge of likely incompatibility between parameter values.

- *Linear integration pathway:* Even given the number of possible combinations of parameter values that apply to all assay stages in a closed system, the nature of assay development prescribes a linear path from one assay stage to the next. Specifically, a separation stage is often developed/optimized first, followed by a capture stage and a detection/readout phase. The task of integration is thus a process of continual redesign of each assay phase, not just to be individually feasible, but also to be feasible as a connected pipeline.

- *Detection challenges:* At each assay stage in a microfluidic device, the experimenter usually encounters material losses, diffusive spreading of material, non-saturating detection reagent interaction with targets, and low optical path lengths. These factors

all contribute to the challenge of achieving limits of detection equal or superior to macroscale gold standard assays, which can offset similar non-ideal assay performance through effective optical detection pathlengths up to 100-times those of microfluidic systems.

1.4.2 Protein Immobilization Chemistries Enabling Coupled Assay Stages

The design and integration of new engineered materials can greatly accelerate innovation of tools for biological discovery. A range of conjugation chemistries can allow for protein biomarker derivatization, capture, and other modes of downstream manipulation. These chemistries leverage reactivity of synthetic materials with specific reactive groups already built into the amino acid scaffold of target proteins, which can produce material-protein interactions of varying stability and spatial orientation.

1.4.2.1 Principles of Protein Reactivity

Many conjugation processes are targeted towards nucleophilic amino acids [28]. Nucleophiles are electron-rich atoms or moieties that can participate in the formation of covalent bonds with electron-poor reaction partners (electrophiles). Residues including lysine and cysteine present ionizable side chains that can act as potent nucleophiles in the unprotonated state. The order of nucleophilic reactivity pertaining to protein conjugation reactions is R—S^- > R—NH_2 > R—COO^- = R—O^-. Thus, primary amine (—NH_2) and thiol (—SH) groups are common targets for protein immobilization and derivatization strategies.

Reaction rates between synthetic reagents or surfaces and proteins depend upon many factors, including the denaturation state of the protein, the solution pH, the presence of small molecules competitors and influence of unproductive side-reactions with solution constituents, the folding (tertiary) structure of the protein target among other contributors to the solvent-accessibility of target residues.

1.4.2.2 Reactions at Primary Amines: NHS Esters & Azlactones

N-hydroxysuccinimide (NHS) esters are common primary amine-specific reagents that form stable amide bonds between synthetic agents and protein targets (Figure 1.8). The broad applicability of such reagents in protein derivatization stems from their high reactivity, tempered by high specificities given that reaction products with other nucleophiles such as sulfhydryl and hydroxyl groups are not stable in aqueous buffers [28]. Reactions are typically performed in the pH 8–9 range in response to a tradeoff between hydrolysis of the ester (affecting the fraction of conjugate available for reaction), and the reactivity of terminal amines on the protein target. Increasing pH decreases the half-life of NHS esters from

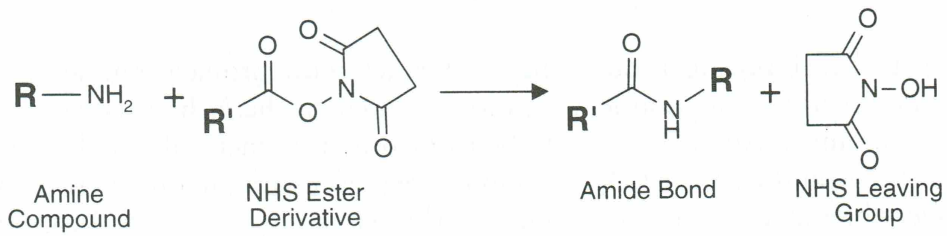

Figure 1.8: General schematic of the reaction between a primary amine and an NHS ester, resulting in the formation of a covalent amide bond (reproduced from [28]).

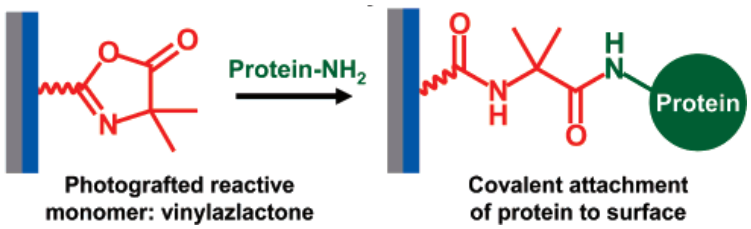

Figure 1.9: Spatially addressable photopatterning of proteins onto microscale polymer structures enabled by primary amine-reactive vinyl dimethyl azlactone comonomers (reproduced from [29]).

1 hour at pH 8 to less than 15 minutes at pH 8.6. However, the deprotonated (reactive) fraction of primary amines increases from approximately 4% to 14% over the same pH range.

Nonetheless, this reaction chemistry is particularly useful in conjugation of fluorescent dyes to target proteins, including antibody probes. Further, an NHS ester of benzophenone becomes a particularly effective reagent in the organic-phase synthesis of light-reactive acrylamide derivatives, as described in Section 1.4.5.

A second immobilization chemistry has also been fruitful in the immobilization of proteins at the microscale. Vinyl azlactone derivatives such as vinyl dimethyl azlactone are capable of undergoing covalent bond-forming ring-opening reactions with aliphatic primary amines and thiolates in the absence of a catalyst at room temperature, and are also well-suited to copolymerization within polyacrylamide matrices (Figure 1.9) [29, 30]. This chemistry has the benefit of allowing spatially addressed protein capture since polymer structures can be adorned with VDMA monomers using mask-based photolithographic techniques [29].

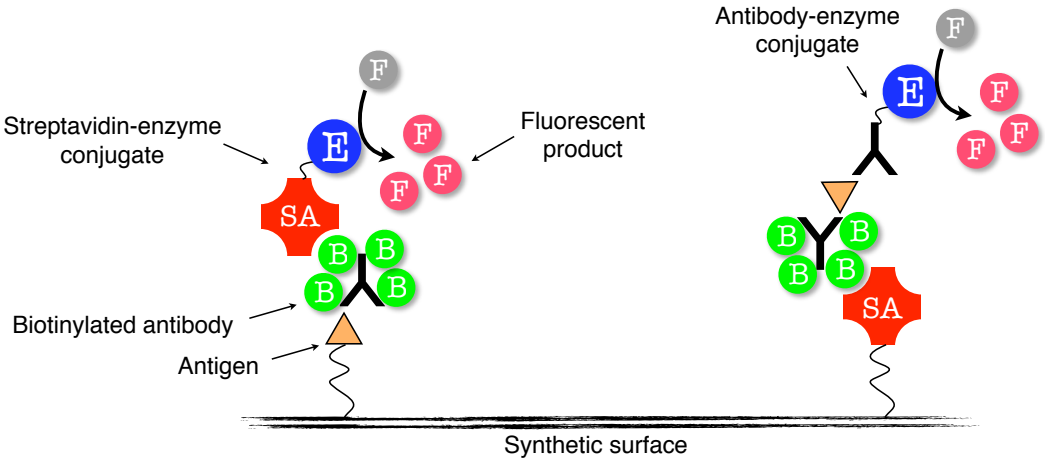

Figure 1.10: Example assay systems comprising detection of an antigen using a specific biotinylated antibody. At left, the biotin moiety on a detection antibody links it to a streptavidin-enzyme conjugate, which catalyzes conversion of a dye precursor to a fluorescent product, thus achieving assay readout. At right, the streptavidin-biotin interaction is used to anchor a capture antibody to the surface, and detection is made using an antibody-enzyme conjugate.

1.4.2.3 Biologically Inspired Protein Conjugation: Biotin-Streptavidin

A popular conjugation system in the protein bioassay field is the high affinity, noncovalent interaction between the small molecule B-vitamin, biotin, and the tetrameric protein streptavidin, from the bacterium *Streptomyces avidinii*. Biotin is typically conjugated to capture antibodies through e.g. NHS chemistry, and the streptavidin protein used to anchor the antibodies to synthetic surfaces, or to act as a bridge to fluorescent assay readouts by direct fluorescent or enzyme labeling of the streptavidin binding partner (Figure 1.10). The biotin-streptavidin interaction is highly specific, and resists dissociation under a range of aqueous conditions, including highly chaotropic ones (e.g. 6–8M guanidine at pH 1.5).

1.4.3 Protein "Pseudo-Immobilization" by Molecular Weight: Pore Limit Electrophoresis

In addition to chemical reactivity, the variation in size of protein molecules can be leveraged to trap proteins between assay stages to enable their integration. Pore limit electrophoresis (PLE) was conceived in the mid-1960s as a slab gel electrophoresis method allowing highly spatially resolved separation of protein bands from complex samples over a broad molecular weight range [31–35]. Proteins electrophorese through a sieving gel whose pore-size decreases to dimensions on the order of the effective diameter of each macromolecule, leading to a progressive retardation of the analytes to a near stop. This behavior can be derived by

considering the mobility of a protein i as it travels through a linear polyacrylamide gradient of length L in a spatial ordinate x, from low to high %T [32]:

$$u_{i,\mathrm{EP}}(x) = \frac{dx}{dt} = E(x)\mu_{i,\mathrm{EP},0}e^{-RG(x)} \tag{1.26}$$

Where $u_{i,\mathrm{EP}}(x)$ is the protein's velocity at a given distance in the separation gel, $\mu_{i,\mathrm{EP},0}$ is the free solution mobility, R is a constant taking into account all retardation terms, and $G(x) = \frac{G_L - G_0}{L}x + G_0$ is a linear gel concentration from G_0 at $x = 0$ to G_L at $x = L$.

Equation 1.26 can be solved for $x_{t=0} = 0$ and constant $E(x) = E$ to give:

$$x(t) = \frac{-L}{R(G_0 - G_L)} \ln\left[1 - \frac{R(G_0 - G_L)e^{G_0 R}E\mu_{i,\mathrm{EP},0}t}{L}\right] \tag{1.27}$$

Thus, each analyte traces a logarithmic trajectory in channel distance as a function of Vt according to its mobility terms $\mu_{i,\mathrm{EP},0}$ and R. Note that true arrest of protein bands is never attained, as the proteins asymptotically approach zero velocity (at least within the Ferguson migration regime).

Conveniently, PLE yields a log-linear relationship between molecular weight and migration distance [31, 32]. Sommer et al. recently described a microfluidic implementation of PLE, and in doing so, demonstrated that the long run times (10-40 hrs [31, 35]) can be significantly reduced with the smaller separation distances and higher electric fields achievable in microchip PLE, given that the approximate time to reach an arbitrarily assigned pore limit can be shown to be $t \propto \frac{L^2}{V}$. Further, complex fabrication protocols required for a slab-gel format can be significantly mitigated on the microscale [32]. The also authors took advantage of the analyte stacking effect inherent in PLE to yield sample concentration factors of up to 40,000-fold from dilute samples.

In Chapter 2, we make use of the size-selective pseudoimmobilization properties of microfluidic PLE to trap and assay enzymes with small molecule fluorogenic probes. However, our interests in achieving non-size selective capture of analytes drove further exploration of chemically-initiated capture mechanisms, allowing us to use larger antibody probes for revealing analyte identity in a quantitative way (Chapters 3-7).

1.4.4 Rationale for Switchable Capture Systems

In the most general terms, integrating distinct assay phases requires careful selection of mechanisms that can isolate these phases from each other temporally, such that e.g. the

performance of separation and reaction (capture or probing) operations can be optimized in an independent fashion. Through a simple simulation, we can consider the impact of overlap between separation and reaction phases in an assay that performs separation and immobilization of protein antigens onto a reactive surface, and the resulting tradeoffs in assay performance that can arise.

Dynamic models of CA-IEF are typically very complex, taking into account the ampholyte distributions in the channel and the various ionization states of each protein species [36, 37]. To gain a general understanding of the interplay between focusing (i.e. migration) and immobilization (i.e. reaction) timescales, a simple IEF model (after Weiss *et al.* [38]) can be formulated under the central assumption that the derivative of the protein mobility μ as a function of channel distance y is a constant (i.e. $\frac{d\mu}{dy} = \frac{d\mu}{d(pH)}\frac{d(pH)}{dy} = -p$). The protein velocity v during focusing is thus $v = pE(y - y_0)$, where y_0 is the position of the isoelectric point of the protein. To this model, we add the provision for first order conversion of protein to an immobilized complex due to reaction with a functionalized separation gel matrix during the focusing process. The governing convection-diffusion equation can thus be cast as follows to allow numerical solution for the free and bound protein concentrations C_1 and C_2:

$$\frac{\partial C_1}{\partial \tau} = pE\frac{\partial[(y - y_0)C_1]}{\partial y} + D\frac{\partial^2 C_1}{\partial y^2} - k_1 C_1 \tag{1.28}$$

$$\frac{\partial C_2}{\partial \tau} = k_1 C_1 \tag{1.29}$$

The following substitutions can be made to remove dimensions from the model:

$$\alpha = \frac{D}{L^2 pE}, t = pE\tau, x = \frac{y}{L}, x_0 = \frac{y_0}{L}$$

Finally, the equations governing evolution of the free and bound protein distributions in time and channel distance x appear as follows:

$$\frac{\partial C_1}{\partial t} = \frac{\partial[(x - x_0)C_1]}{\partial x} + \alpha\frac{\partial^2 C_1}{\partial x^2} - Da.C_1 \tag{1.30}$$

$$\frac{\partial C_2}{\partial t} = Da.C_1 \tag{1.31}$$

Where the Damköhler number $Da = \frac{k_1}{pE}$ is a ratio of the migration and reaction timescales [39]. Thus, the behavior of the model can be explored via the two dimensionless parameters α and Da. Figure 1.11 shows the effect of changes in Da for a single protein species focusing from an initially even distribution to a position at the middle of a straight microfluidic channel based on these simple model equations. Small Damköhler numbers ($Da \ll 1$) are associated with rapid focusing and relatively slow protein immobilization, yielding a

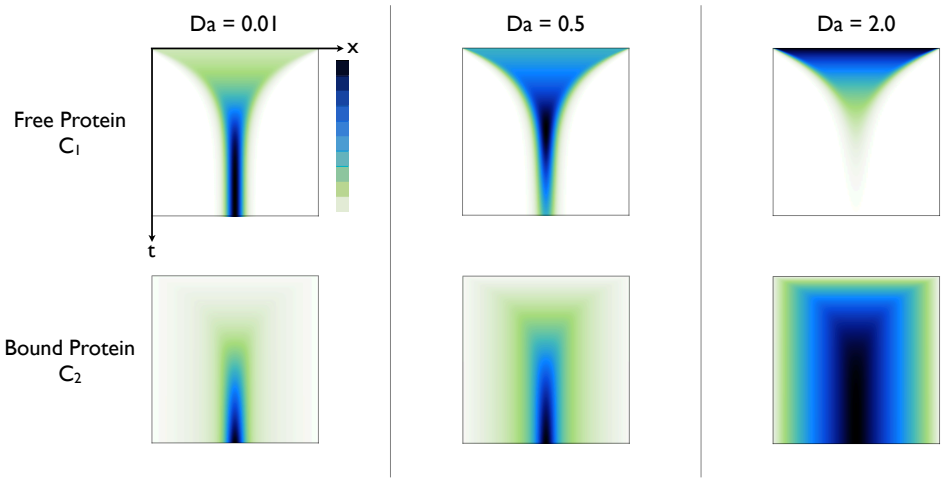

Figure 1.11: A set of density plots created from simulation results for Equations 1.30 and 1.31 describing focusing of a single protein analyte with a pI at the middle of a microfluidic channel ($x_0 = 0.5$) from an initially uniform distribution across the channel at three Da values. Note that color density is normalized separately for each graph. Channel distance x from 0 to 1 is on the x-axis. Dimensionless time t is on the y-axis as indicated. In all cases, $\alpha = 0.001$, $C_1(0, x) = 1 \; \forall \; 0 \leqslant x \leqslant 1$, $C_2(0, x) = 0 \; \forall \; 0 \leqslant x \leqslant 1$, $C_1(t, 0) = C_1(t, 1) = 0 \; \forall \; t > 0$, $C_2(t, 0) = C_2(t, 1) = 0 \; \forall \; t \geqslant 0$.

well-resolved immobilized peak with minimal binding away from the true pI of the species. Conversely, large Damköhler numbers ($Da \gtrsim 1$) denote the dominance of the immobilization reaction over protein focusing, leading to a poorly resolved immobilized protein band. More subtle is the effect of Da on the amount of protein captured in a given timeframe — although the bound protein resolution increases with reducing Da, the reduced reaction rate in turn lowers the amount of analyte immobilized in a given amount of time. Higher Da conversely increases capture efficiency at the expense of band resolution.

Thus, isolation of assay phases through the use of a *switchable* capture chemistry finds a strong rationale in preventing undue interaction between separation and capture stages. Note, however, that even switchable capture chemistries involve changes to gel physicochemical properties (e.g. hydrophobicity), due to the need to "build in" chemical moieties that remain within the gel throughout the span of the assay. Optimization of buffer and other environmental factors still plays a key role in ensuring optimal performance of both separation and capture phases, especially in enclosed microfluidic chips.

1.4.5 Benzophenone Photophores for Switchable, Light-Responsive Protein Immobilization

In the design of switchable protein capture systems to link separation and downstream analysis assay phases, several design parameters can be formulated:

- *Water solubility*: The chemical moiety responsible for capture must be sufficiently soluble in water to allow full capture performance without inducing precipitation of the scaffold or protein ligands to which it is attached.
- *Stability*: The moiety must be resistant to hydrolysis in aqueous solutions for sufficient time to ensure successful function, even after relatively long incubation times during e.g. assay fabrication and prior assay stages. The moiety must not be so sensitive to visible light that a reasonable degree of exposure to ambient light compromises its capture performance.
- *Broad ligand specificity*: The chemical group must have a broad specificity to many proteins through a common chemical target (e.g. C-H bonds), without a particular specificity for nucleophilic X-H bonds.
- *Rapid reaction kinetics*: For applications susceptible to a "race" with the diffusion timescale, e.g. capture of electrophoretically separated protein targets, the reaction must drive efficient capture prior to the loss of spatial information.

In view of this rather strict design space, many switchable chemistries can be eliminated from consideration. For example, diazo esters and aryl azides (Figure 1.12) show poor stability in the presence of reducing agents [28, 40], which are often employed in electrophoresis of denatured protein samples. Diazo compounds are also especially prone to hydrolysis in aqueous systems. Aryl azides typically form nucleophile-reactive dehydroazepines upon photolysis, tipping reaction selectivity away from the broad C-H bond reactivity that is often desired [28].

As a chemical class, benzophenones have several distinct advantages for indiscriminate capture of proteins in aqueous environments [41–44]:

- *Chemical stability*: Benzophenones are more stable to hydrolysis under a range of buffer conditions than several photolabile classes, including the diazo esters, aryl azides, and diazirines.

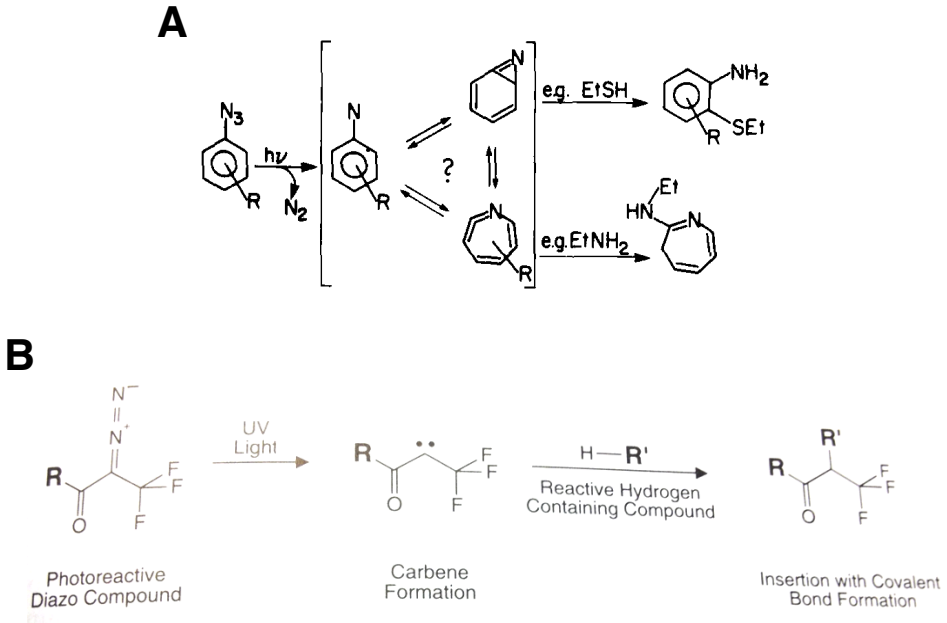

Figure 1.12: Reaction schematics for photolysis of diazo esters and aryl azides. (A) Photolysis of an aryl azide and reaction with thiols and primary amines on biomolecules (reproduced from [40]). (B) UV-induced carbene formation from diazo esters and reaction with a generic biomolecule (reproduced from [28]).

- *Photostability*: Benzophenones are relatively stable under ambient light conditions and can be activated using near-UV light (in the vicinity of 350 nm), avoiding protein damage that can result from deep UV exposure.
- *Broad reactant specificity*: Benzophenones react with C-H bonds in preference to solvent molecules or nucleophiles. In fact, in biological systems the most effective coupling reactions occur via backbone C-H bonds in polypeptides and carbohydrates.

Due to these favorable properties, benzophenone photophores have found use in a wide variety of photoaffinity labeling (PAL) studies, providing crucial insight into protein-protein and protein-drug interactions e.g. for the discovery of novel ligand-receptor interactions and for the mapping of protein-protein interactions in intracellular signaling pathways [45].

1.4.5.1 Reaction Coordinates

Benzophenone moieties undergo hydrogen abstraction and transfer processes with target C-H bond reaction partners upon the absorption of UV light [41,43]. A mechanistic understanding

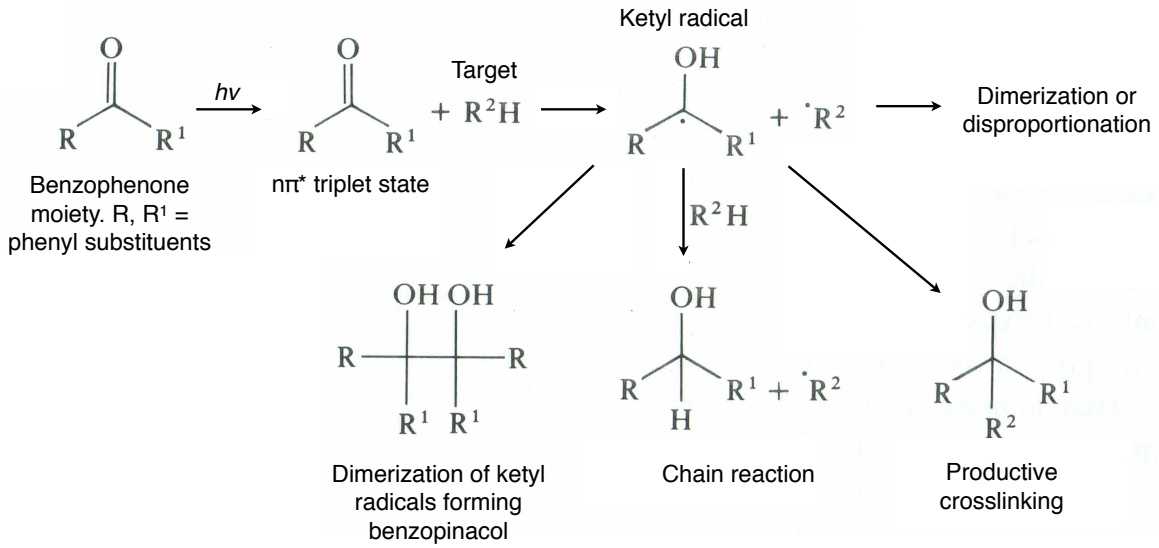

Disproportionation: free radical stripping a hydrogen atom from another free radical, so that one chain stabilizes with the hydrogen, and the other with a double bond.

Figure 1.13: Productive and side reactions of benzophenone photophores instigating hydrogen abstraction and ketyl radical formation upon the application of UV light (Adapted from [46]).

of this process requires knowledge of advanced organic photochemistry, the details of which will not be reviewed here. In brief, upon absorption of a photon in the ∼225–365 nm range, benzophenones are excited into a singlet state (referring to particle spin configurations) and converted to a triplet state by intersystem crossing. Hydrogen abstraction from the reaction partner occurs upon relaxation of the triplet state, forming a benzophenone ketyl radical and an alkyl radical from the reaction partner. Product covalent coupling can then occur by recombination of these radicals to form a new C-C bond, although several unproductive side-reactions also occur (Figure 1.13).

Particular to the benzophenone photophore, the triplet state can relax to the ground state even if a suitable partner and geometry of interaction is not encountered within its lifetime (which at ∼100 μs is already favorably long). This Norrish type II reaction mechanism is one of the major advantages of the benzophenones, since other photoreactive groups are generally subject to photodissociation immediately after activation. Thus, benzophenone moieties can undergo many excitation-relaxation cycles until conditions favorable to hydrogen abstraction are encountered, increasing the yield of productive coupling.

The absorption spectrum of benzophenone in water is characterized by a dominant peak at ∼270 nm corresponding to the $\pi \rightarrow \pi^*$ electronic transition and a ∼330 nm shoulder

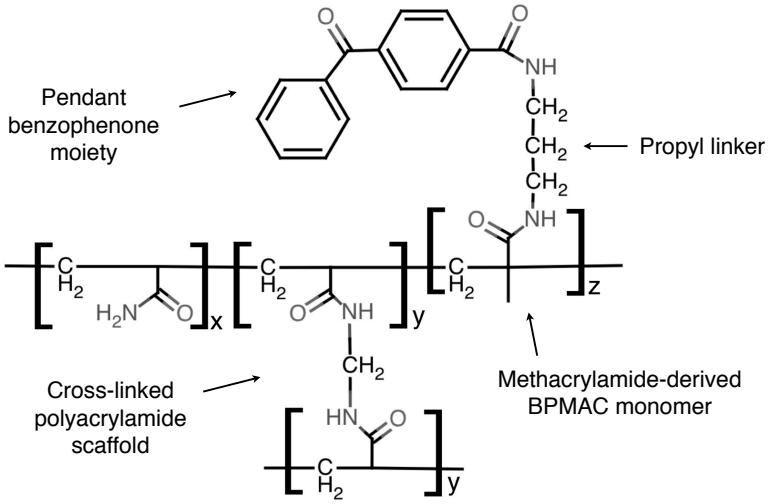

Figure 1.14: Formal chemical structure for LAVAgel/PACTgel matrices. The molar ratio of acrylamide:N,N-methylenebisacrylamide:BPMAC, x:y:z, is generally ∼0.980:0.012:0.008.

corresponding to n $\rightarrow \pi^*$ transitions (both of which result in formation of the reactive triplet intermediate). Thus, benzophenones can be conveniently excited using the 365 nm *i*-line provided by mercury arc lamps, avoiding deeper UV exposure that can damage DNA and protein macromolecules (although these wavelengths are much more effective at exciting benzophenone photophores).

1.4.5.2 Protein-Reactive Polyacrylamide Scaffolds

To leverage the favorable reaction coordinates of benzophenone for macromolecule capture onto polyacrylamide scaffolds in aqueous systems, we sought to build photoreactive benzophenone groups into the gel structure itself (directly inspired by a similar, but proprietary surface photocapture strategy employed in a commercial probed isoelectric focusing device [47]). A simple organic synthesis was devised between the NHS-ester of benzophenone and an amine-terminated methacrylamide monomer having a propyl tether (Appendix A), producing a benzophenone-decorated, methacrylamide monomer known as BPMAC suited to copolymerization into traditional acrylamide-bisacrylamide polyacrylamide gels (Figure 1.14). Two variants of this material are introduced and characterized here, in Chapters 3 and 6.

Even with molar ratios of BPMAC in the <1:100 range compared to other acrylamide monomers in the gel matrix, benzophenone-decorated polyacrylamide hydrogels were found to be exceptionally flexible and effective as protein-capture matrices for linking electrophoretic separations and immunoprobing schemes. In general, these gels were exceedingly useful be-

cause of the following properties falling within the key design parameters identified earlier in this chapter for switchable protein capture chemistries:

- *Water solubility:* BPMAC is soluble at concentrations of at least 5 mM in aqueous solutions, aided by the highly soluble methacrylamide backbone.
- *Stability:* The pendant benzophenone groups retained activity for timescales in the hours to days under ambient temperature and light conditions, providing sufficient time for device fabrication and upstream assay stages prior to the photocapture.
- *Broad ligand specificity:* BPMAC-acrylamide copolymers were found to give similar photocapture yields for a range of protein targets, irrespective of physicochemical properties such as molecular weight.
- *Rapid reaction kinetics:* The time constants of capture reactions were favorable as compared to relevant diffusional transport timescales in IEF and SDS-PAGE applications.
- *Chemical compatibility:* Although capture efficiencies varied between buffers systems, the coupling of proteins to BPMAC-containing gels was found to be robust across wide ranges in solution pH, and in reducing agent and detergent levels.

Chapter 2

Zymography by Pore Limit Electrophoresis

2.1 Introduction

Assays for enzyme activity have fundamental importance to biochemical analysis in the life sciences. Miniaturization of assay platforms has been driven by key performance goals including reduced reagent consumption and improved automation through integration of assay steps. In particular, high throughput screening of candidate drug libraries against panels of enzyme markers of pharmacodynamic or kinetic function is a costly practice in pharmaceutical research [48]. Hence, the use of multiplexed microscale systems is of continued interest in drug discovery and early-stage toxicity testing. In a similar way, probing large libraries of enzyme variants is a potentially rate-limiting facet of directed evolution of biocatalysts for novel synthetic pathways or improved performance in commercial chemical production [49, 50]. In the clinical setting, assays for enzyme markers of organ function, such as the aminotransferases (liver) and creatine kinase (heart), are routinely performed to support medical diagnoses or to monitor progression of disease state [51]. Here, reduction of sample volumes and intermediate processing steps benefits minimally invasive point-of-care diagnostics.

Driven by these considerations, a number of microfluidic enzyme assays have been developed over the last 20 years. Assay formats are diverse and have been based on capillary electrophoresis/electrokinetic flow [52–55], pressure-driven flow [29, 56–60], electrokinetic trapping [61, 62] and digital assays in droplets [63]. Continuous microreactor formats typically use enzyme immobilization to reduce enzyme consumption (in comparison to competing microfluidic approaches) while enabling precise control over substrate-enzyme contact [26, 56, 64–66]. In a recent example, Kerby *et al.* developed a continuous bioreactor consisting of a bed of streptavidin-coated silica beads held within a microfluidic channel by a weir, with a streptavidin-biotin link mediating covalent immobilization of calf intestinal alkaline phosphatase (CIP) to the surface of the beads [26]. Detailed measurements of enzyme activity over a range of substrate flowrates and concentrations were reported. Despite its strengths, several factors make the packed bioreactor paradigm less suited to quantitative functional analysis of samples derived from cell lysates or clinical fluids. Firstly, an enzyme-containing sample must generally be pre-processed for chemical immobilization to a surface. Secondly, the immobilization process inevitably alters the native kinetic properties of the enzyme of interest. For example, Kerby *et al.* report a 28-fold reduction in k_{cat} and 6-fold increase in K_m upon immobilization of CIP (similar findings have been described for CIP enzyme immobilized to a glass slide [56] and glutathione-S-transferase linked to porous silicon [66]). Enzyme deactivation, active site orientation and steric hindrance effects are thought to contribute to these changes in kinetic behavior [26, 56]. Finally, the local enzyme concentration in the reactor is difficult to estimate, which can limit the accuracy of activity measurements [26, 56, 64, 65].

As with surface-immobilization formats, gel encapsulation methods appear to perturb enzyme properties from free solution values by a similar set of mechanisms. An established body

of literature regarding physical entrapment of enzymes in polymer matrices suggests that differences in enzyme conformation and chemical environment of the reaction site, substrate partitioning between the gel and free solution, and diffusional limitations on reaction rates are all factors that may affect the apparent k_{cat} and K_m of microfluidic gel-immobilized enzymes [67–70]. Microfluidic assays of this class have not yet provided the detailed kinetic information necessary for an objective comparison to alternative immobilization techniques [59, 60, 71–73]. That said, Sakai-Kato et al. did find a 19-fold increase in the Km of trypsin encapsulated within a microchip sol-gel matrix as compared to the value in free solution. The authors attributed this to mass transfer limitations on substrate access to the immobilized enzyme [74].

A recently reported microfluidic assay system improved sensitivity and reduced run times using an electrokinetic trapping effect to concentrate enzyme samples in free solution, thereby circumventing the drawbacks of enzyme immobilization [61]. This system showed an ability to assay for kinase activity in dilute lysates prepared from human liver carcinoma cells [62]. While enabling sample preconcentration, the homogeneous (free solution) setting is less conducive to isolation of functional components for downstream analysis and limits the prospect of performing assays unaffected by competing reaction pathways or chemical modulators in a complex biological sample.

Macroscale zymography techniques are widely applied to probe the activity of enzymes in situ following PA gel-based separation of protein samples (in both native and SDS-PAGE variants) [18, 75]. In zymography, electrophoretic separation of protein constituents is directly followed by functional assays for enzymatic activity, often via diffusional exposure of protein bands to a low molecular weight substrate probe. An alternative approach utilizes prior immobilization of macromolecular substrates in the gel medium used for the electrophoretic separation. Zymographic methods enjoy wider use than western blotting for enzyme quantitation owing to the relatively low diversity of proprietary enzyme-specific antibodies currently available [75].

The present work builds upon the sizing and pseudo-immobilization properties of pore-limit electrophoresis (PLE) by integrating PLE output with an enzyme activity assay to yield a microfluidic zymography format. We employ two-stage pore limit electrophoresis with enzyme assay (PLENZ) to report the size, amount, and activity of CIP enzyme from 500 pM stock solutions. This focused analysis is complemented by a proof-of-principle assay for horseradish peroxidase VI-A (HRP). Localized on-chip fluorescent product generation provides significant signal amplification, making the assay sensitive to zeptomole amounts of enzyme using conventional CCD imaging. Our heterogeneous enzyme assay obviates the need for tailored protein immobilization chemistries by taking advantage of the physical pseudo-immobilization effect of PLE. In comparison to slab gel zymography, the microfluidic setting offers the benefits of reduced sample requirement and closer control over substrate access to a putative enzyme band as well as lower run times and higher detection sensitivity. The

new PLENZ format forges a clear path towards quantitative single-input, multiple-output enzyme assays relevant to life science and clinical research.

2.2 Results & Discussion

PLENZ consists of two integrated phases that together report enzyme molecular weight, amount, and activity — phase 1, the PLE protein sizing step (Figure 2.1A) and phase 2, the enzyme assay step (Figure 2.1B; see Appendix B and [76] for details of device operation). The two phases are not independent, as fluorescent ladder (marker) species sized in phase 1 (Figure 2.2A) allow determination of the molecular weight of an unlabeled and/or low-abundance enzyme through the axial location of fluorescent product generation in phase 2 (Figure 2.2B,C,D). In the case of CIP, the minimal overlap in emission spectra of green AF488 and blue DiFMU enabled concurrent imaging of the marker proteins and product generation (Figure 2.2D). This section details development, optimization, and the resulting performance of PLENZ.

2.2.1 PLENZ Phase 1: Protein Sizing via PLE

As described previously for PLE [32], the migration distance $x(t)$ of a given analyte is logarithmically related to the product of the applied voltage and run time according to Equation 2.1.

$$x(t) \sim \ln(1 + Vt) \tag{2.1}$$

Thus, a rapid initial migration period as the analytes travel through the gradient gel is followed by progressive slowing of the constituents towards a pseudo-immobilized state (at which point the "pore limit" is said to have been reached). To arrive at the description of PLE given in Equation 2.1, the applied electric field is assumed to be spatially uniform and the gel composition (%T and C) is assumed to increase linearly along the separation axis.

In the PLE sizing phase, a protein sample was electrophoretically introduced at the 10%T, 2.6%C end of PLENZ devices by applying a constant current of 0.3 μA for loading times of 30–105 s. Five protein species were used as molecular weight markers with a sixth species (CIP) acting as the enzyme target. After the ladder was loaded into a short open-channel loading region, the solution in the well was replaced with run buffer. The 20 min PLE separation phase was then initiated by applying constant current, again at 0.3 μA, while imaging the green fluorescence along the separation axis. Figure 2.2A captures the resulting time-evolution of the molecular weight ladder peak structure generated by PLE.

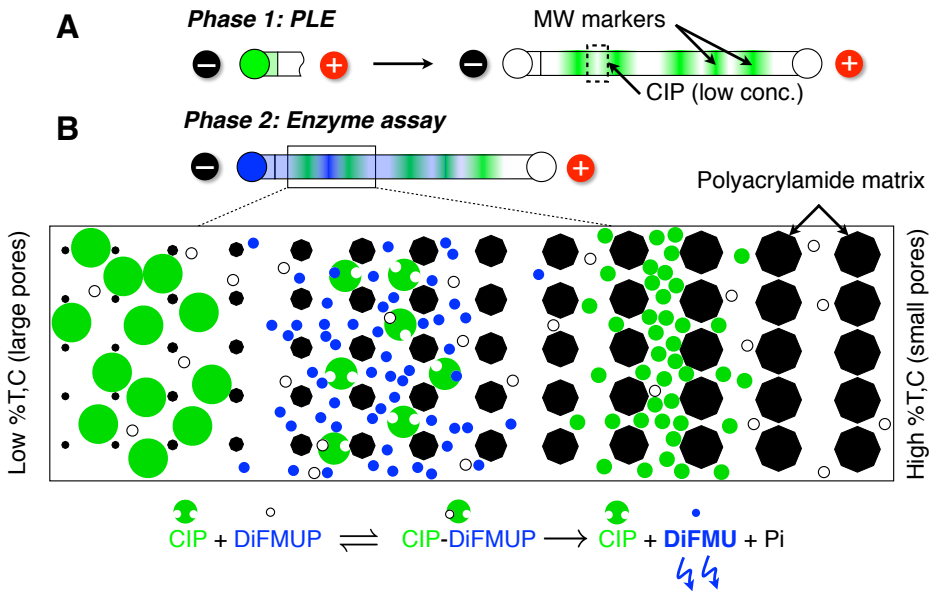

Figure 2.1: Schematic of two-step PLENZ assay for enzyme molecular weight and activity in one separation channel. (A) A heterogeneous protein mixture is separated via PLE for 20 min. Here, the target enzyme CIP is present at low concentration compared to marker proteins. (B) During enzyme activity assay, post-PLE introduction of DiFMUP and subsequent "stopped-flow" conditions reveal axial location of CIP enzyme, with the resulting development of a blue product band yielding quantitative kinetic and sizing information. At bottom, conversion of weakly fluorescent DiFMUP substrate to strongly fluorescent DiFMU product by CIP under the Michaelis-Menten model (reproduced from [76]).

Figure 2.3A demonstrates that species molecular weight was linearly related to migration distance on a log-linear scale in PLENZ devices ($R^2 = 0.98$), as anticipated. The standard deviations in migration distance for the 5 marker protein constituents were between 4.% and 6.2% of the total channel length ($n = 8$ devices). Although the variations in species migration distance between devices were acceptable; the use of a sizing ladder in each gel fully corrects for these as is standard practice in PAGE slab-gels. Judging by extrapolation of the log weight versus migration distance plot to the boundaries of the device for the PLE conditions used here, the 10%T to 35%T gradient gel can accommodate a range in protein size from ∼6 kDa to ∼330 kDa. Analysis of the ladder electropherograms gave an average protein peak capacity of 16.0 ± 0.3 peaks (error reported as SD, $n = 6$) and a minimum resolvable pair-wise molecular weight ratio of ∼1.5 (Figure 2.4). At 1.43, the smallest ratio for the protein ladder is comparable (CA, 30 kDa : TI, 21 kDa).

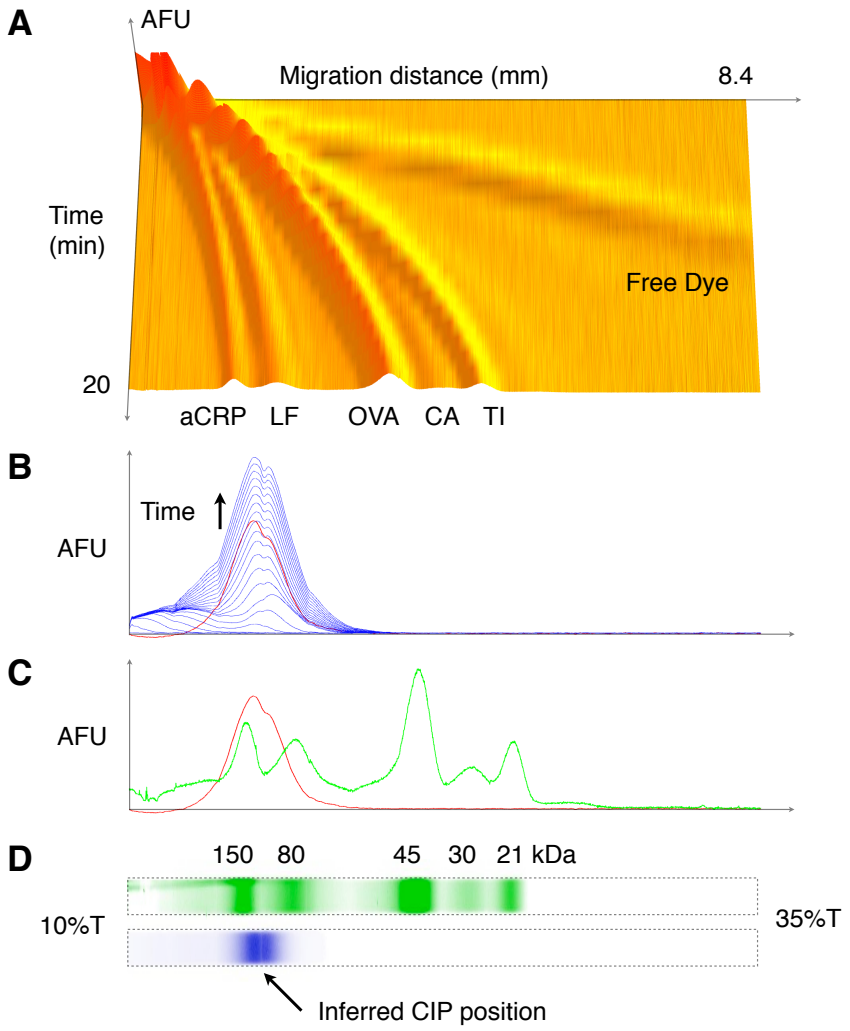

Figure 2.2: Quantitative PLENZ zymography by spectrally resolved protein ("green signal") and product ("blue signal") imaging. (A) Time-evolution of PLE protein sizing for a five component fluorescent protein ladder with 500 pM CIP enzyme (undetectable in green fluorescence profile, $i = 0.3$ μA, ladder loading time = 90 s). (B) Electrophoretic transport of 1000 μM (nominal) DiFMUP substrate across pseudo-immobilized proteins leads to production of blue fluorescent DiFMU, revealing the position of CIP. (C) The time derivative of the blue fluorescence profile (red) is compared to marker peaks (green) to yield CIP molecular weight. (D) Pseudo-color images of the final green fluorescence (top), and blue fluorescence 10 min into the assay phase place the product peak between the 150 and 80 kDa reference peaks (N.B. channel aspect ratios have been increased for clarity). Reproduced from [76].

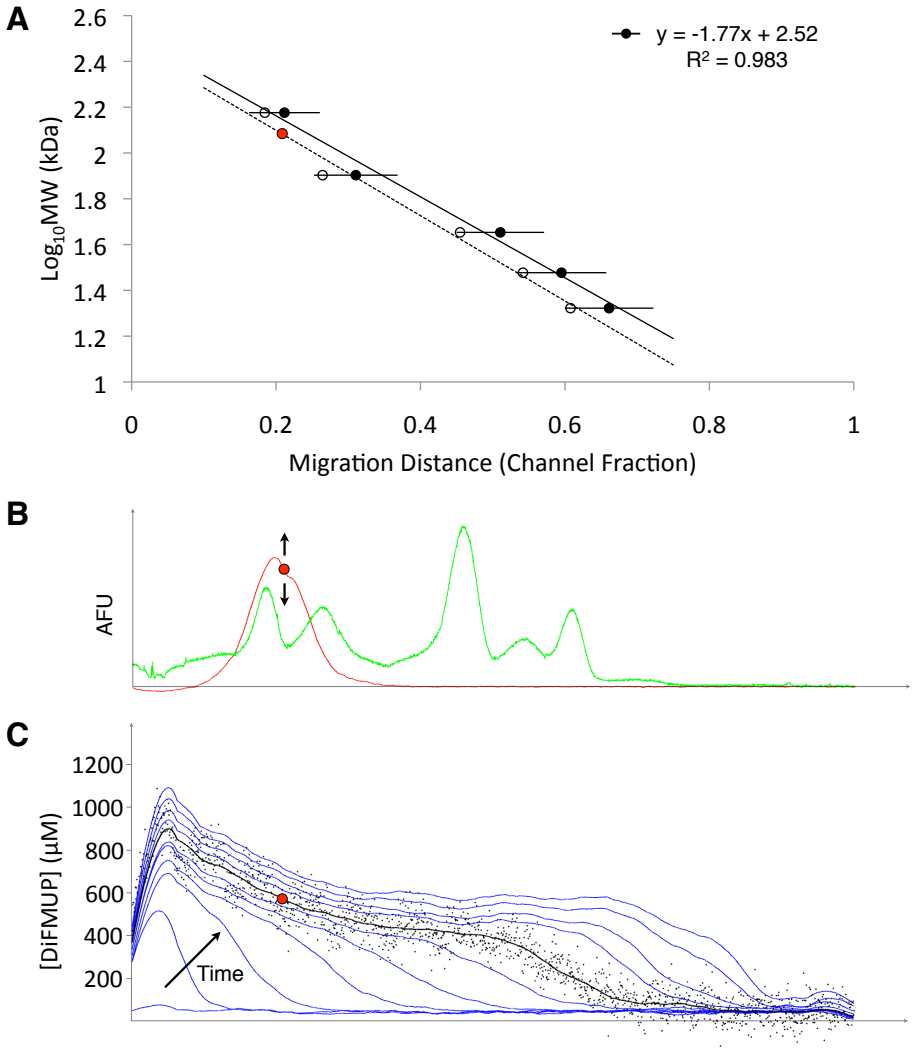

Figure 2.3: Repeatable, linear protein sizing allows accurate inference of enzyme weight and local DiFMUP concentration. (A) Log-linear plot of protein molecular weight against migration distance at the end of the assay phase for 8 devices (solid marker and line, error bars are ± S.D.). Ladder results for the device of interest (open marker and dotted line) illustrate how axial location of maximum enzyme activity reports the molecular weight of CIP (red point). (B) Position of maximum enzyme turnover also reports local DiFMUP concentration from a substrate distribution collected a priori (red point in (C)). For conceptual comparison, data from Figure 2.2C is reproduced. (C) Axial DiFMUP concentration as a smoothed function of distance (blue lines) at 60 s intervals for the first 10 min of continuous loading (nominal [DiFMUP] = 300 μM, i = 0.3 μA). Raw and smoothed data for the sixth minute are shown in black, which otherwise marks the start of the stopped-flow portion of the assay phase (reproduced from [76]).

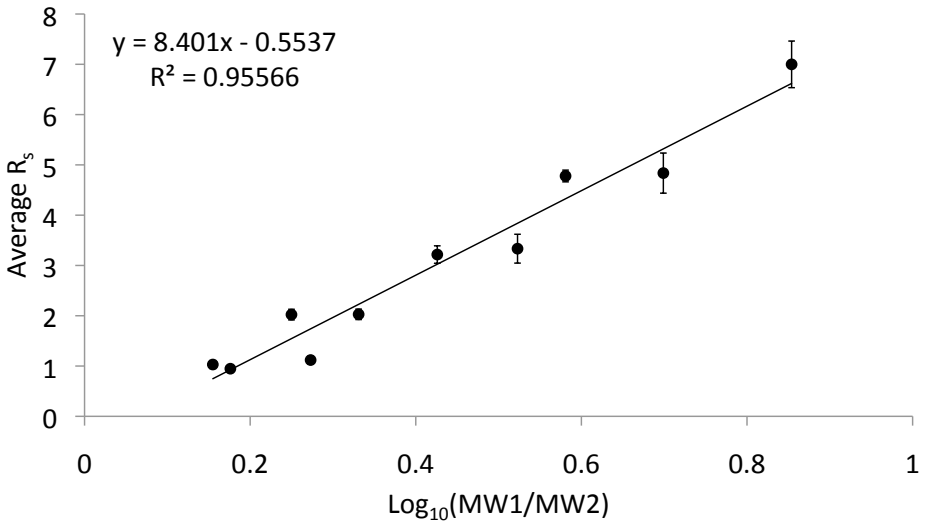

Figure 2.4: Average ladder separation resolution against the log of the pairwise molecular weight ratio for six representative PLENZ devices at the end of the separation phase (error bars are ± S.D.). Reproduced from [76].

The PLE separations developed here were consistent with results presented previously, which showed an increase in the peak capacity for fluorescently-labeled transferrin from ∼17–30 peaks between 13 V-hr (33 min at 24V applied) and 105 V-hr (4.4 hours) as the protein approached its pore limit at ∼100 V-hr in a 5 mm micro-PLE channel [32]. These results support the theoretical expectation that the protein peak resolution increases (to a limit) with the product of time and applied electric field in the separation region [32]. Upon further comparison, it becomes clear that the separations conducted in this work have not been carried to full completion due to the prohibitive run times necessary. To ensure a reasonable assay time given that an upper bound on the applied voltage is enforced by the stability of the gel matrix (~ 300 V cm^{-1} at 0.3 μA), the transition to the activity assay phase is best initiated before the proteins arrive at their absolute pore limits, but after sufficient resolution of all species is established. For PLENZ devices, a separation time of 20 min was found to adequately address the tradeoff between the resolution of ladder constituents (and therefore the accuracy of enzyme sizing) and the assay duration.

Interestingly, the applied voltage across PLENZ devices was observed to have little influence on the migration behavior of analytes, despite the convention of plotting PLE peak migration distances against volt-hours on the abscissa [32, 33]. Indeed, the electric field ranged between 50 and 300 V cm^{-1} for a common applied current of 0.3 μA, even though peak velocity profiles as a function of channel distance were found to be repeatable (data not shown). A lack of strict dependence of peak migration on the product of voltage and time also appears in data presented by Sommer *et al.* over the range of 0–50 V-h (i.e. in

the pre-pore limit regime) [32]. We hypothesize that this departure from theory arises from non-uniformity in the electric field, and in particular, to the discontinuity that the photopatterned membrane presents to the transport of charged species. Fuxman et al. suggest that the pore-size distribution in photopatterned PA structures can be affected by gradients in monomer concentration that emerge during polymerization, leading to especially small pore-size at their edges [77]. This phenomenon has recently been observed and characterized for PA gel membranes in microfluidic channels [78]. Concentration polarization can also be observed when current is applied across high-percentage PA membranes, leading to a progressive increase in membrane electrical resistance over time [79]. The 35%T membranes used in the PLENZ device to halt hydrodynamic flow during gradient formation therefore constitute regions of high and variable resistance to the passage of charged species. As a result, the membrane-associated resistance can dominate the observed well-to-well voltage drop, making it difficult to measure the true electric field in the separation gel. Use of a constant current rather than voltage ensures a consistent electric field in the separation region given repeatable pore characteristics between devices, while allowing for variability in the voltage drop associated with the membrane structure.

2.2.2 PLENZ Phase 2: *In Situ* Enzyme Activity Assay

2.2.2.1 Substrate Transport and Distribution.

Post-electrophoresis enzyme assays in macroscale slab-gels are semi-quantitative at best [80, 81] mainly due to the inability to quantify and control the substrate concentration at a given time and position in the gel. For example, when a small substrate molecule is incubated with the slab-gel, enzyme-mediated conversion of substrate to product is confounded by the kinetics of substrate diffusion from the gel surface to the true reaction site. In contrast, PLENZ uses electrophoresis to direct a small substrate along the separation axis to pseudo-immobilized proteins after the PLE phase. The low background fluorescence of DiFMUP substrate provides sufficient signal to study its transport through the PLE gel, thereby allowing quantitation of the substrate concentration within the gel as a function of time. The substrate(s) to be introduced need not necessarily be charged, as is demonstrated by assay of HRP (Figure 2.5). This assay relies on electrophoretic transport of fluorogenic Amplex Red and H_2O_2 (neutral under the assay conditions) to the site of HRP pseudoimmobilization in the presence of the anionic surfactant sodium cholate. The underlying mechanism here is likely related to that operating in micellar electrokinetic chromatography (MEKC), in which the electrophoretic mobilities of neutral species are modified by their association with charged surfactant molecules [82]. Certainly, alternative modes of substrate introduction taking advantage of the microfluidic setting to allow quantitative kinetic analysis can be envisaged with further innovation of the PLENZ chip geometry, e.g., low characteristic length substrate diffusion into the gel from a neighboring free-solution channel.

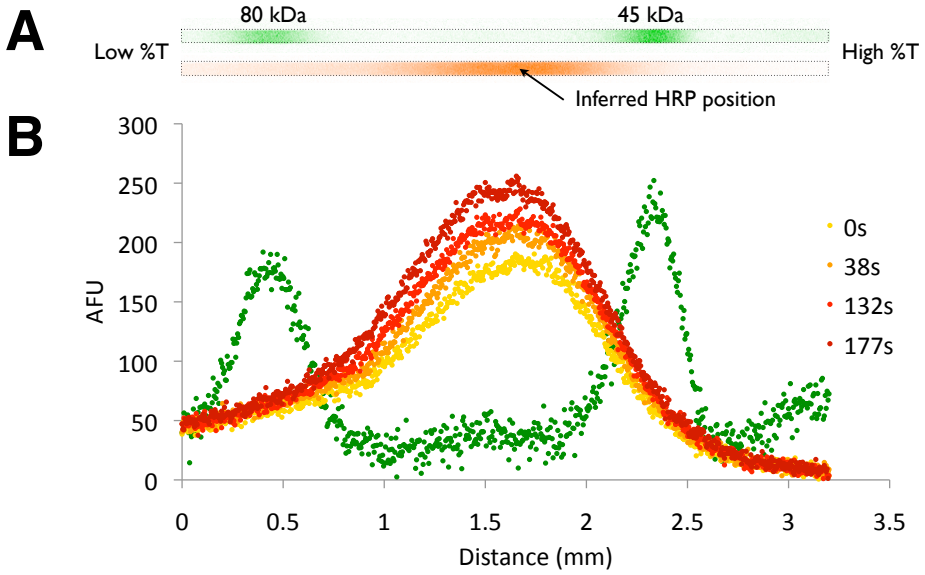

Figure 2.5: Diffusive substrate delivery enables PLENZ assay of HRP. (A) A segment of a PLENZ device at 4× magnification exposed under green (top) and orange-red (bottom) fluorescence conditions reveals the production of resorufin by HRP (nominal concentration of 100 pM) between the 80 kDa and 45 kDa marker peaks. Note that other molecular weight markers are also present in the channel but do not appear in the same field of view. The position of resorufin generation places the HRP VI-A enzyme at a molecular weight of approximately 50–55 kDa. From vendor information, the nominal weight of HRP is around 44 kDa, of which 9.4 kDa is carbohydrate. The deviation in position of the observed activity peak from the expected position is corroborated by literature reports of macroscale SDS-PAGE separation and zymography of HRP VI [83, 84] and is likely attributable to the high degree of glycosylation of the enzyme. (B) The resorufin signal is shown at several time points after measurement began under stopped-flow conditions, along with the initial green fluorescence signal (reproduced from [76]).

Returning to the CIP case study, Figure 2.3C tracks the progression of a DiFMUP substrate front as the interface electrophoreses through a PLENZ device over a period of 10 min (i = 0.3 μA). Blue fluorescence along the channel length was imaged using a series of 200 ms exposures collected every minute, and the resulting axial fluorescence intensity profiles were smoothed using a Savitsky-Golay least squares fitting routine [85]. The decreasing concentration profile away from the low %T end of the device suggests that the electric field increases as the pore-size decreases, skewing the substrate distribution away from the disperse piston-like front expected under the convection-diffusion equation [32, 86]. Also, the DiFMUP concentration established at a given channel position after passage of the initial front is generally higher than the 300 μM nominal concentration in the loading well due to the drop in electrophoretic velocity of DiFMUP between the free solution and gel matrix under

the constraints of conservation of mass [87]. Thus, substrate loading into the gradient gel has complex dependencies on time and channel position that warrant direct measurement of DiFMUP concentration, as is applied for the substrate-limitation experiments in this work.

2.2.2.2 *In Situ* Measurement of Enzyme Activity and Kinetic Parameters.

Subsequent to PLE, an assay for enzyme activity was performed on the set of pseudo-immobilized ladder proteins. The two-parameter Michaelis-Menten relationship is a parsimonious model of enzyme activity that captures the first-order generation of product at low substrate concentrations (i.e. limiting substrate availability), with a gradual shift towards zeroth-order conversion as the substrate concentration increases to saturation (i.e. limiting enzyme active site availability). Although more detailed models of CIP activity have been put forward [88–90] the Michaelis-Menten equation has offered reasonable correspondence to kinetic data arising from several microfluidic platforms utilizing CIP as a model analyte [26, 56, 63]. Equation 2.2 relates the product generation rate $\dot{p}'$ (the activity, in unconventional units of mol s^{-1} rather than M s^{-1}) to the substrate concentration s (which is assumed to be locally constant across a given enzyme peak width). The Michaelis constant K_m is the substrate concentration at which $\dot{p}'$ reaches half of its maximum value, $v'_{\max} = k_{\text{cat}} n_e$, where n_e is the total amount of enzyme present in the system and k_{cat} is known as the turnover number. Here, $\dot{p}$ (s^{-1}) is $\dot{p}'$ normalized by n_e.

$$\dot{p}' = \frac{k_{\text{cat}} n_e s}{K_m + s} \tag{2.2}$$

2.2.2.3 Enzyme-Limiting Conditions.

The expected linear relationship between the rates of product DiFMU generation under approximately saturating DiFMUP concentrations (slopes of solid lines in Figure 2.6A) and the amounts of enzyme loaded is confirmed in Figure 2.6B, which shows an R^2 value of 0.98 across measurements conducted in 15 PLENZ devices on two separate days. In this work, the amount of enzyme loaded was inferred from the total area under the green fluorescence profile during the separation phase (determined by numerical integration) in conjunction with a protein ladder calibration curve. Inherent in this method is the assumption that the composition of the protein aliquot loaded into a PLENZ device was equivalent to that of the bulk solution in the loading well. To achieve a saturating substrate concentration at the site of reaction following ladder separation, a 1000 μM DiFMUP solution was electrophoretically introduced for 6 min at an applied current of 0.3 μA. The "stopped-flow" condition after 6 min was employed to fix the substrate concentration profile in the channel and remove the obfuscating influence of substrate/product transport from the loading well. The assumption of saturating conditions eliminated the need to measure the substrate profile prior to loading and separation of the ladder sample, and is validated by the fact that the local DiFMUP concentrations resulting from introduction of such a high nominal concentration solution

were on the order of 3–5 times higher than the measured K_m of CIP in the PLENZ device. The rate of change in the total area under the blue fluorescence signal collected using sets of 70 ms exposures gave a lumped indication of DiFMU generation in each device, which occurs in a nonlinear fashion as a function of channel distance because the CIP enzyme adopts an approximately Gaussian distribution within the PLENZ gradient. Using the total blue area eliminated much of the complexity of this spatially non-uniform system, leading to the observed linear increases in the blue fluorescence areas after the point at which the electric field was halted in each device (again, solid lines in 2.6A).

Limits of CIP enzyme detection. The minimum amount of CIP enzyme detectable under DiFMUP saturation using the PLENZ system (the "limit of detection", LOD), was evaluated by extrapolating a plot of the blue fluorescence signal:noise ratio (SNR) to a lower threshold value of 3. The SNR was defined as the maximum blue fluorescence at the reaction site less the "shoulder" fluorescence at the entrance to the loading well (the signal), divided by the standard deviation of the brightness over a channel region in which no reaction was observed (the noise). This procedure yields a mass LOD of 5.4 zmol (Figure 2.7). A consistent but less conservative value is offered by the x-intercept of Figure 2.6B at $\sim$4.0 zmol (0.57 fg, or on the order of 2,500 CIP molecules). The approximate PLENZ LOD of 5 zmol (0.7 fg) compares favorably with both the low picogram sensitivities reported for macroscale zymographic techniques [80, 81] and the value of 52 zmol reported by Wu et al. for alkaline phosphatase in a capillary electrophoresis (CE) assay system [91]. However, a potential for optimization exists, as has been demonstrated by the application of laser-induced fluorescence detection in a CE system to study CIP kinetics down to the single molecule level [92].

Practically, the amount of enzyme introduced into PLENZ devices was manipulated in an open-loop fashion using the loading time (Figure 2.8), reinforcing the ability of PLE to concentrate analytes from dilute samples. To this end, Sommer *et al.* report concentration factors up to 4–5 orders of magnitude [32]. Nevertheless, the fidelity of the molecular weight information provided by spatial resolution of the marker protein peaks is adversely affected by extended loading times (as the axial length of the injected plug increases relative to the channel length available for separation). This tradeoff between sample preconcentration and molecular weight determination could be resolved by augmenting PLENZ with a second polyacrylamide exclusion membrane optimized for protein enrichment [79].

2.2.2.4 Enzyme Sizing During Assay.

In Figure 2.2D, visual comparison of pseudo-color images of the PLENZ green and blue fluorescence channels illustrates that the position of enzyme activity can be compared to a fluorescent protein ladder and, thus, directly imparts molecular weight information for the

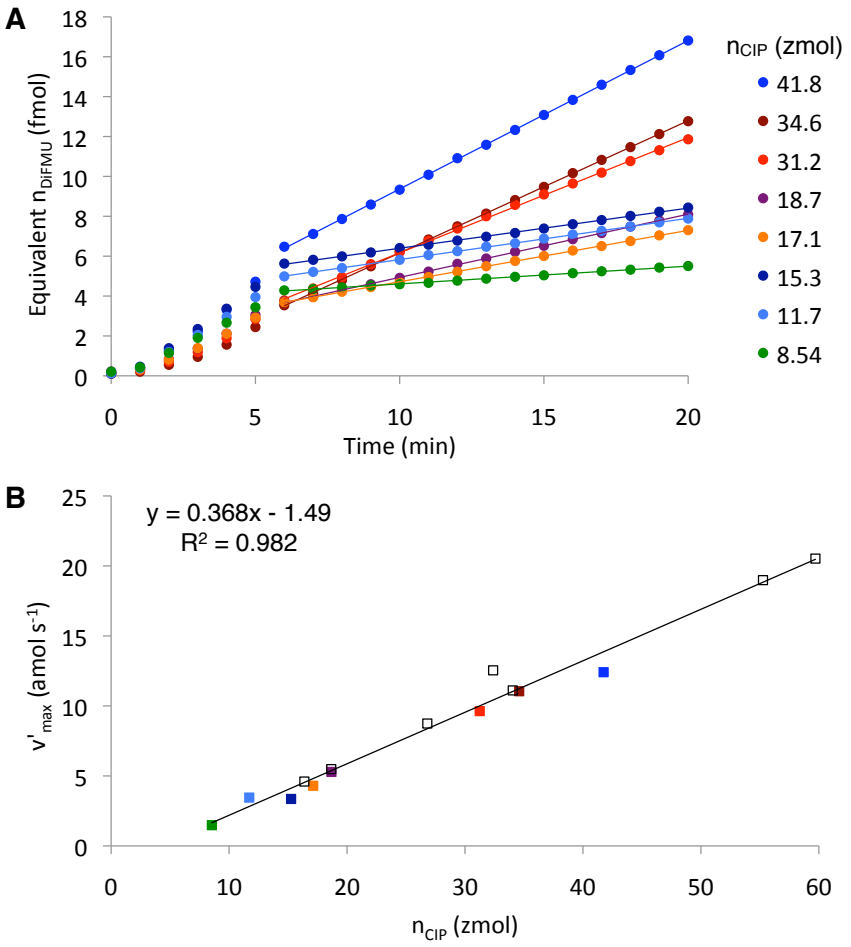

Figure 2.6: Enzyme activity scales linearly with amount of enzyme loaded during PLENZ. (A) Kinetics of DiFMU accumulation for 8 separate devices loaded with the indicated amounts of CIP (ladder loading times of 30–105 s, $i = 0.3$ μA). Assays began at introduction of a saturating 1000 μM DiFMUP solution ($i = 0.3$ μA). Linear product generation is observed after substrate introduction was halted at 6 min. (b) Reaction rate depends linearly on amount of CIP enzyme loaded ($n = 15$ devices). Open and filled squares denote devices run on separate days, colors correspond between (A) and (B). Reproduced from [76].

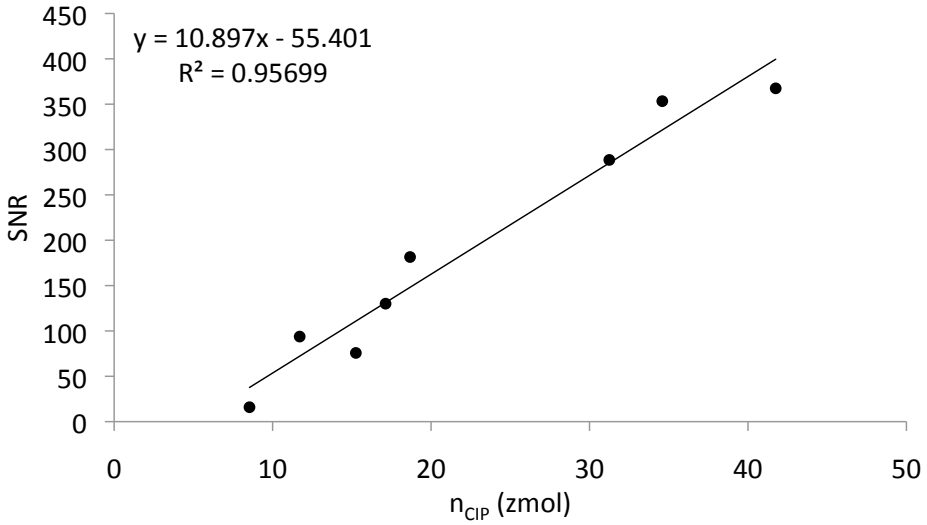

Figure 2.7: Blue fluorescence SNR at the end of the assay phase under DiFMUP-saturating conditions against amount of CIP loaded. These points correspond to the shaded squares in Figure 2.6B (reproduced from [76]).

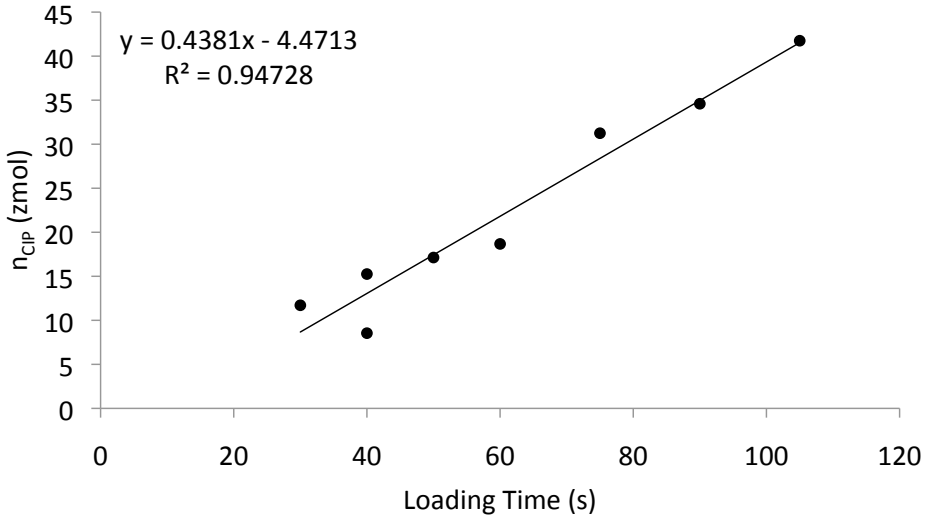

Figure 2.8: Amount of CIP enzyme added to the eight PLENZ devices in Figure 2.7 against the ladder loading time at a constant current of 0.3 μA (reproduced from [76]).

low-abundance enzyme species. The positions of maximum enzyme activity for a set of eight PLENZ devices yield a molecular weight of 127 ± 2.3 kDa (1.8%) for CIP by comparison to the corresponding marker protein migration relationships (%RSD in parentheses, see Figures 2.3A,B). This value compares well with the nominal weight of approximately 140 kDa reported in the literature [93], giving an accuracy of within 10%.

DiFMU is a small molecule and, hence, diffuses away from the reaction site over time. The diffusive broadening of DiFMU erodes the resolution of the position information that guides inference of enzyme molecular weight. Thus, we take the time derivative of the blue fluorescence at the start of the stopped-flow period of the assay phase using quadratic fits to the sets of brightness values at each ROI pixel along the channel length. This measure represents the enzyme activity as a function of distance in a more intuitive manner while minimizing the impact of apparent reaction rates caused by diffusional transport of DiFMU from neighboring pixels as local concentration gradients increase over time. The peak capacity of the blue fluorescence time derivative is approximately 6.5 for the case study in Figure 2.2B, indicating a modest potential for multiplexed assays in the same gel even in the absence of a spectral encoding strategy providing for enzyme products with distinct emission properties. The fact that this capacity is smaller than the averaged value of 16 for the protein bands reflects an intuitive upper bound on the product peak resolution that is set by the underlying protein distribution. In other words, even in the absence of product diffusion, the resolution of multiple enzyme reactions in a microchannel can only ever be as good as the parent enzyme resolution.

2.2.2.5 Substrate-Limiting Conditions.

The saturating relationship between enzyme activity and local substrate concentration prescribed by the Michaelis-Menten model is illustrated for CIP in the PLENZ platform in Figure 2.9. The reaction rates have been normalized by the amount of enzyme loaded to isolate the effect of substrate concentration, which was varied by introducing 10–1000 μM solutions of DiFMUP into separate PLENZ devices for 6 min at 0.3 μA at the beginning of the assay phase. Additionally, the substrate entry profile for each device was directly measured prior to the separation and assay phases. For this step, blue fluorescence imaging of the channel was conducted using an exposure time of 200 ms after a 6 min period of continuous introduction of a 300 μM solution of DiFMUP at 0.3 μA. The substrate was then removed from the channel using a 5 min wash with run buffer to prevent premature contact between enzyme and substrate during the PLE phase. This procedure allowed post hoc inference of the local substrate concentration in the region of maximum enzyme activity observed during the later assay phase, under the assumption that the DiFMUP entry profile could be linearly scaled to suit the appropriate nominal (via well) concentration of DiFMUP applied.

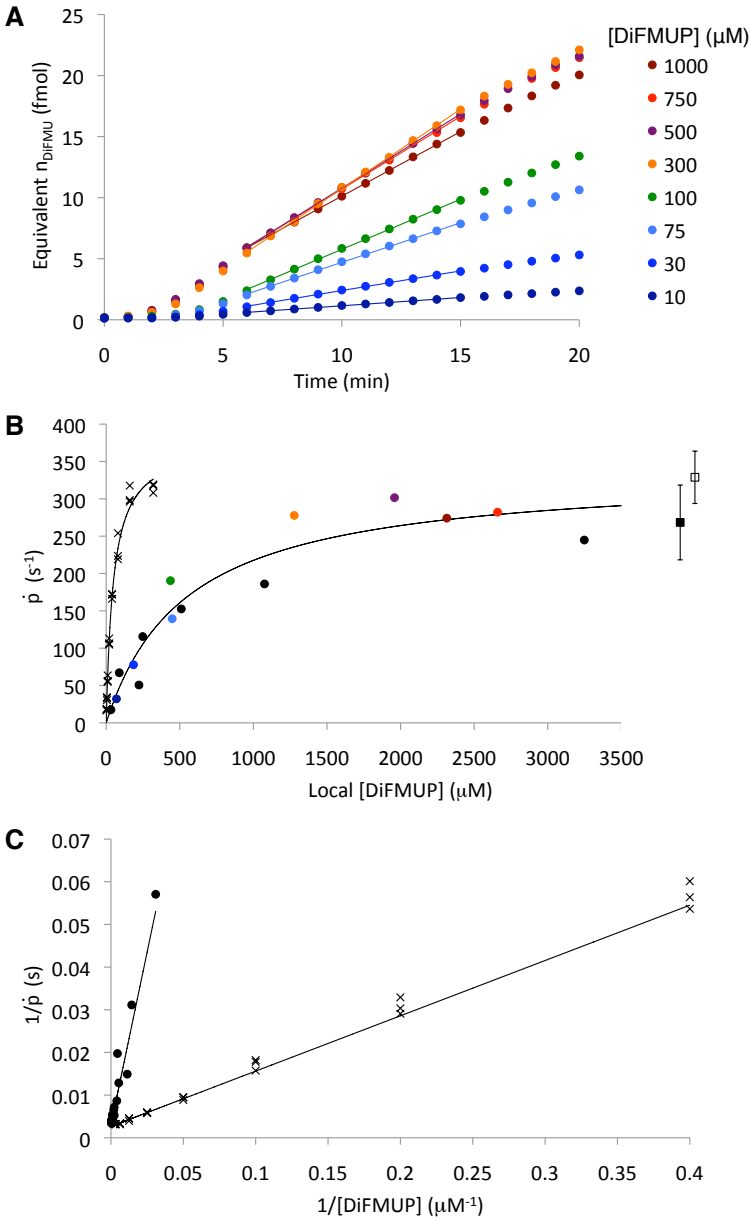

Figure 2.9: Saturating dependence of normalized enzyme activity on local substrate concentration yields kinetic parameters of CIP. (a) DiFMU accumulation after DiFMUP solutions of the indicated concentrations were loaded for 6 min into 8 separate devices (ladder loading time in PLE phase of 60 s at $i = 0.3$ μA for all devices). (b) Normalized reaction rates against local DiFMUP concentration show a characteristic asymptotic relationship ($n = 15$ devices, shaded and black circles denote devices run on separate days, colors correspond between (A) and (B)). Squares are data from Figure 2.6 for $\sim$ saturating concentrations of DiFMUP (filled marker, $n = 8$; open marker, $n = 7$); error bars are $\pm$ S.D. Crosses indicate microplate data. (C) Lineweaver-Burk plot of the PLENZ (filled marker) and microplate (crosses) data from (B). Reproduced from [76].

Table 2.1: Kinetic parameters for CIP enzyme from microplate and PLENZ experiments. Errors are reported as standard deviation with %RSD in parentheses. N.B. all experiments conducted in 75 mM glycine buffer, pH 9.3 with 1% sodium cholate, 1 mM $MgCl_2$, $ZnCl_2$, and DTT.

	k_{cat} s^{-1}	K_m (μM)
Microplate, $n = 3$ replicates	376 ± 10 (2.7%)	49 ± 1.4 (2.9%)
PLENZ rate vs. [DiFMUP]	336	545
PLENZ rate vs. n_{CIP} replicate 1, $n = 7$ devices	329 ± 35 (11%)	—
PLENZ rate vs. n_{CIP} replicate 2, $n = 8$ devices	268 ± 50 (19%)	—

Again, DiFMU accumulation during the assay phase occurred linearly after the electric field was halted at the 6 min mark (solid lines in Figure 2.9A). The Michaelis-Menten plot stemming from the corresponding rates and local substrate concentrations across two separately calibrated experiments is fit well by the saturating two-parameter model, giving a k_{cat} of 336 s^{-1} and K_m of 545 μM (Figure 2.9B). A similar experiment run in triplicate on a fluorescence microplate yielded a comparable k_{cat} of 376 ± 10 s^{-1}, but a greatly reduced K_m of 49 ± 1.4 μM. The two datasets from Figure 2.6B confer precision information on the PLENZ data, giving k_{cat} values of 268 ± 50 s^{-1} and 329 ± 35 s^{-1} (corresponding RSD values are 19% and 11% respectively). The relatively smaller k_{cat} values associated with these data are expected, given that they arise from an assumption of saturating local DiFMUP concentration rather than from a non-linear fit that outputs an asymptotic value for k_{cat}. A summary of the kinetic data arising from the PLENZ and microplate measurements is presented in Table 2.1.

The similarity in the k_{cat} values measured via PLENZ and fluorescence microplate suggests that physical pseudo-immobilization of CIP in the PLENZ gel gradient does not destroy native enzyme activity, as is often the case with covalent enzyme immobilization to channel surfaces or packings [26, 56, 58, 65, 66]. The Lineweaver-Burk plot in Figure 2.9C reinforces this similarity in k_{cat} as a convergence of the two relationships upon approximately the same y-intercept. Here the transformed data are shown with the previously fitted Michaelis-Menten functions rather than with lines of best fit due to the lack of statistical rigor of the latter method [94]. The greatly increased K_m in the PLENZ device without a drop in k_{cat} is reminiscent of competitive inhibition, but in this case can be attributed to the reduced molecular diffusivity of DiFMUP in the gel matrix as compared to the free-solution reaction state in the microplate well. Certainly, diffusional effects on the observed K_m are to be expected following physical entrapment of CIP in the PLENZ polyacrylamide matrix [68–70]. Encouragingly, however, the results reported here suggest that direct loss of activity in a way that alters the observed k_{cat} is bypassed as the enzyme is electrophoretically introduced after gel polymerization.

2.3 Conclusions

We report a robust analytical method for determining enzyme molecular weight and activity information from a dilute aliquot of a heterogeneous protein sample. A PLE system of minimal complexity was optimized to allow rapid physical pseudo-immobilization and sizing of sample proteins in series with a fully quantitative in situ and label-free enzyme assay using microfluidic technology. The use of an electrophoretic physical immobilization strategy brings benefits over covalent immobilization in terms of the fidelity of the enzyme activity information collected and the fact that sample pre-functionalization is not necessary. Electrophoretic transfer of CIP into the microfluidic gel matrix was found to have little effect on its maximum activity, alleviating (but not eliminating) the bias that covalent immobilization strategies impose on the quantification of kinetic data. PLENZ also exhibits excellent sensitivity to enzyme activity with zero dead-volume due to the ability to load an exceedingly small protein aliquot directly onto the gradient gel without the need for accessory channels upstream of the injection point. The PLENZ-based horseradish peroxidase assay further demonstrates the ability of this technique to be adapted to various buffer systems, and to be applied to analytes having substrates with neutral charge.

This microfluidic zymographic platform should prove a useful addition to the molecular biology toolbox, particularly where it is of interest to perform functional screening of gene expression in a highly parallelized fashion. Such a platform could also be useful in functional proteomic studies, in which enzyme identification by mass spectrometry and amino acid sequencing is often performed downstream of an in situ PAGE separation and assay technique [75, 95]. A multiplexed PLENZ system in which a panel of enzymes in an aliquot of biological fluid can be enriched, spatially resolved, and assayed in a single polyacrylamide gradient gel is currently under development, as are efforts to maximize the effective separation resolution through rational spectral encoding of fluorogenic substrates. Demonstrating the ability of PLENZ devices to process complex biological samples with multiple activity readouts from spatially and/or spectrally distinct enzyme bands will ultimately be directed towards improvements over gold-standard screening methods employed in drug discovery, clinical diagnostics and biocatalyst engineering. The analytical techniques developed here for polyacrylamide gel-based fluorescence detection of biocatalytic activity will also complement progress towards a microscale immunoblotting paradigm, which has recently been reported by our group [96].

Chapter 3

Probed Isoelectric Focusing for Cancer Biomarker Isoform Quantitation

3.1 Introduction

In this post-genomic period, personalized medicine is poised to benefit from proteomics [97]. Proteins are key functional components of living organisms and, thus, offer the potential for high-utility disease diagnostics. Nevertheless, the vast majority of protein biomarker candidates stall at the discovery phase, never making it through validation scrutiny and to the clinic [98]. Over the last 15 years an average of just 1-2 new protein biomarkers per year have been approved by the FDA for clinical translation. Compounding concerns, consider two ostensibly accepted protein biomarkers: total PSA and CA-125. Each protein has been used in diagnostics for screening of prostate and ovarian cancer, respectively. Recently, these cancer screening diagnostics have met with limited success and even controversy [99–101]. Consequently, the lackluster progress in protein-based diagnostics highlights important gaps in our approach to defining protein biomarkers. Taken together, a pressing need for innovation exists to expedite translation of informative biomarkers into clinical decision making.

In one important example, the mediocre ability of total and free PSA assays to distinguish between malignant and benign prostatic pathology has spurred study of free PSA isoforms [102, 103]. Proteomic studies suggest a promising link between prostate cancer incidence and differential isoform expression in healthy and cancer patient sera [102, 104, 105]. While promising, rigorous validation studies are needed to translate the potential of protein isoforms to the clinic. Immunoassay formats including ELISA and microarray formats offer powerful multiplexing and high-sensitivity performance. Recent novel ELISA-based formats offer notable gains in analytical sensitivity [106, 107]. Nevertheless, mounting evidence suggests that protein isoform fingerprinting could advance diagnostic performance [102, 105, 108]. Unfortunately, ELISA is severely limited for isoform discrimination, as antibodies specific to protein isoforms often do not exist [108]. Combining protein separations with antibody interrogation (immunoblotting) allows measurement of protein isoforms. High performance immunoblotting assays — particularly those with scalable frameworks — would bridge the gap between biomarker discovery and translation to the clinic [98, 109].

Despite their analytical power, conventional bench-top immunoprobing assays consume tremendous time, labor, reagents and sample resources. Further, performance and implementation characteristics limit scalability, including: disjointed workflows requiring manual intervention across multiple instruments, transfer between platforms, and limited quantitation [98, 110]. To surmount these shortcomings, new analytical technologies based on slab-gel and capillary separations are being introduced [5, 111]. A capillary-based separation with surface reaction approach has been commercialized [47, 112]. However, the proprietary photo-active capillary surface exhibited low target capture efficiency ($\sim$0.01%); necessitated complex interfacing involving pumps, valves, and high voltage control; and availability of characterization data is limited. Consequently, continued advances in targeted proteomics technology are needed, including: minimized reagent consumption, reduced complexity including interfacing, and

automation.

Here we describe microfluidic integration to realize a streamlined, compact assay platform for high-performance protein isoform measurement (see Appendix B and [6] for details of device operation) [76,110]. Microfluidic integration allows us to harness the favorable scaling of electrokinetic transport and reactions, as well as limit consumption of precious diagnostic samples and costly immunoprobing reagents. By utilizing purely electrophoretic transport through our 3D photo-reactive hydrogels, we minimize diffusion distances and maximize binding site densities. We demonstrate 100× gains in analyte capture efficiency, rapid high-resolution protein isoform separations, vanishingly small reagent consumption (<1 ng of each antibody probe is required, as compared to ∼1 μg necessary for macroscale immunoblotting), and a "single-channel, single-instrument" design that requires no bulky pumps or valves for device actuation. This rational engineering design strategy advances new analytical technology for automated, scalable scrutiny of protein isoforms in complex diagnostic fluids as part of a pipeline to realize personalized proteomics in medicine.

3.2 Background: Prostate Specific Antigen Heterogeneity in Diagnostic Assay Design

Prostate specific antigen (PSA) screening in the detection of prostate cancer is a controversial diagnostic tool due to the mediocre performance of total and free PSA measures in delineating healthy and cancer-afflicted patient groups. Efforts to improve the efficacy of PSA measurements have recently focused on analysis of isoforms in the serum free (f)PSA compartment, but have thus far been limited to cumbersome two-dimensional PAGE separations that are ill-suited to clinical implementation.

Prostate cancer (PCa) is the fifth-leading cause of death in men aged 55–74, and is the second-leading cause of death amongst the set of malignant cancers [113, 114]. Modern prostate cancer screening consists principally of measurements of prostate specific antigen levels in the bloodstream; complemented by transrectal ultrasound and digital rectal examination. ELISA-based assays for total (free and inhibitor-bound) and free (intact, nicked and proPSA) serum PSA are a central but controversial tool in the diagnosis of prostate cancer [108,115]. The use of PSA as a prostate cancer biomarker is motivated by increases in total (t)PSA levels in affected individuals, but is complicated by the fact that similar increases are also observed in individuals with clinically innocuous pathology such as benign prostatic hyperplasia (BPH) [115]. The observation that the serum ratio of free (f)PSA to tPSA is lower in men with prostate cancer has improved cancer detection significantly, although considerable overlap still exists between BPH and PCa data sets. For example, the first report recommending fPSA as a replacement for the standard tPSA measurement found prostate cancer in 56% of patients with fPSA<10%, but also in 8% of those with fPSA>25%, which was the threshold below which biopsy was recommended [115].

The mediocre ability of total and free PSA assays to distinguish between malignant and benign prostatic pathology has been addressed in the literature through ongoing research linking various subfractions of serum PSA to higher or lower cancer risk. This in turn has led to increased complexity of ELISA-based assays, in which various combinations of blocking and detection antibodies are necessary to facilitate independent measurement of the set of PSA forms in the homogeneous setting [108]. Further dissection of the heterogeneity of fPSA isoforms via 2D gel electrophoresis (2DE) coupled with enzyme-amplified western blotting (WB) by Jung *et al.* has unveiled an exciting link between the representation of two of these isoforms (F2 and F3) in healthy and PCa patient serum (see Figure 3.1) [102]. This heterogeneity has been partially accounted for by varying degrees of sialic acid content ("sialylation") of PSA glycans that directly impact the observed peak structure in the pI axis [104, 116]. Thus, pathological changes in fPSA glycosylation in PCa tissue and its knock-on effects on blood fPSA can be detected to distinguish between sera from healthy and cancer-afflicted men.

With the choice of a monoclonal antibody to fPSA forms only (rather than the polyclonal antibody used by Jung *et al.* to capture the total serum PSA content), undesired binding to complexed PSA could be circumvented, meaning that a single commercially available detection antibody could allow the serum levels of each fPSA glycoform to be independently quantified along with the canonical fPSA measure with minimal reagent cost and assay complexity. The strong shift in pI associated with the proPSA forms noted in the literature could also allow quantitation of this fPSA subfraction in the same operation, which would offer the potential to integrate the strengths of proPSA and glycoform measurements into a more powerful discriminatory metric [102, 117]. In their original account, Jung *et al.* (2004) recognized that *"...2DE is not suitable for routine use because it is expensive in terms of human labor and consumables and needs substantial experience and a sophisticated technique."* Furthermore, the 2DE-WB technique required the PSA to be extracted from 1 ml of serum by immunoadsorption via antibody-coated magnetic beads prior to gel loading, eventually yielding a modest detection limit of 0.1 ng ml^{-1} [102]. These drawbacks clearly provide motivation for an automated microfluidic IEF separation strategy coupled to enzyme-amplified immunodetection, in which the need for sample preconcentration would be unnecessary and the complexities of 2DE substantially tempered.

A target detection limit of 10 pg ml^{-1} is motivated by the presence of minor proPSA isoforms at serum concentrations in the 10–100 pg ml^{-1} range, with major isoforms expected at concentrations of 100-1000 pg ml^{-1} [102, 108, 118].

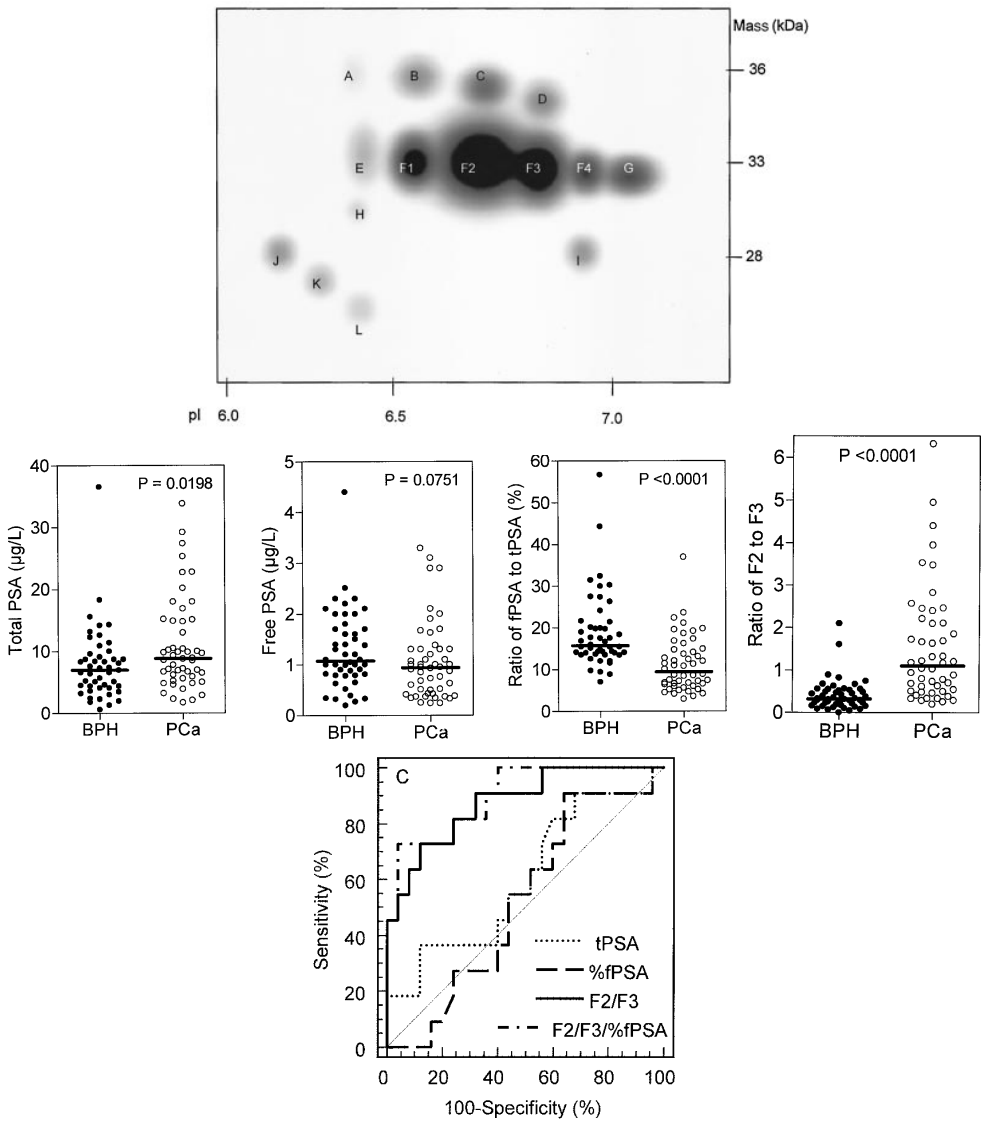

Figure 3.1: Several figures reproduced from Jung *et al.* (2004) [102]. At top, an HRP-amplified western blot of a 2DE gel representing a composite of all PSA spots found across a range of serum samples from healthy (but with observed BPH) and PCa patients. Spots at ∼33 kDa are fPSA isoforms, lower MW spots are internally cleaved PSA forms, and higher MW ones are of unknown composition. Spots F2 and F3 are the only isoforms found in all serum samples, spots A–E, G–I, K and L were observed only occasionally. The more basic spots F4 and G are expected to be proPSA forms, although this was not confirmed by conversion of these peaks to fully processed forms via sample reaction with exogenous hK2 in this paper. At middle, several measures of serum PSA abundance are compared between BPH and PCa serum sets. Note that the ratio of F2 and F3 spot intensities provides a strong metric to distinguish between the sets, and finds significant advantage over the canonical %fPSA measure (especially in patients with %fPSA>15%), as shown by the ROC curve analysis at bottom.

3.3 Design Strategy

3.3.1 Design of Assay and Microdevice

Our targeted proteomics platform is a self-contained microfluidic device (Figure 3.2A,B) that executes all protein isoform analysis steps, namely: isoelectric focusing (IEF) for separation of protein isoforms, immobilization of separated proteins, probing of immobilized proteins with affinity reagents and all washing steps. Underpinning integration is a microfluidic strategy comprised of simple straight microchannels, programmable electrophoretic transport, and adaptable 3D hydrogels that switch from molecular sieving matrices to analyte capture scaffolds upon brief exposure to UV. A distinguishing contribution is use of electrophoretic transport for all assay stages with a 3D photo-clickable hydrogel matrix, termed a light-activated, volume-accessible gel (LAVAgel) strategy (Figure 3.2C). To our knowledge, this is the first report of a microfluidic device for fully electrokinetic single-channel immunoblotting.

Our "single-channel, multi-stage" microfluidic assay offers several advantages for protein studies in minimally processed samples. Chiefly, the use of microfluidic technology enables automation and workflow completion in one unified instrument. Five additional advantages arise compared to competing approaches: (i) unification of all assay stages into a single microchannel for minimal operator intervention, (ii) realization of rapid protein separations (<20 min) owing to miniaturization, (iii) reduced consumption of sparingly available biospecimens and costly affinity reagents, (iv) programmable electrokinetic control to eliminate pumps and valves, thus simplifying external hardware complexity, and (v) no blocking steps prior to antibody probing.

3.3.2 Materials and Transport

Two major operational advantages underpin microfluidic LAVAgel design and performance (Figure 3.2C). Firstly, use of a channel-filling (3D) photoactive hydrogel maximizes protein immobilization efficiency by offering an increased number of available reactive sites, compared to capillary surface capture approaches. For comparison, consider a capillary of inner radius r$\sim$50 μm with a reactive inner surface. The 3D LAVAgel reactive surface area can be approximated as a simple cubic arrangement of $\sim 5 \times 10^5$ cylindrical nanopores (r $\sim$120 nm, mean pore radius of a 4%T, 2.6%C polyacrylamide gel [119]) packed into a 50 μm radius channel. Since capture efficiency, η, scales with surface area, comparison of surface immobilization to 3D LAVAgel immobilization yields $\frac{\eta_{\text{gel}}}{\eta_{\text{cap}}} \sim \frac{A_{\text{gel}}}{A_{\text{cap}}} \sim 300$ (see Chapter 4). Thus the LAVAgel offers a $\sim$2–3 orders-of-magnitude increase in capture efficiency over a reactive capillary inner surface. Empirically, we observe a $\sim$180-fold improvement in η over that measured for capillary surface photoimmobilization (see Results and Discussion) [47].

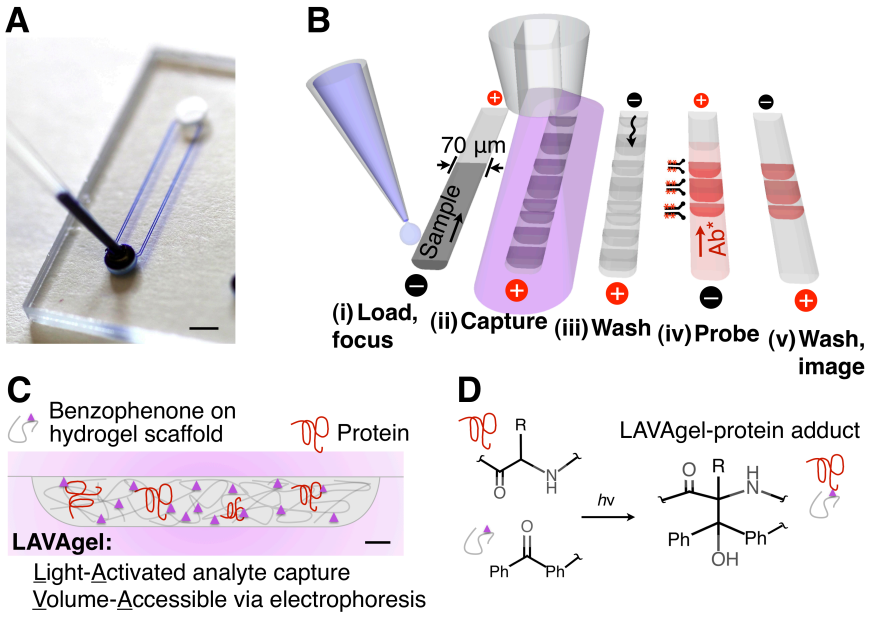

Figure 3.2: Design and operation of the microfluidic LAVAgel assay for high-specificity protein isoform analysis. (A) Glass microfluidic device with microchannels linking two fluid reservoirs (dye added for clarity). Scale bar: 2 mm. (B) The 80-min five-stage immunoprobing assay is completed in a single microchannel. (C) Schematic of microchannel cross-section depicting principle of the LAVAgel: Analytes are electrophoresed through the nanoporous hydrogel, exposed to UV, and covalently immobilized on the reactive hydrogel. Scale bar: 5 μm. (D) Schematic of reaction between polypeptide backbone and pendant LAVAgel benzophenone groups. "Ph" denotes phenyl group. For clarity, the electrophilic triplet state of benzophenone, hydrogen abstraction and radical intermediates are omitted. Reproduced from [6].

Secondly, directed electrokinetic transport through the nanoporous LAVAgel minimizes diffusion distances, yielding efficient mass transport to reaction sites. Short diffusion distances eliminate the need for mixing and reduce the overall reaction time [120], as is important for both the photoimmobilization and the immunoprobing stages. Electromigration of a reaction partner through reactive gel pores can be framed as a homogeneous reaction occurring between two crossing reactant bands [120]. In contrast, boundary layer characteristics can dominate surface reactions, limiting analyte transport. The 3D distribution of captured analyte in the LAVAgel approach removes this extra mass transfer resistance term for both analyte capture and antibody probe reactions. Consequently, the appropriate mass transfer timescale for the pseudo-homogeneous LAVAgel system can be estimated as $t_{\text{cross}} = \frac{w}{u_{\text{rel}}} \sim 2s$ where w is the width and u_{rel} is the velocity of a given mobile analyte zone, respectively. As is advantageous to performance, the LAVAgel system is reaction-limited (see Chapter 4).

3.3.3 Design of Volume-Accessible Photo-Clickable Hydrogel

The LAVAgel polymer was synthesized using a benzophenone methacrylamide monomer (N-[3-[(4-benzoylphenyl)formamido]propyl] methacrylamide or BPMAC) (Figure 3.2D, Appendix A). Free radical polymerization forms the sieving gel in the microchannel. Upon brief exposure to UV light (350–365 nm, ∼10 s), the gel switches from a molecular sieve to an immobilization scaffold. Exposure to UV promotes the carbonyl groups of the BPMAC monomer termini to an electrophilic triplet state [41]. Subsequent hydrogen abstraction is preferential towards C–H bonds in target polypeptides and other buffer constituents [41], leading to formation of stable covalent linkages to the gel matrix. Importantly, the use of polyacrylamide gels with strong resistance to non-specific adsorption and this UV-initiated covalent attachment mechanism eliminates the need for separate and time-consuming blocking steps common with conventional blotting materials (e.g., PVDF, nitrocellulose).

3.4 Results & Discussion

3.4.1 Integrated Protein Isoform Assay Operation

We designed our multi-stage assay to reduce instrument complexity. Consequently, we employ a single microchannel and programmable electrophoretic transport for all stages, including washing. With performance on par with conventional slab gel and capillary methods, the total assay duration was <120 min, with hands-on time of <15 min. To facilitate technical and biological replicates, the prototype glass device houses four separation channels per fluid reservoir pair (Figure 3.2A). With four reservoir pairs on each chip in this prototype, sixteen channels can be run in parallel. Results from a complete assay are shown in Figure 3.3 and detailed here.

During the first assay stage (Figure 3.3A,B), IEF is used to separate proteins based on differences in isoelectric point (pI). IEF is an ideal separation mechanism for resolving protein isoforms which may have only slight differences in molecular mass. IEF is achieved by establishing a pH gradient along the channel length using a commercially available mixture of polyprotic amino carboxylic acids (carrier ampholytes) that buffer at their pI's [7]. Analysis of a cocktail of fluorescent pI marker peptides revealed that a linear broad range pH gradient (pH 4–8.7) was established in <20 min (within-chip %RSD in slope = 6.5%, $R^2 \sim 0.99$). Focusing of a fluorescent model protein (wtGFP) yielded clear resolution of three well-characterized isoforms (Figure 3.3B), with baseline resolution of the two closest neighbors. A resolution of $\Delta\text{pI} = 0.15$ pH units was achieved with broad pH range ampholytes (Figure 3.4). We estimate a peak capacity of 110 ± 22 ($n = 3$), on par with conventional IEF [7, 12]. Using a starting volume of 3 μL and a detectable concentration minimum of ∼0.1 nM (2.7 ng/ml), we estimate that ∼8 pg of starting material is needed for detection of wtGFP during

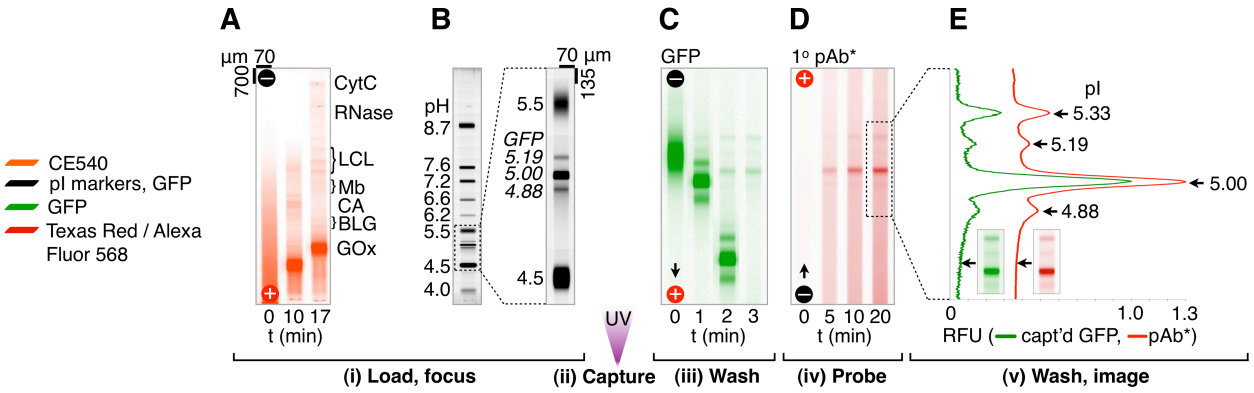

Figure 3.3: Characterization of protein isoforms using the single-microchannel 80-min LAVAgel immunoblot. Fluorescence micrographs show: (A) loading and IEF of a CE540-labeled protein ladder with 617 nM green wtGFP. (B) IEF readout via UV excitation. (C) After UV photoactivation, the pH gradient is washed out with retention of a portion of each wtGFP isoform. (D, E) Antibody probing of wtGFP with 100 nM Texas Red-labeled polyclonal antibody (pAb*) demonstrates specificity and low-background. Reproduced from [6].

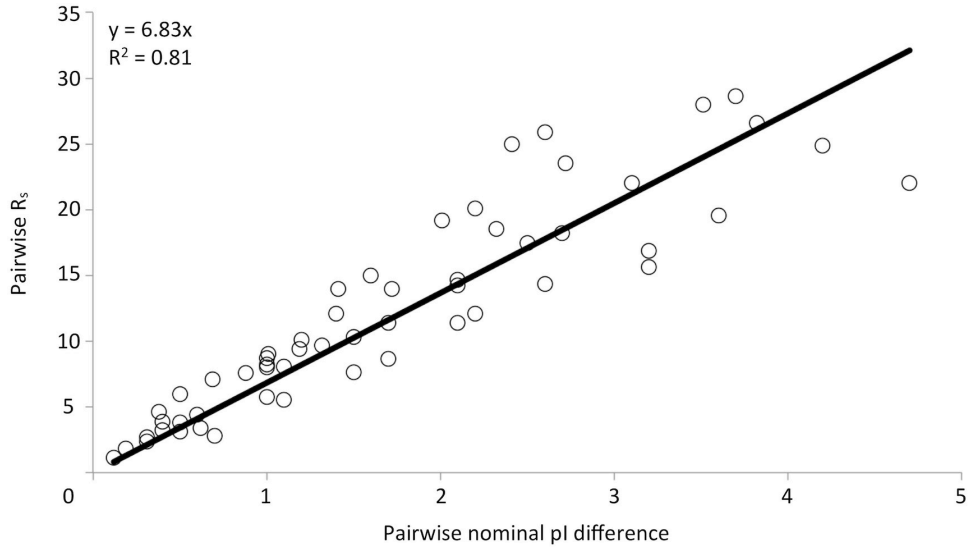

Figure 3.4: Separation resolution of analyte pairs under focusing conditions for the 8 pI markers and 3 GFP isoforms presented in Figure 3.3B (55 total comparisons). A threshold of $R_s = 1$ yields a minimum separable pI difference of 0.15 via linear regression. Reproduced from [6].

IEF, with just ∼15 fg injected into the 5.8 nL microchannel.

After IEF, the second assay stage is a transition to in situ immunoprobing of the IEF resolved species (Figure 3.3B,C). As discussed in Section 3.3, the IEF-focused species and the microfluidic LAVAgel are exposed to UV light to induce photoimmobilization of species to the light-activatable copolymer. The IEF pH gradient is then exchanged to uniform pH buffer conditions using a 20 min chemical mobilization step (Figure 3.3C). Gradient "washout" by chemical mobilization eliminates the need for pumps and valves, thus dramatically simplifying the hardware interface.

Finally, during the third stage (Figure 3.3D,E), immunoaffinity probes are electrophoresed through the protein-decorated 3D LAVAgel. In addition to yielding efficient mass transfer, as described in Section 3.3, electrophoretic transport simplifies hardware interfacing and, importantly, requires only ∼1 ng of antibody. Electrophoretic washout of unbound probe reveals the target protein isoform pattern (Figure 3.3E). Two color fluorescence imaging shows the resolved wtGFP isoforms (green) and the resultant signal from a red-labeled polyclonal antibody for wtGFP. Comparison of the blot signal to the protein signal reveals specificity for GFP and low off-target background signal, even amidst a ∼20-fold excess of off-target ladder proteins. A fourth GFP isoform is apparent at pI 5.33 only after immunoprobing, an intriguing consequence hypothesized to arise from a protein charge photoswitching process that is explored in detail in Chapter 5.

3.4.2 Characterization of Microfluidic LAVAgel Photoimmobilization

We sought to quantitatively assess performance of our volume-accessible microfluidic LAVAgel material. The LAVAgel capture efficiency is a critical performance metric, as previous reports of analyte photocapture on capillary surfaces (in both research and commercial instruments) report strikingly low capture efficiencies of ∼0.01% [47]. Characterization requires assessment of analyte capture efficiency in the non-uniform pH conditions of IEF. Using a two-pronged approach, we measured capture efficiency for both: (i) a well-characterized three isoform model protein (wtGFP) and (ii) a broad pH range using a novel fluorescence labeling strategy to visualize ampholytes that constitute the pH gradient.

We first define capture efficiency, η, as the ratio of fluorescence signal measured after photocapture ($I_{\text{immobilized}}$ i.e., after IEF and pH gradient washout) to the fluorescence signal measured during IEF (I_{IEF}) or:

$$\eta = \frac{I_{\text{immobilized}}}{I_{\text{IEF}}}.\epsilon.100\% \tag{3.1}$$

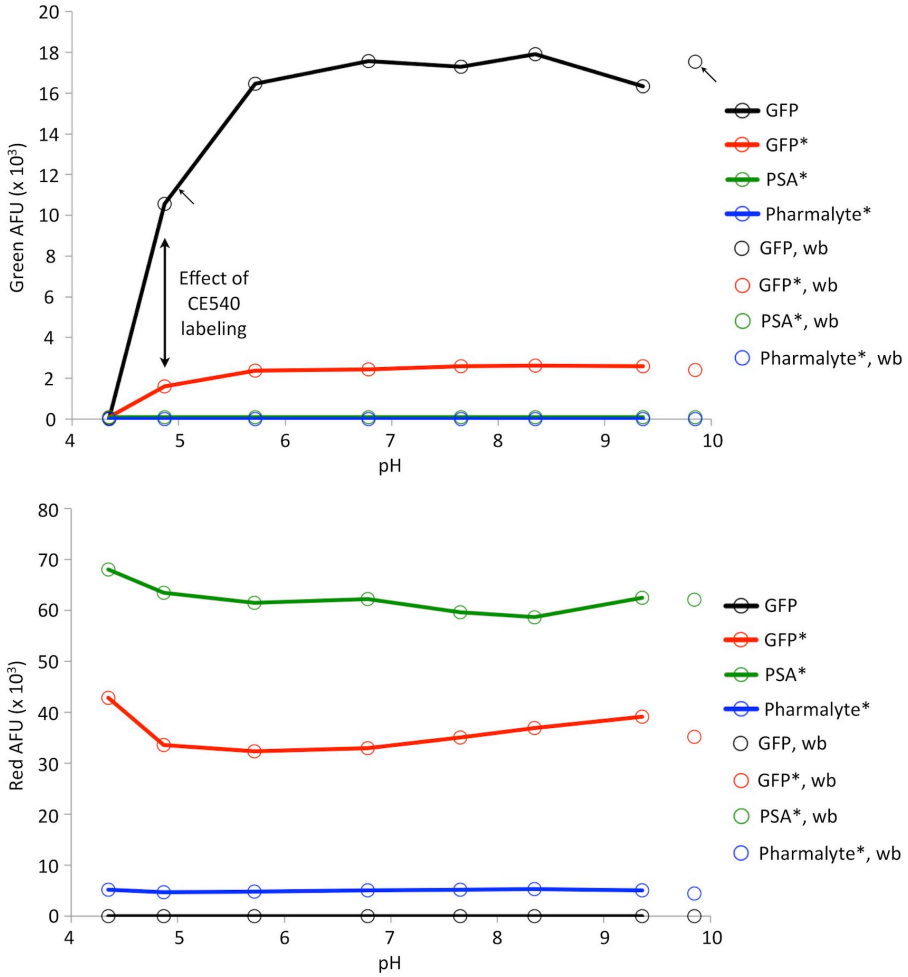

Figure 3.5: Microplate experiments reveal denaturing effect of GFP labeling and allow extraction of η. Top, solid lines are microplate green fluorescence data for analytes (1 μM each) in 50 μl aliquots of loading buffers titrated to the measured pH values shown with 2M HCl or NaOH. Data points at pH 9.9 are for washout buffer (wb) samples. ϵ for GFP is approximated via the ratio of fluorescence values at the points indicated by short arrows. The strong pH effect of GFPs fluorescence in the vicinity of its pI is well known in the literature [103]. Bottom, corresponding red fluorescence values for each analyte, note the negligible dependence of CE540 fluorescence on pH for all labeled species. Reproduced from [6].

Recall that the pH of the washout buffer differs from the local pH during IEF ($\mathrm{pH}_{\mathrm{washout}} = 9.9$ while $\mathrm{pH}_{\mathrm{IEF}} = \mathrm{pI}$), thus correction for the anticipated influence of pH on the fluorescence signal of each species is needed. We employ an empirical correction factor, ϵ, determined to be: $\epsilon \approx 0.75$ for wtGFP and $\epsilon \approx 1.0$ for all fluorescently labeled ampholytes (see Figure 3.5).

In the wtGFP portion of the study, we observed a maximum photoimmobilization efficiency of 1.8% with photoimmobilization well-described by a first-order model relating η to the UV exposure time (Figure 3.6A). Importantly, the capture efficiency represents a more than 100-fold improvement over reported surface photoimmobilization values ($\eta \sim 0.01\%$) [47]. As discussed, we attribute the substantial increase in capture efficiency measured here in the 3D LAVAgel to the high surface area offered by the reactive nanoporous matrix [25]. The reaction time constant is 5.5 s. The small time constant suggests that the photocapture dynamics of the microfluidic LAVAgel system are compatible with IEF, but likely also compatible with a wide range of on-chip and non-equilibrium separation methods, including protein sizing by SDS-PAGE as is currently under study in our group.

Dispersion (band broadening) added during the photoimmobilization process will reduce the information content in the immobilized separation, thus reducing the overall performance of the integrated assay. Thus, an assay design tradeoff exists between the dominant transport processes and the duration of UV exposure after IEF. Although IEF is an equilibrium separation method, we observed non-negligible electroosmotic drift during IEF (1.0 μm s^{-1} to 3.3 μm s^{-1} for $E_{\text{IEF}} = 300$ V cm^{-1} at IEF completion). Drift is attributed to the slight negative charge of polyacrylamide gels (22). A 10 s UV exposure yielded a drift distance of 10–33 μm for a focused protein band, on par with the average peak width of focused GFP isoforms (100 μm). Thus, photoimmobilization under IEF conditions should adversely impact overall assay resolution and total peak capacity. Consequently, we limited captured analyte dispersion by performing photocapture of IEF bands under zero-field conditions ($E = 0$ V cm^{-1}, or floating). Under zero-field conditions, the drift and the focusing force of IEF go to zero, making molecular diffusion the dominant transport process. Using empirically-determined diffusion-associated resolution losses and capture efficiencies for two neighbor peaks (two isoforms of GFP) in the microfluidic LAVAgel system, we found that a 10 s UV exposure under zero-field conditions confers 84% of the achievable capture efficiency for a loss in separation resolution of just 22% from that in the focused-state (Figure 3.6A).

In the second portion of the photocapture efficiency study, we characterized photoimmobilization performance across a broad pH range (Figure 3.6B). Given that the ampholytes themselves are excellent structural analogs to polypeptides, we imaged fluorescently labeled ampholytes (reporter ampholytes) to map η across the pH 5–7.5, as this range encompasses a preponderance of protein isoforms [121]. To create reporter ampholytes with a broad continuum in pI, we fluorescently labeled the amine termini of the ampholytes using a CE540 fluorophore that offers a charge-compensating reaction mechanism (Figure 3.8). This charge-compensation mechanism is thought to avoid the charge heterogeneity that makes other reactive dyes largely incompatible with IEF [122]. As shown in Figure 3.3B, the immobilized reporter ampholytes distributed along the microfluidic LAVAgel reveal a ~2-fold monotonic rise in the capture efficiency from the acidic to basic end of the pH range studied.

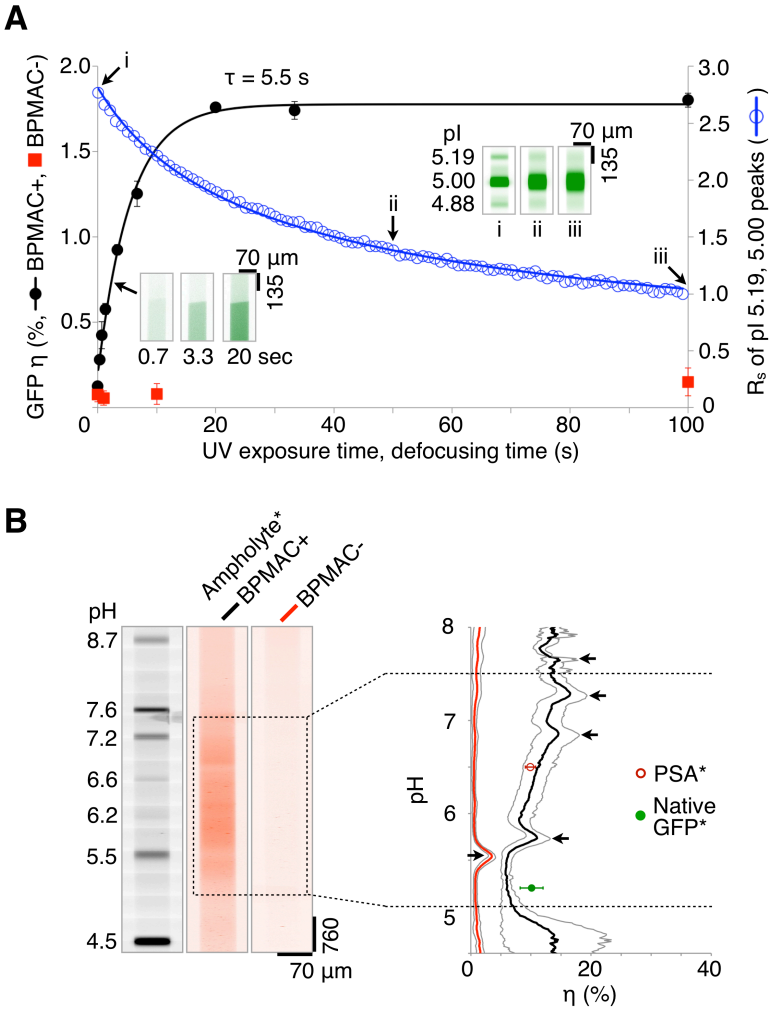

Figure 3.6: Characterization of LAVAgel photoimmobilization kinetics, capture efficiency, and pH dependence. (A) LAVAgel capture efficiency and resolution losses are optimized by tuning UV exposure duration. Photoactive LAVAgel (BPMAC+, 15 μM wtGFP, $\pm$ SD, $n = 4$, black solid circles) is compared to a non-photoactive negative control (BPMAC$-$, red squares). Inset: fluorescence micrographs show captured wtGFP fluorescence. Blue open circles and inset images (i–iii) show separation resolution loss for wtGFP isoforms during de-focusing, following an inverse square root dependence on time. GFP concentration is 617 nM, resolution measured between the pI 5.00 and 5.19 isoforms. (B) Reporter ampholytes (ampholyte*) allow measurement of capture efficiency under focusing conditions for a broad pH range. Left: fluorescence micrographs show pI ladder and photocaptured reporter ampholytes after pH gradient washout. Right: reporter ampholyte capture efficiency versus pH in BPMAC+ and BPMAC$-$ LAVAgels, black arrows indicate artifact peaks caused by enhanced local photobleaching of reporter ampholytes in the vicinity of pI marker bands (Figure 3.7; [ampholyte*] = 0.025% w/v, grey envelopes are $\pm$ SD, $n = 4$). Reproduced from [6].

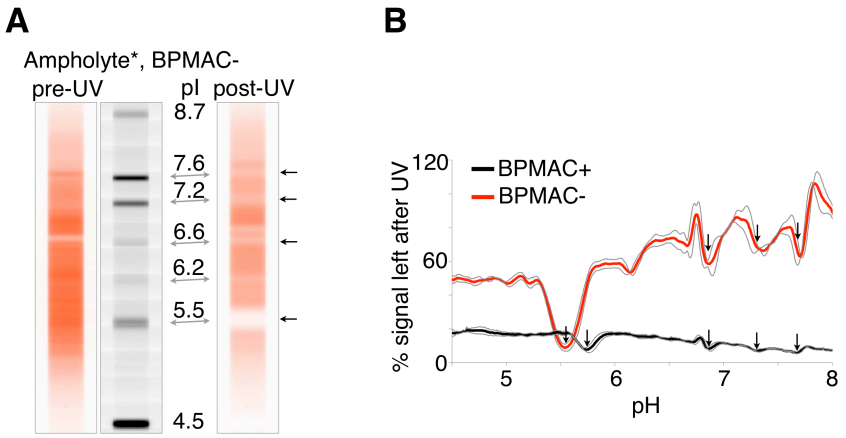

Figure 3.7: Colocalized ampholyte* species and pI markers yields enhanced photobleaching. (A) Effect of 10 s flood UV exposure on ampholyte* profile in the focused state prior to washout. pI markers exacerbate local ampholyte* bleaching (grey and black arrows). (B) Ampholyte* signal retained after UV exposure. Troughs in pI marker regions are marked by black arrows. Note, higher overall bleaching occurs in BPMAC+ LAVAgels, presumably due to side reactions between ampholyte* radicals and other reactive species generated upon BPMAC photoactivation [120]. Reproduced from [6].

In absolute terms, the capture efficiency for the reporter ampholytes ranges from $7.2 \pm 2.0\%$ (near pH 5, $n = 4$) to $13.3 \pm 1.7\%$ (near pH 7.5, $n = 4$) in the LAVAgel. From an assay design perspective, the pH response of η is suitable for protein isoform analyses, given the absence of a strong bias towards any particular pH zone and the fact that protein isoforms are typically clustered over a relatively tight pI range [121]. We hypothesize that the increase in η with pH stems from a change in the chemical properties of the ampholyte species, which are also graded along the pH axis [123].

A corollary investigation was undertaken to understand the high capture efficiencies observed using reporter ampholytes, as compared to the wtGFP single protein analysis. We hypothesized that the hydrophobic structure of CE540 [122] may contribute to a higher η by increasing weak "pre-covalent" interactions of labeled species with the LAVAgel matrix. To elucidate the role of the CE540 dye in photocapture efficiency, we studied two model proteins using the same approach applied to the reporter ampholytes. Both GFP and PSA were labeled with CE540 (GFP*, PSA*) and subjected to IEF and photocapture. Both species exhibited η on par with the reporter ampholytes, here $\eta_{\mathrm{GFP}^*} = 10.1 \pm 1.91\%$ ($n = 8$) and $\eta_{\mathrm{PSA}^*} = 9.92 \pm 0.86\%$ ($n = 3$). Interestingly, and with perhaps important implications, we found appreciable effects of the CE540 labeling on the conformational

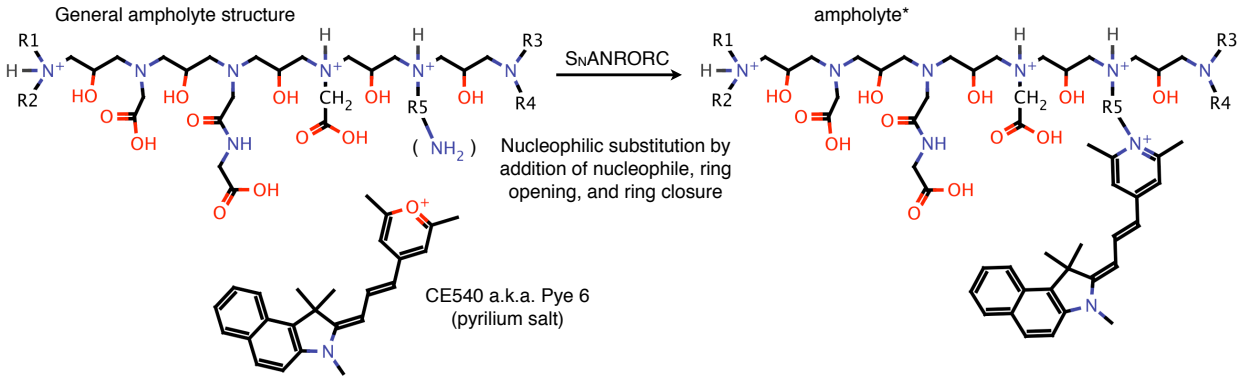

Figure 3.8: General reaction scheme for the synthesis of reporter ampholytes [124].

heterogeneity and capture efficiency of wtGFP, see Figure 3.9. Specifically, all CE540 labeled proteins/peptides had capture efficiencies notably higher than unlabeled protein (cf. $\eta_{\mathrm{GFP}^*} \sim 10\%$ to $\eta_{\mathrm{GFP}} = 1.30 \pm 0.17\%$, $n = 44$). Results indeed suggest that pre-covalent interactions stemming from increased analyte hydrophobicity (affected by both labeling and denaturation state) enhance capture efficiency. Further, CE540-labeled wtGFP* exhibits native and denatured protein sub-populations (Figure 3.9). During IEF, the native population is characterized by co-localized green (endogenous) and red (CE540) fluorescence (i.e., green+, red+) as anticipated. However, a dominant GFP* population is also observed that lacks any co-localized green signal (i.e., green−, red+). We hypothesize that in this latter population of GFP*, CE540 induces unfolding of GFP sufficient to destroy the green fluorescence of its chromophore. In supporting studies, a microplate experiment showed a 7-fold reduction in green fluorescence of GFP* from that of GFP in an isoelectric ampholyte buffer, providing further evidence for labeling-induced denaturation (Figure 3.5). The denatured GFP* segment gives η_{red} based on its red CE540 signal of 34.5% (versus 10.1% for the native GFP* segment, see Table 3.1). This measurement is consistent with the observation that minor conformational increases in solvent-accessible surface area of protein targets produce disproportionately large jumps in diazirine-mediated photolabeling efficiency, suggesting higher protein-label reactivity for looser protein conformations [125]. Indeed for labeled, reduced, and denatured proteins in a size-based (SDS-PAGE) assay format described in Chapter 6, we have observed capture efficiencies of 70-100% in LAVAgels. These observations suggest strong and distinct contributions of protein labeling and conformational disruption on the achievable η.

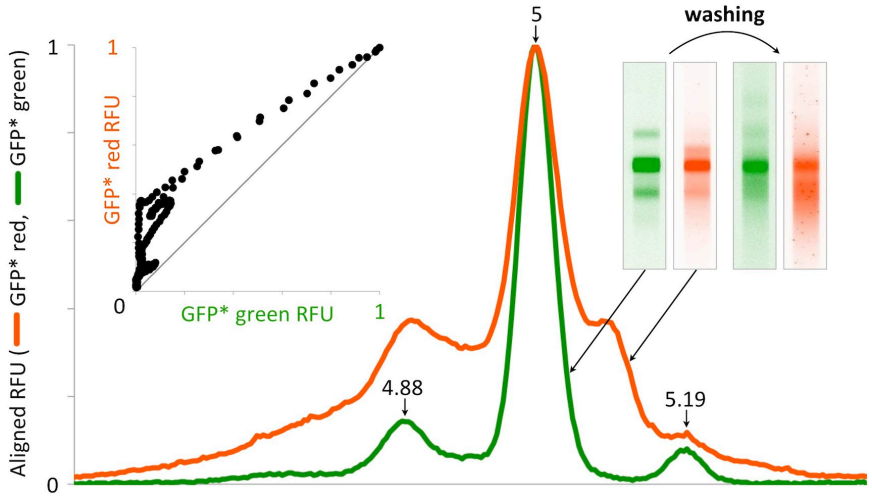

Figure 3.9: CE540-labeled GFP exists as native (green+, red+) and denatured (green−, red+) subpopulations. Aligned relative fluorescence data from sequential imaging on green and red spectral channels for GFP* focused at 300 V cm^{-1} in a single LAVAgel (nominal [GFP*] = 617 nM). The red fluorescence readout is dominated by the denatured population, presenting as a diffuse set of bands with rough correspondence to those of the native GFP* population (green fluorescence readout). The canonical 3-band structure observed for the native GFP* population is very similar to that of unlabeled GFP (Figure 3.3B). Reproduced from [6].

Table 3.1: LAVAgel capture efficiencies η (%) under focusing conditions. Red CE540-labeling indicated by "*", fluorescence emission channel used to determine η denoted by "green" and "red".

Target	pH	η_{green}	η_{red}
GFP	~ 5.2	1.30 ± 0.17 $(n = 44)$	–
GFP*	~ 5.2	10.1 ± 1.91 $(n = 8)$	34.5 ± 3.04 $(n = 8)$
PSA*	~ 6.5	–	9.92 ± 0.86 $(n = 3)$
Pharm. 3–10*	5.0	–	7.17 ± 1.95 $(n = 4)$
	7.5	–	13.3 ± 1.70 $(n = 4)$

3.4.3 Microfluidic LAVAgel Analysis of PSA Isoforms in Crude Cell Lysate

We first tested the LAVAgel assay on purified unlabeled PSA as a well-controlled model system (Figure 3.10A). PSA was probed after IEF and photoimmobilization using sequential introduction of specific primary and secondary detection antibodies. Two major isoforms with pIs of 6.27 ± 0.02 and 6.77 ± 0.04 ($n = 4$) are baseline resolved, accompanied by several minor peaks below baseline resolution. Gold-standard comparisons to macroscale slab gel IEF (Figure 3.11) and capillary IEF [126] show good agreement between the isoform patterns. Specifically, slight differences between the LAVAgel and conventional Novex slab gel assays of PSA were mitigated using a custom slab gel with the same buffer composition as the LAVAgel. In contrast, the GFP isoforms arising by differential C-terminal proteolytic cleavage [127] exhibited similar behavior in the chip and Novex gels. This comparison study suggests that the isoform pattern of PSA is sensitive to the presence of the solubilizing additives used in LAVAgels (CHAPS, sorbitol and NDSB-256) that may modulate PSA glycan solvation.

Linear calibration curves were generated for two scenarios: probing captured PSA with a fluorescently labeled primary antibody and, as is more broadly relevant, probing of the primary antibody with a labeled secondary antibody. In Figure 3.10B, the relationship between the spiked PSA concentration and fluorescence readouts for the dominant isoform (pH 6.0–6.5) is linear from ∼10–500 nM. Quantitative capacity is maintained to ∼5 nM PSA (165 ng ml^{-1}) or ∼1.1 pg of PSA. Improvement of the absolute lower limit of detection should be feasible through, for example, incorporation of amplified readout approaches to yield a LAVAgel assay sensitivity on par with conventional bench top 2D electrophoresis with western blotting (∼0.1 ng ml^{-1}) [76, 102]. Such approaches should also increase the dynamic operating range of the present assay. The PSA isoform characterization study allows inference of the stoichiometry of secondary:primary antibody probing from the ratio of the respective fluorescence traces and indicates negligible effects of the gel pore environment on achievable probe-target valency (Figure 3.10B and Figure 3.12). Note that the degrees of labeling of each antibody probe are similar, and that the labeling dye is the same (red Alexa Fluor 568). The binding stoichiometry was determined to be ∼2.5 across the relevant pH range, exhibiting somewhat higher values at the acidic end of the isoform pattern due to a non-specific contribution of the secondary Ab* to the assay readout. Remarkably, the observed stoichiometry is in excellent agreement with that of 2.5 determined by Yu *et al.* using a surface plasmon field-enhanced fluorescence spectroscopy study of polyclonal secondary:primary antibody binding [128].

We next assayed a PSA-producing cell line relevant to the study of prostate cancer (Figure

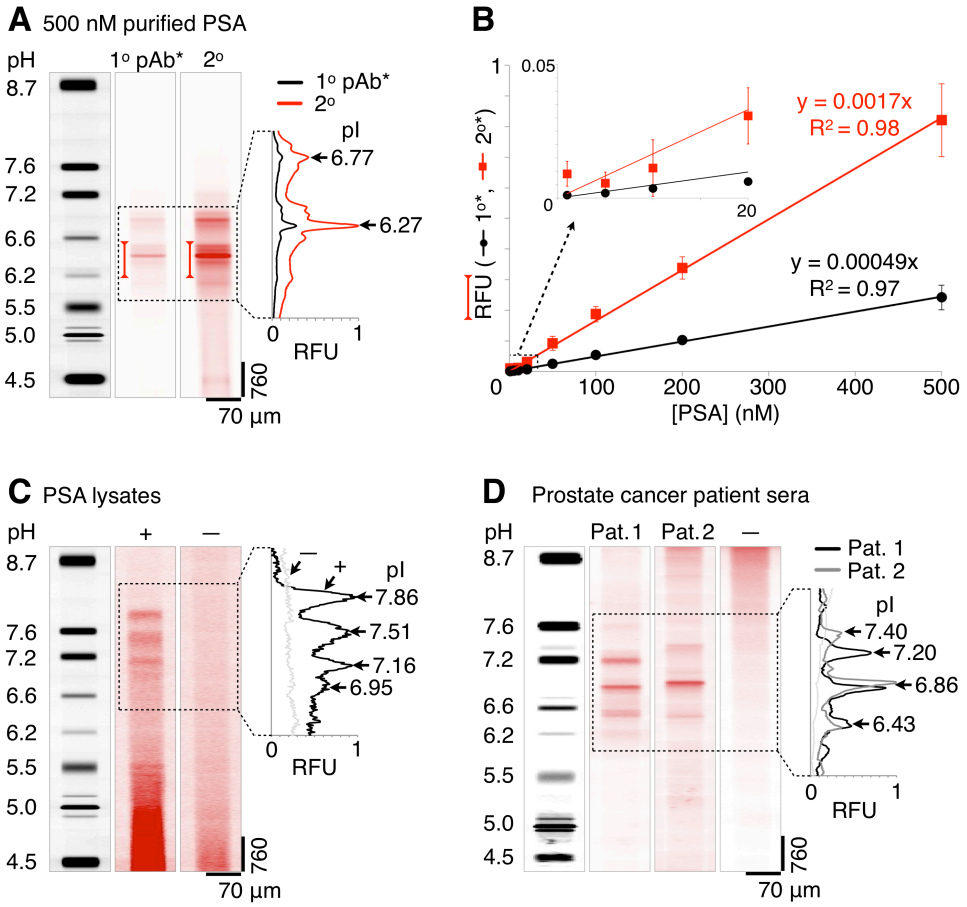

Figure 3.10: LAVAgel assay enables quantitation of PSA isoforms in minimally processed prostate cancer cell lysate and human sera. (A) Fluorescence micrographs and electropherograms for probing of unlabeled PSA purified from human seminal fluid (500 nM): focused pI markers, primary (1°) and secondary (2°) antibody probe signals. Bracketed peak areas used to construct calibration curves. (B) Linear PSA calibration curves for primary (black circles) and secondary (red squares) antibody readouts (± SD, $n = 4$ for all points except 5 nM, $n = 2$). (C) Primary antibody probing of endogenous PSA isoforms in lysate from a PSA-producing cell line (LAPC–4 cells, +) with negative control lysate (DU145 cells, –). (D) Serum samples from metastatic prostate cancer patients probed with primary antibody to PSA (patients 1 and 2), alongside a low-PSA negative control serum (–). Reproduced from [6].

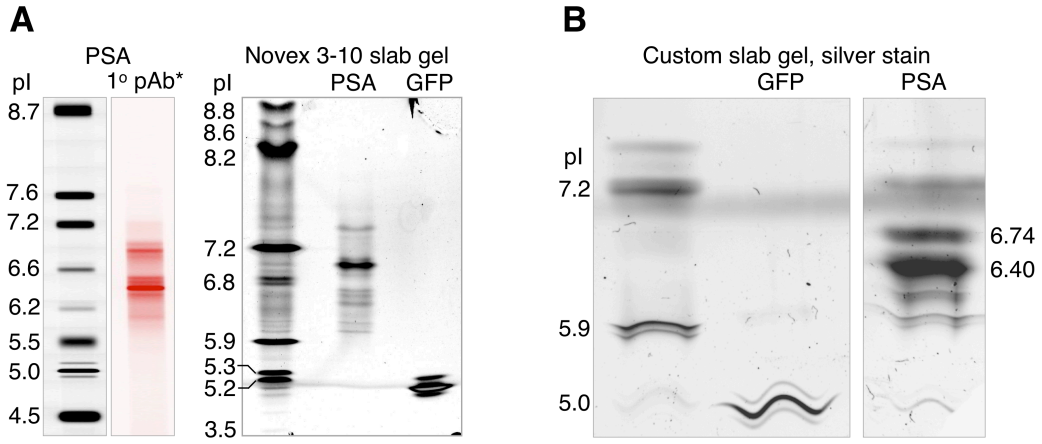

Figure 3.11: LAVAgel and companion slab-gel IEF assays. (A) Comparison of purified PSA and GFP readouts in LAVAgel to Novex slab gel (LAVAgel GFP visible in pI marker set). (B) PSA isoform pattern in custom slab gel agrees with major band assignments in LAVAgels (gel buffer compositions here were identical to those in LAVAgels). Reproduced from [6].

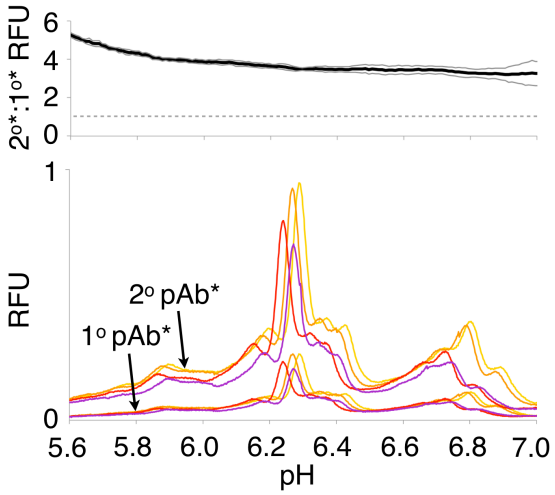

Figure 3.12: Inference of probe stoichiometry for purified PSA. Bottom: comparison of signal after 1° and 2° probing for 500 nM PSA. Top: 2°:1° signal amplification ratio (dotted line marks baseline of nil 2° signal at 2°:1° = 1, grey envelope is ± SD, $n = 4$). Reproduced from [6].

3.10C). Here, we quantify endogenous PSA isoforms present in 3 μl of minimally processed lysate from LAPC–4 cells derived from a lymph node of a human prostate cancer patient. The probed LAPC–4 lysate presents a distinctive four peak pattern in the pI 6.9–7.9 range that is similar to slab gel assays of PSA purified from LAPC–4 cell culture medium [104,117]. As a negative control, lysate from a PSA negative cell line (DU145) was assayed and shows no detectable PSA isoform readout, as expected. The crude cell lysate samples yielded some non-specific signal near the anodic well, likely due to that channel region being the electrophoretic introduction point for both sample and labeled antibody probe. The total PSA concentration via the microfluidic LAVAgel assay was determined to be 27.8 ± 4.7 nM ($n = 4$) using the purified PSA calibration curve of Figure 3.10B, in reasonable agreement with benchmark ELISA measurements (see Materials and Methods).

To validate the capability of the microfluidic LAVAgel assay to measure immunoreagent isoform specificity, we compared the isoform distribution of IEF-focused CE540-labeled PSA* to the fluorescence readout after capture and probing with both monoclonal and polyclonal PSA antibodies (Figure 3.13). Alignment between each pair of fluorescence intensity profiles (PSA*, Ab*) was accomplished by applying a translation inferred from their cross-correlation. The translational shift corrects for the slight drift ($\sim$190 μm) between imaging of focused PSA* and the photoimmobilization step. The focused PSA* isoform pattern agrees well with that of the probed unlabeled PSA, suggesting little impact of CE540 on the pIs of the native PSA isoforms (compare Figure 3.13A,B and Figure ProbedIEFPSAA). Ratiometric comparison of the probed and focused PSA* signals suggests spatially uniform probe layering onto immobilized PSA* across the pH region of interest, for both polyclonal and monoclonal detection antibodies (Figure 3.13C,D). Some apparent variation across the pH range is induced by diffusional band broadening during photoimmobilization, which has the expected "peak blunting" effect on the probing data. Nonetheless, comparison of the monoclonal and polyclonal probing ratios again reveals a 2.5:1 pAb*:PSA* stoichiometry (Figure Figure 3.13E, assuming a 1:1 stoichiometry inherent in the monoclonal readout with [Ab*]$\gg K_D$, equilibrium in binding [25], and negligible PSA "epitope disfigurement" upon immobilization). Intriguingly, this capability offers use of high-throughput LAVAgel IEF assays for isoform-specific immunoreagent selection assays to enable rapid development of next-generation ELISA microplate-based bioassays and clinical diagnostics with isoform resolution.

3.4.4 Microfluidic LAVAgel Analysis of PSA Isoforms in Metastatic Prostate Cancer Patient Sera

We further demonstrated clinical utility of the LAVAgel assay by separating and probing PSA isoforms in minimally processed sera from advanced metastatic prostate cancer patients (Figure 3.10D). The low volume requirement of the assay (3 μl) is critical for screening of often ephemeral and volume-limited human biospecimen repositories.

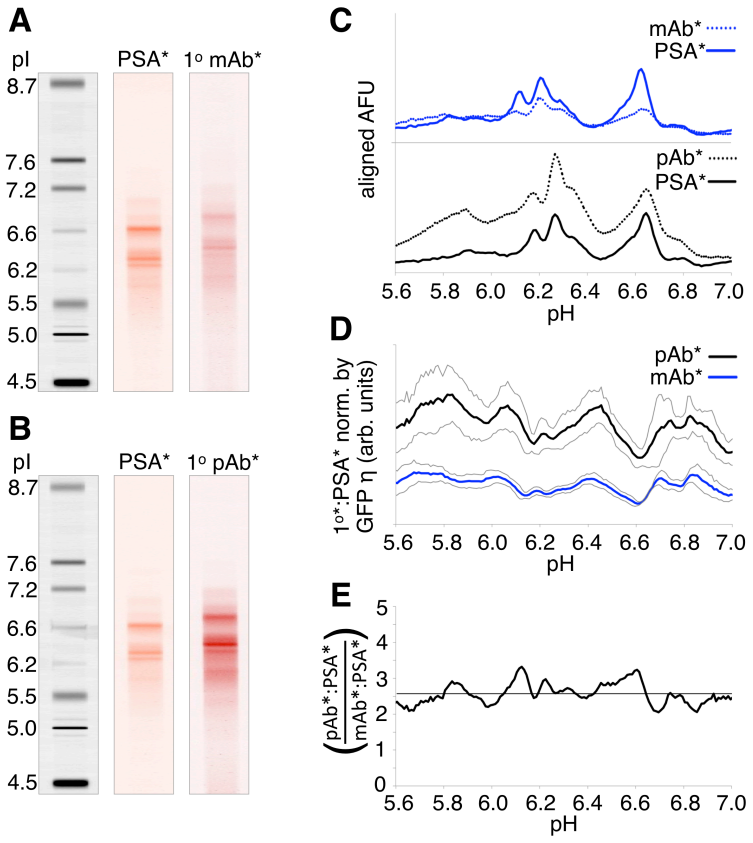

Figure 3.13: LAVAgel assays in recognition mapping mode for isoform-resolution probe screening. (A) CE540-labeled PSA* in focused and probed states for monoclonal and (B) polyclonal Ab* (all gel images adjusted for identical contrast, [PSA*] = 500 nM, [mAb*, pAb*] = 1 μM). Electrophoretically washed PSA* data showed negligible contribution to probe signals by immobilized PSA* detected on the same spectral channel. (C) 1° Ab* readouts aligned to corresponding focused PSA* traces from (A) and (B). (D) Probed:focused signal ratios adjusted by GFP capture efficiency (grey envelopes are ± SD, $n = 8$ for each of mAb* and pAb* sets). (E) Ratio of pAb*:mAb* data from (D). Reproduced from [6].

Human sera from two patients were assayed in addition to a low-PSA negative control sample, all at 10× dilution. The two PSA+ samples each show three major PSA isoforms falling within the pI 6.4–7.5 range, in good agreement with comparatively laborious slab gel IEF studies [102, 104]. Patient-specific differences in PSA isoform representation and pI are clearly apparent, recapitulating the potential utility of isoform ratio measurements in clinical diagnostics and personalized medicine [102, 103]. Ongoing studies are currently in progress to validate the LAVAgel assay for rapid, high-throughput classification of cancer and benign prostate pathology patient groups.

3.5 Conclusions

Quantitative, robust protein isoform assays designed for analysis of minimally processed fluids are needed to advance diagnostics for personalized medicine. We demonstrate a quantitative protein isoform assay that harnesses microfluidic integration, fully electrophoretic control, and a photoactivatable 3D hydrogel for automated, pump-free operation. The automated assay reports isoform levels in 80–120 min, a 5- to 15-fold improvement in assay time over 2D electrophoresis with western blotting and a 2-fold improvement over capillary immunoblotting [47, 102]. Two aspects of our design rationale distinguish the present study and underpin observed performance gains, as compared to currently available immunoblotting assays. Firstly, the 3D LAVAgel significantly boosts protein immobilization and probing efficiency over 2D surface capture approaches owing to the availability of $\sim 10^2 - 10^3$ more reactive sites and use of directed electrokinetic transport through the nanoporous LAVAgel. The strategy yields capture efficiencies that are two to three orders of magnitude higher than competing surface capture approaches (0.01% vs. 1.3% to 13% demonstrated here).

In contrast to ELISA-based approaches, the microfluidic LAVAgel platform allows quantitation of distinct biomarker isoforms and requires just a single primary antibody (not capture and detection matched pairs) and an optional secondary detection antibody. We demonstrate PSA isoform detection in crude cell lysate and serum repository biospecimens from metastatic prostate cancer patients. Microfluidic integration yields sparing consumption of precious biospecimens (1–5 μL), low consumption of costly probing antibodies (1 ng antibody), and total assay completion in one unified instrument. The measurement operating range of the assay was optimized for clinical relevance to PSA and isoforms in prostate cancer sera. Adaptation and optimization should allow for protein isoform assessment (including quantitation) in other human diagnostic fluids and tissue samples (e.g., from laser capture microdissection). This first report of a self-contained, electronically controlled immunoblotting platform fills an important gap in translation of promising protein biomarkers from as-discovered to validated high-utility biomarkers of disease. We continue to actively develop the platform as a core technology adaptable to protein biomarker scrutiny in a broad range of local and systemic diseases, rapid analysis of promising diagnostic biomarkers from biospecimens only available in minute volumes. Continued innovation is focused on realiz-

ing higher throughput through scale-up of electrode and liquid handling architectures for simultaneous analysis of panels of protein biomarkers in larger patient sample sets while maintaining compatibility with existing microplate handling systems.

Chapter 4

Antibody-Antigen Kinetics in LAVAgel Systems

4.1 Introduction

In the development of assays heavily reliant upon in-gel antibody probing, we were interested to identify possible limitations to the speed and equilibrium readout intensity of such strategies. Here, we review potential contributors to altered kinetics of in-gel probing in comparison to standard probing kinetics on flat surfaces in e.g. traditional western blotting and ELISA. Further, we provide a first-principle rationale for the high capture efficiencies observed in LAVAgel/PACTgel implementations in comparison to published in-capillary protein immobilization employing the benzophenone photophore.

4.2 Results & Discussion

4.2.1 Target Antigen Immobilization Kinetics

The reaction between BPMAC and the protein target of interest occurs against a strong background of competing reactions. The bulk of the BPMAC sites are likely to form conjugates with off-target species, namely the ampholytes, gel matrix, sorbitol, NDSB 256 and CHAPS in the case of the probed IEF assay developed in Chapter 3. The combined concentration of these off-target species is >20% w/v in the LAVAgel precursor, constituting a $\sim 10^6$ fold excess over protein targets in the normal device operating regime. Thus, we consider a simple kinetic scheme that characterizes the capture efficiency of a protein target in this regime. Consider parallel irreversible reactions between one reactant (BPMAC, species A) and a set of competing species (species B_i), one of which is the target protein of interest. The reaction scheme is as follows [129]:

$$A + B_1 \xrightarrow{k_1} P_1, \quad A + B_2 \xrightarrow{k_2} P_2, \quad A + B_3 \xrightarrow{k_3} P_3, \ \ldots \ A + B_n \xrightarrow{k_n} P_n \tag{4.1}$$

For low capture efficiencies η, it can be assumed that the free species concentrations do not change appreciably from their initial values, i.e. $b_i \sim b_{i,o}$ (lower case denotes concentration of a species). The rate of disappearance of BPMAC is thus:

$$\frac{da}{dt} = -k'_T a \tag{4.2}$$

Where $k'_T = \sum_{i=1}^{n} k'_i = \sum_{i=1}^{n} b_{i,o} k_i$ is a sum of the pseudo-first-order rate constants k'_i of the competing species.

Integrating this expression gives:

$$a = a_o e^{-k'_T t} \tag{4.3}$$

For generation of a given product P_i:

$$\frac{dp_i}{dt} = b_{i,o} k_i a \tag{4.4}$$

Substituting Equation 4.3 into Equation 4.4 and integrating gives:

$$\int_0^{p_i} dp_i = b_{i,o} k_i a_o \int_0^t e^{-k'_T t} dt \tag{4.5}$$

$$\Rightarrow p_i = \frac{b_{i,o} k_i a_o}{k'_T}(1 - e^{-k'_T t}) \tag{4.6}$$

This result reveals the unusual property that despite each individual reaction having different pseudo-first-order rate constants ($k'_i = b_{i,o} k_i$) the product generation rates are identical and are characterized by a time constant $\tau = \frac{1}{k'_T} = \frac{1}{\sum_{i=1}^{n} b_{i,o} k_i}$. As we expect $k'_T \gg b_{\text{target,o}} k_{\text{target}}$ (subscript "target" denotes the reaction between the protein target of interest and BPMAC), i.e. that the contribution of k'_{target} to k'_T is small given the vast excess of off-target species in the reaction, we can expect the observed reaction rate to be approximately independent of the target protein concentration. Thus, the observed LAVAgel immobilization time constant is expected to be invariant across the target calibration curve concentration range.

For long reaction times ($t \to \infty$), from Equation 4.6:

$$p_{\text{target}} = \frac{b_{\text{target,o}} k_{\text{target}} a_o}{k'_T} \tag{4.7}$$

$$\Rightarrow \eta = \frac{p_{\text{target}}}{b_{\text{target,o}}} \times 100 = \frac{k_{\text{target}} a_o}{k'_T} \times 100 \tag{4.8}$$

Again, for k'_T approximately independent of $b_{\text{target,o}}$, the LAVAgel capture efficiency is also expected to be independent of $b_{\text{target,o}}$ (i.e., constant across the calibration curve). Further,

note that increased k_{target}, increased a_o (increased [BPMAC]), or decreased k_T (decreased concentration of competing species and/or rates of competing reactions) all increase η, in accordance with intuition.

Given that the immobilized target concentration is expected to be a constant fraction of the nominal concentration, and that probe saturation of captured target is guaranteed across the calibration curve at equilibrium for $Da \ll 1$ and sufficiently high probe concentration above K_D [25], we expect a linear calibration relationship in the LAVAgel system, which indeed is observed in the experimental data for PSA (Figure 3.10B).

Finally, the benefit of high immobilization surface area is revealed by considering the volumetric concentration of BPMAC, a_o given a consistent site density $a_{o,s}$ distributed across an immobilization surface with surface area to volume ratio of $\frac{A_s}{V}$:

$$a_o = \frac{a_{o,s} A_s}{V} \tag{4.9}$$

Substituting Equation 4.9 into Equation 4.8 allows us to determine a ratio of gel to open capillary capture efficiencies:

$$\frac{\eta_{\text{gel}}}{\eta_{\text{cap}}} = \frac{\frac{A_{s,\text{gel}}}{V}}{\frac{A_{s,\text{cap}}}{V}} \tag{4.10}$$

The gel surface area $A_{s,\text{gel}}$ can be roughly compared to an open capillary $A_{s,\text{cap}}$ by approximating the gel structure to be a bundle of packed cylinders in simple cubic arrangement with radius r_{gel} equal to that of the mean pore radius of 120 nm for a 4%T, 2.6%C gel [119], giving:

$$\frac{A_{s,\text{gel}}}{V} \sim \frac{2\pi r_{\text{gel}} l}{(2r_{\text{gel}})^2 l} = \frac{\pi}{2r_{\text{gel}}} \tag{4.11}$$

$$\frac{A_{s,\text{cap}}}{V} = \frac{2\pi r_{\text{cap}} l}{\pi r_{\text{cap}}^2 l} = \frac{2}{r_{\text{cap}}} \tag{4.12}$$

From Equation 4.10:

$$\frac{\eta_{\text{gel}}}{\eta_{\text{cap}}} \sim \frac{\pi r_{\text{cap}}}{4r_{\text{gel}}} = 327 \tag{4.13}$$

With $r_{\text{cap}} = 50$ μm.

We thus expect a $\sim$2–3 order-of-magnitude increase in capture efficiency within the gel matrix as compared to the capillary surface, which is matched well by our experimental observation of an $\sim$180-fold improvement in η over that observed by O'Neill *et al.* [47].

4.2.2 Probe Binding to Immobilized Antigen

Here we compare the timescales of probe mass transfer and binding for a target analyte (P_{target}) immobilized to the wall of an open capillary or to the LAVAgel matrix. In the following analysis, gel and free solution antibody probe diffusivities of $\sim 4.5 \times 10^{-12}$ and $\sim 3.4 \times 10^{-11}$ m^2 s^{-1} respectively are used (see Appendix C). The capillary tube length y in the open-channel case we take to be the approximate length of an immobilized target peak ($\sim$100 μm) with tube diameter 100 μm. The surface concentration of target antigen p_{target} is taken to be that resulting from attachment of focused analyte at $\eta = 1\%$ from a 100 nM nominal solution assuming an IEF concentration factor of $\sim \frac{10.4 \text{ mm}}{0.1 \text{ mm}} \sim 100$ onto a surface area arising from the cylindrical pore model already described. This gives $p_{\text{target}} = 7.6 \times 10^{-12}$ mol m^{-2}. For equivalence of the two cases, we assume the same p_{target} for the open capillary. The values of $k_{\text{off}} \sim 10^{-3}$ s^{-1} and $k_{\text{on}} \sim 10^{6}$ M^{-1} s^{-1} for Ab-Ag interactions [25, 130].

Consider an immobilized antigen target P_{target} attached to a capillary wall and probed with a detection antibody C to form a stationary complex X:

$$P_{\text{target}} + C \underset{k_{\text{off}}}{\overset{k_{\text{on}}}{\rightleftharpoons}} X \tag{4.14}$$

Our interest is in determining when mass transfer limitation of the reaction timescale will occur due to probe depletion near the reaction surface. The rate equation for immunocomplex formation at the surface is:

$$\frac{dx}{dt} = k_{\text{on}} c_s p_{\text{target}} - k_{\text{off}} x, \text{units: mol m}^{-2}\text{s}^{-1} \tag{4.15}$$

Where c_s is the surface concentration of probe, which is equal to the bulk probe concentration c_o under conditions of reaction limitation, but is between zero and c_o where mass transfer (by convection at the edge of a boundary layer and diffusion through this layer) to the surface is limiting. Neglecting the "off" term in x, we find the surface flux of probe $\dot{n}_{c_s}$:

$$\dot{n}_{c_s} = -\frac{dx}{dt} = -k_{\text{on}} p_{\text{target}} c_s \tag{4.16}$$

Here, we consider low probe concentration compared to captured target, which allows the possibility of mass transfer limitation on surface flux of probe. Thus, we lump p_{target} (mol m^{-2}) with k_{on} (M^{-1} s^{-1}) into a pseudo-first-order rate constant k' (standard units of m s^{-1}):

$$\dot{n}_{c_s} = -k' c_s, \;\; k' = k_{\text{on}} p_{\text{target}} \tag{4.17}$$

This simplified kinetic is sufficient to demonstrate the effect of mass transfer resistance in the surface boundary layer on the apparent rate of immunocomplex formation. For convection, diffusion and reaction under simplifying assumptions that the probe is not depleted at the edge of the boundary layer, and that the probe diffusion profile is at steady state (linear c between c_s and c_o), it can be shown that [25, 131]:

$$\dot{n}_{c_s} = -\frac{k' c_o}{1 + \frac{k'}{\beta}} \tag{4.18}$$

Essentially the probe consumption at the surface depends on a bulk reaction rate $k' c_o$ adjusted by a factor $(1 + \frac{k'}{\beta})$ accounting for mass transfer resistance in the boundary layer, where β is the mass transfer coefficient (ms^{-1}). The dimensionless factor that evaluates the interplay between reaction and mass transfer is the Damköhler number:

$$Da_1 = \frac{k'}{\beta} \tag{4.19}$$

Thus for $Da_1 \gg 1$, reaction outstrips mass transfer and the system is mass transfer limited with apparent rate $\dot{n}_{c_s} = -\frac{dx}{dt} = -\beta c_o$; whereas for $Da_1 \ll 1$, mass transfer outstrips reaction and the system is reaction limited with apparent rate $\dot{n}_{c_s} = -\frac{dx}{dt} = -k' c_o$.

The mass transfer coefficient β is a component of the Sherwood number Sh (a mass transport analog of the Nusselt number in heat transfer), which can be estimated from empirical relations determined for different flow properties and interface geometries [132].

$$Sh = \frac{\beta l}{D} = \frac{\text{mass transfer velocity}}{\text{diffusion velocity}} \tag{4.20}$$

Where l is a characteristic length in the system. For the open capillary case, an accurate

(within ∼1%) relationship for laminar flow in a cylindrical tube is readily available [132]:

$$Sh = \frac{\beta d}{D} = 1.62 \left(\frac{d^2 u}{yD} \right)^{\frac{1}{3}} \tag{4.21}$$

Where d is the tube diameter, y the tube length (length of the reaction zone in our case), u the average velocity in the tube and D the diffusivity of the probe in free solution.

Equations 4.19 and 4.21 give $Da_1 < 1$ for probe flowrates greater than $u \sim 1$ mm s^{-1}. Further decreases in Da_1 occur relatively "slowly" with increases in u due to the cube root dependence of Sh on u. However, given that $\eta \sim 0.01\%$ would be much more reasonable in the open capillary case, we quickly find $Da_1 \ll 1$, and thus that the probing step is reaction rather than mass transfer limited.

For LAVAgel probing, the target antigen is distributed throughout the channel volume, suggesting that probe driven through the gel pores reacts with captured antigen in a homogeneous fashion (i.e. no boundary layer resistance exists). An alternative Damköhler number has been posited for such electrophoretic band crossing reactions [120]:

$$Da_2 = \frac{t_{\text{cross}}}{\tau_R} \tag{4.22}$$

Where $t_{\text{cross}} = \frac{w}{u_{\text{rel}}}$ is the time required for the probe front to sweep through the captured band, which is ∼2 s given an observed probe velocity of $u_{\text{rel}} \sim 50$ μm s^{-1} in LAVAgels and a target band width $w = 100$ μm. We also expect reaction-limited conditions ($Da_2 \ll 1$) in this framework given the experimental observation that $t_{\text{cross}} \ll \tau_R$ (Figure 3.3).

To summarize, we expect $Da_{1,2} \ll 1$ such that the relevant probe transport timescale is always much smaller than the reaction timescale (i.e. mass transfer faster than reaction). With this result, we recast the binding reaction at the surface to focus on depletion of captured target as it is occupied by relatively unconstrained delivery of probe:

$$\frac{dx}{dt} = k_{\text{on}} c_s p_{\text{target}} - k_{\text{off}} x \tag{4.23}$$

This equation is identical to Equation 4.15, but here we take $c_s \sim c_o$ and $p_{\text{target}} = (p_{\text{target, total}} - x)$

where $p_{\text{target, total}}$ is the total concentration of immobilized target and solve to find [25]:

$$\frac{x(t)}{p_{\text{target, total}}} = \frac{c_o/K_D}{1 + c_o/K_D}(1 - e^{-(k_{\text{on}}c_o + k_{\text{off}})t}) \text{ for } Da_{1,2} \ll 1 \tag{4.24}$$

Where $K_D = \frac{k_{\text{off}}}{k_{\text{on}}}$ is the equilibrium dissociation constant for the Ab-Ag interaction.

We choose the bulk probe antibody concentration c_o to be in large excess compared to K_D at $c_o > 100$ nM, giving $\tau_R \lesssim \frac{1}{k_{\text{on}}c_o} = 10$ s (note that in hindsight, $t_{\text{cross}} \ll \tau_R$, as observed experimentally), and at equilibrium $\frac{x(t)}{p_{\text{target, total}}} = \frac{c_o/K_D}{1+c_o/K_D} \sim 1$ (i.e. probe binding saturates captured target). The fact that the observed value of τ_R is instead on the order of 5 min in LAVAgels (Figure 3.3D) perhaps points to the fact that the kinetic "on" and "off" rates are distorted in the gel environment (likely both will be decreased due to the presence of the gel matrix, as is currently under study [76]). In any case, values for k_{on} and k_{off} can vary considerably depending on the antibody-antigen pair used [130], so the 10 s result can be viewed as being in the expected range given the assumptions made.

Chapter 5

Isoelectric Point Photoswitching in Green Fluorescent Proteins

5.1 Introduction

Benchtop separations are central to preparative and analytical advances in protein characterization [6, 133]. However, the use of endpoint-measurement gel electrophoresis methods places practical limitations on the observation of protein band dynamics during separations. While capillary electrophoresis technologies have been employed for kinetic characterization of aptamer-ligand [134] and enzyme reactions [54, 135], the methods typically rely on single-point detection that prevents real-time observation of dynamic analyte band interaction, formation, or decay processes [136]. The planar, compact form factor of microfluidic devices lowers practical barriers to electrophoretic separations operated with wide-field and whole-channel imaging [137, 138]. In this way, microfluidic methods are well suited to facile measurement of dynamic protein reaction processes in real time. Augmenting dynamic readouts, miniaturized electrophoretic separations also offer high analytical performance, owing to reduced migration timescales and high electric fields operation [6, 76, 139, 140]. Such quantitative and time-resolved analytical methods may enhance our understanding of dynamic protein processes, including the photophysics of fluorescent proteins.

While of fundamental interest, the diverse photophysical properties of the fluorescent proteins have also driven important practical advances spanning the life and engineering sciences [141]. Originally extracted from bioluminescent jellyfish and corals, development of protein variants with novel spectral (specifically far-red emitting [142] and switchable variants) and physicochemical properties has impacted applications as wide-ranging as cellular transport [143], high resolution imaging [144], and biological information storage [145]. To uncover the structural underpinnings of photophysical fluorescent protein behaviors, conventional characterization methods combine spectroscopic tools (including time-resolved fluorescence correlation) with molecular dynamics modeling and crystallography [146, 147]. A challenging and ongoing area of study is the complex proton dynamics of photoswitchable fluorescent proteins, in analogy to well-studied proton shuttling processes (e.g., bacteriorhodopsin, cytochrome c oxidase [148, 149]). Importantly, fluorescent protein chromophore emission properties are tightly coupled to the electrostatic environment of the chromophore pocket [150] and to internal and longer-range proton transport influenced by the bulk solvent [151, 152]. Consequently, advanced analytical methods are needed to determine how specific protein mutations impact the coupled electrostatic and photophysical properties of the fluorescent proteins. Such tools will inform rational engineering of extreme and tunable properties across the fluorescent proteins.

In this study we use microfluidic isoelectric focusing (IEF) to study a photoswitching phenomenon observed in both wild-type avGFP and the E222G mutant acGFP (Figure 5.1). IEF is a powerful electrophoresis technique that separates proteins according to isoelectric point (pI) when an electric field is applied along the axis of a stable pH gradient (formed by polyprotic amphoteric buffers) [6]. During IEF, a native protein focuses at the channel position where the local pH equals the protein pI. Proteins focus into a stationary zone at

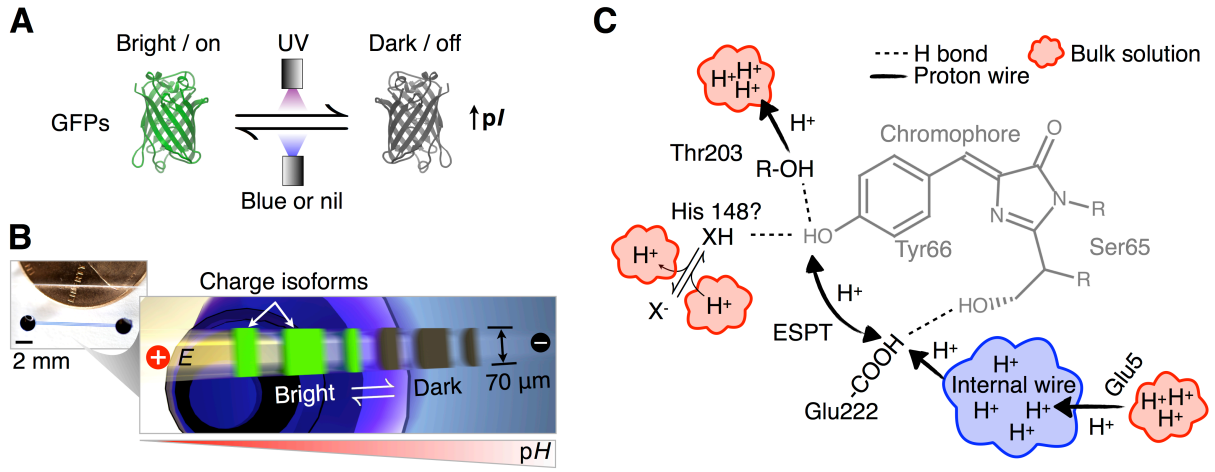

Figure 5.1: Immunoprobed isoelectric focusing allows dynamic and immunoreactivity-verified monitoring of GFP isoform dynamics during reversible photobleaching. (A) Reversible photobleaching upon UV illumination creates dark GFP isoforms with increased pI's relative to their bright "parents". (B) Microfluidic chip with three parallel channels between each pair of access wells. Dynamic isoelectric photoswitching processes can be monitored in real time, or isoforms can be captured by the LAVAgel matrix and probed in situ with fluorescently labeled anti-GFP antibody. (C) A sketch of avGFP chromophore and proton wire dynamics [154–157]. Hydrogen bond networks allow proton exchange of the chromophore pocket with the external solvent. Glu222 is involved in excited state proton transfer (ESPT) with the chromophore Tyr66. The E222G mutation in acGFP inhibits ESPT and perhaps proton exchange with the internal wire proposed by Agmon *et al.* [156, 158]. The dependence of reversible photobleaching magnitude on pH suggests involvement of a titratable residue, X, in the chromophore vicinity that affects chromophore protonation state by hydrogen bonding [159] (see text for details). Reproduced from [160].

this location because the species have a net zero electrostatic charge and thus no net electrophoretic mobility [7, 8]. The IEF pH gradient can be generated in free solution or in a sieving matrix, such as polyacrylamide gel. Protein pI is a physicochemical property determined by amino acid composition, three-dimensional conformation, and modifying chemical groups affecting protein charge. Protein isoforms are common and important. Isoforms are versions of a protein having slight differences in pI. These pI differences are generally attributable to post-translational modifications including enzymatic glycosylation or primary sequence cleavage processes occurring within cells [153]. IEF can resolve a single electrostatic charge difference between protein isoforms [16], making IEF a powerful tool for the study of biophysical phenomena. IEF is particularly suited to study of proton dynamics, which impact pI but have little impact on other measureable protein properties (i.e., molecular weight).

Using dynamic IEF, we observe and characterize dark (non-fluorescent) and bright (fluorescent) populations of avGFP and acGFP by measuring changes in protein fluorescence and pI. After IEF, we integrate an immunoblotting step to extend our analytical tool to non-fluorescent analytes (see Appendix B and [160] for details of device operation). Incubation of fluorescently labeled antibodies with IEF-resolved — and immobilized — proteins yields pI and mass distribution for each target, including non-fluorescent forms of GFP. To immobilize proteins, we conduct IEF in a light responsive benzophenone-decorated, polyacrylamide gel (light-activated volume-accessible separation gel or LAVAgel). Brief exposure of the LAVAgel to UV light covalently attaches proteins to the LAVAgel matrix [6], allowing subsequent protein probing via introduction of fluorescently labeled antibodies. The ability to blot and probe proteins with near-lithographic spatial control in direct series with controlled light pre-exposure sequences enables quantitation in the absence of an endogenous fluorescence signal from the protein target [6]. In the case of GFP, immunoblotting corroborates pI photoswitching measurements inferred from intrinsic fluorescence data. The GFP fluorescence signals have complex dependencies on light exposure history [154, 161] and chemical environment [127, 162] and, thus, can confound the true protein mass distribution in the microchannel. These dependences make an independent fluorescence probing readout essential.

5.2 Results

We first applied the microfluidic IEF assay to analysis of two GFP species of interest, avGFP and acGVP (Figure 5.1). IEF analysis yielded three predominant isoforms for each variant in the pI 4.8-5.5 range under continuous blue light excitation (isoforms are denoted α, β and γ for avGFP; and δ, ϵ and ζ for acGFP, see Figure 5.2). These heterogeneous isoform patterns have been ascribed to differential C-terminal cleavage by non-specific proteases during bacterial expression of the recombinant proteins [127]. Random terminal cleavage of the tail, which contains two basic (His and Lys, pK_a 6.6 $\pm$ 1.0 and 10.5 $\pm$ 1.1) and two acidic (Asp and Glu, pK_a 3.5 1.2 and 4.2 0.9) residues [127, 163], should produce isoforms differing by roughly one formal charge if the pK_a's of the differentially cleaved residues are distinct by at least $\sim$1 pH unit from the isoform pIs. High-resolution intact-mass spectrometry of purified recombinant avGFP revealed a 128 Da mass difference between two major peaks (Figure 5.3). This difference is consistent with cleavage of the C-terminal lysine in the α isoform of avGFP. Given that the cleaved lysine residue contributes a full positive charge, the pI shift attributable to a single electrostatic charge can be estimated at roughly 0.12-0.15 pH units from the relative bright isoform displacements in the pH axis of Figure 5.2, and from further computational estimation of the expected isoform pIs resulting from differential C-terminal cleavage (data not shown) [164]. Thus, the magnitudes of isoelectric point photoswitching can be calibrated using a ruler of electrostatic charge to allow direct inference of the stoichiometry of charge transfer events at single-charge resolution [165]. The effect of charge transfer on the pI of a protein via its titration behavior has

complex dependencies on, for example, the pI itself, and the molecular weight and amino acid composition of the protein [166, 167]. Thus, we adopt this charge ruler approximation under the assumption that the pI range over which charge shifts are estimated is narrow enough to assume a constant local slope in the charge vs. pH titration curve of the isoforms considered [8, 38].

Next, we sought to investigate the effect of UV and blue light illumination on avGFP and acGFP isoform distributions during dynamic IEF. For both avGFP and acGFP, isoforms exhibited dynamic changes in isoelectric point distributions upon exposure of the focused proteins to sequences of UV and blue light illumination (Figures 5.4, 5.5). To summarize the observed photoswitching phenomena: brief exposure of the focused fluorescent isoform bands to UV light induced formation of dark (reversibly bleached) isoform populations with increased pI compared to bright isoforms (Figures 5.2–5.6). Following UV exposure, application of blue illumination initiated a dynamic "switch-on" of the fluorescence of the dark isoforms with first-order time constants of 700 ms for avGFP and 720 ms for acGFP (Figures 5.6A, 5.7). Concomitantly, we observed migration of the switched-on isoforms to the pIs of their parent bright isoforms on the ∼5–10 s timescale. More prolonged exposure to UV on the focusing timescale caused a transient increase in the *apparent* pIs of bright isoforms to values intermediate between the static bright and dark isoform pIs. This apparent bright isoform pI increase reversed when UV illumination was halted (Figure 5.4B), while dark isoforms assumed their higher pIs until blue light was applied (or until the dark isoforms relaxed back to the bright state during prolonged nil illumination).

Measurement of the dark isoform peak areas as a function of UV pre-exposure time revealed single-exponential switch-off kinetics with a time constant of 67 ms. This kinetic approximately matches the fast bleaching time constant of 56 ms under direct UV exposure of avGFP (Figure 5.6B). These results suggest reversible bleaching of bright GFP isoforms by UV exposure as the trigger for formation of dark state isoforms with alkaline-shifted pIs. The dark isoform populations, constituting 25% of the total mass for avGFP after >150 ms UV exposure, also decayed back to the bright state under nil illumination conditions (Figure 5.6C). The relatively short 5-10 s focusing timescale (compared to the characteristic time of dark population decay) enabled resolution of dark from bright populations, an observation that would be impossible in longer separation-length capillary or slab gel systems. This decay process was again described by single-exponential kinetics, with a time constant of 42.2 s for avGFP, which is similar to those of 58 and 54 s measured by Sinnecker et al. in mammalian cells for ECFP and EYFP respectively (see Discussion) [159]. Thus, blue photon absorption reduced the fluorescence switch-on time of reversibly bleached dark isoforms by

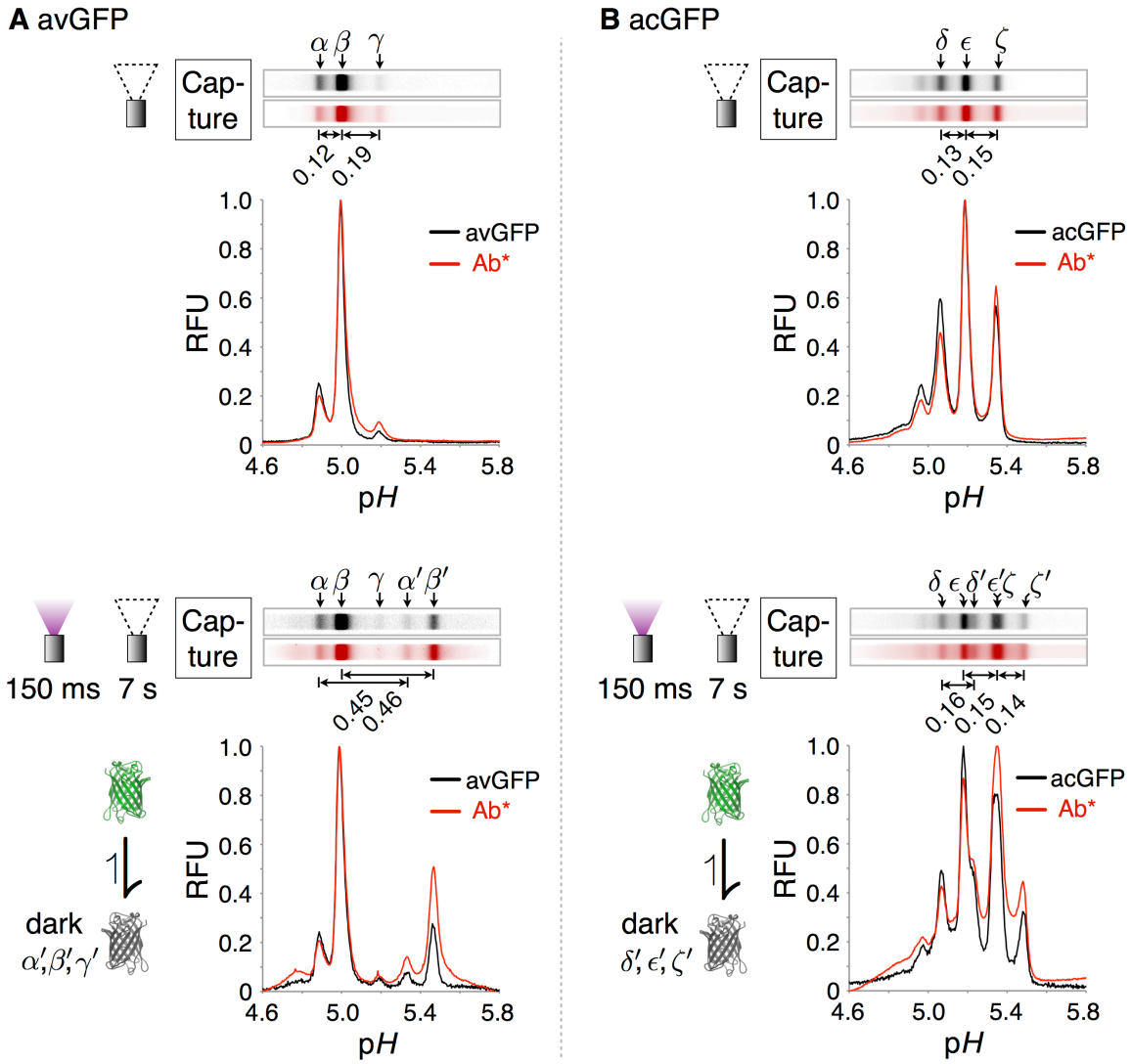

Figure 5.2: Probed isoelectric focusing of avGFP and acGFP reveals base-shifted reversibly photobleached isoforms. (A) Static LAVAgel fluorescence images and electropherograms of immobilized avGFP isoforms (bright: α, β, γ; dark: α' and β'; γ' is below the assay limit of detection) within the microchannel (black; excitation 445–495 nm, emission 508–583 nm) after focusing under — top: nil light exposure conditions, bottom: 150 ms pre-exposure to 100% UV (270 mW cm^{-2}, 300–380 nm). Isoform capture was initiated immediately after the indicated pre-exposure protocol by 15 s UV irradiation of the LAVAgel under non-focusing conditions. Red fluorescence (excitation 525–555 nm, emission >575 nm) gel images and electropherograms are produced following pH gradient washout and LAVAgel probing with 600 nM Texas Red-labeled anti-GFP antibody (Ab*) for immobilized isoforms. N.B. fluorescence of captured dark isoforms (α' and β') is switched on during imaging under blue illumination. (B) The corresponding micrographs and electropherograms for immobilized acGFP isoforms (bright: δ, ϵ, ζ; dark: δ', ϵ' and ζ') probed with the same anti-GFP antibody. Reproduced from [160].

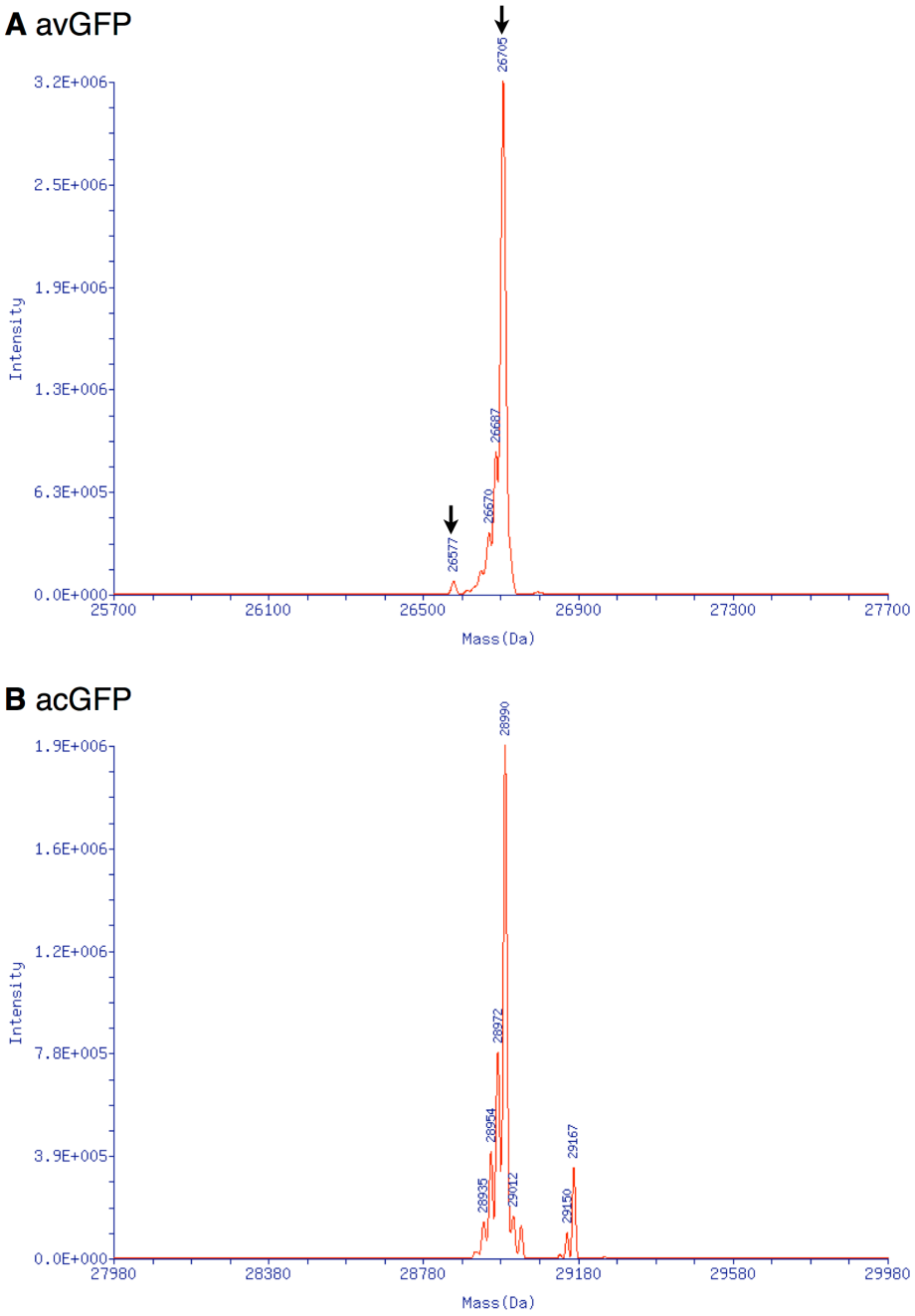

Figure 5.3: Deconvoluted intact mass spectra for purified, recombinant avGFP and acGFP. The avGFP spectrum shows a major peak at 26,705 Da (black arrow), with dehydration adducts at 26,687 and 26,670 Da. The peak at 26,577 Da (black arrow) is distinct from the major peak by 128 Da, the mass of the C-terminal lysine reported to be cleaved by non-specific protease activity during bacterial expression [127]. Distinct isoform-specific mass differences were not resolved in the case of acGFP. N.B. the mass scales in each graph are not the same. Reproduced from [160].

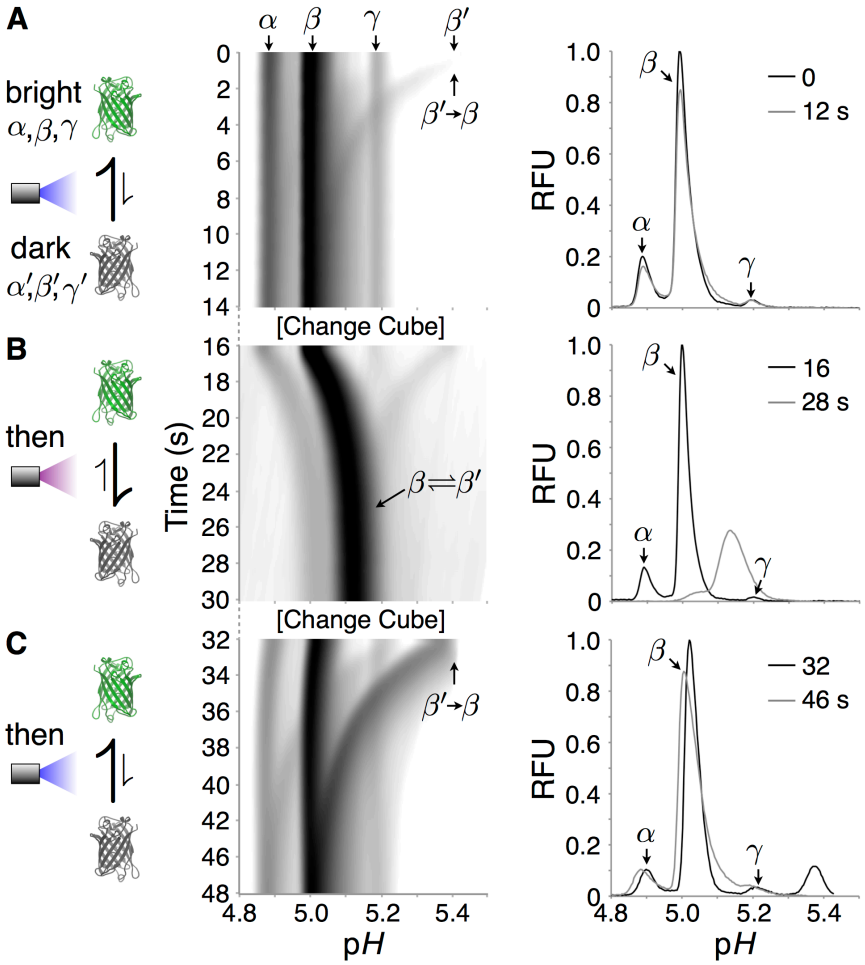

Figure 5.4: Real-time observation of isoelectric point photoswitching in avGFP. (A–C) Log-transformed fluorescence micrographs corrected for cathodic pH gradient drift showing dynamic isoelectric point evolution of avGFP isoforms during isoelectric focusing over time (100 ms streamed exposures, $E = 300$ V cm^{-1}). Initial and final electropherograms in linear relative fluorescence units accompany each timelapse micrograph. The three panels show typical behavior upon applying a sequence of microchannel exposure conditions — (A) Nil-to-blue light exposure. (B) 100% UV exposure (excitation 300–380 nm, emission >410 nm). (C) Blue light exposure. Delay between micrographs due to filter cube exchange is ∼2 s. Reproduced from [160].

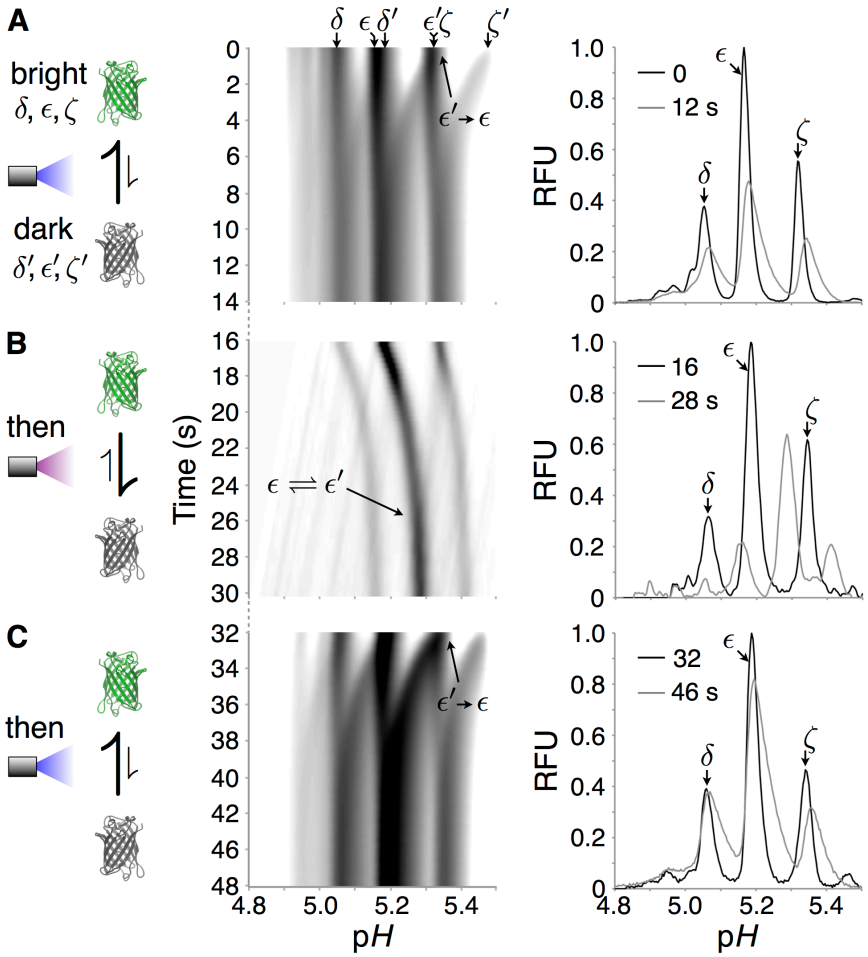

Figure 5.5: Real-time observation of isoelectric point photoswitching in acGFP. Experimental details are identical to those in Figure 5.4. Reproduced from [160].

a factor of 60-fold (from 42 to 0.7 s) under the experimental conditions employed.

We postulate that the distributions of the photoswitched isoforms carry key information about the charge transfer events underlying the changes in isoelectric point. Two mutant-specific differences in these focusing behaviors were observed for avGFP and acGFP. Firstly, prolonged application of UV light caused apparent pI shifts of 0.12 and 0.10 units for all bright avGFP and acGFP isoforms respectively, as well as broadening of the focused zone band widths (4σ) by 2.47– and 1.24–fold respectively (as measured for the major β and ϵ isoforms, Figures 5.4B and 5.5B). Secondly, the final pI shifts of each of the dark isoforms (e.g., β') from their parent bright bands (e.g., β) after halting illumination were 0.45 and 0.15 pI units for avGFP and acGFP respectively ($\sim$3–4 and $\sim$1 charge units, Figure 5.2). The

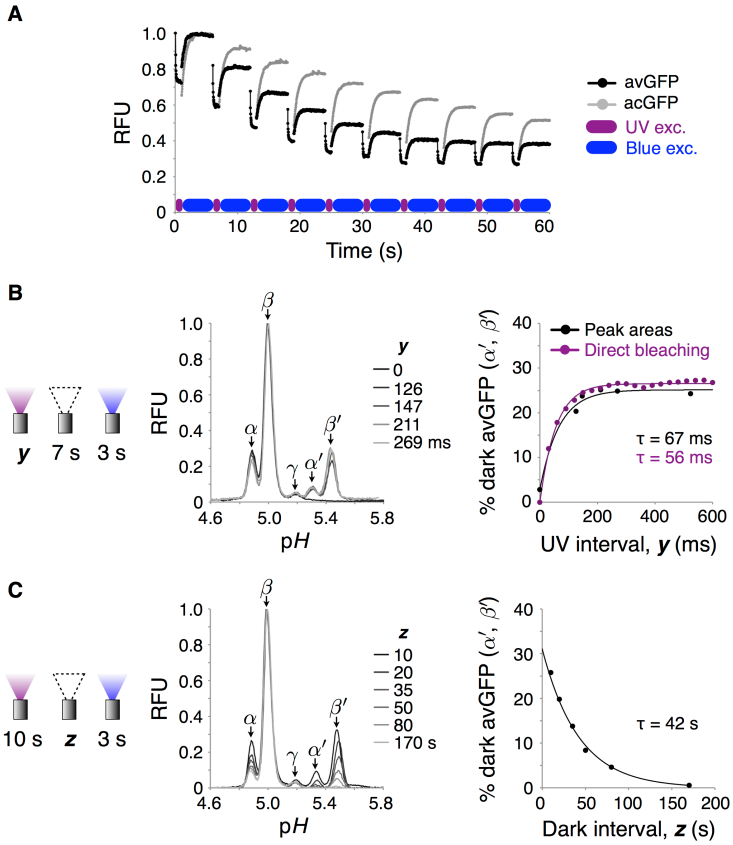

Figure 5.6: Isoelectric photoswitching kinetics of GFPs. (A) Fluorescence photoswitching in avGFP and acGFP. Ten consecutive illumination cycles of 100% UV (1 s per cycle) and blue light (5 s per cycle) were conducted via 10x objective and total isoform fluorescence plotted over time for 10 ms frames. (B) Fast reversible bleaching of isoforms under UV illumination. Left: Dark isoforms of avGFP were generated by pre-exposure of bands to 100% UV light for the indicated exposure times y, followed by a focusing equilibration period of 7 s under nil illumination. Focusing field was then halted and dark isoforms converted to the bright state by 3 s blue light exposure and quantified by measuring peak areas. Electropherograms show increase in dark isoform (α' and β') representation as a function of UV pre-illumination period. Right: Growth of dark state isoform peak areas in pI 5.25–5.6 range determined from electropherogram data at left (black) and inferred by direct observation of bleaching under 100% UV (purple, from the first exposure cycle of (A)), both fit to RFU $= a(1 - e^{-\frac{t}{\tau}}) + b$. (C) Slow isoform fluorescence recovery under nil illumination. Left: Dark isoforms of avGFP were generated by 10 s pre-exposure of bands to 100% UV light via 10× objective, followed by a nil illumination period z of between 10 and 170 s. Focusing field was then halted and remaining dark molecules converted to the bright state by 3 s blue light exposure. Electropherograms show decay in the representation of dark isoform (α' and β') peak areas in the pI 5.25–5.6 range as a function of nil illumination period. Right: Dark isoform peak areas fit to a single exponential of the form RFU $= \text{RFU}_{\max} e^{-\frac{t}{\tau}}$ (±SD, $n = 3$, error bar heights smaller than marker size). Reproduced from [160].

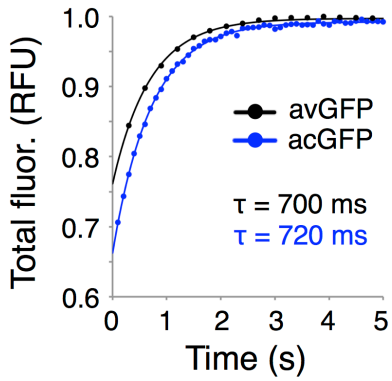

Figure 5.7: Kinetics of reversible photobleaching of GFPs. Fast total fluorescence recovery under focusing conditions and blue light illumination measured after 10 s pre-exposure of avGFP and acGFP bands to 100% UV light *via* 10× objective. Single exponential fits of the form RFU $= a(1 - e^{-\frac{t}{\tau}}) + b$ are shown for each recovery trace. Reproduced from [160].

fact that these bright-to-dark pI shifts were discrete, rather than spread over a distribution, points to an all-or-nothing conversion process. Thus, these GFPs are hypothesized to exhibit a bistable switch with respect to pI (at least on the fluorescence timescale) and with respect to fluorescence.

We explored the GFP bistable switching hypothesis by modeling the isoelectric photoswitching of the predominant avGFP isoform between bright (β) and dark (β') states having distinct pIs. GFP molecules interconvert between these states according to an equilibrium reaction of the form $\beta \rightleftharpoons \beta$' with forward and backward rate constants of $k_{\beta\rightarrow\beta'}$ and $k_{\beta'\rightarrow\beta}$ respectively. The rate constants were determined by least squares fitting of the equilibrium bright population distributions obtained from the model to experimentally measured distributions. Focused avGFP isoform distribution fits were made across a range of UV illumination intensities. Governing equations for this model considered focusing and diffusive spreading of peaks (terms 1 and 2 on the right hand side of each equation), as well as first-order interconversion of bright and dark populations (terms 3 and 4):

$$\frac{dC_\beta}{dt} = p_\beta(x - x_{pI,\beta})E_x\frac{dC_\beta}{dx} + D_\beta\frac{d^2C_\beta}{dx^2} - k_{\beta\rightarrow\beta'}C_\beta + k_{\beta'\rightarrow\beta}C_{\beta'} \tag{5.1}$$

$$\frac{dC_{\beta'}}{dt} = p_{\beta'}(x - x_{pI,\beta'})E_x\frac{dC_{\beta'}}{dx} + D_{\beta'}\frac{d^2C_{\beta'}}{dx^2} - k_{\beta'\rightarrow\beta}C_{\beta'} + k_{\beta\rightarrow\beta'}C_\beta \tag{5.2}$$

Where C is concentration, t is time, x is distance along the separation axis, $p_\beta \approx p_{\beta'} = p$ is

slope in analyte mobility with respect to x, E is applied electric field, and $D_\beta \approx D_{\beta'} = D$ is the diffusivity of GFP in the separation gel. Non-dimensionalization of the model with respect to the characteristic diffusion time $\left(\frac{\Delta x_{pI}^2}{D}\right)$ between population peaks with a difference in pI of Δx_{pI} yielded three parameters 1) a Peclet number $Pe = \frac{p\Delta x_{pI}^2 E_x}{D}$, the ratio of diffusive and convective (focusing) timescales, 2) a Damköhler number $\kappa = \frac{k_{\beta\to\beta'}\Delta x_{pI}^2}{D}$, the ratio of diffusive and forward reaction timescales, and 3) an equilibrium constant $\gamma = \frac{k_{\beta'\to\beta}}{k_{\beta\to\beta'}}$, the ratio of backward and forward reaction rates.

The dimensional analysis in Figure 5.8A captures the diverse behavior of this convection-diffusion-reaction model. The reaction:focusing speed ratio $\frac{\kappa}{Pe}$ and the equilibrium constant γ divide the $(k_{\beta'\to\beta}, k_{\beta\to\beta'})$ parameter space into several behavioral regimes that were directly mapped onto experimental data. At low UV intensities ($\frac{\kappa}{Pe} < 1$), the bright and dark populations interchange slowly enough compared to the focusing timescale that distinct bright and dark peaks are formed, producing a wide overall concentration distribution in the pI axis. Notably, as the UV intensity increases, the populations interchanged more rapidly, and the rate constants $k_{\beta'\to\beta}$ and $k_{\beta\to\beta'}$ increase at an approximately fixed ratio over the intensity range studied ($\gamma \sim 2.9$, Figure 5.8B,C). Rapid interconversion causes the observed bright and dark distributions of the major avGFP isoform to converge along the pI axis at a weighted mean pH of 5.12 at $\frac{pI_{\beta'} - pI_\beta}{1+\gamma} = 0.12$ pH units from $pI_\beta = 5.00$, since $\gamma = \frac{C_\beta}{C_{\beta'}}$ at equilibrium. Simply put, the 5–270 mW cm^{-2} range in UV intensity we studied produced an intensity-independent equilibrium [168] in which each GFP molecule was bright with pI 5.00 around 74% of the time, and dark with pI 5.45 around 26% of the time. Increasing the UV intensity reduced the average time spent by a molecule in each state between switching events. Increases in each rate constant, and thus $\frac{\kappa}{Pe}$, explain the transitions in shape (wide to narrow) and position (lower pI to higher pI) of the observed bright isoform distributions, since the ability to resolve the bright and dark populations by focusing is eroded as populations interconvert more and more rapidly.

Dynamic analysis over lower intensity ranges was limited by detection sensitivity, given that the GFP stimulation and imaging conditions were one and the same. Under nil illumination conditions, only the bright isoform populations exist (Figure 5.2), predicting a transition to the $\gamma_{\text{avGFP}} \sim 2.9$ equilibrium over the 0–5 mW cm^{-2} UV intensity range and the ability to manipulate the mean avGFP pI from 5.00–5.12 in a rheostatic fashion. Similar fitting of experimental data for acGFP was confounded owing to a low fluorescence SNR caused by the heavily reduced UV absorbance in E222G mutants. However, assuming that the simple two-state model also holds for acGFP, the equilibrium bright distribution pI shift of 0.1 units at 100% UV yields $\gamma_{\text{acGFP}} \sim 0.5$ at most, meaning that at least 67% of the acGFP was in the dark state at equilibrium.

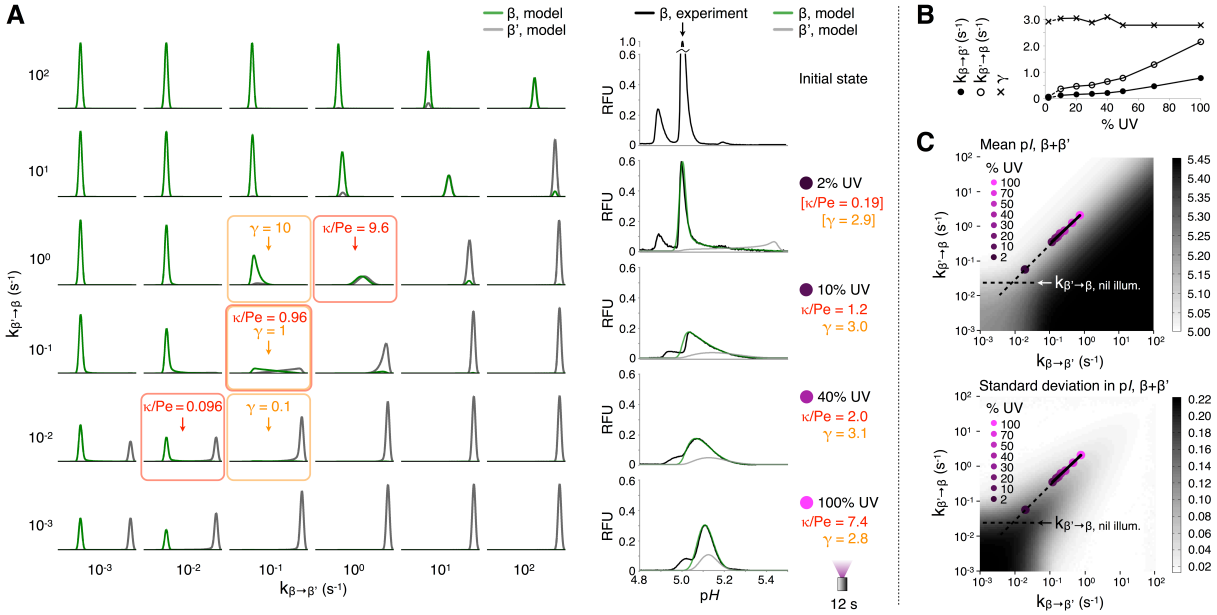

Figure 5.8: Two-state convection-diffusion-reaction model predicts focusing dynamics during perturbation of avGFP with UV light. (A) At left, sketch of concentration distributions from 1D model of focusing of bright (β) and dark (β') states of the major avGFP isoform over a range of interconversion rates; x-axes are pI 4.8–5.5, y-axes are arbitrary fluorescence units. $\frac{\kappa}{Pe}$ compares reaction to focusing speeds, governing the observed morphology of the β peak during focusing. Concentration distributions of the bright and dark states can be distinct ($\frac{\kappa}{Pe} < 1$) or overlapping ($\frac{\kappa}{Pe} > 1$) depending on the UV intensity, even for the same equilibrium constant γ. Right hand column, least-squares fits of model distributions of β to experiment data for the indicated UV intensities. Fits from 10%–100% UV were global optima, while that at 2% assumed an average γ value from the other fits (square brackets and dashed lines denote this here and in (B) and (C)). (B) Interconversion rates between β and β' states and their ratio, γ, from fits in (A). (C) Intensity plots of pI mean and standard deviation for the sum of β and β' distributions. Interconversion rates determined from experimental data in (B) are overlayed. Best-fit slope of 0.94 reflects approximately constant γ and mean pI across the UV range. Reproduced from [160].

5.3 Discussion

The photophysics of the family of green fluorescent proteins derived from *Aequorea sp.* are characterized by a rich interconnection between spectral properties and short and long-range proton dynamics involving their chromophores [154–156,169]. The diversity of photophysical phenomena of the fluorescent proteins reflect complex dynamics involving pH-dependent and -independent protonation equilibria [151,154,168–170], proton exchange with the bulk solvent [147, 156, 171], chromophore and pocket residue conformation [150, 172–175], electrostatic interactions between the chromophore and surrounding residues in the chromophore pocket [152, 154], and irreversible chemical reactions at the chromophore or surrounding residues [143,176]; all of which contribute to the divergent absorption, emission, photoactivation and reversibility aspects of the fluorescence of GFP family members [177].

Here we sought to reconcile the unusual UV intensity-dependent IEF focusing behavior of GFP isoforms at the ensemble level by recognizing the interplay between reaction and transport timescales. Specific to the GFP studies conducted here, the wild type *Aequorea victoria* avGFP, a β-barrel structure containing a buried tripeptide chromophore formed autocatalytically from Ser65, Tyr66 and Gly67, exhibits robust fluorescence with absorption bands at both $\sim$400 and $\sim$475 nm [154,155]. These absorption bands are comprised of two subpopulations A and B having, respectively, neutral (protonated) and anionic (deprotonated) charge at the hydroxyl group of Tyr66 of the buried chromophore [154]. While the neutral A form dominates B by 6:1 in wild-type avGFP, S65T (e.g., EGFP) and E222G (e.g., acGFP [178]) mutants favor the anionic B state in the physiological pH range, thus suppressing the 404 nm absorption peak and simplifying their photophysical behavior [154, 179]. Picosecond spectroscopy studies have detailed an excited-state proton transfer (ESPT) process that occurs upon excitation of the protonated A state, which causes the phenolic proton at Tyr66 to delocalize and transfer to Glu222 via a network of hydrogen bonds due to a drop in the pKa of the tyrosyl phenol in the excited state [154, 155, 170].

The ESPT process is usually reversible, but prolonged, high-intensity exposure of wild type avGFP to UV or blue light can cause nearly permanent (timescale hours) photoisomerization to the anionic B state [154, 161, 170]. S65T and E222G mutants favor the anionic chromophore state by suppressing ionization of, and deleting altogether, the glutamate 222 side chain central to the ESPT process [154]. This conventional picosecond-scale proton transfer phenomenon accounts for short-range migration of the photodissociated proton between Tyr66 and Glu222 within the chromophore cavity. Additionally, nano- to millisecond-scale proton transfer to and from the external solution via a set of proton wires consisting of hydrogen bond networks spanning the GFP β-barrel has been hypothesized on the basis of crystallographic, fluorescence autocorrelation, and pH-jump spectroscopic evidence [156, 169, 180, 181]. Proton escape to the bulk solution can occur via at least two proposed exit points, e.g., by rotation of Thr203 via His148 to the protein surface. Additionally, longer-range proton migration along a wire connecting a negatively charged patch of

the avGFP surface at Glu5 through Glu222 to its chromophore is expected to allow replenishment of the proton lost by escape to the bulk solvent [156], suggesting a proton pumping function [158]. This hypothesis is to first order compatible with the aforementioned effect of the E222G mutation in acGFP in encouraging chromophore deprotonation, as the proton wire serving as a replenishing proton conduit is likely compromised [156]. It is important to recognize, however, that in EGFP (in which this conduit is also bisected at Thr65 [156]), chromophore protonation to form a non-fluorescent population proceeds at acidic solution pH with an apparent pK_a of 5.8 [169] (similarly in wild-type avGFP with a pKa $\sim$5 [127]), indicating further redundancy in proton exchange with the bulk solvent, especially at sub-physiological pH [157]. Indeed, the prevailing view of the effect of mutations targeting E222 in inducing the *B* chromophore state is that the existence of two negative charges (from E222 and Tyr66 in the excited state) within the spatially confined chromophore pocket is thermodynamically unfavorable, meaning that mutations at E222 that eliminate its charge tend to stabilize the ionized *B* state chromophore.

While a wide-ranging analysis of all irreversibly (photoactivatable) and reversibly (photochromic) photoswitchable fluorescent proteins is beyond the scope of the present study, several relevant and intriguing phenomena have been recently described and are germane to the present study. Reversible photoswitching processes have been described for green, yellow and cyan avGFP mutants with a range of switching yields [159, 182, 183]. Random blinking behaviors observed in single molecule studies of fluorescent proteins result from thermodynamic sampling of several chromophore states within individual fluorescent proteins, where at least one is a non-emissive dark state with respect to the excitation wavelength employed [169]. Several varieties of more directed photoswitching have also been described, in which a given state can be favored through the application of different wavelengths of light. Non-reversible examples necessarily involve permanent biochemical changes to the amino acid scaffold in the vicinity of the chromophore. Examples include UV-induced photoconversion of dark wild-type avGFP and PA-GFP to a fluorescent B state by decarboxylation of E222 [143, 184] and redding processes caused by as-yet unknown chromophore conversion processes either in the absence of oxygen [185] or in the presence of oxidizing agents [162].

With these reported phenomena in mind, we hypothesize that the well-known decarboxylation-driven photoconversion process described for wild-type avGFP is likely only a minor contributor to our observations, due to a known irreversibility and to the relatively low illumination intensities applied in this work [143,184]. Similarly, a contribution from GFP molecules with incorrectly formed chromophores is unlikely, as these species have been observed to remain non-fluorescent even upon successive denaturation and renaturation cycles [161]. Important here is the immunoprobing functionality; as the probing fluorescence readout is introduced to detect non-fluorescent GFP species (as well as allow similar analysis of other photoactive proteins that lack appreciable fluorescence at their pI's). Thus, immunoblotting allows independent verification of isoelectric points owing to in situ binding of fluorescently labeled antibody to the target of interest.

Examples of both negative and positive reversible photobleaching have been discovered. Directly relevant to our dynamic IEF observations, Sinnecker *et al.* characterized a model of positive reversible photobleaching in EGFP, EYFP, Citrine, and ECFP. The model included a switch-off transition from a protonated P state to a reversibly bleached form B_r upon application of blue 460 nm light (for ECFP) in bulk solution [151,159]. Decay of the reversibly bleached population to the bright state occurred in the dark on a ∼60 s timescale. This kindling effect was accelerated by application of lower energy green 500 nm light (again, for ECFP). Importantly, reversible bleaching was more efficient under acidic conditions, implicating protonation of a titratable residue in the vicinity of the chromophore in the P state as a prerequisite for transition to the dark state. Likely candidates include Glu222 and His148 [169], but not the Tyr66 phenol itself, as ECFP (which carries a non-titratable indole ring instead) is also subject to reversible bleaching [159]. Thus, although the P and B_r states likely fall within the canonical $A/B/I$ state framework put forward by Chattoraj *et al.* [170], their properties reflect a more complex involvement of proton dynamics linking the chromophore, its surrounding pocket residues, and the bulk solvent.

We hypothesize that the isoelectric point photoswitching phenomenon in avGFP is consistent with the reversible bleaching observations of Sinnecker *et al.* [159]. The arrangement of the switching wavelengths (higher energy light shifts equilibrium towards dark state; lower energy light hastens fluorescence recovery), kinetic parameters, and GFP variants studied are most consistent with our observations. Adding to these observations, we observed that the P and B_r fluorescence states are characterized by distinct electrostatic charge states at the whole molecule level via direct physicochemical measurement with dynamic IEF. We hypothesize that these distinct electrostatic charge states corroborate proton exchange with the bulk solvent [156]. The polarity of the observed pI shifts further imply that the transition of GFPs to the dark state involves proton uptake into their structures (causing increased pI), and vice versa, that the return to the bright state involves expulsion of protons (causing decreased pI). More generally, our single-charge resolution pI observations recapitulate the necessity for at least one proton uptake event for the P to B_r transition [159, 169], although the specific residue(s) involved in this process cannot be identified via our whole molecule-level measurements of electrostatic charge. However, the observed difference in protonation stoichiometry between avGFP and acGFP may hold important insights into the structural rearrangements underlying the reversible bleaching process.

Specifically, the all-or-nothing uptake of 3–4 protons by avGFP isoforms during fluorescence switch-off may reflect a cascade of rearrangements in the proposed internal hydrogen bonding network buried within the avGFP structure extending from the chromophore pocket beyond the E222 bridge [156, 180, 186]. Indeed, several authors have pointed out the potential for multiple proton storage within the GFP structure at buried hydronium ions and titratable residues [156,181]. Given that proton travel between the proposed internal and exit hydrogen bond clusters is expected to be restricted or rerouted (if not fully severed) by the E222G mutation in acGFP41, the single-charge shift between bright and dark states observed for

the acGFP isoforms may stem from titration dynamics restricted to the chromophore pocket that are facilitated by acid-induced protonation of the unknown pocket residue prescribed by Sinnecker *et al.* [159] (among others [168,169]) that governs transition between the bright P and dark B_r states. While the details of the structural mechanism underlying coupling of photochromism and long-range charge transfer in the GFPs is yet to be elucidated, further studies of key GFP mutants targeted at proposed proton wire pathways is a promising avenue. Specifically, our assay could complement crystallographic and spectroscopic characterization of mutants differing at key hydrogen bonding residues along the proposed internal proton wire that are distant from the chromophore pocket, such as S72 [156].

Relevant to future study, the coral fluorescent protein Dronpa [145] offers a remarkable example of negative reversible photobleaching processes. Dronpa exhibits distinct and stable dark (non-fluorescent, triggered by blue light irradiation) and bright (fluorescent, triggered by violet light) subpopulations [147,150]. Despite widespread use of Dronpa in high-resolution microscopy, the structural and biophysical mechanisms underpinning photoswitching of Dronpa (and other reversible fluorescent proteins) is still in debate. Cis-trans chromophore isomerization, changes in chromophore protonation state with proton transfer to the bulk solution, and changes in the structural flexibility of the chromophore pocket have all being implicated as playing a role in photoswitching [147,150,152,174]. Chromophore isomerization and protonation have also been identified in the positive reversible fluorescent protein Padron0.9, in which violet light induces the dark state and blue/green light induces the bright state [146] (the opposite of Dronpa, and similar to asFP595 [174]). Still other switching mechanisms have been described, including an unusual chromophore hydration/dehydration process for the Citrine derivative Dreiklang [187]. The dynamic IEF assay introduced here may prove useful for detailed study of a range of switching mechanisms.

5.4 Conclusions

Microfluidic dynamic IEF brings the advances in separation timescale and resolution necessary for real-time modulation and readout of protein reaction processes, of which photoswitching is an intriguing example explored here. Dynamic IEF analysis generates a rich diversity in GFP focused band morphology from a relatively simple two-state process. Thus, our ability to resolve and track fluorescent protein populations through physicochemical properties rather than by traditional fluorescence or static crystallographic measurements opens the door to a range of dynamic perturbation analyses. Such dynamic analyses should continue to find use in probing the chemical and structural nature of conformational photoswitching processes. We see this analytical capability as relevant to a range of fluorescent and other light-reactive proteins. For example, the ability to characterize GFP constructs genetically encoded with light-switchable charge could benefit a broad range of applications from the study of cellular membrane transport processes to the rational engineering of electrostatic aggregation in signaling molecule or metabolic networks [188,189]. The fact that reversible

fluorescence (and thus isoelectric point) photoswitching is amplified at pH values in the vicinity of the fluorescence pK_a's of GFPs [159] suggests that mutants developed as sensitive pH indicators in the physiologic range [157,190] would be attractive candidates for achieving maximum charge switching in biological systems. Further, the more radical photochromism of photoactivatable GFPs (e.g., Dronpa [145], Padron0.9 [146] and PA-GFP [143], among others [141,144]) may engender additional benefits in the magnitude and temporal stability of charge conversion, as is currently under study. Beyond studies in cell biology, charge-switchable proteins could be useful in the engineering of biomimetic smart materials with light-actuated transitions in zeta potential, hydrophilicity / wetting behavior, and adhesion properties [191–193]. The rapid, high resolution dynamic IEF approaches we describe could also be used in high-throughput screening for rational or directed tuning of photoactivatable protein phenomena, from reversible photochromism [142] to light-induced protein-protein interactions [189].

Chapter 6

Microfluidic Western Blotting for Rapid HIV Diagnosis from Human Sera

6.1 Introduction

Western blotting is an indispensable analytical tool; benefiting applications from clinical diagnostics to fundamental questions in the life sciences [21, 194, 195]. The broad relevance of blotting stems from its highly specific results. Unlike separations or immunological probing alone, blotting reports not one, but two physicochemical characteristics: molecular mass and immunoaffinity. Owing to this specificity, numerous immunoblotting variants have emerged for measurements of proteins to RNA to biomolecular interactions [194, 196–198]. Nevertheless, despite being an information-rich and widely utilized assay, the western blot has crucial inadequacies. In particular, limitations in data density and throughput hinder progress for pursuits such as systems biology.

A major shortcoming of western blotting is the resource intensive nature of the assay, being comprised of several steps requiring disparate pieces of equipment (Figure 6.1A). In the first stage of western blotting, protein sizing, samples are analyzed by denaturing polyacrylamide gel electrophoresis (PAGE). During PAGE, proteins electromigrate through a polyacrylamide sieving gel, allowing determination of molecular mass. Once protein size is determined, the protein separation is incubated with antibodies (probing), thus allowing detection of interactions. Target identity is then established by linking immunoaffinity information to molecular mass. While conceptually straightforward, substantial preparation and manual intervention are required for probing. To prepare for probing, the sized proteins are transferred from the sieving gel to a blotting membrane. The blotting membrane immobilizes the protein separation and is then subjected to a series of handling steps including blocking of non-specific membrane interactions through coating with a dummy protein (e.g. bovine serum albumin, BSA), incubation with antibodies to accomplish the probing step, and washing before obtaining assay readout. Several fundamental limitations impede performance, including slow mass transport. In fact, antibody probing often requires an overnight incubation period to compensate for diffusional limitations on antibody equilibration with antigen captured on the blotting material. Moreover, material and reagent consumption is extensive. A single 12-lane western blot requires ∼300 ml of buffer and, most importantly, 1 μg of each detection antibody per analyte of interest. Owing to the power of the assay and in light of these deficiencies, western blotting requires continued innovation to improve throughput, minimize resource usage, and advance analytical sensitivity and dynamic range [110].

Alternative single-step assays have emerged to overcome conventional western blotting drawbacks — yet none afford the specificity of the two-pronged blotting assay [106, 107, 200–203]. Primarily relying on spatially encoded antibody-probing, single-readout assays have been developed for ultra-high sensitivity yet remain inherently vulnerable to non-specific bias. Cross-reactivity is especially challenging for biological matrices and availability of specific antibodies can be limited [5, 202, 204]. The inability of single-step assays to guarantee specificity in complex biological samples underpins the need for targeted immunoblotting methods

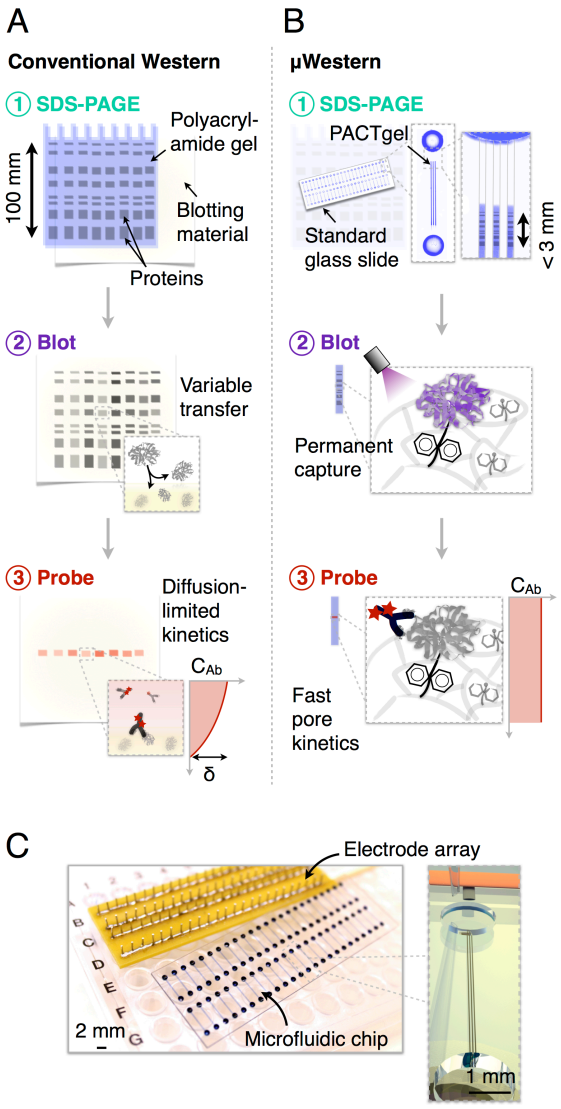

Figure 6.1: μWestern assay and device design in single microchannels enables high device density formats. Aspects of scale, reagent usage, blotting efficiency, and probe binding kinetics are illustrated by comparative schematics for the conventional (A) and μWestern (B) assays (δ indicates a diffusion boundary layer thickness). The microfluidic workflow is comprised of: (i) analyte stacking and SDS-PAGE within the PACTgel matrix. (ii) Band capture ("blotting") onto the benzophenone-decorated PACTgel in response to UV light (as opposed to transfer to a separate sheet of hydrophobic material in conventional western blotting). (iii) Removal of SDS by brief electrophoretic washing and electrophoretic introduction of fluorescently-labeled primary and (optionally) secondary detection antibodies specific to the target. Finally, excess probe is electrophoretically driven out of each device and peak intensities determined by fluorescence micrograph analysis. (C) Modular interfacing of standard microscope slide-sized chips with a scalable electrode array accommodating 48 blots per chip in triplicate (144 microchannels). Reproduced from [199].

coupled to protein separation processes [205]. Recent innovation in protein analysis tools recognizes the crucial protein separation stage and seeks to retain separations-based information. In an approach using slab gels, Ciaccio *et al.* achieved remarkable miniaturization and scale-up of the western blot workflow through a novel combination of highly multiplexed fluid handling and a large format slab gel [5]. However, the approach conceded a loss in PAGE separation resolution owing to elimination of sample stacking by isotachophoresis (ITP), a sample pre-concentration step standard in conventional slab-gels that requires pore size and buffer chemistry discontinuities in the polyacrylamide sieving matrix. Further, the workflow retained the conventional membrane transfer and antibody probing paradigm. In a commercial approach using capillary electrophoresis, downstream membrane electrotransfer was replaced with photoactivated capture of proteins onto the inner wall of the capillary [47,112]. The capillary platform streamlined and automated western blotting, but suffered from low protein capture efficiencies of $\sim$0.01% (10^4-fold lower than membrane electrotransfer) and 3–5 hour run times. In our own approaches using microfluidics, integration overcame some of the macroscale shortcomings, but we accepted either substantial complexity in interfacing and device architecture or did not implement the most widely used separation approach — protein sizing — as the first assay stage [6, 110].

In this study, we introduce scalable, automated μWesterns uniting protein sizing and antibody probing in a single microfluidic platform. The precision and control offered by microfluidic integration and photoresponsive materials achieves advances not realized previously, including development of rapid 48 concurrent μWesterns on a standard microscope slide footprint, multiplexed analysis of 3 protein targets per blot, and quantitation over a linear dynamic range of 3.6 logs with 50 pM lower limits of detection. We apply the μWestern to multiplexed protein analyses of complex proteinaceous samples, including crude cell lysate and crude human sera. Results suggest that purely microfluidic technologies are a viable means to imbue core analytical tools with automation, quantitative capability, and speed; thus paralleling advances that have positioned protein microarrays for high throughput proteomics duty.

6.2 Background: HIV Latency and Diagnostic Paradigms

Rapid, confirmatory diagnosis of disease has a strong motivation in the context of the time course of HIV infection (Figure 6.2). It is instructive to consider the life history of a man infected with HIV in his 20's in 1996. A brief and transient flu-like illness occurs with a spike in antigens detectable in the bloodstream, however, within several months, levels of the virus become almost undetectable for a period of 5–10 years. During this time, the patient generally lives symptom-free, even without administration of drug therapy. Such a patient may live 10–20 years beyond the time of initial exposure to the HIV virus. On a population

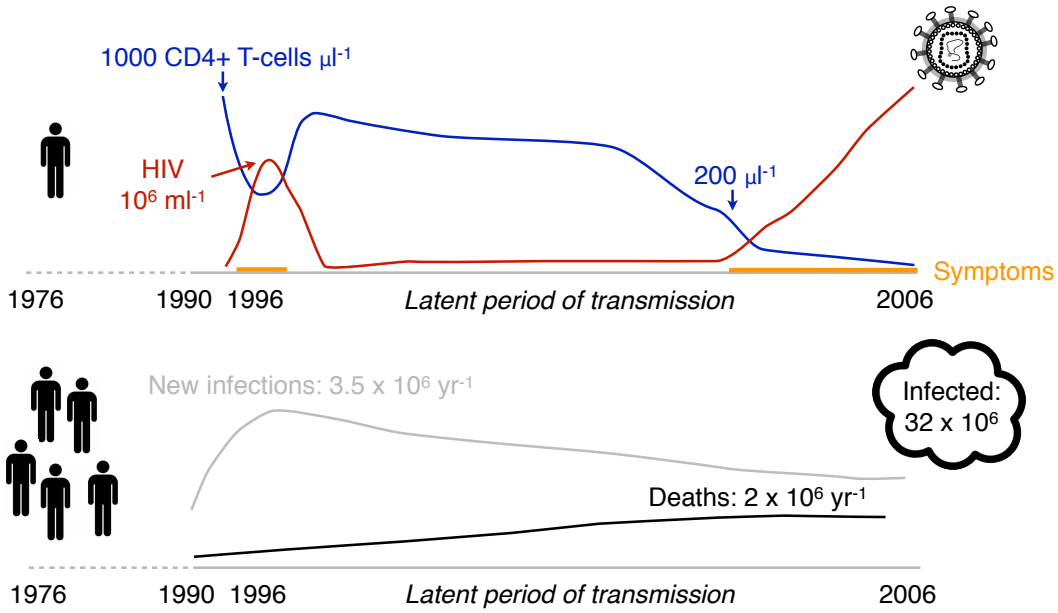

Figure 6.2: Time course of HIV virus infection from single patient and population-wide perspectives (adapted from [207, 208]).

level, the same period (1996–2006) has seen a peak and fall in the annual rate of infections worldwide from 1996, but with a peak in deaths not occurring until at least 2006. This trajectory of infection and morbidity, combined with recent clinical trial data revealing a 96% reduction in transmission risk for serodiscordant couples in which the infected partner receives oral antiretroviral therapy (ART) [206], places an emphasis on early detection of transmission.

Recently, a rapid test for endogenous anti-HIV antibodies present within human saliva of infected individuals has gained FDA approval for over-the-counter availability [209]. Infected individuals develop antibody responses to HIV antigens within 6 months of transmission in a process known as seroconversion. This milestone in diagnostics makes at-home testing possible, a remarkable resource for individuals that may not be comfortable with clinic-based diagnosis of HIV. The OraSure test, however, shows an 8% false-negative rate, meaning that 8% of HIV-positive individuals that take the test are incorrectly categorized as HIV-negative [209]. The false-negative rate in standard western blotting, however, is typically <1%, revealing a significant opportunity to improve analytical performance through development of a rapid, confirmatory western blotting assay suited to use at the point-of-care or in the home.

Beyond the development of such an assay, which this Chapter attempts to address, a significant demand exists for HIV assays that measure the incidence (rate of new infections) of HIV in specific communities to provide predictive information for planning of future therapeutic intervention [210]. The ability to measure HIV incidence is critically important for determining intervention strategy and efficacy. Incidence estimation from cohort studies or prevalence statistics is especially daunting in developing nations, in which the resources for long-term, large sample-size studies or collection of census data are often limited. These constraints place emphasis on the use of direct incidence measurement through diagnostic tests for recent infection (TRIs). While a class of assays tracking maturation of immune-response to infection following seroconversion (including the standard BED assay) have been available for more than 10 years, they are limited primarily in false-recent rate by misclassifying >2% of chronically infected individuals as being recently infected. Further, significant throughput and reagent storage constraints limit point-of-care / point-of-census measurements in far-flung and resource-limited populations in the developing world by demanding sample transport to, and processing at centralized laboratories.

Beyond binary antibody tests for seroconversion, several quantitative metrics could be pursued to provide recency-of-infection information (Figure 6.3), including:

- *Serotrajectory:* 2+ time-point measurements spaced 3–6 months apart could be used to derive patient-specific trajectories of antibody responses to optimize clinical specificity by delineating recent from false-recent patient groups. Temporal structuring of the sampling protocol could distinguish the evolving endogenous serological response of recently infected individuals from those with static but misleading serological profiles (i.e. in cases of immunocompromised or ART-treated patients).

- *End-point reactivity barcode:* A capability for true quantitation of antigen immunoreactivity could allow independent trajectory measurements of serum immunoreactivity to a panel of HIV antigens separated and immobilized within μWestern devices. This structured barcode readout would leverage differential immunoreactivity to HIV antigens, key to determining robustness to patient population and HIV subtype, while also encoding recency information.

- *Avidity:* Controlled serum residence time leveraging tuned electrophoretic control of serum contact with HIV antigens could allow patient-specific measurement of antibody avidity parameters including the "on" rate k_{on}. The known evolution in serological avidity could be measured in concert with the antigen-bias and trajectory of response to minimize false-recent rate and maximize performance.

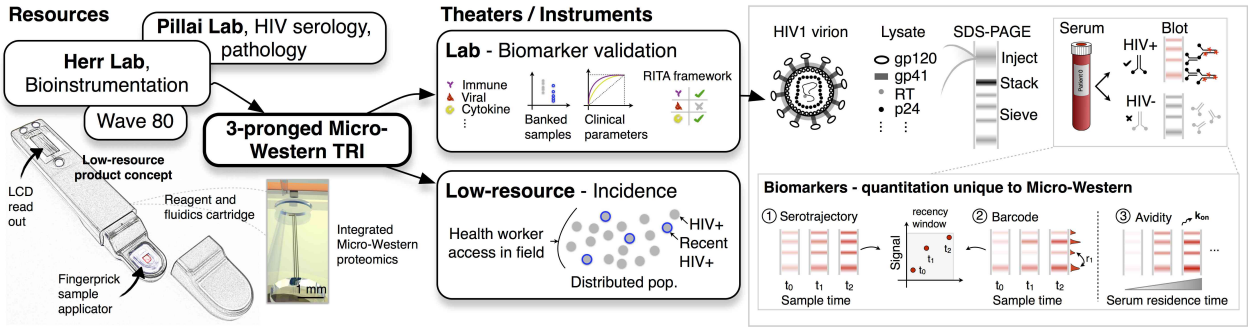

Figure 6.3: Planned project framework for μWestern HIV incidence in laboratory and low-resource embodiments, enabled by modular, adaptable microfluidic platform technology. At right, three-pronged serotrajectory measurements via quantitative anti-HIV serum profiling and precise on-chip electrophoretic manipulation of samples and reagents.

6.3 Results & Discussion

6.3.1 μWestern Device Design and Assay Operation

Performance advances in slab gel-based western blotting are limited by fundamental processes including slow transport timescales, variable blotting transfer, and diffusion-limited kinetics (Figure 6.1A). To overcome these limits on macroscale performance, we explored a microscale western blot (Figure 6.1B, μWestern blot). We hypothesized that miniaturization applied in conjunction with photopatternable, light-responsive polymers would enable high analytical performance. We used this combined approach to integrate the distinct stages of the canonical western blot into a simple, passive microchannel (see Appendix B and [199] for details of device operation). Specifically, the μWestern blot is comprised of isotachophoretic sample stacking during sample injection, weight-based separation of denatured protein analytes through the widely used sodium dodecyl sulfate polyacrylamide gel electrophoresis separation (SDS-PAGE), and *in situ* immunoblotting with fluorescently labeled primary and secondary antibodies (Figure 6.1B). We first describe the microfluidic design strategy followed by details of the μWestern assay operation, experimental observations, and resulting performance.

We employ a simple single glass microchannel design to facilitate high-density integration of μWestern blots within the footprint of a standard microscope slide (Figure 6.1C). As such, each μWestern is comprised of a pair of access wells linking three parallel microchannels (technical triplicates, each 70 μm wide $\times$ 10 μm deep) with electrical connectivity provided by an electrode array. To facilitate integration of the μWestern stages in the single microchannel geometry, we designed a new photoactive gel with tunable porosity (PACTgel) that is both (i) photopatternable and (ii) light-responsive. Photopatterning of the sieving gel is needed

for reproducible control of the gel interface position along the channel axis and, hence, assay repeatability (Figure 6.1B). A light-responsive material functionality was sought to allow the resulting photopatterned gel to switch from a molecular sieving gel during sizing to a blotting polymer for subsequent antibody probing. To introduce these new functionalities, we utilized two spectrally distinct chemical mechanisms. First, a riboflavin-driven photopolymerization strategy is used to photopattern the material (using 470 nm light). Second, a spectrally-distinct benzophenone-driven photoimmobilization strategy allows the sieving matrix to form covalent bonds with proteins in the gel (via UV excitation, Figure 6.1B, see Materials and Methods). Benzophenone is incorporated in the polyacrylamide gel via a methacrylamide comonomer (BPMAC). As a corollary outcome, the light-activated mechanism of the benzophenone-functionalized, hydrophilic gel means that no separate blocking steps are needed after protein immobilization and prior to antibody probing. Owing in large part to the PACTgel functionality, the μWestern design is compatible with 48-sample throughput within a standard $1'' \times 3''$ microscope slide footprint (Figure 6.1C).

6.3.2 Stage 1 — Single Microchannel Protein Sizing

In seeking a broadly relevant protein separation assay, we adapted the widely used tris-glycine SDS-PAGE system of Laemmli [20, 21]. Importantly, the assay requires a transient-ITP buffer arrangement and a large-to-small pore-size discontinuity a short distance along the microchannel axis to yield high-resolution protein sizing (Figure 6.4A). For the gel discontinuity, we employ an open channel-to-7.5%T sieving PACTgel interface at $\sim$400 μm into the microchannel. Transparency mask lithography of the photopatternable PACTgel is used to define the gel interface. Photopatterning yields fine control of the interface position (coefficient of variation, CV, of 3.5%, $n = 60$). During the ITP stacking phase, a diffuse plug of protein injected at the microchannel entrance is electrophoretically compacted into a $\sim$200 μm zone prior to electromigration across the sharp sieving gel interface. As is also shown in Figure 6.4A, protein electromigration through the gel interface transitions ITP to SDS-PAGE, as the protein stack slows down substantially and the trailing glycine electrolyte over-speeds the stack [20, 21]. In characterizing ITP, we observe reduced injection dispersion and >2-fold sample stacking factors. In seeking to understand the sample enrichment limits in this system, the length of the sample loading region was extended to 4 mm and the sample loading times were increased to 30 s, yielding $\sim$100-fold stacking factors (Figure 6.5). These enrichment and stacking qualities are important to obtaining high separation resolution in subsequent sizing. Interestingly, we observe that band ordering in the ITP stack is not necessarily governed by molecular mass, thus dynamic band reordering is often detected during the brief transition from ITP to PAGE (see band "x" in Figure 6.4A).

Given this observation, we next sought to confirm that the separation mechanism in the PACTgel is indeed governed by protein molecular mass differences. Analysis of protein

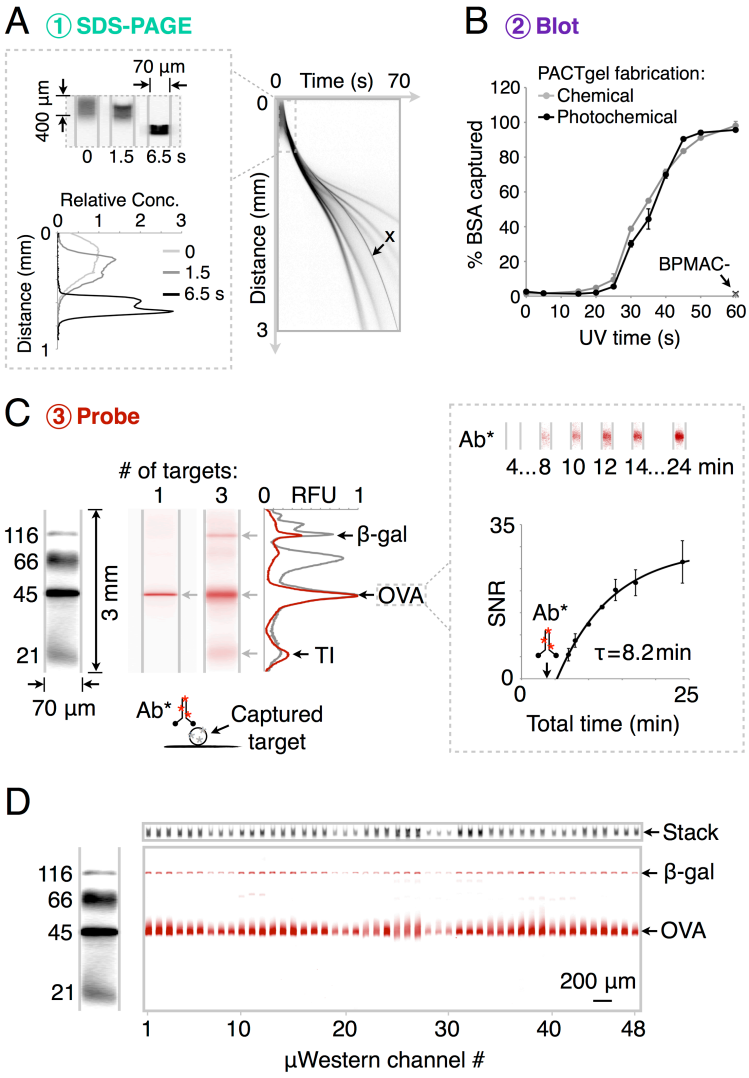

Figure 6.4: Compact μWestern with integrated high-resolution SDS-PAGE, blot, and detection. (A) SDS-PAGE of fluorescently-labeled six protein ladder (black), complete in 60 s (4× magnification; band weights are 155, 98, 63, 40, 32, and 21 kDa). Channel aspect ratios are adjusted to produce gel-like images (see dimensions). (B) Capture efficiency of bovine serum albumin (BSA, ± SD, $n = 3$) for PACTgels fabricated chemically or photochemically. (C) Left: Multiplexed μWestern readout (red) in 40 min total assay times using primary antibodies for (i) ovalbumin (OVA), and (ii) β-galactosidase (β-gal), OVA and trypsin inhibitor (TI); all at 1 μM. Right: fluorescence micrographs and plot of signal-to-noise ratio (SNR, ± SD, $n = 3$) for electrophoretic introduction of red fluorescent primary antibody (Ab*) to OVA band at 4 min total assay time (arrow). (D) 48 parallel μWesterns of the four-protein fluorescent ladder probed for ovalbumin (OVA) and β-gal targets (1 μM each) with unlabeled primary and red fluorescent secondary antibodies in 60 min total assay time. At top, total injected ("stack") fluorescence on weight marker spectral channel at the end of the ITP phase of SDS-PAGE acts as loading control. Reproduced from [160].

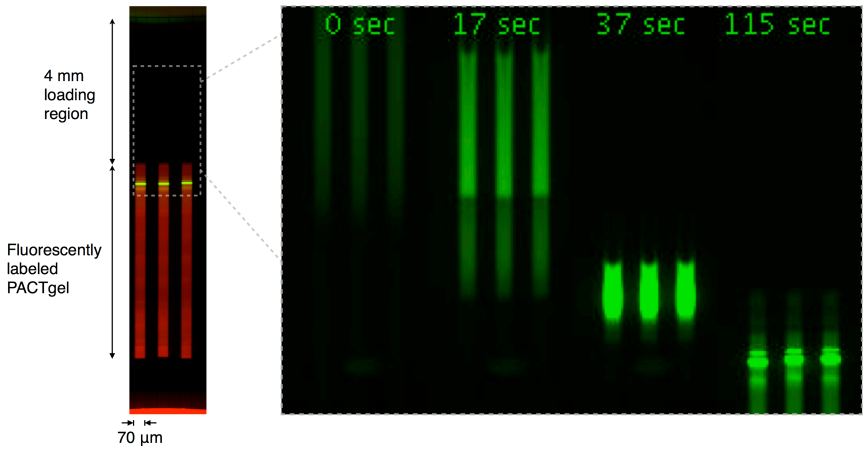

Figure 6.5: High stacking factor SDS-PAGE in μWestern devices. At left, the 8%T PACTgel is copolymerized with 3 μM red fluorescent acrylate monomer, showing an extended 4 mm open channel loading region. At right, fluorescent ladder sample (green) is electrophoresed near-homogeneously into the loading region for 30 s at 100 V cm^{-1} and subsequently separated (starting at the 0 s timestamp). Resolution of β-gal, BSA, and OVA peaks is observed at the 115 s time point. The stacking factor of ~100 is estimated by dividing the initial loaded sample width of ~4 mm by the separated band widths of ~40 μm each. Reproduced from [160].

migration in the PACTgel yields a log-linear molecular mass versus migration distance relationship over the 20–150 kDa analyte range ($R^2 > 0.98$ for ladder proteins, Figure 6.6), thus confirming this characteristic of SDS-PAGE [23]. Protein peaks with molecular mass differences of > 19% were resolvable (separation resolution $R_s \geq 1$, Figure 6.7), with resolution similar to conventional slab-gel western blotting. Although only uniform pore size gels are studied here, the PACTgel pore size distributions are tunable, thus allowing enhanced resolution over specific weight ranges of interest [76, 78, 211]. Importantly, the first sizing stage is observed to complete in compact 3 mm separation distances in separation times of ~60 s. Consequently, the duration of the sizing step in μWestern blotting compares favorably to the 40–90 min required for macroscale protein sizing. The high-performance of protein sizing benefits from the favorable scaling of electrophoretic transport with miniaturization.

6.3.3 Stage 2 — In-chip Protein Blotting by Photocapture

Next, to permit antibody-based probing of the sized protein bands, we immobilize each species on the PACTgel polymer using UV irradiation of the entire separation channel (Figure 6.4B, Figure 6.8A). UV exposure activates benzophenone groups to undergo hydrogen abstraction and covalent coupling to nearby biomolecules by a radical mechanism [6, 41].

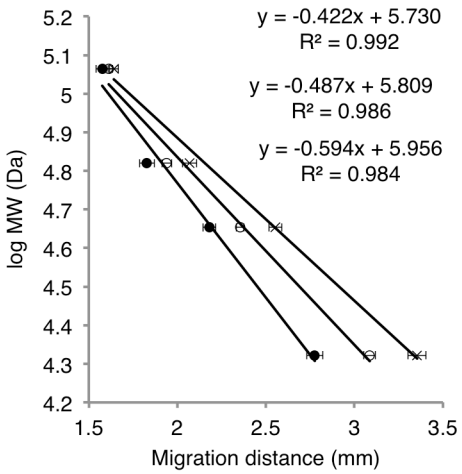

Figure 6.6: Ladder sizing in μWestern blotting. Log-linear plots of marker protein molecular weight (MW) versus migration distance during SDS-PAGE in the μWestern chip ($\pm$ SD, $n = 3$, marker proteins were β-gal, 116 kDa; BSA, 66 kDa; OVA, 45 kDa; and TI, 21 kDa). Three devices are shown (each with 3 technical replicates run simultaneously), with separations complete in roughly 3 mm in the axial dimension. Reproduced from [160].

First, we compare protein capture efficiencies for both chemically and photochemically fabricated PACTgels (i.e., gels without and with riboflavin) to determine the impact of the riboflavin-driven polymerization mechanism on the UV-initiated protein capture. In both cases, characterization of fluorescence retained on the PACTgel after photocapture and electrophoretic washout reveals a sigmoidal dependence of fluorescently labeled BSA capture efficiency on UV exposure time (Figure 6.4B). The capture time courses for chemically and photochemically initiated PACTgel formulations show $\sim$100% BSA capture when UV exposure times are $>$ 45 s. As negative controls, PACTgel formulations lacking benzophenone were studied and exhibited negligible protein blotting.

Interestingly, PACTgel protein capture efficiencies are significantly higher than those previously reported by our group for gels operating under non-denaturing isoelectric focusing conditions (1.3-13%, Chapter 3). We hypothesize that the capture efficiency improvement for SDS-PAGE stems from the denatured state of the target proteins. Denaturation likely exposes buried protein residues to the sieving matrix, thus promoting hydrophobic interactions between the unfolded analytes and the PACTgel benzophenone groups [6]. Further, the reduced requirement for protein solubilizing agents (especially detergents) in SDS-PAGE as compared to IEF likely reduces steric (among other) barriers to productive coupling between proteins and the PACTgel. Secondly, we observe low capture efficiencies for exposure times of $<$20 s. We hypothesize that this is an initial inhibitory phase perhaps caused by scaveng-

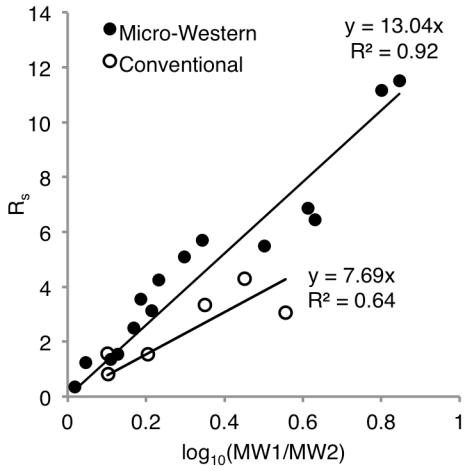

Figure 6.7: Separation resolution in μWestern and conventional western blots. Assuming consistent protein band widths (standard deviation σ_i), plots of separation resolution $R_s = \frac{|x_1 - x_2|}{2\sigma_1 + 2\sigma_2}$, where x_i are migration distances, between band pairs are expected to be linear in the log ratio of their molecular weights (MW) [212]. Linear fits of these data are shown, yielding separable molecular weight differences of 19% and 35% respectively for the μWestern and conventional western blot assays upon substitution of $R_s = 1$. Immunoblotted protein bands used for analysis — μWestern: all four reverse transcriptase bands, gp120 and p24 bands in Figure 6.9B; total of 6 bands, 15 comparisons. Conventional: two reverse transcriptase bands, gp120 and p24 bands; total of 4 bands, 6 comparisons. Reproduced from [160].

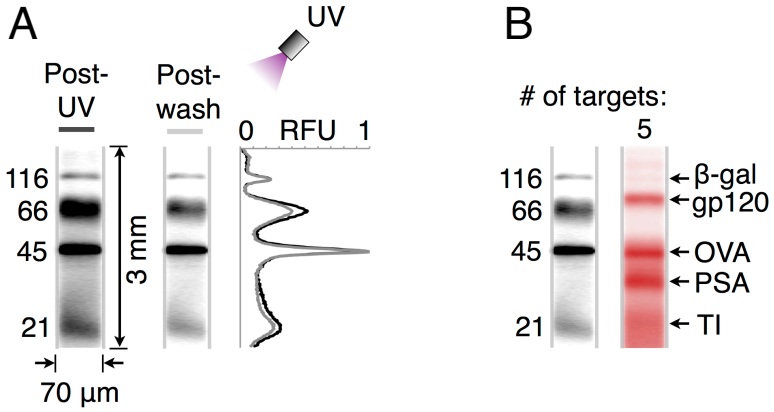

Figure 6.8: Multiplexed analyte capture and probing in the μWestern assay. (A) Fluorescence images and intensities for four ladder proteins photoimmobilized after SDS-PAGE (1 μM each, weights in kDa); before and after washout of uncaptured protein. (B) 5-plex μWestern blot readout (red) in 40 min total assay time using primary antibodies for β-gal, gp120, OVA, prostate specific antigen (PSA, 34 kDa) and TI (gp120, 200 nM; others antigens, 1 μM). Reproduced from [160].

ing of reactive benzophenone sites by dissolved oxygen prior to a productive phase of analyte capture onto the PACTgel [43]. In sum, we conclude that photopatterning using riboflavin and blue light does not compromise subsequent UV-mediated protein photocapture by the benzophenone-decorated polyacrylamide gels.

Next, we examine capture efficiencies for a wider range of proteins under the 45 s UV exposure conditions that lead to highly productive capture. We now consider only the photochemically fabricated gels of interest. We observe appreciable immobilization of a set of test proteins on the PACTgels: 97.5±0.7%, 93.1±3.4%, and 75.2±0.8% for β-galactosidase (β-gal, 116 kDa), ovalbumin (OVA, 45 kDa) and trypsin inhibitor (TI, 21 kDa), respectively (all ± SD, $n = 3$). These capture efficiencies rival conventional electrotransfer blotting efficiencies on polymer membranes [213]. Further, the nearly complete protein capture in the photoactive bulk polyacrylamide gels is an orders-of-magnitude improvement over reported capture efficiencies for photoactive inner capillary surfaces (0.01% for GFP [47]). Moreover, we observe high capture efficiencies for protein concentrations up to 100 pg nl^{-1} ($\sim 10^9$ proteins nl^{-1} or 0.1 mg ml^{-1}), a capacity attributed to an estimated benzophenone site density of $\sim 10^{12}$ nl^{-1} of the gel structure. Thus, the 3D reactive gel offers a high volumetric density of binding sites. This large number of binding sites distributed throughout the channel volume enables efficient photocapture in <60 s. In contrast, membrane electrotransfer in conventional bench top western blotting requires 90 min to complete. This rapid capture kinetic of the μWestern is critical, firstly, to yield low overall assay durations. Secondly, the rapid kinetic is essential to maintain performance. This is because diffusional band broadening erodes both SDS-PAGE separation resolution and analytical sensitivity of subsequent probing given the small inter-peak displacement distances and peak widths [6, 130].

6.3.4 Stage 3 — Probing

The final assay stage is in situ antibody probing of the immobilized, sized proteins. In the μWestern, probes are electrophoresed through and along the length of the microchannel by an applied electric field. The approach ensures that probes sample positions along the entire length of the protein-decorated PACTgel. Results for probing of OVA with a red fluorescently-labeled antibody are shown in Figure 6.4C. Antibody was electrophoretically introduced 4 min after the start of the assay and required ∼1 min to migrate through the gel pores to the immobilized OVA band. We observe negligible red signal away from the OVA peak suggesting that probe retention arises from specific interactions with immobilized protein targets. Building on the single protein probing result, Figure 6.4C reports simultaneous probing of 3 analytes in a single microchannel using a three-antibody cocktail applied in one electrophoretic step. Again, negligible off-target signal is detected. As the number of antibodies present in the probing cocktail increases (see 5-probe cocktail in Figure 6.8B), multiplexing on one spectral channel becomes limited by increasing background arising from overlap of minor components in each target protein. The use of spectrally distinct dyes is supported by the current platform, pushing the conceptual multiplexing limit to $\sim 5n$ ana-

lytes per blot, where n is the number of dyes that can be imaged without significant spectral bleed-through. Between-device peak area CVs for identical samples probed simultaneously for OVA and β-gal were 25% each, with the ratio of peak areas varying with a CV of 14.7%. Use of internal migration controls allows data comparison across channels and chips.

Next, we sought to develop an ultra-rapid μWestern blot. In designing this assay, we employ dynamic imaging of fluorescent antibody probe accumulation at the site of captured analytes (Figure 6.4C). This dynamic imaging mode yields a primary antibody probing time constant of 8.2 min for a 1 μM OVA band captured on the PACTgel after SDS-PAGE. A probe band signal-to-noise ratio (SNR) of >10 is recorded for a 10 min total assay time. We ascribe the rapid probing kinetics to the electrokinetic through-pore probe delivery strategy that leverages favorable overall reaction kinetics that are minimally impeded by surface boundary layer diffusion resistances [6]. Dynamic monitoring of target peak SNR enables the assay to trade-off between readout signal and assay time. Lastly, we sought to introduce a broadly relevant μWestern using unlabeled primary antibodies and fluorescently labeled secondary antibodies, as is common in conventional slab-gel western blotting (Figure 6.4D). In the 48-channel μWestern device, we probe both OVA and β-gal with unlabeled primary antibodies specific to the target. We also probe with secondary fluorescently-labeled antibody probes and obtain the endpoint readout after electrophoretic washout of excess probes. This dual antibody approach gives higher SNRs over the full separation range [6] while still maintaining relatively rapid assay times of less than 60 min.

6.3.5 High-Sensitivity and Quantitative Measurements for Proteinaceous Biospecimens

Next, we sought to ascertain the robustness of the μWestern to analysis of biological samples. In a first study, we apply the μWestern to measurement of the transcription factor NFκB (p105, p50) in lysate from an NFκB-transfected 293T cell line (Figure 6.9A). Western blotting is commonly applied to protein measurement in lysate, as part of e.g. protein signaling studies. An unlabeled primary and a fluorescently-labeled secondary antibody are employed for immunoprobing. Assays of NFκB transfected lysate and untransfected negative controls yield similar probing patterns in on-chip and conventional formats. We include conventional GAPDH probing as loading and biological controls, as well as utilize measurement of the total injected zone fluorescence for the ladder proteins as a μWestern loading control. With important implications to antibody screening frameworks and systems biology, we observe total assay operation to consume <1 ng of each antibody, in contrast with $\sim$1 μg consumed in conventional western blotting.

In a second study to assess assay relevance, we apply our μWestern assay to several purified human immunodeficiency virus (HIV) proteins (Figure 6.9B). HIV confirmatory diagnosis

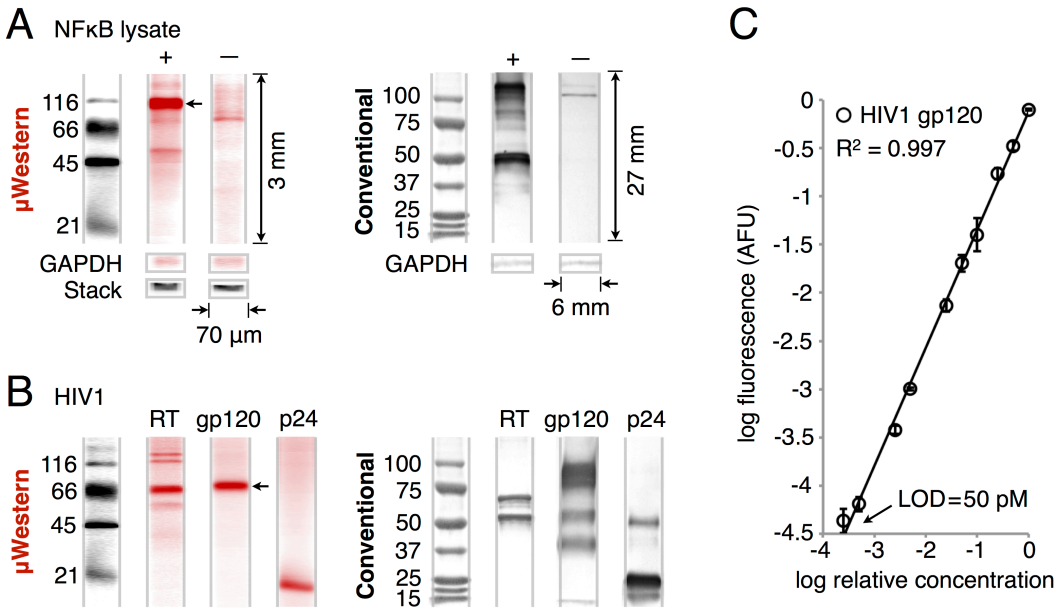

Figure 6.9: Validation of μWestern for cell lysate and purified proteins. (A) 60 min μWestern of 0.5 mg ml^{-1} transfected 293T lysate probed for NFκB with unlabeled primary and fluorescently labeled secondary antibodies (red). Untransfected negative control lysate and loading controls (GAPDH and total injected fluorescence, "stack") are included. At right, the corresponding conventional 6–8 hr western blot readouts for visual comparison. Note relative dimensions of the conventional blot. (B) 40 min μWestern of purified human immunodeficiency virus (HIV) proteins (reverse transcriptase, RT, 200 nM; gp120, 200 nM; p24, 1 μM) after probing targets with fluorescently labeled primary antibodies (red). (C) Standard curve for gp120 over the 50 pM – 200 nM range ($\pm$ SD, $n = 3$) constructed from peak areas of the band indicated by an arrow in (B). See Figure 6.10 for standard curve of the NFκB p105 peak indicated by an arrow in (A). Reproduced from [160].

— presently a process that requires a central lab and hours to complete — relies on western blotting. The μWestern and slab gel western blot results agree to within 12% for the mass of the major bands of viral reverse transcriptase and the envelope glycoprotein gp120 (Table 6.1). For the smallest protein, capsid protein p24, a 25% error in the measured weights is attributed to the reduced performance of SDS-PAGE at the lower mass end of the sizing range, which is incurred regardless of format. Nevertheless, precision in molecular mass prediction on-chip gives within-device CVs <2% ($n = 3$ for each) across the entire mass range. Minor bands for both gp120 (56, 40 kDa) and p24 (49 kDa) observed only on conventional western blots are attributed to differences between the macro- and microscale workflows, including differences in blotting efficiency, in the SDS-PAGE and probing buffer systems, and in the degree of analyte renaturation prior to immunoprobing. Potentially relevant to point-of-care μWestern applications, the total wash and transfer buffer requirement is ~300

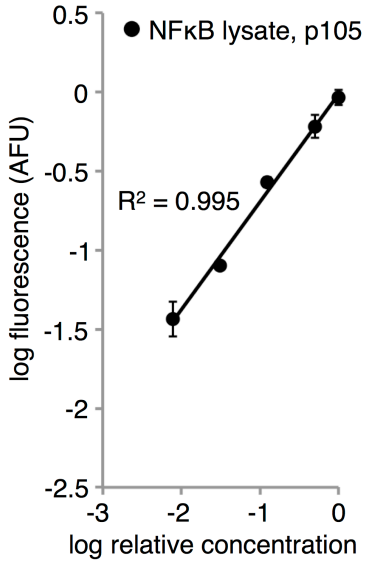

Figure 6.10: Standard curve for NFκB p105 over the 1:1 to 1:128 lysate dilution range ($\pm$ SD, $n = 3$) constructed from the peak areas of the band indicated by an arrow in Figure 6.9A. Reproduced from [160].

μl, as compared to 300 ml consumed in the conventional assay.

In both of the above studies we sought to realize high sensitivity measurement while enabling a capacity for quantitation in μWestern blotting. For both NFκB and gp120 we observe quantitative antibody signal readout over a linear dynamic range of up to 3.6 logs, on par with expected performance for macroscale counterparts (Figures 6.9C, 6.10). Using ITP to obtain a high stacking factor enrichment, we measure a lower limit of detection of 50 pM for the latter analyte. This lower detection limit is comparable to enzyme-amplified chemiluminescent readouts in conventional blots. Considered another way, the detection capacity translates into measurement of 12 pg per 2 μl sample or a total mass of 17 fg of gp120 per sample injection volume. These results compare favorably to recent low mass sensitivity (340 fg) slab gel western blots [5]. The mass limits also suggest that we can detect the equivalent of $\sim$4,000 virus particles on a gp120 basis (4–35 copies per virion) or as few as $\sim$20 particles for p24 (5,000 copies per virion) [214]. As relevant to single-cell proteomics, the mass detection limit of $\sim$80,000 molecules we demonstrate is within the $10^4 - 10^6$ molecule range expected for signaling proteins in single mammalian cells [215].

Building on the above HIV antigen study we conducted a third study, in which we sought to measure HIV antibodies directly in human sera. Currently, HIV diagnosis employs a

Table 6.1: Molecular weight (MW) estimation in μWestern and conventional western blots. Molecular weight estimates in the μWestern assay were determined from calibration curves of fluorescent marker proteins run concurrently with the immunoblotted analytes listed ($\pm$ SD, $n = 3$, within-device). Errors between the microchip data and weights similarly estimated from conventional ("Conv.") western blots are shown at right.

Species	Nominal MW (kDa)	MW (kDa), Chip	MW (kDa), Conv.	% Error
Rev. Trans.	66	74.3 $\pm$ 0.3	68.5	8.4
	51	57.6 $\pm$ 0.4	54.2	6.4
gp120	120	77.4 $\pm$ 0.1	87.0	11.0
p24	24	18.1 $\pm$ 0.2	24.2	25.1
NFκB lysate	105	106.7 $\pm$ 0.4	119.9	11.0
	50	51.9 $\pm$ 0.1	50.4	3.0

conventional western blot as the final (confirmatory) assay, following a positive ELISA-based screening result [204]. In a 6–18 hr workflow, an HIV viral lysate is subjected to SDS-PAGE and immunoblotting (Figure 6.11A). Diluted patient serum is incubated with a nitrocellulose strip carrying the HIV protein bands. Any HIV-reactive antibodies in the serum bind to specific HIV proteins on the strip. A positive result is indicated if two or more of the p24, gp41 and gp120/160 bands exhibit reactivity at least as intense as that of the p24 band on a blotting strip subjected to a weakly reactive control serum [204]. We translate the confirmatory HIV diagnostic assay to the μWestern by assaying human sera against purified gp120 and p24 HIV proteins (Figure 6.11B). A mixture of these antigens is subjected to the μWestern assay, and the first probing step performed with 1:100 diluted human serum. Specific serum reactivity to each "bait" protein is determined using a fluorescently labeled secondary antibody directed to human IgG on the PACTgel. The resulting dose-response is consistent with the expected antibody titer in each of three sera (strongly reactive, weakly reactive, non-reactive); in accordance with guidelines for determining HIV infection in humans [204]. While promising, ongoing development of integrated serum processing [216] and optimization of assay conditions is underway to reduce non-specific background in the μWestern. We attribute the background evident in the micrograph data to non-specific probing of off-target human IgGs present in serum at high concentrations ($\sim$10$-$15 mg ml^{-1}). After fully scrutinizing clinical specificity and sensitivity performance, we see potential for a 60 min stand-alone, rapid confirmatory HIV diagnostic for near-patient application.

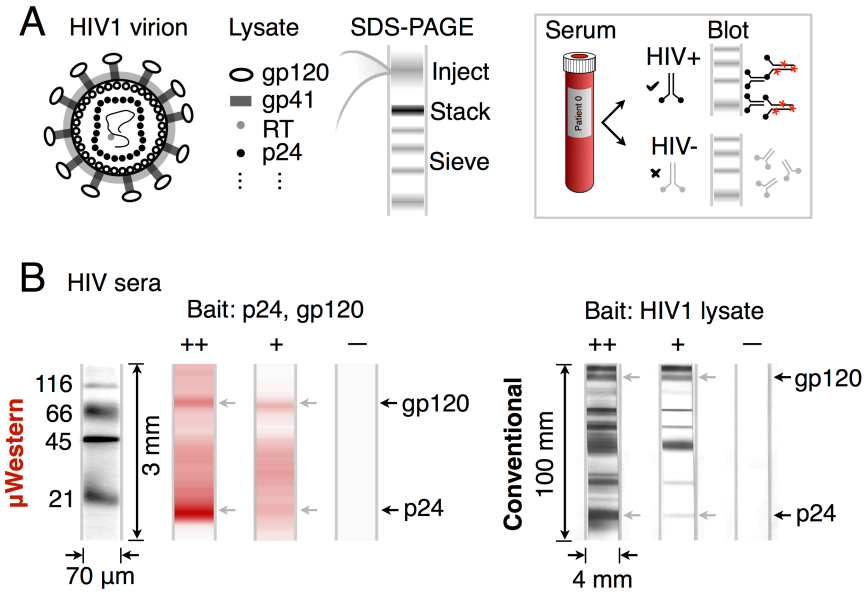

Figure 6.11: 60 min μWestern for human immunodeficiency virus (HIV) antibody detection in human sera. (A) Conventional confirmatory HIV diagnostic assay schematic. (B) Reactivity of 1:100-diluted strongly reactive (++), weakly reactive (+) and non-reactive control (−) human sera to gp120 (200 nM) and p24 (1 μM) "bait" proteins revealed by fluorescently-labeled secondary antibody to human IgG (red). At right, the conventional 6–18 hr HIV western blot, with gp120- and p24-reactive bands indicated by arrows. The conventional blot employs whole HIV lysate, whereas the μWestern uses specific HIV antigens, accounting for the additional reactive bands visible in the conventional blot. Reproduced from [160].

6.4 Conclusions

Protein measurement tools that are high throughput yet afford high specificity quantitation hold great promise for advances across a swath of inquiry, from systems biology to clinical medicine. The studies detailed here introduce a fully microfluidic western blot that modernizes and automates conventional western blotting. Owing to the precision and control offered by microfluidic integration, we achieve advances in four key aspects of analytical performance: exceptional protein blotting efficiency with near complete analyte capture, accelerated run times as all steps from sample separation to probing are completed in 10–60 min, small device footprint (800-fold smaller device area compared to conventional gel lane) and superb reagent economy with a 10^3-fold reduction in antibody and buffer requirements over conventional western blot. In an advance over conventional capability, the μWestern yields quantitative readouts from multiplexed analyte probing in a single sample and from 48-blot microchips. As is important to myriad protein measurements, the μWestern achieves desired limits of detection across numerous specifications, including starting sample concen-

tration (low pM), starting sample total mass and volume (pg per 2 μl of sample) and, finally, total detected mass (tens of fg of material per injected volume). To ensure relevance, we validate our μWestern for purified proteins, crude cell lysate and crude human sera. To further enhance the μWestern performance, ongoing efforts focus on minimizing non-specific background through on-chip sample cleanup and alternative approaches for probe introduction and washout.

Looking forward, success in microfluidic integration of disparate separation, blotting and immunoprobing stages into a unified workflow presents an exciting opportunity for "quantitative western blot microarrays". Such approaches may eventually rival the throughput capacity of protein microarrays while retaining a currently missing and crucial separation step. As relevant to personalized medicine, our flexible electrophoretic blotting strategy is likely amenable to diverse probing (e.g., lectin) and gel staining strategies needed for characterization of protein post-translational modifications [139], characterization that is difficult with spatially-encoded immunoreagents alone. Intriguingly, stable PACTgel analyte capture offers the ability to archive and reanalyze μWestern chips. Taken together, we see promise for challenging analytical applications in systems biology, cancer biology and infectious disease diagnostics.

Chapter 7

Single-Cell Proteomic Analysis by Separative Immunoblotting Microarrays

7.1 Introduction

Building upon the advances in integration, throughput, and quantitative capabilities of the microscale western blotting assay developed in Chapter 6, we sought to bring the integrative power of the PACTgel matrix to the analysis of single biological cells. In the context of the state-of-the-art in single-cell analysis today, the ability to separate cell contents prior to specific identification and quantification of protein targets is a crucial aspect of improving analytical performance. Further, the possibility to visualize protein-protein interactions provided a strong motivation for a separative analytical stage to augment existing tools in the single cell space.

The principal proteomic tool for single cell analysis is flow cytometry, a technique in which cells probed for cell surface or intracellular markers are hydrodynamically focussed and directed in single-file through laser-induced fluorescence or mass cytometry detectors. The principal drawback of flow cytometry are the rigorous validation protocols required to delineate specific from off-target antibody signals, along with the complicated cell processing and instrumentation workflows. Although a myriad of alternative single cell analysis tools have been forwarded in the life sciences and microfluidics communities, none match the throughput and analytical performance of flow cytometry (Table 7.1).

To orient our design approach, we chose to study rat neural stem cells (NSCs), a readily cultured cell line that exhibits a broad range of biological processes of strong interest to the regenerative medicine community [223–225]. NSCs can be induced to differentiate into a range of cell types, including glia (astrocytes) and neurons. Intriguingly, this process exhibits some hallmarks of stochastic cellular response to homogeneous environmental cues — individual NSCs exposed to the same biochemical cocktail that induces differentiation may respond by producing glial or neuronal daughter cells (Figure 7.1). Second, NSCs respond to biochemical cues via canonical signaling pathways, e.g. phosphorylation cascade downstream of the FGF receptor, and the β-catenin equilibrium downstream of Frizzled, the receptor for the secreted signaling protein Wnt.

We thus set out to develop a single-cell method to quantitatively measure proteomic responses at the short timescales of signal transduction, as well as at the longer timescales of cell differentiation in order to address hypotheses underlying differential NSC response to environmental cues. Further, we directed our efforts towards measurements that would complement the power and throughput of flow cytometry, namely measurements at phosphorylated residues of intracellular signaling proteins that are difficult to quantify using standard techniques, and the exploration of heterogeneity in the molecular weights of key markers of cell state along the differentiation timescale.

Table 7.1: A qualitative comparison of some selected single-cell analysis methods, from proteome to metabolome. Several methods are evaluated qualitatively for performance [217–222]. Capillary or chip electrophoretic methods typically require sample preprocessing by fluorescent labeling or fluorescent fusion construct expression. ELISA methods lack spatial separation of protein forms, preventing ready discrimination of specific and off-target probing, a property shared by flow cytometry. Mass spectrometry, at present, lacks the analytical sensitivity to detect all but the most abundant proteins in single cells, and is better suited to metabolome analysis. ELISA, enzyme-linked immunosorbent assay; MDA, multiple-displacement amplification; MALBAC, multiple annealing and looping-based amplification cycles; FISH, fluorescence *in situ* hybridization; qPCR, quantitative polymerase chain reaction.

				Readout					
Single-Cell Method	Cells/day	No cell labeling/ pretreatment?	Accessible workflow	Species identity	Species interactions	Species size	Species variants	Species localization	Quantitative
Proteome									
This work	10^4	●	●	●	▲	●	●	■	●
Immunocytochemistry	10^3	●	●	●	▲	■	▲	●	■
ELISA / Pulldown	10^3	●	●	●	▲	■	▲	■	●
Electrophoresis	10^2	■	▲	■	▲	●	▲	■	●
Flow cytometry	10^9	■	▲	●	■	■	▲	■	●
Mass spectrometry	10^2	▲	■	▲	■	●	▲	■	■
Genome									
MDA	10^1	●	▲	●	N/A	N/A	●	■	▲
MALBAC	10^1	●	▲	●	N/A	N/A	●	■	▲
Trancriptome									
FISH	10^3	■	●	●	N/A	N/A	●	●	●
qPCR	10^2	●	●	●	N/A	N/A	●	■	▲
Metabolome									
Mass spectrometry	10^2	▲	■	▲	N/A	●	▲	■	■

● Yes
▲ In principle / unclear
■ No

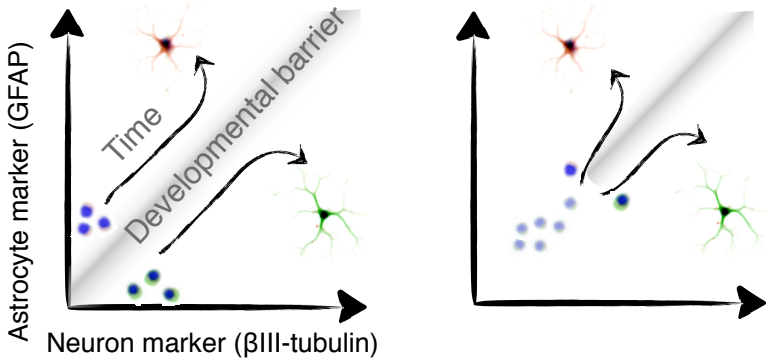

Figure 7.1: Disparate models of neural stem cell (NSC) differentiation require single-cell mapping of proteomic changes underlying cell fate. The existence of heterogeneity in cultured NSCs may predispose cell populations to particular developmental trajectories during mixed differentiation to astrocytes and neurons. Alternatively, differential response of individual cells to environmental and biochemical differentiation cues may dominate the determination of cell fate over the differentiation timescale.

Here, we report a single-cell immunoblotting technique that enables targeted, quantitative proteomics with a throughput in the thousands of cells per assay in an accessible, readily adoptable workflow reminiscent of protein microarrays. We achieve analytical limits of detection in the 10,000-100,000 molecule range, allowing immediate access to around half of the mammalian proteome [226], providing primary antibody probes are available to protein targets of interest. The assay shares the protein sizing and off-target probing discrimination capabilities of standard western blotting, but at a single cell resolution that has not been previously achieved. We explore cellular heterogeneity in the NSC system, studying differential cell response to signaling and differentiation stimuli in timecourse experiments over hours to days, revealing the broad capability of the tool to tackle cell responses to environmental stimuli through quantitative measurement of a range of proteomic targets.

7.2 Results & Discussion

We began development of the microfluidic single-cell immunoblotting assay by taking inspiration from a microfabricated embodiment of the popular comet assay for DNA damage analysis developed by Wood *et al.* [227]. Here, cells are settled into arrays of microwells fabricated in agarose by gravity, covered in a second layer of agarose, lysed and electrophoresed. DNA damage induced by e.g. ionizing radiation produces breaks in the DNA, causing a comet-like tail of DNA fragments to run from the central spot of genomic material according to the applied electric field.

We adapted this microwell method to allow high cell throughput in the nascent immunoblotting assay. A thin PACTgel layer is formed by polymerization on a methacrylate-functionalized glass slide against a silicon master patterned with microposts by SU-8 photolithography (Figure 7.2; see Appendices B and D, and [228] for detailed methods). Arrays of microwells are formed in the PACTgel sheet after removing the glass slide from the master, allowing settling of suspended cells by gravity. Cells can be rapidly lysed (within 10 s) by applying a modified radio immunoprecipitation assay (RIPA) lysis buffer directly to the slide surface, without any additional requirement for a second material layer to cover the wells.

Following lysis, the entire slide is subjected to an electric field in a custom electrophoresis chamber, causing proteins to migrate from the wells through the walls of the sieving PACTgel layer, and to separate by size. The PACTgel can be activated upon the application of UV light, trapping protein analytes prior to antibody probing by simple diffusion.

7.2.1 Purified Protein Separations

To validate the separation performance of microwell-patterned PACTgels in the standard microscope slide format, we incubated a PACTgel-functionalized slide with purified Dronpa

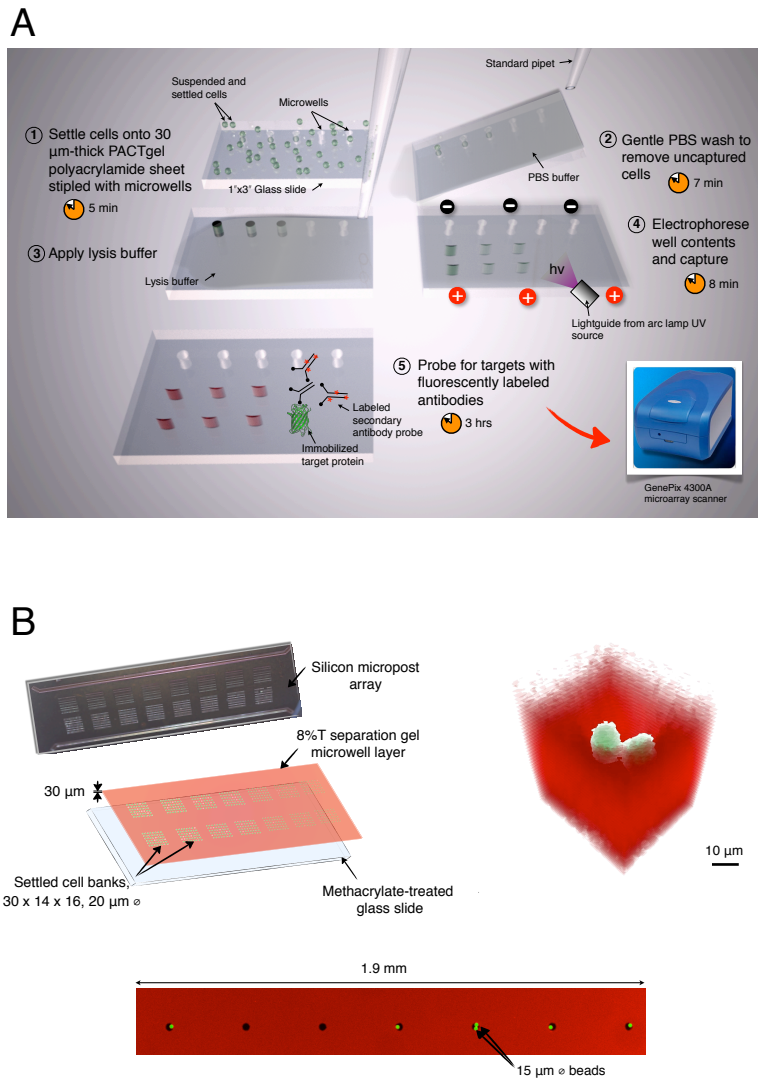

Figure 7.2: Schematic of 3 hr single cell immunoblotting assays at $> 10^3$ cell throughput. (A) A standard methacrylate-functionalized $1'' \times 3''$ glass slide is patterned with a 30 μm-thick PACTgel sheet stippled with (typically) 20 μm $\varnothing$ microwells. Suspended cells are settled onto the PACTgel layer and allowed to enter wells by gravity. Gentle washing removes excess cells, while cells trapped within wells are left behind. Lysis buffer is then applied to the top of the slide, lysing cells and mixing well contents just prior to electrophoresis. An electric field is applied across the entire slide to drive cell contents through the PACTgel, separating protein analytes. After PACTgel capture using UV light, the slide is probed using diffusion-mediated delivery of specific primary antibodies, followed by secondary fluorescently-labeled antibodies. (B) Microwells are created in a 2×8 block arrangement with dimensions to match an Arrayit microarray gasket system, with 420 microwells per block, by polymerizing the PACTgel against a silicon micropost array created *via* SU-8 photolithography.

(a green fluorescence protein variant), rapidly exchanged the buffer to the modified RIPA buffer by submersion of the slide for ∼5 s, and "sandwiched" the PACTgel film containing the Dronpa protein using a second layer of plain glass. Intriguingly, the Dronpa tended to accumulate within the microwell structures (Figure 7.3), a process that we hypothesize is rooted in a partitioning effect that controls the equilibrium concentrations of proteins in the microwells as a function of their gel concentrations.

Indeed, particles including proteins are expected to partition between dense hydrogel networks and free solution according to a partition coefficient, K (see Chapter 1.3.2).

Tong *et al.* provide an instructive dataset from measurements of fluorescently-labeled proteins in equilibrium with polyacrylamide gels, showing that the model proteins RNase and bovine serum albumin (BSA), behave according to Equation 1.25 [27]. Even for the 13.7 kDa RNase, the partition coefficient is as low as ~ 0.2 for a gel volume fraction of 0.1, indicating the strong exclusion effect of protein into the free solution from the dense gel network at equilibrium (Figure 7.4).

Returning to the purified Dronpa experiment, the exclusion of Dronpa into the well enables repeated "injection" of aliquots of Dronpa from the microwells into the PACTgel matrix upon the application of electric field across the entire slide (Figure 7.3). Upon halting the electric field, Dronpa accumulates within the wells to an equilibrium concentration set by Equation 1.25 on the $\sim$ 5 s timescale.

Although encouraging, the Dronpa results do not rule out the possibility that proteins exiting the microwells in fact electrophorese in a thin layer between the PACTgel and the upper glass slide. To demonstrate that proteins enter the PACTgel and are effectively sieved, we similarly incubated a slide in a mixture of labeled proteins. Indeed, applying an electric field across the sandwiched slide reveals stacking of the proteins against the rim of the microwell, followed by separation of protein bands within the PACTgel (Figure 7.5).

Given the anticipated partitioning effect, which is expected to be exacerbated by the large (∼150 kDa) size of probe antibodies, we determined the equilibration time of probe antibodies in an 80 μm-thick PACTgel layer (Figure 7.6). After incubating a fluorescently labeled primary antibody in the free solution above a PACTgel-coated slide for more than 30 min, the slide was washed in probing buffer (TBST, see Appendix D) and imaged for washout times of 0, 10, 20, and 30 min. As antibody left the slide by diffusion, an exponential decay in the slide fluorescence was observed with a time constant τ of roughly 5 min, and the time for complete washout of say $4\tau = 20$ min compares well with an estimated diffusion time $t \sim \frac{x^2}{4D} = 27$ min (see Appendix C). In practice, the PACTgel layers are typically 30 μm

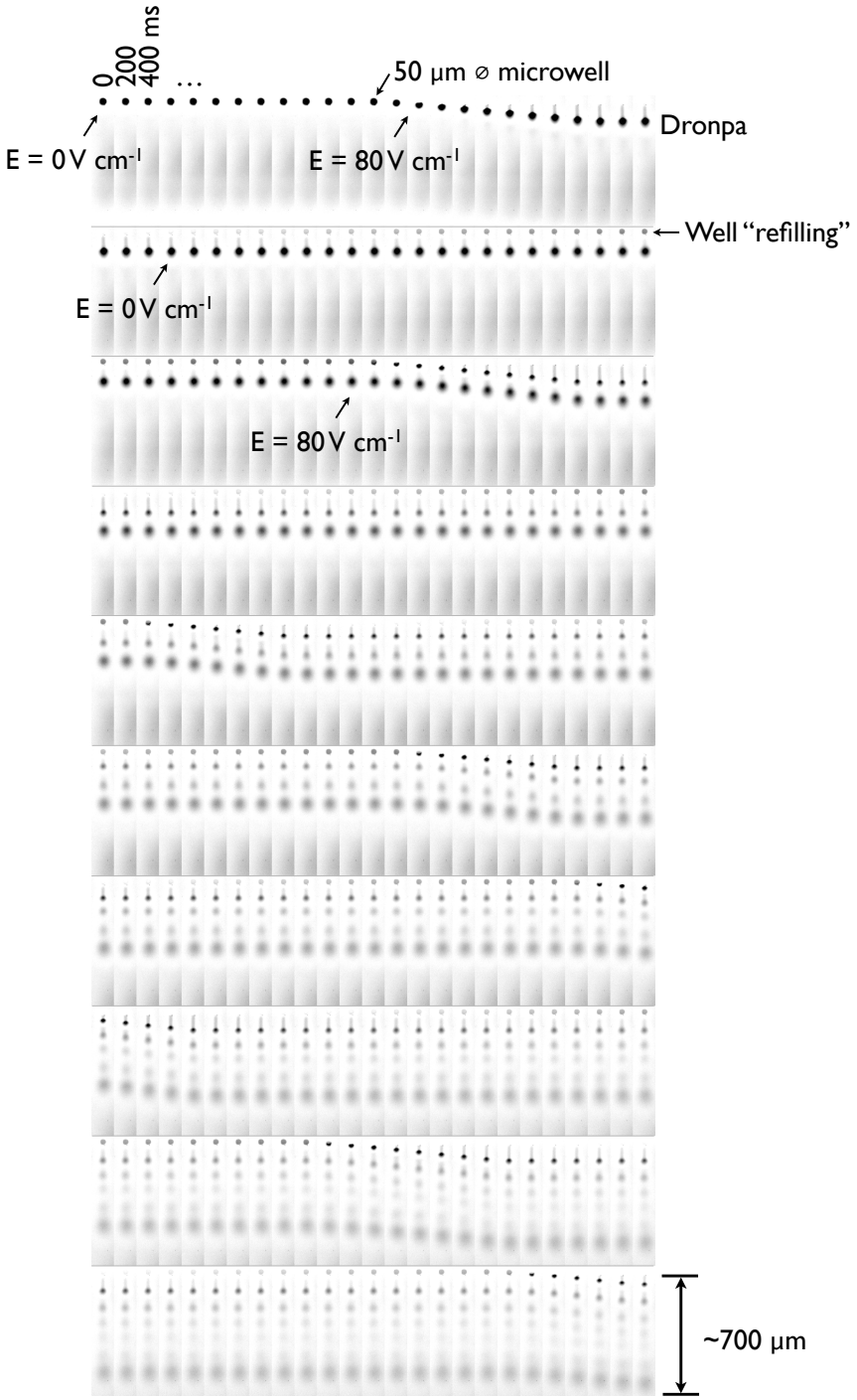

Figure 7.3: Kymograph of repeated injection of 1 μM Dronpa at 70 V cm^{-1} from glass-enclosed 50 μm $\varnothing$ microwells enabled by passive well refilling (caused by Dronpa preferentially partitioning to the open well from the surrounding gel matrix). Note little band dispersion except by diffusion over the 180 s time course (read left-to-right, top-to-bottom).

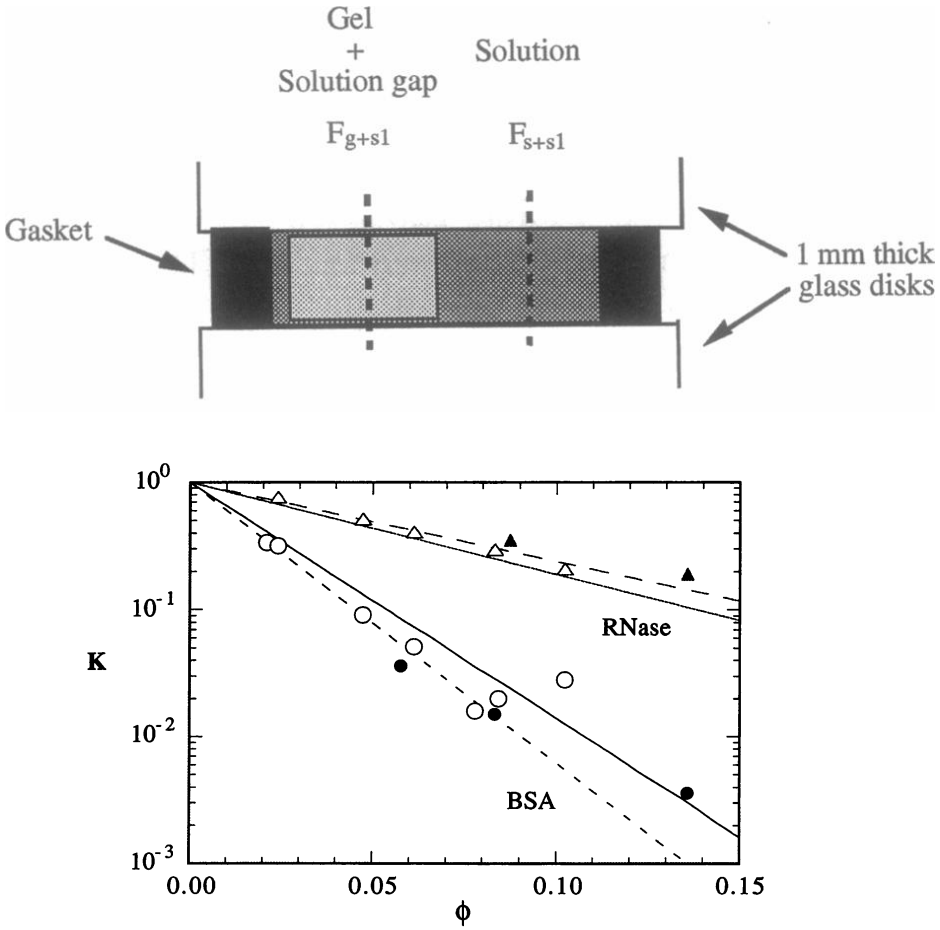

Figure 7.4: Proteins in equilibrium with dense hydrogel networks are subject to partitioning based on size. Top, experimental setup used by Tong *et al.* [27] to monitor FITC-labeled protein concentrations in both free solution and within a hydrogel segment. Bottom, a graph of the partition coefficient K against the polyacrylamide volume fraction ϕ fitted to Equation 1.25, showing characteristic log-linear relationships for RNase (13.7 kDa) and BSA (67 kDa) based on molecular size.

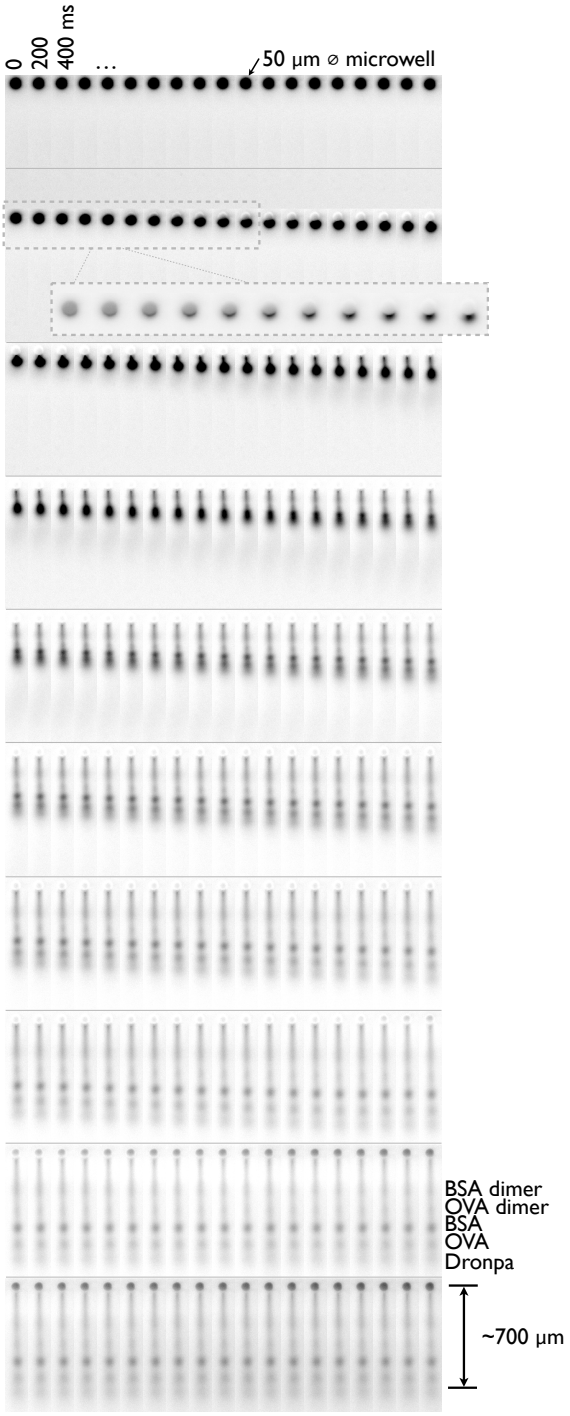

Figure 7.5: Kymograph of injection of three-protein ladder (1 μM Dronpa, OVA*, BSA*) at 70 V cm^{-1} from glass-enclosed 50 μm $\varnothing$ microwells over a 30 s period prior to capture via UV exposure (read left-to-right, top-to-bottom). Inset shows stacking of protein at transition of protein plug from well to gel.

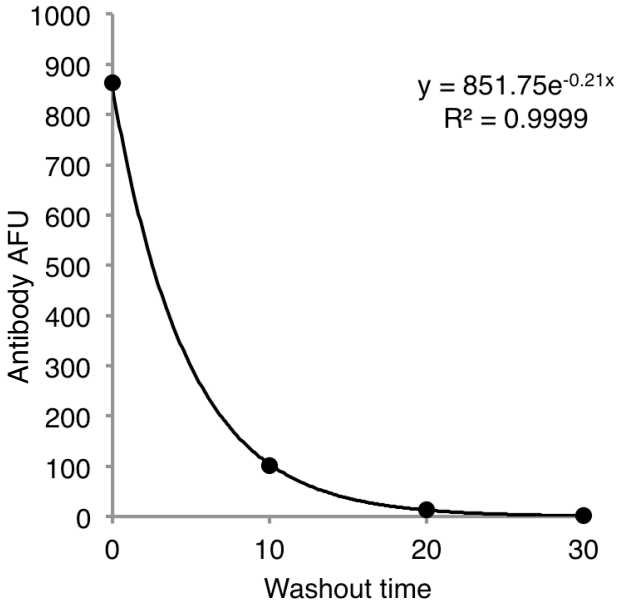

Figure 7.6: Anti-β-gal* washout kinetics for an 80 μm-thick, 8%T PACTgel sheet, note $\tau \sim 5$ min.

thick to limit the incidence of vertical stacking of multiple cells within the microwells by more closely matching the dimension of a cell. Here, we would expect antibody equilibration times of roughly 4 min.

This experiment indicates that rapid equilibration of probe antibodies with the PACTgel can be achieved during probing and washing, given its microscale thickness, although the solution concentration of probe must be increased to compensate for the effect of partitioning in reducing the gel concentration of the probe by perhaps a factor of 10^{-2}–10^{-3} with respect to its bulk solution concentration.

After validating the sieving capacity of the PACTgel in the thin, open film arrangement and determining the relevant physicochemical factors governing probe antibody penetration and washout from the gel, we attempted to probe for purified proteins separated and captured on the slide. Figure 7.7A shows that a mixture of fluorescently labeled OVA and BSA as purified model analytes could be separated and captured in the sandwich slide configuration over separation distances that were consistent across the entire slide (distance of probed OVA band from well lip within block: 167 ± 6.5 μm, CV = 3.9%, $n = 6$ devices; between blocks: 164 ± 3.8 μm, CV = 2.3%, $n = 3$ blocks). Further, the OVA and OVA dimer bands could be probed using a specific primary antibody and a fluorescently labeled secondary antibody on a separate spectral channel from the Alexa Fluor 488 dye used to label the captured analytes.

The non-specific background on the slide was found to be very low, in keeping with the use of standard TBST-based antibody and wash buffers to deliver antibodies by diffusion, and the partitioning effect of the gel, which would tend to expel unbound antibodies effectively from the gel during washing. Intriguingly, dimer bands were observed, indicating the possible applicability of these quasi-denaturing separation conditions to analyses of protein-protein interactions. The data also indicate that the standard log-linear relationship between protein molecular weight and migration distance expected for denaturing SDS-PAGE separations [199] holds here, at least for a limited set of purified proteins (Figure 7.7B).

7.2.2 Neural Stem Cell Separations

Given the demonstrated capability to separate, capture, and probe purified proteins, we studied the settling and lysis of neural stem cells. Capture of cells by microwells was found to vary according to the number of cells applied during the initial settling step, in line with previous reports of gravity-driven microwell seeding [227,229]. Microwells of 20 μm diameter showed single cell occupancies of 40–50% for cell numbers in the 2–3.5$\times 10^6$ range, or 1,000–1,800 cells per mm^2 of slide area and settling times of 5–10 minutes (Figure 7.8). These values are consistent with those of Rettig *et al.*, who found single NIH 3T3 cell occupancies of 30–60% for microwells in PDMS of 27 μm height, 20 μm diameter, settling times of 5–10 minutes, and cell densities of 2500–6200 cells mm^{-2} [229].

Looking towards integrating extraction and electrophoresis of total cell protein, it was of interest to study the cell lysis process. We employed a modified RIPA buffer designed to maximize protein extraction from the cell contents while maintaining a suitable conductivity for a serial electrophoresis step (Appendix D). Applying the buffer directly to the slide surface caused cell lysis within 2 s, followed by protein extraction within a period of approximately 10–20 s (Figure 7.9). The lysis and protein distribution kinetics exhibit some hallmarks of timescale separation, since diffusion of a Venus GFP marker present in the NSCs throughout the well crossection occurred significantly faster than the apparent diffusion of the protein through the walls of the PACTgel and out-of-plane away from the slide surface.

Perhaps against intuition, directly pouring the lysis buffer over the microwells does not cause rapid convective purging of the cell contents from the wells, even though the wells are not covered by another material layer that would serve to halt convective flow inside them. We modeled this process in COMSOL by assuming laminar flow and no-slip boundary conditions at the PACTgel surface, and applying a maximum expected velocity in the bulk fluid above the slide during pouring of 0.1 ms^{-1}. The model clearly shows a recirculating flow within the microwells during the initial high-velocity conditions in the lysis step, but massless particle trajectories in this simplified steady-state model tend to show entrainment of material within

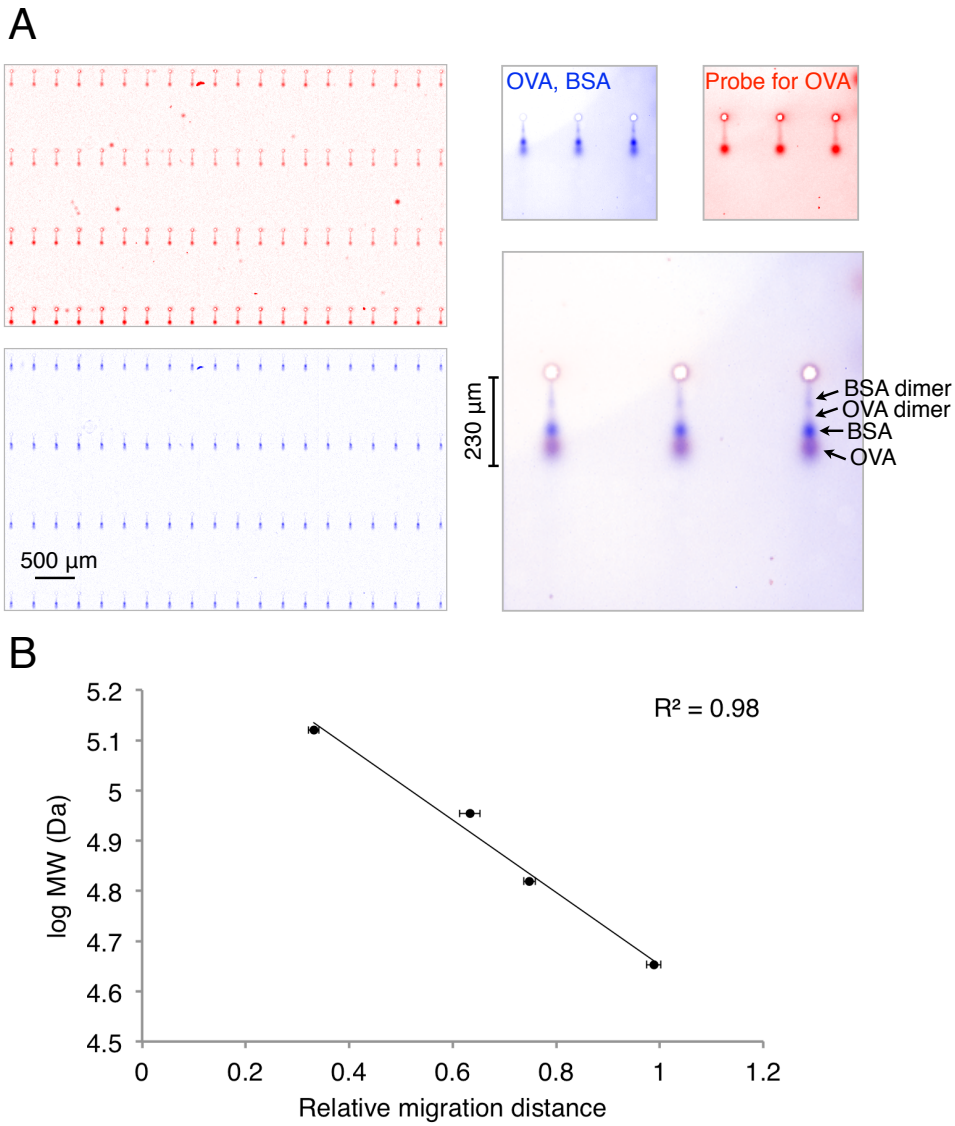

Figure 7.7: Arrays of purified protein separations can be probed by diffusive delivery of antibody probes, revealing weight-based analyte sieving. (A) At left, a 4× fluorescence micrograph (blue) of captured Alexa Fluor 488-labeled ovalbumin (OVA) and bovine serum albumin (BSA) following separation in an 8%T PACTgel sheet, and of the probe signal subsequent to incubation with 1:20 diluted primary and secondary antibodies to OVA (latter labeled with Alexa Fluor 568, red). At right, 10× images of three adjacent separations with an overlay of fluorescence data. (B) Log-linear plot showing the capacity for molecular weight determination from the migration distance of a given protein species in the purified protein assay.

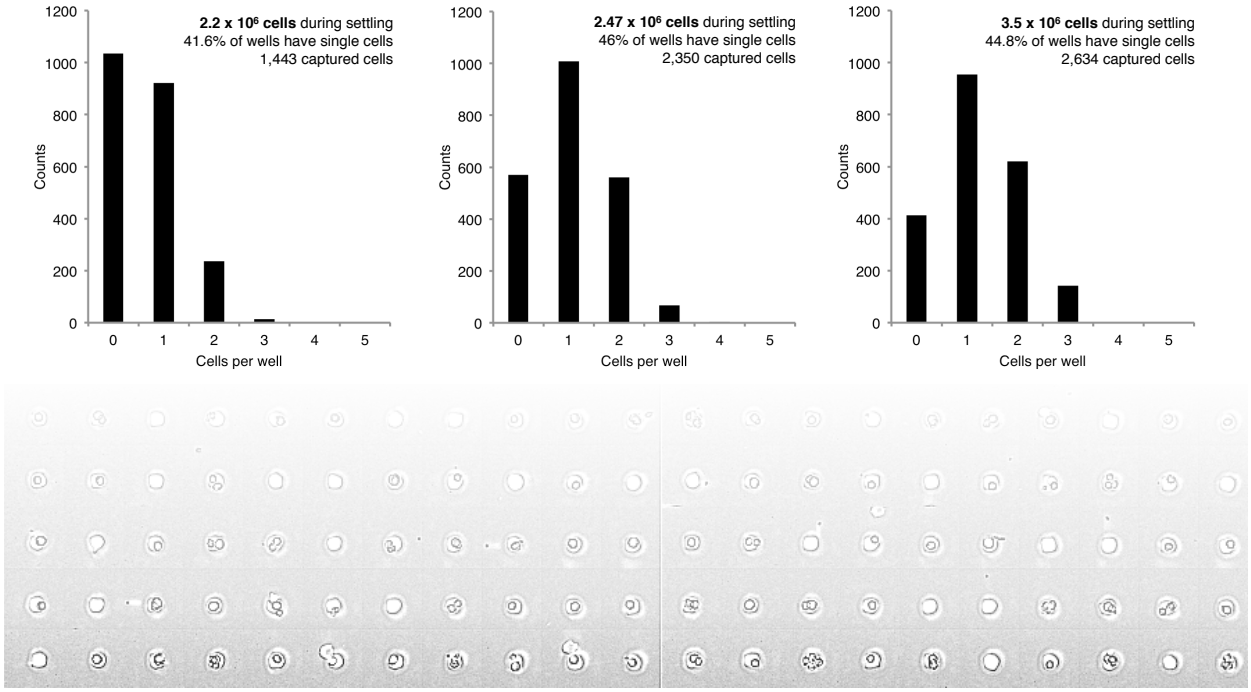

Figure 7.8: Manually counted cell-per-well distributions across single-cell immunoblotting devices subjected to different numbers of NSCs during settling and cell seeding. Note that 40–50% of wells contain single cells after seeding and washing for cell numbers in the $\sim$ 2–3.5$\times 10^6$ range ($\sim 1,000$–1,800 cells mm^{-2}). Bottom: a typical bright-field micrograph recorded prior to cell lysis and assay for counting purposes. All wells in the $1'' \times 3''$ array can be captured with 192 images at 4$\times$ magnification in roughly 3 min.

the well, although likely the average diffusion distance from the bulk fluid above the well is reduced. In practice, protein material losses for a low MW protein such as Venus GFP (27 kDa) during lysis can be estimated at roughly 30–40% from analysis of the fluorescence material balance around the well during lysis and separation.

Early in assay development, we experimented with the use of a 1% low melting-point agarose layer applied to slides seeded with cells to suppress convection in the vicinity of the microwells. An agarose preparation at 40°C in PBS was applied to slides, and a second glass slide used to trap, level and reduce the thickness of the agarose layer to approximately 10-30 μm prior to setting it by brief incubation at 4°C. Although perhaps limiting initial loss of protein during lysis, the agarose was found to produce high non-specific antibody binding during subsequent probing for protein targets, even after removing the agarose by suction and resuspension at 40°C immediately prior. In the absence of an alternative material for suppressing convective protein losses during cell lysis, short of dramatically increasing device

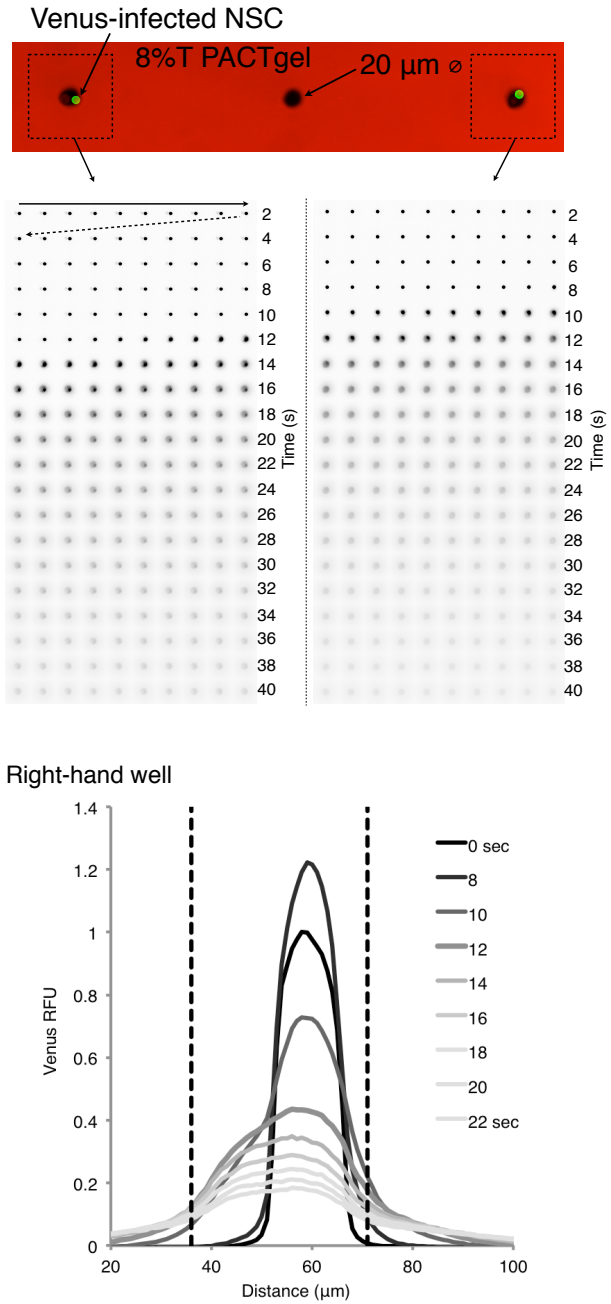

Figure 7.9: Cell lysis and distribution of fluorescent protein contents shows timescale separation. Top, 20 μm ⌀ PACTgel microwells. Green objects are Venus-transfected human NSCs. Middle, kymograph showing lysis by application of modified RIPA buffer to the top of the slide. Lysis occurs at 8–10 s after application, protein diffuses uniformly across the well on the ∼3 s timescale, and into the surrounding polyacrylamide / out of plane on the ∼10 s timescale. Note initial increase in GFP brightness upon lysis, perhaps due to release of molecular crowding, increase in buffer pH, or presence of SDS.

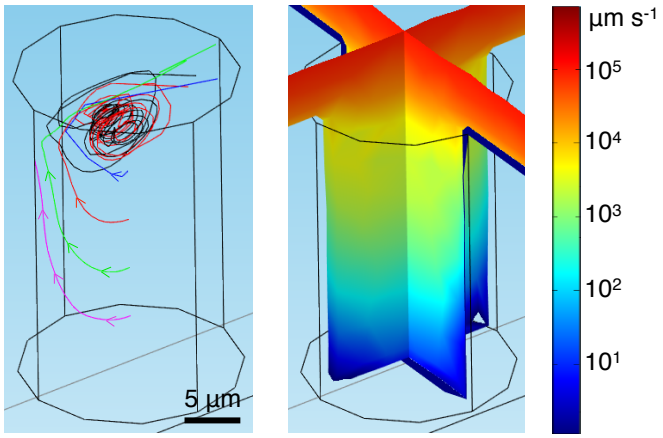

Figure 7.10: Fluid modeling of flow over microwells during cell lysis procedure reveals vortices buried within microwells. A COMSOL model of unidirectional, steady-state laminar flow during pouring of water over a 20 μm $\varnothing$ microwell in a 30 μm-thick PACTgel with a bulk fluid velocity of 0.5 ms^{-1} (an estimate for the maximum velocity experienced in the current system). Note the presence of a vortex in the well parallel to the bulk flow direction that is traced by streamlines representing the movement of massless, non-buoyant particles from starting locations at 0, 5, 10, 15, and 20 μm into the well. Flow boundary conditions on the well surfaces were "no slip". Modeling and data analysis performed by Zhuchen Xu.

complexity by e.g. enclosing the system in a suitable micropatterned gasket, we decided to accept the modest protein losses as a compromise with assay simplicity.

Given that cells can be effectively lysed after seeding in such a way that only marginal protein losses to the bulk are incurred even without an enclosed microdevice design, we studied the separation of Venus GFP after NSC lysis within the PACTgel microwells. Figure 7.11 shows typical separations data, tracking electrophoresis of GFP molecules against the lip of a microwell (achieving a mild stacking effect), prior to transfer of a circular band through the PACTgel matrix. A faint leading band is likely constituted by GFP molecules that had diffused from the well out of the separation plane during lysis, migrating in free solution upon application of electric field and not being subject to the sieving effect of the gel.

The sieved GFP band appears to show minimal dispersion by mechanisms other than diffusion, given the circularity of the band from shortly after stacking to the end of the separation step. Further, the band retains a reasonably compact spatial distribution, spreading from a diameter of roughly 35 μm shortly after stacking to 50 μm at the end of the separation approximately 10 s later. These measurements predict an effective diffusion coefficient under a dispersion model consisting of diffusion alone of $\sim 1.1 \times 10^{-11}$ m^2s^{-1}, which matches the

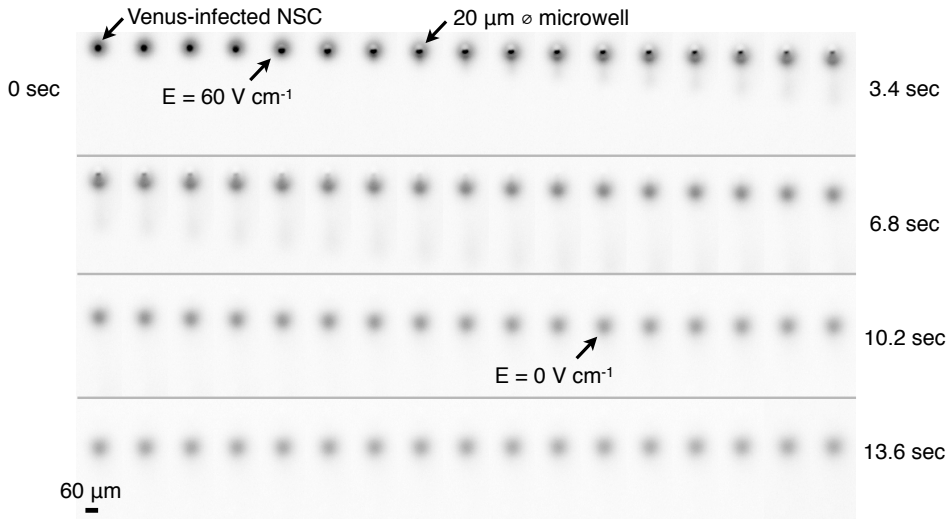

Figure 7.11: Kymograph of cell lysis and separation of contents in 8%T PACTgel at ∼60 V cm^{-1}. Note faint leading band, presumably constituting GFP that had diffused out of the device plane prior to application of field.

theoretical diffusion coefficient for GFP in an 8%T gel of $\sim 1.35 \times 10^{-11}$ m^{2}s^{-1} (see Appendix C) to within 20%.

Encouraged by our demonstrated ability to separate, capture, and probe purified protein analytes, and to lyse and separate proteins within cells, we integrated the capture and probing steps with the cell lysis and electrophoresis workflow. Figure 7.12 shows large-scale results of the simultaneous assay of NSCs infected with an EGFP vector under the control of a "Tet-off" promoter at high multiplicity of infection. Indeed, distinct EGFP and β-tubulin bands could be independently imaged at assay completion, indicating successful integration of all of the steps needed to constitute a single-cell immunoblotting assay. A subset of the devices were monitored in real time for EGFP fluorescence during the lysis, separation, and capture steps, and the repeatability of separation distances across the slide measured in Figure 7.7 ensured that parallel devices behaved in a similar manner to those directly observed.

To begin analysis and validation of the fluorescence data, we plotted the device-wise total fluorescence of β-tubulin bands and found a linear relationship between the average fluorescence and the number of cells per well previously counted from brightfield images taken prior to cell lysis (Figure 7.13). This correlation suggests linearity in the assay readout, as well as a rough scaling of β-tubulin levels with total amount of cell matter within the

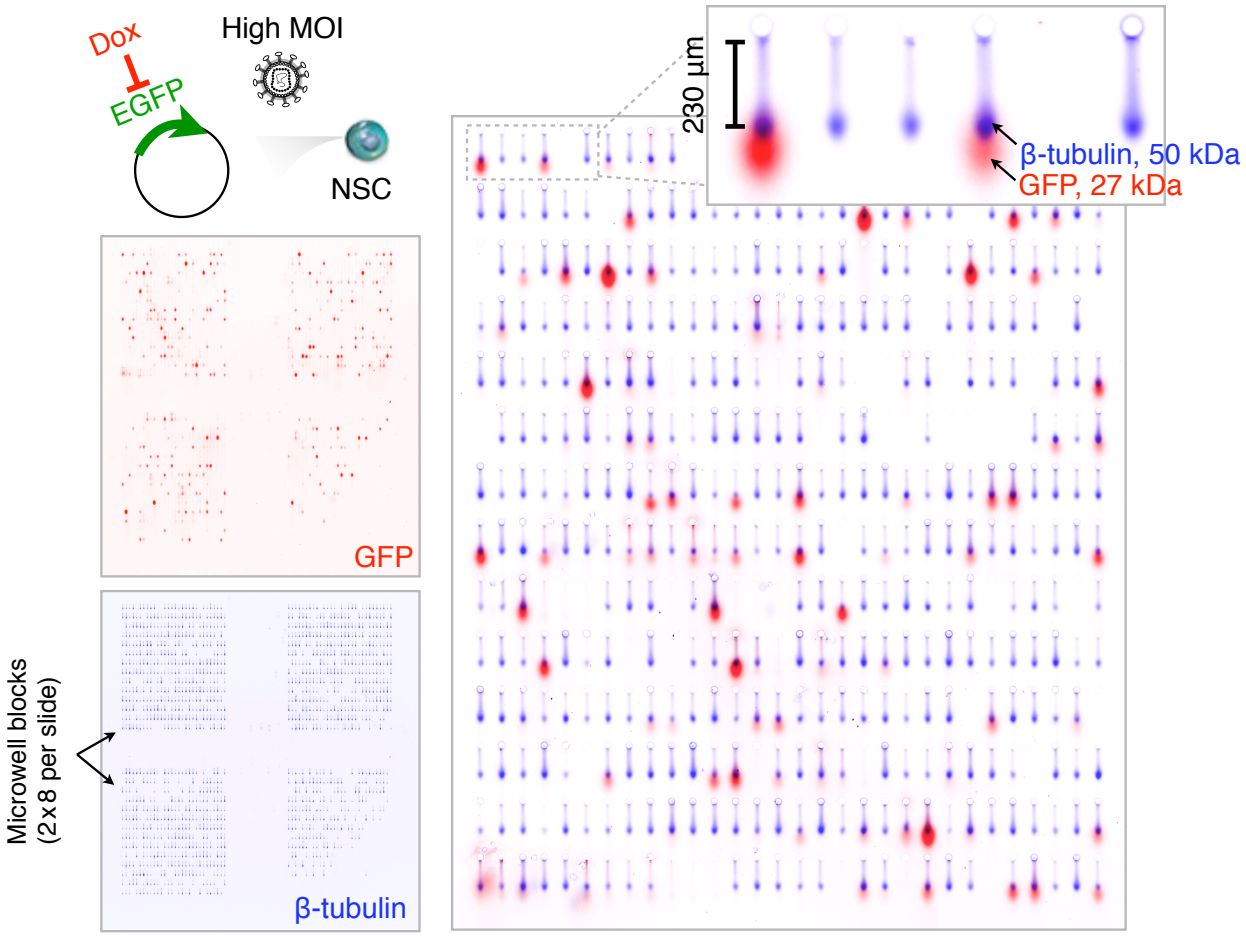

Figure 7.12: Large-scale integration of single cell separative immunoblotting demonstrated by a model system consisting of EGFP-expressing neural stem cells. Neural stem cells constitutively expressing EGFP were produced by retroviral infection using the Moloney murine leukemia virus (MMLV) vector CLPIT (containing a tetracycline-repressor element and a puromycin selection locus) at a multiplicity of infection (MOI) of 3 [230, 231]. High MOI infection produces a wide range in EGFP expression, determined by primary and fluorescently-labeled secondary antibody probing for GFP (red), in comparison to cell expression of (total) β-tubulin (blue), a common "loading control" protein in traditional western blotting.

wells. By design, the EGFP fluorescence readout stemming from the antibodies used to probe it shows a wide dynamic range, which was expected given the high-MOI infection process used to produce the EGFP-expressing NSCs. These data are currently being validated against flow cytometry to correlate the population-level dynamic range and distribution in cell fluorescence.

Given the partitioning of antibodies from the PACTgel matrix during probing, we tested various antibody dilution factors in the single cell assay in an effort to optimize the antibody usage per experiment. Figure 7.14 shows gains in specific β-tubulin signal in the same experiment as Figure 7.13 for dilution factors as small as 10×. Presently, blocks of 420 separations are typically incubated with 40 μl of antibody cocktail for both primary and secondary probing steps, meaning that antibody usage can be significant at up to 64 μl of undiluted antibody per slide of 16 device blocks, although on a per-separation basis, this usage corresponds to just 9.5 ng of antibody compared to $\sim$ 1000 ng per lane of a traditional western blot. In practice, primary and secondary antibody dilutions of 20–40× have been found to be sufficient for several analyte-antibody pairs (e.g. the signaling proteins anti-phospho MEK, anti-MEK, anti-phospho ERK, and ERK). Further innovation of the probing step, perhaps by enclosing the device using a suitable microfabricated gasket could further reduce per-assay antibody demands.

In order to determine the linear dynamic range and limit of detection of the single-cell immunoblot assay, we devised two methods to calibrate it using purified EGFP (Figure 7.15). The first method relies on direct measurement of EGFP concentrations in microwells immediately before separation, capture and probing, for wells incubated with a range in nominal concentrations of EGFP. The endpoint probe fluorescence is plotted on a curve against the number of EGFP molecules originally present in the corresponding microwell, inferred by calibrating the EGFP fluorescence measurements against those made in microchannels of the same depth as the thickness of the PACTgel sheet (30 μm). The second method does not require direct measurement of the EGFP present within the microwells, and instead uses large spot exposures to capture EGFP from free solution, where the gel concentration of EGFP is known from a microchannel-calibrated partition coefficient plot (Figure 7.16). The end result is a calibration curve of the fluorescent probe readout for EGFP against the number of EGFP molecules present within a spot roughly the size of that expected if the captured EGFP had originated from a microwell separation. Thus, lower concentrations of EGFP than can be directly observed by fluorescence can be used in the calibration curve, since the gel concentration is known from the nominal solution concentration and the partition coefficient.

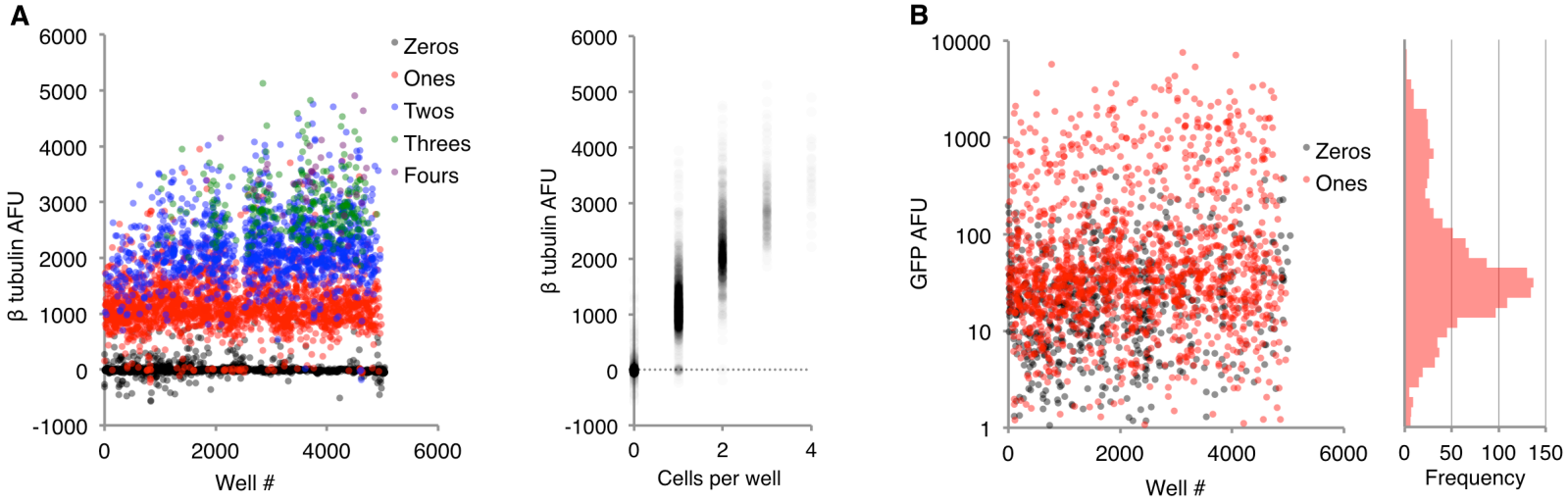

Figure 7.13: Quantitation of slide-wide loading control and EGFP fluorescence suggests quantitative capability in the single cell immunoblot assay. (A) Total fluorescence of β-tubulin bands across $\sim$5,000 separations on a single slide from the same experiment as Figure 7.12 delineated by manual count of cells-per-well. The total fluorescence scales roughly linearly with the number of cells originally in each individual well, indicating a quantitative capability in the β-tubulin concentration range explored. (B) Total EGFP probe fluorescence, here on a log scale, shows a roughly two order-of-magnitude range.

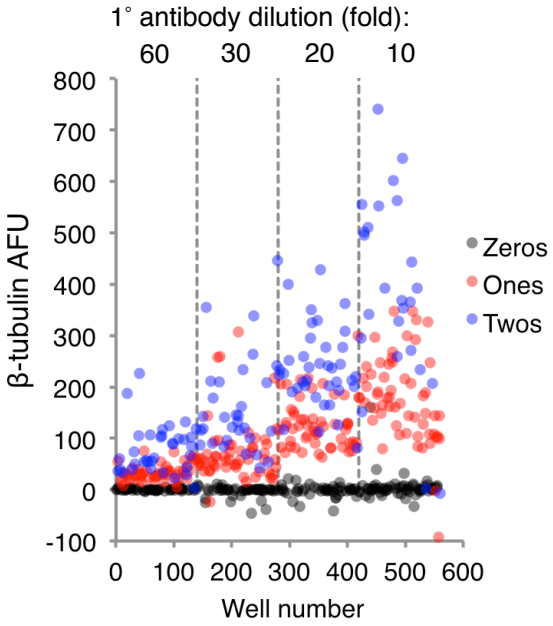

Figure 7.14: High antibody concentrations reap benefits in signal readout. Here, NSCs are analyzed for total β-tubulin at different primary antibody dilutions. Note the increased total fluorescence with decreasing antibody dilution for one and two cell-per-well devices in comparison to empty well-devices. The fluorescently labeled secondary antibody was at 10-fold dilution for all devices.

The results of these two calibration experiments overlap to a substantial degree (Figure 7.17), revealing linear dynamic ranges of up to two orders of magnitude from limits of detection that both fall within the 40,000–70,000 molecule range (0.07–0.11 attomol). A recent proteome-wide SILAC (stable isotope labeling by amino acids in cell culture) study of $\sim$ 5,300 protein in NIH3T3 mouse fibroblasts found a median protein copy number per cell of 50,000 [226], indicating that around 50% of the mammalian proteome is likely to be accessible using our single-cell immunoblotting technique, even without additional enzyme-amplified assay readout schemes.

Moving towards multiplexed measurements of differentiation and signaling markers in NSCs, we tested probed slides for the capability to chemically strip detection antibodies from them, allowing reprobing using additional sets of probes on the same slide. By incubating slides with a strongly denaturing buffer containing 2.5% SDS and 1% β-mercaptoethanol, we were able to achieve significant ($> 10\times$) reduction in the signal-to-noise ratio associated with the probe set to EGFP, and further, were able to reprobe the slide for EGFP to obtain a similar SNR to that achieved in the first probing round (Figures 7.17 and 7.18). This process was

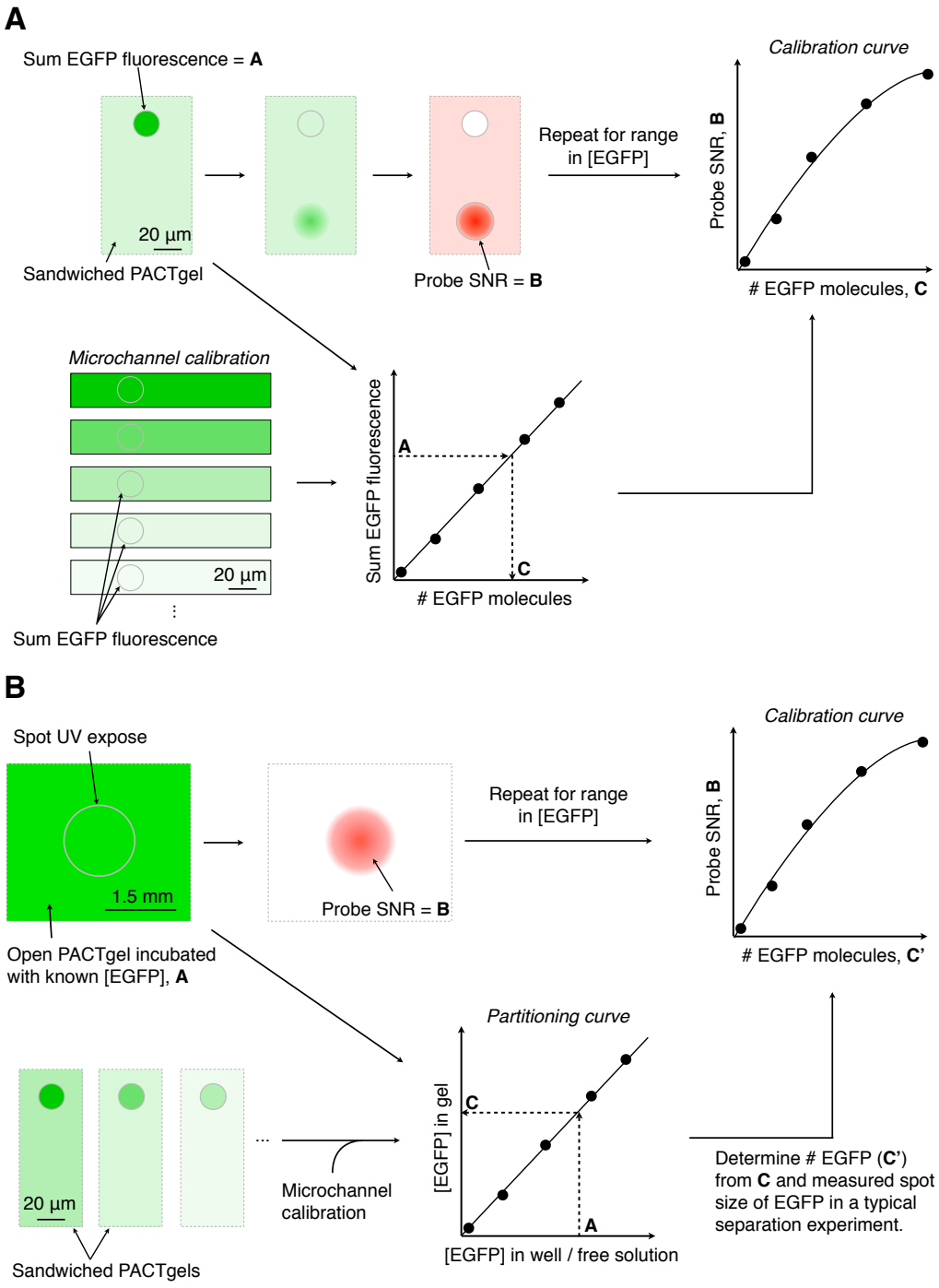

Figure 7.15: A sketch of two calibration methods used to determine dynamic range and limit of detection in the single-cell immunoblotting assay (see text). (A) Calibration by counting EGFP molecules in microwells prior to separation and capture. (B) Calibration by inferring number of EGFP molecules from a "partitioning curve" constructed in a separate experiment in which the microwell and gel EGFP concentrations are inferred from fluorescence values taken at equilibrium.

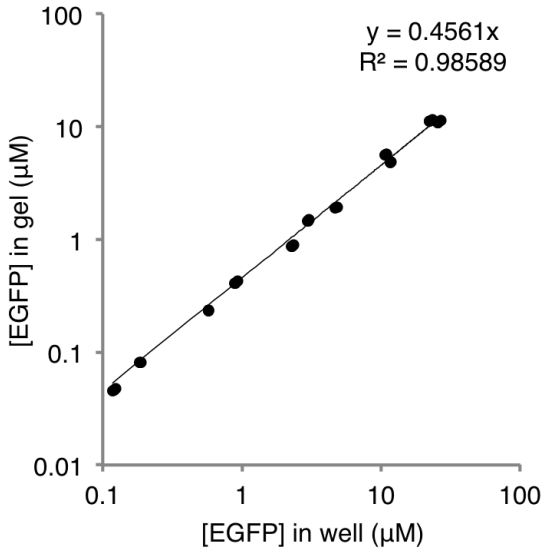

Figure 7.16: Determination of EGFP partition coefficient across a wide concentration range enables quantitative assay calibration. The concentrations of EGFP in microwells and in the surrounding gel matrix were inferred for a range in nominal EGFP concentration by calibrating the well and gel EGFP fluorescence values against equivalent values taken from microchannels containing known EGFP concentrations. The partition coefficient is the slope of this relationship (0.46). This parameter allows the gel concentration of EGFP to be inferred in calibration experiments in which the solution concentration above the gel is known (see Figure 7.17).

also found to be robust to extended (>1 month) storage of slides in a dry state — probed slides stored dry could be rehydrated, stripped, and reprobed at least 5 times without any apparent loss of immunoreactivity. We hypothesize that the loss of protein targets from the slide during stripping and wash steps (a common problem in standard western blotting) is negligible, providing that the covalent coupling between the PACTgel and protein analytes is stable under the stripping conditions. Further, the strongly denaturing conditions employed to remove antibodies from their targets are of no consequence to subsequent probing, since western blotting antibodies are typically optimized for immunoreactivity against denatured epitopes.

After validating sufficient linearity and sensitivity of the single-cell assay for the model analyte EGFP, we studied timecourse experiments of two varieties to track population-level changes in the expression of differentiation and signaling markers at single cell resolution.

In the first experiment, NSCs were subjected to a mixed differentiation protocol involving

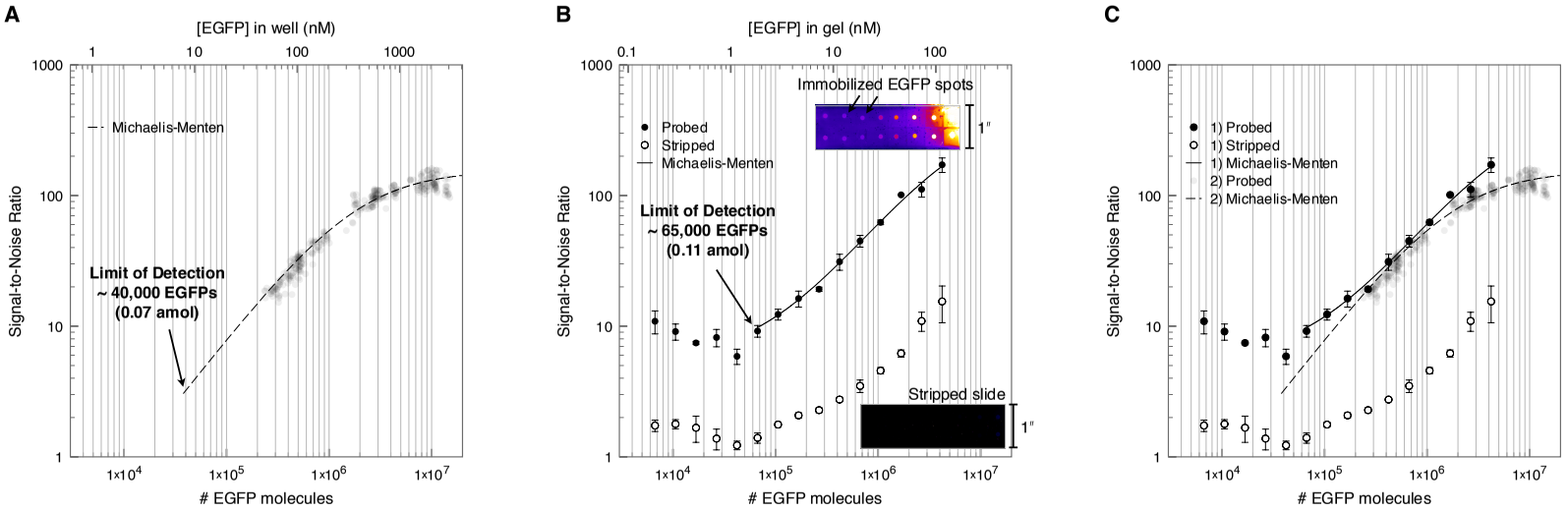

Figure 7.17: Calibration of single-cell immunoblotting assay reveals 10^4-10^5 molecule limits of detection, even without enzyme amplified assay readout. At left, original calibration data extracted from counting EGFP molecules in microwells prior to separation, capture, and probing (see Figure 7.15A). At middle, a calibration experiment that inferred the gel concentration of EGFP from the partition coefficient measurements in Figure 7.16 (see Figure 7.15B). This calibration curve extends into EGFP concentrations that cannot be imaged *a priori* with good SNR. Also shown is micrograph and calibration data for the slide before and after stripping with a "harsh" stripping buffer containing 2.5% SDS and 1% β-mercaptoethanol (see Appendix D and Figure 7.18 for details). At right, an overlay of the two calibration experiments, note good correspondence between the two despite quite different analytical routes.

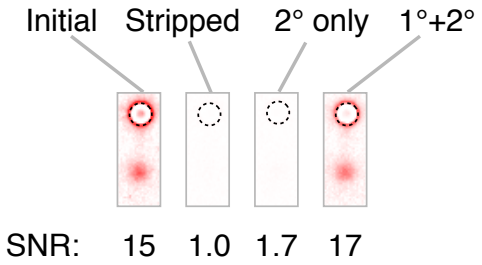

Figure 7.18: Single-cell immunoblotting slides can be effectively stripped and reprobed for additional captured analytes. The EGFP calibration slide from Figure 7.17A was imaged, stripped (see Appendix D) and reprobed with either a secondary antibody only (a negative control), or with a primary and fluorescently labeled secondary antibody to EGFP. The signal-to-noise ratio (SNR) of the reprobed slide approximately matches that of the original probing, while the negative control shows negligible specific signal.

the use of retinoic acid and fetal bovine serum to stimulate differentiation towards astrocytic and neuronal cell subpopulations. Total fluorescence of the undifferentiated cell markers nestin and sox2 were quantified for immunoblotting experiments conducted on 7 consecutive days under the mixed differentiation protocol (Figure 7.19). Both markers undergo pulses of expression at around day 3, the data for nestin tentatively matching population-level RT-PCR data [232].

In addition to the total fluorescence readout of the assay, it was also of interest to examine heterogeneity in the separation profiles of markers across cells assayed on the same day and on different days over the differentiation timecourse. The most visually apparent heterogeneity occurred in the nestin separation profiles, in which higher and a lower apparent molecular weight bands were observed that showed a striking distribution of relative intensities between cells on day 0. Plotting the ratio of the lower apparent MW band to the total nestin fluorescence shows a tailed distribution in the single cell data, as well as a correlation with the total nestin fluorescence signal (i.e. the lower MW band tends to be more highly represented for cells with high nestin levels). We hypothesize that this heterogeneity in the nestin separation profiles may stem from either the existence of alternatively spliced forms of nestin [233], or the interaction of nestin with especially vimentin in perhaps a cell-cycle dependent fashion, since one hypothesized role of nestin is to mediate disassembly of vimentin intermediate filaments by forming a heterodimer with it [234]. We are currently exploring the latter hypothesis by attempting to correlate vimentin and nestin separation profiles in the single cell immunoblot to test for the possibility of a measurable molecular interaction between the two.

Turning to the expression of the differentiation markers glial fibrillary acidic protein (GFAP,

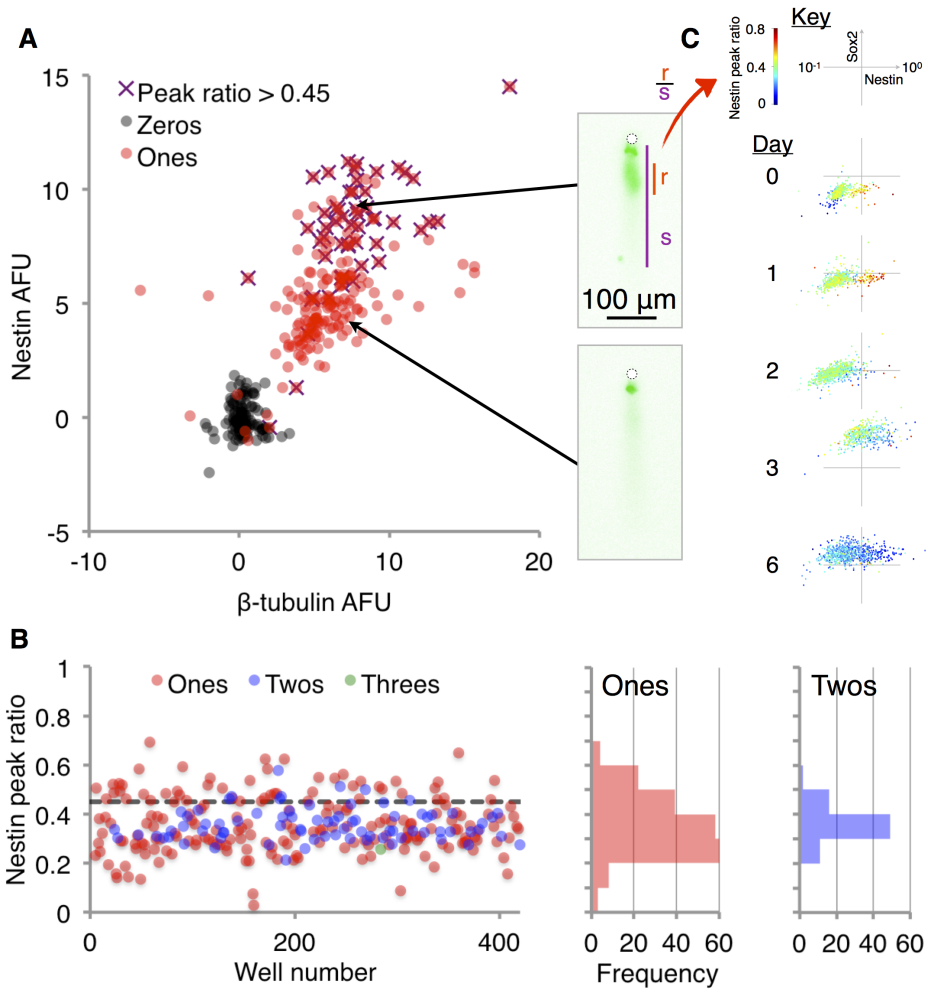

Figure 7.19: A ratio of low MW:high MW nestin peak intensities computed across a mixed differentiation time course spanning 6 days indicates changes in nestin heterogeneity. (A) Neural stem cells were subjected to mixed differentiation conditions *in vivo* using retinoic acid and fetal bovine serum (see [235] for a detailed protocol). The total probe signals across single cell devices for nestin and β-tubulin hints at the presence of two sub-populations. In parallel, single-cell separations show either the presence of a single higher-MW band, or the same band in addition to a lower MW band. (B) Plotting the ratio of the lower MW band fluorescence to the total nestin signal reveals a gaussian tailed towards higher peak ratio in the single-cell data. Even two-cell-per-well data shows an averaged profile that does not reveal this structure. Setting a threshold in the ratio at 0.45 delineates the visually apparent subpopulation in the nestin scatter data. The peak ratio can be plotted as a heat map over the total sox2 vs. nestin axis to show changes in the apparent separation heterogeneity over differentiation time.

astrocytes) and βIII-tubulin (neurons), we normalized each marker to the total GAPDH levels measured for single cell devices and plotted the two ratios against each other for each day of the differentiation experiment. While the expression of GFAP shows a strong increase at day 5–6 for approximately 15% of single cells assayed, βIII-tubulin shows only a mild pulse in expression at around day 2, and does not show a marked increase thereafter. These preliminary observations point to the fact that seeding of neurons into the PACTgel microwells may be dissuaded by the strong morphological changes in differentiated cells, particularly neurons. This potential bias is currently being validated by traditional western blotting, and by immunocytochemistry of cells settled into the microwell arrays.

Given the ability to measure target protein abundances and heterogeneity in migration distance of targets from cell to cell that perhaps provide quantitative information about protein-protein interactions or the presence of splicing variants, we decided to study short-timescale response of NSCs to environmental stimuli at the level of signal transduction within individual cells. NSCs were starved of FGF for 16 hours, seeded into 6 PACTgel slides, and incubated with media containing FGF at 20 mg ml^{-1}. This process stimulates a phosphorylation cascade upon ligation of the FGF receptor, which is expected to affect levels of phosphorylation of key signaling proteins in the downstream pathway including MEK, ERK, and AKT [230]. In preliminary experiments, the 6 slides were incubated with the FGF-supplemented media for 0, 5, 12, 20, 30, or 60 min and analyzed for phospho-ERK (Thr202/Tyr204), followed by successive stripping and reprobing steps to measure total ERK, phospho-MEK (Ser217/221), total MEK, and β-tubulin as a loading control for the same separations.

Indeed, the representation of phosphorylated ERK undergoes a strong increase over the stimulation timecourse peaking at the 12 min time point, with significant cell-to-cell variability in response (Figures 7.21 and 7.22). The importance of separating cell contents before measurement of phospho-ERK levels is emphasized by the fact that the phospho-specific ERK antibody probe exhibits some off-target probing when compared to the distinct localization of the total ERK band. In particular, a higher molecular weight band appears in the phospho-ERK data that does not overlay with total ERK fluorescence. This band may represent off-target probing, or perhaps probing of a complexed phospho-ERK form for which the C-terminal epitope of the total ERK monoclonal antibody (Cell Signaling #4695) is obstructed by a binding partner.

The phosphorylation of MEK shows a milder pulse leading the ERK pulse, and peaking at the 5–12 min time points, both expected from fact that MEK acts upstream of ERK in the FGF-response pathway within an amplifying "phosphorylation cascade" [236]. The localization of the MEK peak is not as punctate as that of ERK, perhaps due to its extensive known and hypothesized interactions with scaffold/anchor proteins such as KSR1 near the plasma membrane, and Sef1 on Golgi membranes [236, 237]. Nevertheless, the ability to

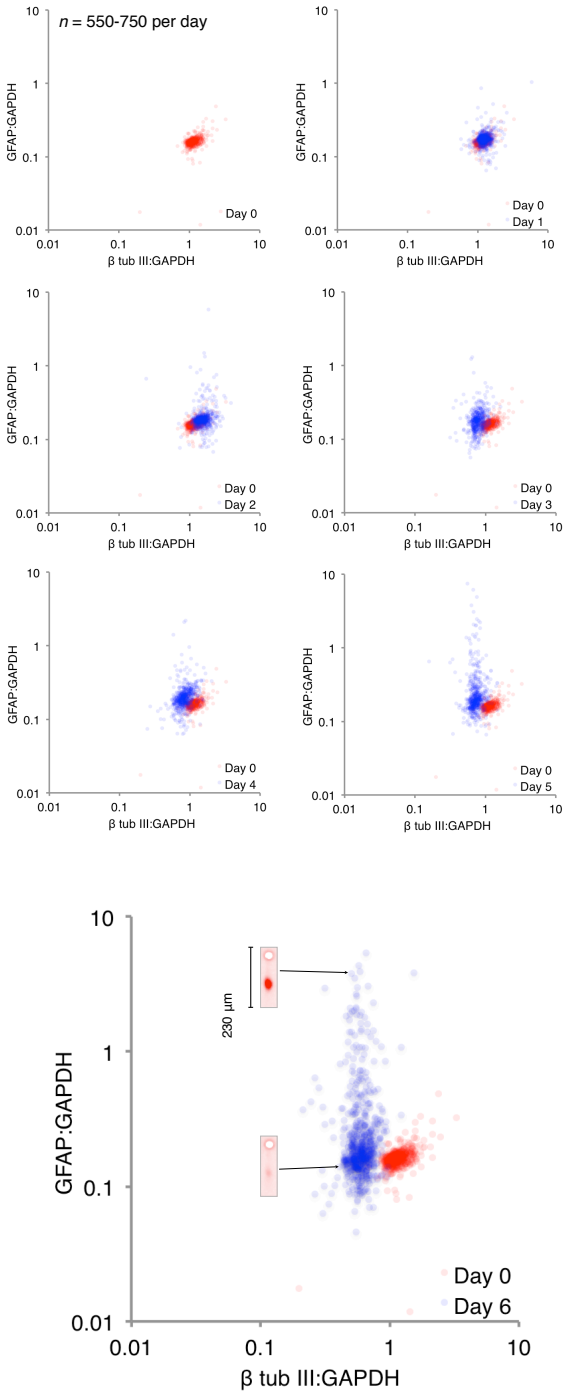

Figure 7.20: Preliminary mixed differentiation time course data for neural stem cells strongly indicates the presence of astrocytes, but not neurons. The astrocyte and neuronal markers, glial fibrillary acidic protein (GFAP) and βIII-tubulin, respectively, were probed in the same experiment as Figure 7.19. βIII-tubulin shows a small pulse in expression at day 2, but does not show the marked up regulation that GFAP does at day 5–6.

separate monomeric MEK from these hypothesized dimer/oligomer species and/or off-target probing of higher MW species allows the phosphorylation of only the monomeric MEK to be analyzed in isolation. These preliminary data are currently being validated by flow cytometry (which would be expected to be adversely affected by the presence of off-target probing that is not spatially resolved from specific immunoreactivity) and traditional western blotting to determine the correspondence of the magnitude and timecourse of ERK and MEK phosphorylation signatures in response to FGF stimulation.

7.2.3 Validation Efforts

As a proposed counterpart to current gold-standard and widely used protein quantitation assays such as immunocytochemistry and flow cytometry, the single cell assay requires thorough validation. We are currently validating total protein marker expression against flow cytometry and standard western blotting in conjunction with producing calibration curves for certain targets using purified proteins that have already given tentative confirmation of assay linearity. Quantitative PCR assays are expected to be a useful counterpart to these efforts, although the correlation between transcript and protein levels for a given target at the single cell level can be rather poor [226].

Validation of antibody specificity is a shared effort with other protein analysis tools, and requires negative control assays on cell lines not expressing the targets of interest, or on purified off-target proteins. In the case of neural stem cell markers such as nestin, sox2, GFAP, and βIII-tubulin, we are currently running antibodies to these targets on negative control cell types that we expect to have only basal expression, e.g. epithelial cell lineages.

Also of interest for validation purposes is the investigation of other cell types beyond neural stem cells, particularly those that do not readily form single cell suspensions. The results of the neural stem cell differentiation experiment described in Section 7.2.2 hint at the fact that differences in cell morphology in a heterogeneous cell population may bias seeding against cell subpopulations exhibiting extreme morphological features such as membrane projections. The extent of this possible challenge is currently being investigated by comparison of immunocytochemistry data from seeded cells and the originally suspended cell populations to unveil any such bias.

7.2.4 Future Opportunities for Single-Cell Immunoblotting Assays

A rich array of applications and improvements can be envisaged for single cell separative immunoblotting assays. Examples include:

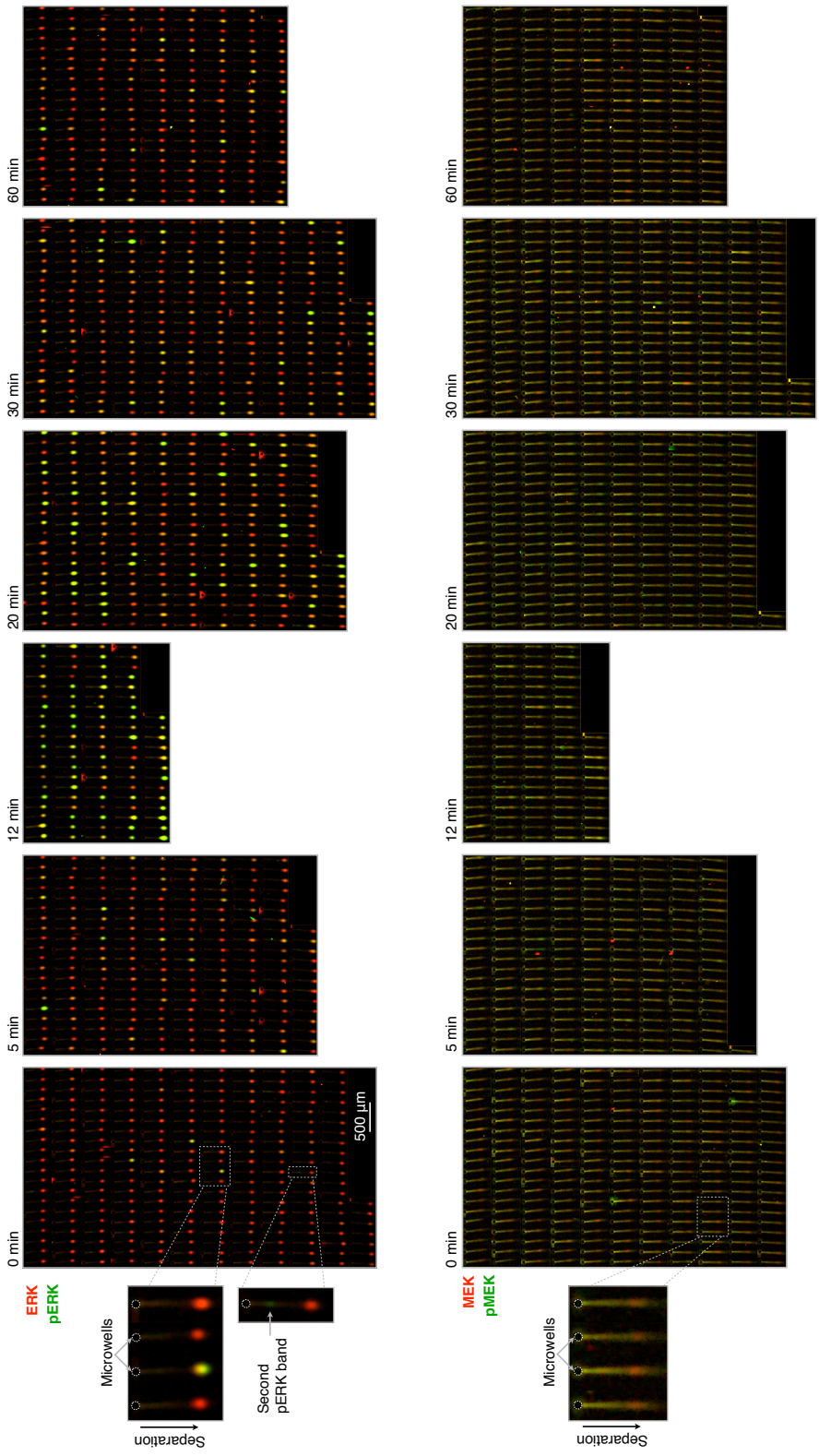

Figure 7.21: Summary fluorescence micrographs of all single-cell, "successful" devices (not affected by fluorescence artifacts caused by e.g. dust particles) for an experiment in which FGF-containing media was applied to FGF-starved NSCs seeded into the PACTgel microwells for the labeled exposure times prior to lysis, separation, capture, and immunoprobing of cell contents.

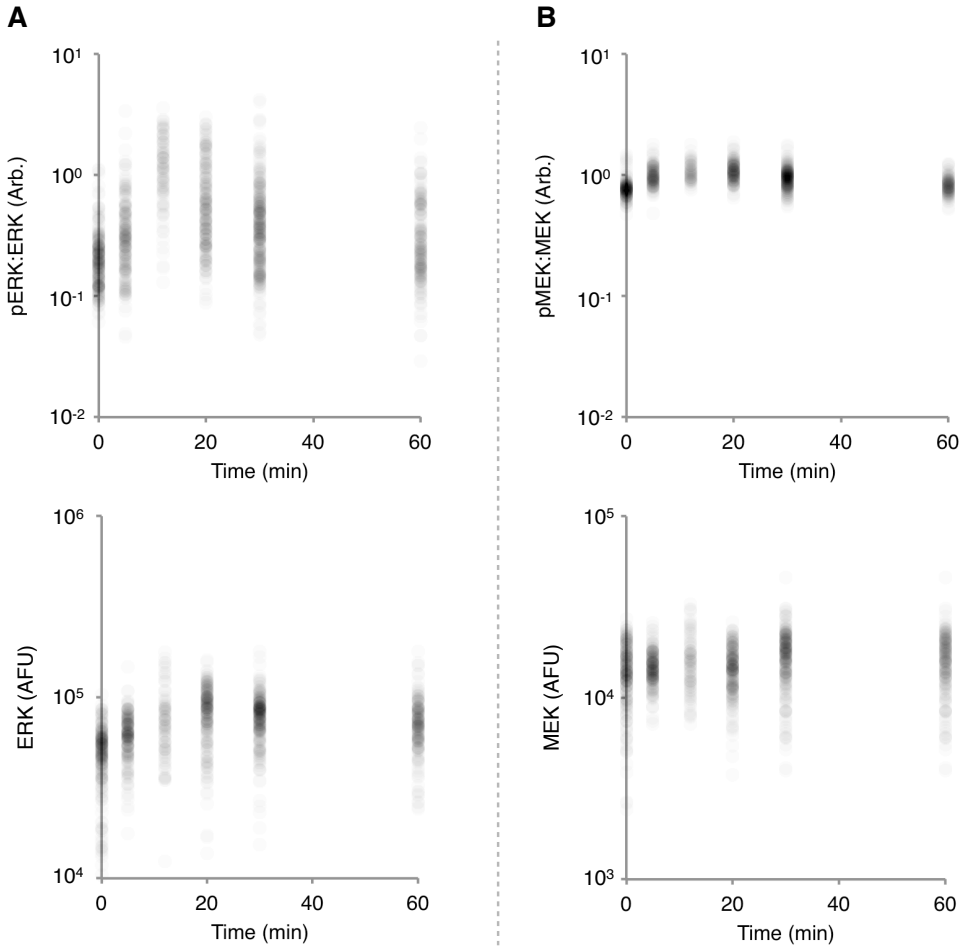

Figure 7.22: Dot plots of total fluorescence for phosphorylated and total monomeric ERK and MEK bands extracted from the single-cell separations in Figure 7.21. (A) The ratio of arbitrary fluorescence for phospho-ERK and total ERK (top) shows a ∼10-fold increase with a peak at the 12 min timepoint with considerable variation between cells, followed by a decline to approximately baseline levels over the 60 min stimulation period. The total ERK levels are approximately consistent across the set of six slides (bottom). (B) Similar data for MEK, which shows a peak in the representation of phosphorylated forms at 5–12 min, albeit with a maximum fold increase of ∼1.3. Statistical analysis of these data is currently underway.

- More effectively enclosing individual microwells during the lysis process to limit protein losses and enable the use of more dispersive sample treatments (e.g. full protein denaturation, reduction, and heating prior to separations).
- Improving separation resolution in conjunction with assay sensitivity (given the dominant tradeoff between the two), perhaps using enzyme-mediated amplification of analyte detection as is standard in e.g. ELISA and traditional western blotting.
- Linking cell seeding and culture to integrate upstream perturbation of cells for the analysis of microenvironmental influences on cell state (including the development of small molecule screens).
- Analysis of rare cell populations including cancer stem cells, likely in conjunction with upstream purification methods.
- Analysis of small cell populations from e.g. fine-needle aspirate biopsies to complement current histological detection strategies in cancer diagnostics.
- Investigation of protein-protein interactions with the introduction of controlled lysis conditions on a spectrum of dispersion strengths; separation conditions that preserve native protein-protein interactions while fully extracting proteins of interest from cell contents would allow predicted interactions to be teased apart by direct observation of the apparent molecular weights of protein complexes.
- Integration analysis pipelines for assaying enzyme activity (e.g. using activity-based probes [238]) or mapping post-translational modifications using lectin blotting or mass spectrometry.

These opportunities identify a broad range of future research objectives from basic biology to drug development to clinical diagnostics, driven by the designed accessibility of single-cell assays to a large audience of investigators.

Chapter 8

Conclusions & Future Directions

The various projects outlined in this thesis center around a key opportunity in microfluidics and the life sciences — to leverage the advantages of microscale design to achieve integrated, automated proteomic assays that offer new analytical capabilities and reduce the time and resource consumption associated with existing ones.

The challenge for the engineer in the context of tackling limitations in current biological inquiry is to develop a deep understanding of the *process* of this inquiry. Whether through the literature, or through direct hands-on experience, or through day-by-day interaction and tailoring of engineered systems for the needs of collaborators; to be successful in the business of developing tools is to strive for a knowledge base that spans academic disciplines, primarily for the purpose of achieving relevance. The notion of engineering for the sake of developing toy systems with limited potential for penetration into the broader life sciences community is a bygone one, and the engineers that temper their materials and transport-centered views of the physical world with the understanding of flux, chemical and biological stability, and individuality of life in the context of the biological cell, are the ones that succeed.

To do this is to face the challenges of the rigor with which life scientists achieve certainty in the face of such inherent variability. Studies of biological relevance rely upon incremental advances that are tightly controlled and validated. This area is where I have grown most as a researcher, to develop not only methods for measuring protein levels, modifications, interconversion and interactions, but also methods to quantify and verify them. Quantitation is as much an art as the original engineering contribution, and requires a keen sense of calibration. How do we put standard units to arbitrary ones?

Chapter 2 dealt with using polyacrylamide gradient gels to tightly control the separation and confinement of enzymes within straight microfluidic channels to enable quantitative assays with fluorogenic substrates. Further innovations around the spatial control over target protein distribution after analytical separations by weight and size open paths towards the miniaturization of workhorse immunoblotting techniques for biophysical, clinical and broader life science applications in Chapters 3–7.

Looking forward, several of the tools developed in this thesis are the focus of ongoing development to extend them towards new biological applications. In particular, the quantitation of PSA isoforms spearheaded in Chapter 3 could be readily extended to a clinical study of patient-to-patient variability in serum levels of PSA isoforms to potentially extend the diagnostic efficacy of existing PSA assays. So too for the proof-of-concept HIV diagnostic developed in Chapter 6, which would require a larger patient data set to determine clinical performance specifications such as population-wide sensitivity and specificity. The novel GFP isoelectric photoswitching phenomenon discovered and characterized in Chapter 5 could be exploited for a range of exciting purposes, including light-actuated transitions in zeta potential, hydrophilicity/wetting behavior, or adhesion properties; particularly if the phenomenon can be verified and amplified using high-throughput screening for rational or

directed tuning of photoactivatable protein phenomena.

I anticipate that my work in the development of the single-cell western blotting tool laid out in Chapter 7 will be most suited to ongoing research. The power of this technique to separate and quantitatively analyze protein constituents from single cells may put it on equal footing with well-established proteomic tools such as protein microarrays, immunocytochemistry, and flow cytometry. The "fingerprinting" appeal of western blotting in terms of sieving away non-specific probing signal and providing molecular weight information as reassurance of assay specificity are crucial contributions that make this technique complementary to the "gold standard" ones listed. The general applicability of this technique to many cell types and targets opens up a range of possibilities in the study of heterogeneity of rare cells (e.g. circulating tumor cells), cell differentiation and development processes, and signal transduction. Many efforts are already underway within the Herr lab to expand the utility and automation of the process, including exploration of on-slide culturing, selective lysis and analysis of particular cell organelles, optimization of lysis/separation buffer conditions to fully support quantitation of protein-protein interactions, and integration of the slide arrays with robotic liquid handling and a more diverse set of analytical readout chemistries to improve throughput and limits of detection.

My vision as a researcher is to transcend limitations in biological inquiry through the design of integrated, engineered tools that make use of novel physical principles in materials and transport. The current state of proteomics research is hampered by a severe tradeoff between analytical capability (mainly throughput) and accessibility of research tools. Western blotting and immunocytochemistry, for example, are highly accessible and have permeated the life sciences, yet suffer from poor throughput. On the other hand, tools that excel at throughput or analytical capability, such as flow cytometry and mass spectrometry, have high barriers to adoption in terms of cost and expertise. Many sets of questions revolve around collecting and interpreting the multi-dimensional data sets that define individual biological units — calling for the ability to rapidly screen or quantify responses of e.g. single cells to pathogens, drugs, or microenvironmental cues.

I intend to pursue the grand challenges in clinical and basic science realms that center around understanding of the individual (molecule, cell) without losing the context of the collective (metabolic pathway, organism) using quantitative analytical approaches that are better at negotiating the tradeoff between capability and adoption. Areas of particular interest include the interaction of the environment with the organization of living functional units over generational time — namely the evolution of cooperation and the hierarchy of biological complexity. The field of evolutionary biology is at the forefront of efforts to understand how order arises from selfish individual units, and this question presents strong analytical needs that integrate measurements across spatial and organizational scales.

Bibliography

1. Mark D, Haeberle S, Roth G, von Stetten F, Zengerle R (2010) Microfluidic lab-on-a-chip platforms: Requirements, characteristics and applications. Chem Soc Rev 39: 1153–1182.

2. Squires T, Quake S (2005) Microfluidics: Fluid physics at the nanoliter scale. Rev Mod Phys 77: 977–1026.

3. Thorsen T, Maerkl S, Quake S (2002) Microfluidic large-scale integration. Science 298: 580–584.

4. Martinez A, Phillips S, Whitesides G (2008) Three-dimensional microfluidic devices fabricated in layered paper and tape. Proc Natl Acad Sci USA 105: 19606–19611.

5. Ciaccio M, Wagner J, Chuu C, Lauffenburger D, Jones R (2010) Systems analysis of egf receptor signaling dynamics with microwestern arrays. Nat Methods 7: 148–155.

6. Hughes A, Lin R, Peehl D, Herr A (2012) Microfluidic integration for automated targeted proteomic assays. Proc Natl Acad Sci USA 109: 5972–5977.

7. Righetti P (1983) Isoelectric Focusing: Theory, Methodology and Applications, volume 11 of *Laboratory Techniques in Biochemistry and Molecular Biology*. New York: Elsevier.

8. Rilbe H (1973) Historical and theoretical aspects of isoelectric focusing. Ann NY Acad Sci 209: 11–22.

9. Righetti P (2006) The alpher, bethe, gamow of isoelectric focusing, the alpha-centaury of electrokinetic methodologies. Part I. Electrophoresis 27: 923–938.

10. Righetti P (1984) Isoelectric focusing in immobilized ph gradients. J Chromatogr 300: 165–223.

11. Righetti P (2007) The alpher, bethe, and gamow of ief, the alpha-centaury of electrokinetic methodologies. Part II: Immobilized pH gradients. Electrophoresis 28: 545–555.

12. Sommer G, Singh A, Hatch A (2008) On-chip isoelectric focusing using photopolymerized immobilized pH gradients. Anal Chem 80: 3327–3333.

13. Herr A, Molho J, Drouvalakis K, Mikkelsen J, Utz P, et al. (2003) On-chip coupling of isoelectric focusing and free solution electrophoresis for multidimensional separations. Anal Chem 75: 1180–1187.

14. Han J, Singh A (2004) Rapid protein separations in ultra-short microchannels: Microchip sodium dodecyl sulfate-polyacrylamide gel electrophoresis and isoelectric focusing. J Chromatogr A 1049: 205–209.

15. Svensson H (1961) Isoelectric fractionation, analysis, and characterization of ampholytes in natural pH gradients. I. The differential equation of solute concentrations at a steady state and its solution for simple cases. Acta Chem Scand 15: 325–341.

16. Cossu G, Righetti P (1987) Resolution of G_γ and A_γ foetal haemoglobin tetramers in immobilized pH gradients. J Chromatogr 398: 211–216.

17. Probstein R (2005) Physicochemical Hydrodynamics: An Introduction. New York: Wiley, 2nd edition.

18. Bischoff K, Shi L, Kennelly P (1998) The detection of enzyme activity following sodium dodecyl-sulfate polyacrylamide gel electrophoresis. Anal Biochem 260: 1–17.

19. Kohlrausch F (1897) Ueber concentrations-verschiebungen durch electrolyse im innern von lösungen und lösungsgemischen. Ann Physik 62: 209.

20. Ornstein L (1964) Disc electrophoresis — I Background and theory. Ann NY Acad Sci 121: 321–349.

21. Laemmli U (1970) Cleavage of structural proteins during the assembly of the head of bacteriophage T4. Nature 227: 680–685.

22. Ferguson K (1964) Starch-gel electrophoresis — Application to the classification of pituitary proteins and polypeptides. Metabolism 13: 985–1002.

23. Herr A, Singh A (2004) Photopolymerized cross-linked polyacrylamide gels for on-chip protein sizing. Anal Chem 76: 4727–4733.

24. Goldstein L (1976) Kinetic behavior of immobilized enzyme systems. Methods Enzymol 44: 397–443.

25. Squires T, Messinger R, Manalis S (2008) Making it stick: Convection, reaction and diffusion in surface-based biosensors. Nat Biotechnol 26: 417–426.

26. Kerby M, Legge R, Tripathi A (2006) Measurements of kinetic parameters in a microfluidic reactor. Anal Chem 78: 8273–8280.

27. Tong J, Anderson J (1996) Partitioning and diffusion of proteins and linear polymers in polyacrylamide gels. Biophys J 70: 1505–1513.

28. Hermanson G (2008) Bioconjugate Techniques. New York: Academic Press, 2nd edition.

29. Logan T, Clark D, Stachowiak T, Svec F, Frechet J (2007) Photopatterning enzymes on polymer monoliths in microfluidic devices for steady-state kinetic analysis and spatially separated multi-enzyme reactions. Anal Chem 79: 6592–6598.

30. Heilmann S, Rasmussen J, Krepski L (2001) Chemistry and technology of 2-alkenyl azlactones. J Polym Sci Part A: Polym Chem 39: 3655–3677.

31. Andersson L, Borg H, Mikaelsson M (1972) Molecular weight estimations of proteins by electrophoresis in polyacrylamide gels of graded porosity. FEBS Lett 20: 199–202.

32. Sommer G, Singh A, Hatch A (2009) Enrichment and fractionation of proteins via microscale pore limit electrophoresis. Lab Chip 9: 2729–2737.

33. Slater G (1969) Stable pattern formation and determination of molecular size by pore-limit electrophoresis. Anal Chem 41: 1039–1041.

34. Margolis J, Kenrick K (1967) Polyacrylamide gel-electrophoresis across a molecular sieve gradient. Nature 214: 1334–1336.

35. Margolis J, Kenrick K (1968) Polyacrylamide gel electrophoresis in a continuous molecular sieve gradient. Anal Biochem 25: 347–362.

36. Shim J, Dutta P, Ivory C (2007) Modeling and simulation of IEF in 2-D microgeometries. Electrophoresis 28: 572–586.

37. Chou Y, Yang R (2010) Numerical solutions for isoelectric focusing and isotachophoresis. J Chromatogr A 1217: 394–404.

38. Weiss G, Catsimpoolas N, Rodbard D (1974) Transient state isoelectric focusing: Theory. Arch Biochem Biophys 163: 106–112.

39. Bharadwaj R, Park C, Kazakova I, Xu H, Paschkewitz J (2008) Analysis and optimization of nonequilibrium capillary electrophoresis of α-fetoprotein isoforms. Anal Chem 80: 129–134.

40. Bayley H (1983) Reagents for photoaffinity labeling. In: Work T, Burdon R, editors, Laboratory Techniques in Biochemistry and Molecular Biology, Elsevier, New York, volume 12. pp. 25–65.

41. Dorman G, Prestwich G (1994) Benzophenone photophores in biochemistry. Biochemistry 33: 5661–5673.

42. Stachowiak T, Svec F, Frechét J (2006) Patternable protein resistant surfaces for multifunctional microfluidic devices via surface hydrophilization of porous polymer monoliths using photografting. Chem Mater 18: 5950–5957.

43. Schneider M, Tran Y, Tabeling P (2011) Benzophenone absorption and diffusion in poly(dimethylsiloxane) and its role in graft photo-polymerization for surface modification. Langmuir 27: 1232–1240.

44. Hu S, Ren X, Bachman M, Sims C, Li G, et al. (2004) Surface-directed, graft polymerization within microfluidic channels. Anal Chem 76: 1865–1870.

45. Dorman G, Prestwich G (2000) Using photolabile ligands in drug discovery and development. Trends Biotechnol 18: 64–77.

46. Gilbert A, Baggott J (1991) Essentials of Molecular Photochemistry. Cambridge, MA: Blackwell.

47. O'Neill R, Bhamidipati A, Bi X, Deb-Basu D, Cahill L, et al. (2006) Isoelectric focusing technology quantifies protein signaling in 25 cells. Proc Natl Acad Sci USA 103: 16153–16158.

48. Hayes D, Mellor G (2002) In: Eisenthal R, Danson M, editors, Enzyme Assays, Oxford: Oxford University Press. 2nd edition, pp. 235–247.

49. Arnold F (2001) Combinatorial and computational challenges for biocatalyst design. Nature 409: 253–257.

50. Luetz S, Giver L, Lalonde J (2008) Engineered enzymes for chemical production. Biotechnol Bioeng 101: 647–653.

51. Trull A, Demers L, Holt D, Johnston A, Tredger J, et al. (2002) Biomarkers of Disease: An Evidence-Based Approach. New York: Cambridge University Press.

52. Pei J, Dishinger J, Roman D, Rungwanitcha C, Neubig R, et al. (2008) Microfabricated channel array electrophoresis for characterization and screening of enzymes using RGS-G protein interactions as a model system. Anal Chem 80: 5225–5231.

53. Burke B, Regnier F (2003) Stopped-flow enzyme assays on a chip using a microfabricated mixer. Anal Chem 75: 1786–1791.

54. Bao J, Regnier F (1992) Ultramicro enzyme assays in a capillary electrophoretic system. J Chromatogr 608: 217–224.

55. Hadd A, Raymond D, Halliwell J, Jacobson S, Ramsey J (1997) Microchip device for performing enzyme assays. Anal Chem 69: 3407–3412.

56. Gleason N, Carbeck J (2004) Measurement of enzyme kinetics using microscale steady-state kinetic analysis. Langmuir 20: 6374–6381.

57. Kerby M, Chien R (2001) A fluorogenic assay using pressure-driven flow on a microchip. Electrophoresis 22: 3916–3923.

58. He P, Greenway G, Haswell S (2009) Development of enzyme immobilized monolith micro-reactors integrated with microfluidic electrochemical cell for the evaluation of enzyme kinetics. Microfluid Nanofluid .

59. Koh W, Pishko M (2005) Immobilization of multi-enzyme microreactors inside microfluidic devices. Sens Actuat B 106: 335–342.

60. Heo J, Crooks R (2005) Microfluidic biosensor based on an array of hydrogel-entrapped enzymes. Anal Chem 77: 6843–6851.

61. Lee J, Song Y, Tannenbaum S, Han J (2008) Increase of reaction rate and sensitivity of low-abundance enzyme assay using micro/nanofluidic preconcentration chip. Anal Chem 80: 3198–3204.

62. Lee J, Cosgrove B, Lauffenburger D, Han J (2009) Microfluidic concentration-enhanced cellular kinase activity assay. J Am Chem Soc 131: 10340–10341.

63. Miller E, Wheeler A (2008) A digital microfluidic approach to homogeneous enzyme assays. Anal Chem 80: 1614–1619.

64. Seong G, Heo J, Crooks R (2003) Measurement of enzyme kinetics using a continuous-flow microfluidic system. Anal Chem 75: 3161–3167.

65. Mao H, Yang T, Cremer P (2002) Design and characterization of immobilized enzymes in microfluidic systems. Anal Chem 74: 379–385.

66. DeLouise L, Miller B (2005) Enzyme immobilization in porous silicon: Quantitative analysis of the kinetic parameters for glutathione-S-transferases. Anal Chem 77: 1950–1956.

67. Trevan M (1980) Immobilized Enzymes: An Introduction and Applications in Biotechnology. New York: John Wiley and Sons.

68. Hinberg I, Korus R, O'Driscoll K (1974) Gel entrapped enzymes: Kinetic studies of immobilized β-Galactosidase. Biotechnol Bioeng 16: 943–963.

69. O'Driscoll K, Hinberg I, Korus R, Kapoulas A (1974) Kinetic behavior of gel entrapped enzymes. J Polymer Sci 46: 227–235.

70. Sundaram P, Tweedale A, Laidler K (1970) Kinetic laws for solid-supported enzymes. Can J Chemistry 48: 1498–1504.

71. Zimmermann S, Fienbork D, Flounders A, Liepmann D (2004) In-device enzyme immobilization: Wafer-level fabrication of an integrated glucose sensor. Sens Actuat B 99: 163–173.

72. Zhan W, Seong G, Crooks R (2002) Hydrogel-based microreactors as a functional component of microfluidic systems. Anal Chem 74: 4647–4652.

73. Kim Y, Park C, Clark D (2001) Stable sol-gel microstructured and microfluidic networks for protein patterning. Biotechnol Bioeng 73: 331–337.

74. Sakai-Kato K, Kato M, Toyo'oka T (2003) Creation of an on-chip enzyme reactor by encapsulating trypsin in sol-gel on a plastic microchip. Anal Chem 75: 388–393.

75. Manchenko G (2003) Handbook of Detection of Enzymes on Electrophoretic Gels. New York: CRC Press, 2nd edition.

76. Hughes A, Herr A (2010) Quantitative enzyme activity determination with zeptomole sensitivity by microfluidic gradient-gel zymography. Anal Chem 82: 3803–3811.

77. Fuxman A, McAuley K, Schreiner L (2005) Modeling of polyacrylamide gel dosimeters with spatially non-uniform radiation dose distributions. Chem Eng Sci 60: 1277–1293.

78. Hou C, Herr A (2010) Ultrashort separation length homogeneous electrophoretic immunoassays using on-chip discontinuous polyacrylamide gels. Anal Chem 82: 3343–3351.

79. Hatch A, Herr A, Throckmorton D, Brennan J, Singh A (2006) Integrated preconcentration SDS-PAGE of proteins in microchips using photopatterned cross-linked polyacrylamide gels. Anal Chem 78: 4976–4984.

80. Hattori S, Fujisaki H, Kiriyama T, Yokoyama T, Irie S (2002) Real-time zymography and reverse zymography: A method for detecting activities of matrix metalloproteinases and their inhibitors using FITC-labeled collagen and casein as substrates. Anal Biochem 301: 27–34.

81. Kaberdin V, McDowall K (2003) Expanding the use of zymography by the chemical linkage of small, defined substrates to the gel matrix. Genome Res 13: 1961–1965.

82. Otsuka K, Terabe S (1998) Micellar electrokinetic chromatography. Mol Biotechnol 9: 253–271.

83. Loustau M, Romero L, Levin G, Magri M, Lopez M, et al. (2008) Expression and purification of horseradish peroxidase in insect larvae. Process Biochem 43: 103–107.

84. Kuhtreiber W, Serras F, van den Biggelaar J (1987) Spreading of microinjected horseradish peroxidase to nondescendant cells in embryos of *patella* (mollusca, gastropoda). Development 100: 713–722.

85. Savitsky A, Golay M (1964) Smoothing and differentiation of data by simplified least squares procedure. Anal Chem 36: 1627–1639.

86. Brenner H (1962) The diffusion model of longitudinal mixing in beds of finite length. Numerical values. Chem Eng Sci 17: 229–243.

87. Vaidya D, Nitsche J, Diamond S, Kofke D (1996) Convection-diffusion of solutes in dynamic media. Adsorption 3: 41–54.

88. Fernley H (1971) In: Boyer P, editor, The Enzymes, New York: Academic Press, volume 4. 3rd edition, pp. 417–447.

89. Chappelet-Tordo D, Fosset M, Iwatsubo M, Gache C, Lazdunski M (1974) Intestinal alkaline phosphatase. Catalytic properties and half of the sites reactivity. Biochemistry 13: 1788–1795.

90. Fernley H, Walker P (1965) Kinetic behaviour of calf-intestinal alkaline phosphatase with 4-methylumbelliferyl phosphate. Biochem J 97: 95–103.

91. Wu D, Regnier F (1993) Native protein separations and enzyme microassays by capillary zone and gel electrophoresis. Anal Chem 65: 2029–2035.

92. Craig D, Arriaga E, Wong J, Lu H, Dovichi N (1996) Studies on single alkaline phosphatase molecules: Reaction rate and activation energy of a reaction catalyzed by a single molecule and the effect of thermal denaturation — The death of an enzyme. J Am Chem Soc 118: 5245–5253.

93. Durchschlag H, Christl P, Jaenicke R (1991) Comparative determination of the particle weight of glycoproteins by SDS-PAGE and analytical ultracentrifugation. Progr Colloid Polym Sci 86: 41–56.

94. Cornish-Bowden A (2002) In: Eisenthal R, Danson M, editors, Enzyme Assays, Oxford: Oxford University Press. 2 edition, pp. 249–268.

95. Patterson S (1994) From electrophoretically separated protein to identification: Strategies for sequence and mass analysis. Anal Biochem 221: 1–15.

96. He M, Herr A (2009) Microfluidic polyacrylamide gel electrophoresis with *in situ* immunoblotting for native protein analysis. Anal Chem 81: 8177–8184.

97. Brennan D, O'Connor D, Rexhepaj E, Ponten F, Gallagher W (2010) Antibody-based proteomics: Fast-tracking molecular diagnostics in oncology. Nat Rev Cancer 10: 605–617.

98. Rifai N, Gillette M, Carr S (2006) Protein biomarker discovery and validation: The long and uncertain path to clinical utility. Nat Biotechnol 24: 971–983.

99. Zhu C, Pinsky P, Cramer D, Ransohoff D, Hartge P, et al. (2011) A framework for evaluating biomarkers for early detection: Validation of biomarker panels for ovarian cancer. Cancer Prev Res 4: 375–383.

100. Esserman L, Shieh Y, Thompson I (2009) Rethinking screening for breast cancer and prostate cancer. JAMA 302: 1685–1692.

101. Etzioni R, Urban N, Ramsey S, McIntosh M, Schwartz S, et al. (2003) The case for early detection. Nat Rev Cancer 3: 243–252.

102. Jung K, Reiche J, Boehme A, Stephan C, Loening S, et al. (2004) Analysis of subforms of free prostate-specific antigen in serum by two-dimensional gel electrophoresis: Potential to improve diagnosis of prostate cancer. Clin Chem 50: 2292–2301.

103. Sarrats A, Comet J, Tabares G, Ramirez M, Aleixandre R, et al. (2010) Differential percentage of serum prostate-specific antigen subforms suggests a new way to improve prostate cancer diagnosis. The Prostate 70: 1–9.

104. Tabares G, Radcliffe C, Barrabes S, Ramirez M, Aleixandre R, et al. (2006) Different glycan structures in prostate-specific antigen from prostate cancer sera in relation to seminal plasma PSA. Glycobiology 16: 132–145.

105. Kyselova Z, Mechref Y, Al Bataineh M, Dobrolecki L, Hickey R, et al. (2007) Alterations in the serum glycome due to metastatic prostate cancer. J Proteome Res 6: 1822–1832.

106. Gaster R, Hall D, Nielsen C, Osterfeld S, Yu H, et al. (2009) Matrix-insensitive protein assays push the limits of biosensors in medicine. Nat Med 15: 1327–1333.

107. Rissin D, Kan C, Campbell T, Howes S, Fournier D, et al. (2010) Single-molecule enzyme-linked immunosorbent assay detects serum proteins at subfemtomolar concentrations. Nat Biotechnol 28: 595–600.

108. Vickers A, Cronin A, Aus G, Pihl C, Becker C, et al. (2008) A panel of kallikrein markers can reduce unnecessary biopsy for prostate cancer: Data from the european randomized study of prostate cancer screening in Göteborg, Sweden. BMC Med 6: 19.

109. Zolg W (2006) The proteomic search for diagnostic biomarkers: lost in translation? Mol Cell Proteomics 5: 1720–1726.

110. He M, Herr A (2010) Polyacrylamide gel photopatterning enables automated protein immunoblotting in a two-dimensional microdevice. J Am Chem Soc 132: 2512–2513.

111. Anderson G, Cipolla C, Kennedy R (2011) Western blotting using capillary electrophoresis. Anal Chem 83: 1350–1355.

112. Fan A, Deb-Basu D, Orban M, Gotlib J, Natkunam Y, et al. (2009) Nanofluidic proteomic assay for serial analysis of oncoprotein activation in clinical specimens. Nat Med 15: 566–571.

113. US Congress Office of Technology and Assessment (1995) Costs and Effectiveness of Prostate Cancer Screening in Elderly Men. US Government Printing Office, Washington DC.

114. Baker M (2003) The prostate puzzle: What's behind the controversy over screening and treating. Stanford Medicine Magazine http://stanmed.stanford.edu/2003fall/prostate.html.

115. Lilja H, Ulmert D, Vickers A (2008) Prostate-specific antigen and prostate cancer: Prediction, detection and monitoring. Nat Rev Cancer 8: 268–278.

116. Peracaula R, Tabares G, Royle L, Harvey D, Dwek R, et al. (2003) Altered glycosylation pattern allows the distinction between prostate-specific antigen (PSA) from normal and tumor origins. Glycobiology 13: 457–470.

117. Väisänen V, Lövgren J, Hellman J, Piironen T, Lilja H, et al. (1999) Characterization and processing of prostate specific antigen (hK3) and human glandular kallikrein (hK2) secreted by LNCaP cells. Prostate Cancer P D 2: 91–97.

118. Jansen F, Roobol M, Jenster G, Schröder F, Bangma C (2009) Screening for prostate cancer in 2008 II: The importance of molecular subforms of prostate-specific antigen and tissue kallikreins. Eur Urol 55: 563–574.

119. Holmes D, Stellwagen N (1991) Estimation of polyacrylamide gel pore size from ferguson plots of linear dna fragments II. comparison of gels with different crosslinker concentrations, added agarose and added linear polyacrylamide. Electrophoresis 12: 612–619.

120. Matta A, Knio O, Ghanem R, Chen C, Santiago J, et al. (2004) Computational study of band-crossing reactions. JMEMS 13: 310–322.

121. Gianazza E, Righetti P (1980) Size and charge distribution of macromolecules in living systems. J Chromatogr 193: 1–8.

122. Craig D, Wetzl B, Duerkop A, Wolfbeis O (2005) Determination of picomolar concentrations of proteins using novel amino reactive chameleon labels and capillary electrophoresis laser-induced fluorescence detection. Electrophoresis 26: 2208-2213.

123. Righetti P, Simo C, Sebastiano R, Citterio A (2007) Carrier ampholytes for IEF, on their fortieth anniversary (1967–2007), brought to trial in court: The verdict. Electrophoresis 28: 3799–3810.

124. Katritzky A, Awartani R, Patel R (1982) Deethoxycarbonylation of 2-(ethoxycarbonyl)pyridinium salts with primary amines and competing S_NANRORC reactions. J Org Chem 47: 498–502.

125. Jumper C, Schriemer D (2011) Mass spectrometry of laser-initiated carbene reactions for protein topographic analysis. Anal Chem 83: 2913–2920.

126. Donohue M, Satterfield M, Dalluge J, Welch M, Girard J, et al. (2005) Capillary electrophoresis for the investigation of prostate-specific antigen heterogeneity. Anal Biochem 339: 318-327.

127. Ward W (2006) Biochemical and physical properties of green fluorescent protein. In: Chalfie M, Kain S, editors, Green Fluorescent Protein: Properties, Applications and Protocols, Hoboken, NJ: John Wiley & Sons.

128. Yu F, Yao D, Knoll W (2003) Surface plasmon field-enhanced fluorescence spectroscopy studies of the interaction between an antibody and its surface-coupled antigen. Anal Chem 75: 2610–2617.

129. Steinfeld J, Francisco J, Hase W (1989) Chemical Kinetics and Dynamics. Englewood Cliffs, NJ: Prentice Hall.

130. Tia S, He M, Kim D, Herr A (2011) Multianalyte on-chip native western blotting. Anal Chem 83: 3581–3588.

131. Baehr H, Stephan K (2006) Heat and Mass Transfer. Berlin: Springer-Verlag, 2nd edition.

132. Cussler E (1997) Diffusion: Mass Transfer in Fluid Systems. Cambridge, UK: Cambridge University Press, 2nd edition.

133. He M, Herr A (2010) Automated microfluidic protein immunoblotting. Nat Protoc 5: 1844–1856.

134. Bao J, Krylova S, Reinstein O, Johnson P, Krylov S (2011) Label-free solution-based kinetic study of aptamer-small molecule interactions by kinetic capillary electrophoresis with UV detection revealing how kinetics control equilibrium. Anal Chem 83: 8387–8390.

135. Wong E, Okhonin V, Berezovski M, Nozaki T, Waldmann H, et al. (2008) "inject-mix-react-separate-quantitate" (IMReSQ) method for screening enzyme inhibitors. J Am Chem Soc 130: 11862–11863.

136. Petrov A, Okhonin V, Berezovski M, Krylov S (2005) Kinetic capillary electrophoresis (KCE): A conceptual platform for kinetic homogeneous affinity methods. J Am Chem Soc 127: 17104-17110.

137. Liu Z, Pawliszyn J (2004) Capillary isoelectric focusing with laser-induced fluorescence whole column imaging detection as a tool to monitor reactions of proteins. J Proteome Res 3: 567–571.

138. Lemma T, Mandal R, Li X, Pawliszyn J (2008) Investigation of interaction between human hemoglobin A0 and platinum anticancer drugs by capillary isoelectric focusing with whole column imaging detection. J Sep Sci 31: 1803–1809.

139. He M, Novak J, Julian B, Herr A (2011) Membrane-assisted online renaturation for automated microfluidic lectin blotting. J Am Chem Soc 133: 19610–19613.

140. Goldsmith R, Moerner W (2010) Watching conformational- and photo-dynamics of single fluorescent proteins in solution. Nat Chem 2: 179–186.

141. Chudakov D, Matz M, Lukyanov S, Lukyanov K (2010) Fluorescent proteins and their applications in imaging living cells and tissues. Physiol Rev 90: 1103–1163.

142. Subach F, Piatkevich K, Verkhusha V (2011) Directed molecular evolution to design advanced red fluorescent proteins. Nat Methods 8: 1019–1026.

143. Patterson G, Lippincott-Schwartz J (2002) A photoactivatable GFP for selective photolabeling of proteins and cells. Science 297: 1873–1877.

144. Chang H, Zhang M, Ji W, Chen J, Zhang Y, et al. (2012) A unique series of reversibly switchable fluorescent proteins with beneficial properties for various applications. Proc Natl Acad Sci USA 109: 4455–4460.

145. Ando R, Mizuno H, Miyawaki A (2004) Regulated fast nucleocytoplasmic shuttling observed by reversible protein highlighting. Science 306: 1370–1373.

146. Brakemann T, Weber G, Andresen M, Groenhof G, Stiel A, et al. (2010) Molecular basis of the light-driven switching of the photochromic fluorescent protein padron. JBC 285: 14603–14609.

147. Bizzarri R, Serresi M, Cardarelli F, Abbruzzetti S, Campanini B, et al. (2010) Single amino acid replacement makes aequoria victoria fluorescent proteins reversible photoswitchable. J Am Chem Soc 132: 85–95.

148. Adelroth P, Brzezinski P (2004) Surface-mediated proton-transfer reactions in membrane-bound proteins. Biochim Biophys Acta 1655: 102–115.

149. Gutman M, Nachliel E (1997) Time-resolved dynamics of proton transfer in proteinous systems. Annu Rev Phys Chem 48: 329–356.

150. Andresen, Stiel A, Trowitzsch S, Weber G, Eggeling C, et al. (2007) Structural basis for reversible photoswitching in dronpa. Proc Natl Acad Sci USA 104: 13005–13009.

151. Henderson J, Ai H, Campbell R, Remington S (2007) Structural basis for reversible photobleaching of a green fluorescent protein homologue. Proc Natl Acad Sci USA 104: 6672–6677.

152. Mizuno H, Mal T, Walchli M, Kikuchi A, Fukano T, et al. (2008) Light-dependent regulation of structural flexibility in a photochromic fluorescent protein. Proc Natl Acad Sci USA 105: 9227–9232.

153. Tran J, Zamdborg L, Ahlf D, Lee J, Catherman A, et al. (2011) Mapping intact protein isoforms in discovery mode using top-down proteomics. Nature 480: 254–258.

154. Tsien R (1998) The green fluorescent protein. Annu Rev Biochem 67: 509–544.

155. Brejc K, Sixma T, Kitts P, Kain S, Tsien R, et al. (1997) Structural basis for dual excitation and photoisomerization of the *Aequoria victoria* green fluorescent protein. Proc Natl Acad Sci USA 94: 2306–2311.

156. Shinobu A, Palm G, Schierbeek A, Agmon N (2010) Visualizing proton antenna in a high-resolution green fluorescent protein structure. J Am Chem Soc 132: 11093–11102.

157. Bizzarri R (2012) The proton sensitivity of fluorescent proteins: Towards intracellular pH indicators. In: Jung G, editor, Fluorescent proteins I: From understanding to design, Berlin: Springer-Verlag, volume 11 of *Springer Series on Fluorescence*. pp. 59–98.

158. Agmon N (2005) Proton pathways in green fluorescence protein. Biophys J 88: 2452–2461.

159. Sinnecker D, Voigt P, Hellwig N, Schaefer M (2005) Reversible photobleaching of enhanced green fluorescent proteins. Biochemistry 44: 7085–7094.

160. Hughes A, Tentori A, Herr A (2012) Bistable isoelectric point photoswitching in green fluorescent proteins observed by dynamic immunoprobed isoelectric focusing. JACS 134: 17582–17591.

161. Patterson G, Knobel S, Sharif W, Kain S, Piston D (1997) Use of the green fluorescent protein and its mutants in quantitative fluorescence microscopy. Biophys J 73: 2782–2790.

162. Bogdanov A, Mishin A, Yampolsky I, Belousev V, Chudakov D, et al. (2009) Green fluorescent proteins are light-induced electron donors. Nat Chem Biol 5: 459–461.

163. Pace C, Grimsley G, Scholtz J (2009) Protein ionizable groups: pK values and their contribution to protein stability and solubility. JBC 284: 13285–13289.

164. Gasteiger E, Hoogland C, Gattiker A, Duvaud S, Wilkins M, et al. (2005) Protein identification and analysis tools on the ExPASy server. In: Walker J, editor, The proteomics protocols handbook, Totowa: Humana press. pp. 571–607.

165. McGrath M, Vasquez J, Craik C, Yang A, Honig B, et al. (1992) Perturbing the polar environment of Asp102 in trypsin: Consequences of replacing conserved Ser214. Biochemistry 31: 3059–3064.

166. O'Farrell P (1975) High resolution two-dimensional electrophoresis of proteins. JBC 250: 4007–4021.

167. Bobb D, Hofstee B (1971) Gel isoelectric focusing for following the successive carbamylations of amino groups in chymotrypsinogen A. Anal Biochem 40: 209–217.

168. Schwille P, Kummer S, Heikal A, Moerner W, Webb W (2000) Fluorescence correlation spectroscopy reveals fast optical excitation-driven intramolecular dynamics of yellow fluorescent proteins. Proc Natl Acad Sci USA 97: 151–156.

169. Haupts U, Maiti S, Schwille P, Webb W (1998) Dynamics of fluorescence fluctuations in green fluorescent protein observed by fluorescence correlation spectroscopy. Proc Natl Acad Sci USA 95: 13573–13578.

170. Chattoraj M, King B, Bublitz G, Boxer S (1996) Ultra-fast excited state dynamics in green fluorescent protein: Multiple states and proton transfer. Proc Natl Acad Sci USA 93: 8362–8367.

171. Wang Q, Byrnes L, Shui B, Rohrig U, Singh A, et al. (2011) Molecular mechanism of a green-shifted, pH-dependent red fluorescent protein mKate variant. PLoS ONE 6: e23513.

172. Weber W, Helms V, McCammon J, Langhoff P (1999) Shedding light on the dark and weakly fluorescent states of green fluorescent protein. Proc Natl Acad Sci USA 96: 6177–6182.

173. Baranov M, Lukyanov K, Borissova A, Shamir J, Kosenkov D, et al. (2012) Conformationally locked chromophores as models of excited-state proton transfer in fluorescent proteins. J Am Chem Soc 134: 6025–6032.

174. Andresen M, Wahl M, Stiel A, Grater F, Schafer L, et al. (2005) Structure and mechanism of the reversible photoswitch of a fluorescent protein. Proc Natl Acad Sci USA 102: 13070–13074.

175. Fang C, Frontiera R, Tran R, Mathies R (2009) Mapping GFP structure evolution during proton transfer with femtosecond raman spectroscopy. Nature 462: 200–204.

176. Nienhaus K, Nienhaus G, Wiedenmann J, Nar H (2005) Structural basis for photo-induced protein cleavage and green-to-red conversion of fluorescent protein EosFP. Proc Natl Acad Sci USA 102: 9156–9159.

177. Shaner N, Patterson G, Davidson M (2007) Advances in fluorescent protein technology. J Cell Sci 120: 4247–4260.

178. Gurskaya N, Fradkov A, Pounkova N, Staroverov D, Bulina M, et al. (2003) A colourless green fluorescent protein homologue from the non-fluorescent hydromedusa *aequorea coerulescens* and its fluorescent mutants. Biochem J 373: 403–408.

179. Ehrig T, O'Kane D, Prendergast F (1995) Green-fluorescent protein mutants with altered fluorescence excitation spectra. FEBS Lett 367: 163–166.

180. Agmon N (2007) Kinetics of switchable proton escape from a proton-wire within green fluorescence protein. J Phys Chem B 111: 7870–7878.

181. Helms V, Gu W (2012) Proton travel in green fluorescent protein. In: Jung G, editor, Fluorescent proteins I: From understanding to design, Berlin: Springer-Verlag, volume 11 of *Springer Series on Fluorescence*. pp. 171–181.

182. Abbruzzetti S, Bizzarri R, Luin S, Nifosi R, Storti B, et al. (2010) Photoswitching of E222Q GFP mutants: "concerted" mechanism of chromophore isomerization and protonation. Photochem Photobiol Sci 9: 1307–1319.

183. Dickson R, Cubitt A, Tsien R, Moerner W (1997) On/off blinking and switching behavior of single molecules of green fluorescent protein. Nature 388: 355–358.

184. van Thor J, Gensch T, Hellingwerf K, Johnson L (2002) Phototransformation of green fluorescent protein with UV and visible light leads to decarboxylation of glutamate 222. Nat Stuct Biol 9: 37–41.

185. Elowitz M, Surette M, Wolf P, Stock J, Leibler S (1997) Photoactivation turns green fluorescent protein red. Curr Biol 7: 809–812.

186. Di Donato M, van Wilderen L, van Stokkum I, Stuart T, Kennis J, et al. (2011) Proton transfer events in GFP. Phys Chem Chem Phys 13: 16295–16305.

187. Brakemann T, Stiel A, Weber G, Andresen M, Testa I, et al. (2011) A reversibly photoswitchable GFP-like protein with fluorescence excitation decoupled from switching. Nat Biotechnol 29: 942–947.

188. Wang X, Chen X, Yang Y (2012) Spatiotemporal control of gene expression by a light-switchable transgene system. Nat Methods 9: 266–269.

189. Strickland D, Lin Y, Wagner E, Hope C, Zayner J, et al. (2012) Tulips: tunable, light-controlled interacting protein tags for cell biology. Nat Methods 9: 379–384.

190. Bizzarri R, Serresi M, Luin S, Beltram F (2009) Green fluorescent protein based pH indicators for in vivo use: A review. Anal Bioanal Chem 393: 1107–1122.

191. Burkert S, Bittrich E, Kuntzsch M, Muller M, Eichhorn K, et al. (2010) Protein resistance of PNIPAAm brushes: Application to switchable protein adsorption. Langmuir 26: 1786–1795.

192. Oroszi L, Der A, Kirei H, Ormos P (2006) Control of electro-osmotic flow by light. Appl Phys Lett 89: 2635081–2635083.

193. Zhang L, Zhang Z, Wang P (2012) Smart surfaces with switchable superoleophilicity and superoleophobicity in aqueous media: Toward controllable oil/water separation. NPG Asia Mater 4: e8.

194. Towbin H, Staehelin T, Gordon J (1979) Electrophoretic transfer of proteins from polyacrylamide gels to nitrocellulose sheets: procedure and some applications. Proc Natl Acad Sci USA 76: 4350–4354.

195. Kurien B, Scofield R (2009) Protein blotting and detection: Methods and protocols. Methods in molecular biology. New York: Springer.

196. Southern E (2006) Southern blotting. Nat Protoc 1: 518–525.

197. Alwine J, Kemp D, Stark G (1977) Method for detection of specific RNAs in agarose gels by transfer to diazobenzyloxymethyl-paper and hybridization with DNA probes. Proc Natl Acad Sci USA 74: 5350-5354.

198. Wu Y, Li Q, Chen X (2007) Detecting protein-protein interactions by far western blotting. Nat Protoc 2: 3278–3284.

199. Hughes A, Herr A (2012) Microfluidic western blotting. Proc Natl Acad Sci USA 109: 21450–21455.

200. Lequin R (2005) Enzyme immunoassay (EIA)/enzyme-linked immunosorbent assay (ELISA). Clin Chem 51: 2415–2418.

201. MacBeath G, Schreiber S (2000) Printing proteins as microarrays for high-throughput function determination. Science 289: 1760–1763.

202. Spurrier B, Ramalingam S, Nishizuka S (2008) Reverse-phase protein lysate microarrays for cell signaling analysis. Nat Protoc 3: 1796–1808.

203. Zhu H, Bilgin M, Bangham R, Hall D, Casamyor A, et al. (2001) Global analysis of protein activities using proteome chips. Science 293: 2101–2105.

204. CDC (1989) Interpretation and use of the western blot assay for serodiagnosis of human immunodeficiency virus type 1 infections. MMWR 38(S-7): 1–7.

205. Ramaswamy A, Lin E, Chen I, Mitra R, Morrisett J, et al. (2005) Application of protein lysate microarrays to molecular marker verification and quantification. Proteome Sci 3: 9.

206. Cohen J (2011) Breakthrough of the year: HIV treatment as prevention. Science 334: 1628.

207. Rowland-Jones S (2003) AIDS pathogenesis: what have two decades of HIV research taught us? Nat Rev Immun 3: 343–348.

208. Biswas M (2012) AIDS epidemic worldwide and the millennium development strategies: A light for lives. HIV & AIDS Rev 11: 87–94.

209. McNeil D (July 4, 2012) F.D.A. approves rapid HIV test for use at home. New York Times : A1.

210. Mastro T, Kim A, Hallett T, Rehle T, Welte A, et al. (2010) Estimating HIV incidence in populations using tests for recent infection: Issues, challenges, and the way forward. J HIV AIDS Surveill Epidemiol 2: 1–14.

211. Lo C, Throckmorton D, Singh A, Herr A (2008) Photopolymerized diffusion-defined polyacrylamide gradient gels for on-chip protein sizing. Lab Chip 8: 1273–1279.

212. Giddings J (1991) Unified Separation Science. New York: John Wiley and Sons.

213. Jungblut P, Eckerskorn C, Lottspeich F, Klose J (1990) Blotting efficiency investigated by using two-dimensional electrophoresis, hydrophobic membranes and proteins from different sources. Electrophoresis 11: 581–588.

214. Swanson C, Malim M (2008) Snapshot: HIV-1 proteins. Cell 133: 741.

215. Milo R, Jorgensen P, Moran U, Weber G, Springer M (2010) Bionumbers - the database of key numbers in molecular and cell biology. Nucleic Acids Res 38: D750-D753.

216. Apori A, Herr A (2011) Homogeneous immunosubtraction integrated with sample preparation enabled by a microfluidic format. Anal Chem 83: 2691–2698.

217. Bendall S, Simonds E, Qiu P, Amir E, Krutzik P, et al. (2011) Single-cell mass cytometry of differential immune and drug responses across a human hematopoietic continuum. Science 332: 687–696.

218. Huang B, Wu H, Bhaya D, Grossman A, Granier S, et al. (2007) Counting low-copy number proteins in a single cell. Science 315: 81–84.

219. Wang D, Bodovitz S (2010) Single cell analysis: the new frontier in 'omics'. Trends Biotechnol 28: 281–290.

220. Lu S, Zong C, Fan W, Yang M, Li J, et al. (2012) Probing meiotic recombination and aneuploidy of single sperm cells by whole-genome sequencing. Science 338: 1627–1630.

221. Stadler C, Rexhepaj E, Singan V, Murphy R, Pepperkok R, et al. (2013) Immunofluorescence and fluorescent-protein tagging show high correlation for protein localization in mammalian cells. Nat Methods 10: 315–323.

222. Fritzsch F, Dusny C, Frick O, Schmid A (2012) Single-cell analysis in biotechnology, systems biology, and biocatalysis. Annu Rev Chem Biomol Eng 3: 129–155.

223. Ashton R, Conway A, Pangarkar C, Bergen J, Lim K, et al. (2012) Astrocytes regulate adult hippocampal neurogenesis through ephrin-B signaling. Nat Neurosci 15: 1399–1406.

224. Suh H, Consiglio A, Ray J, Sawai T, D'Amour K, et al. (2007) In vivo fate analysis reveals the multipotent and self-renewal capacities of sox2+ neural stem cells in the adult hippocampus. Cell Stem Cell 1: 515–528.

225. Graf T, Enver T (2009) Forcing cells to change lineages. Nature 462: 587–594.

226. Schwanhausser B, Busse D, Li N, Dittmar G, Schuchhardt J, et al. (2011) Global quantification of mammalian gene expression control. Nature 473: 337–342.

227. Wood D, Weingeist D, Bhatia S, Engelward B (2010) Single cell trapping and dna damage analysis using microwell arrays. PNAS 107: 10008–10013.

228. Hughes A, Spelke D, Xu Z, Lin R, Schaffer D, et al. (2013) Single-cell western blotting in highly multiplexed polyacrylamide microwell arrays. *In prep* .

229. Rettig J, Folch A (2005) Large-scale single-cell trapping and imaging using microwell arrays. Anal Chem 77: 5628–5634.

230. Peltier J, O'Neill A, Schaffer D (2007) PI3K/Akt and CREB regulate adult neural hippocampal progenitor proliferation and differentiation. Dev Neurobiol 67: 1348–1361.

231. Yu J, Schaffer D (2006) Selection of novel vesicular stomatitis virus glycoprotein variants from a peptide insertion library for enhanced purification of retroviral and lentiviral vectors. J Virol 80: 3285–3292.

232. Abranches E, O'Neill A, Robertson M, Schaffer D, Cabral J (2006) Development of quantitative PCR methods to analyse neural progenitor cell culture state. Biotechnol Appl Biochem 44: 1–8.

233. Su P, Chen C, Chang Y, Wong Z, Chang K, et al. (2013) Identification and cytoprotective function of a novel nestin isoform, Nes-S, in dorsal root ganglia neurons. JBC 288: 8391–8404.

234. Chou Y, Khuon S, Herrmann H, Goldman R (2003) Nestin promotes the phosphorylation-dependent disassembly of vimentin intermediate filaments during mitosis. Mol Biol Cell 14: 1468–1478.

235. Peltier J, Agrawal S, Robertson M, Schaffer D (2010) In vitro culture and analysis of adult hippocampal neural progenitors. In: Conboy I, Schaffer D, Barcellos-Hoff M, Li S, editors, Protocols for Adult Stem Cells, Springer-Verlag, New York. pp. 65–87.

236. Zehorai E, Yao Z, Plotnikov A, Seger R (2010) The subcellular localization of MEK and ERK—a novel nuclear translocation signal (NTS) paves a way to the nucleus. Mol Cell Endocrinol 314: 213–220.

237. McKay M, Ritt D, Morrison D (2009) Signaling dynamics of the KSR1 scaffold complex. Proc Natl Acad Sci USA 106: 11022–11027.

238. Simon G, Niphakis M, Cravatt B (2013) Determining target engagement in living systems. Nat Chem Biol 9: 200–205.

239. Hopman A, Ramaekers F, Speel E (1998) Rapid synthesis of biotin-, digoxigenin-, trinitrophenyl-, and fluorochrome-labeled tyramides and their application for in situ hybridization using CARD amplification. J Histochem Cytochem 46: 771–777.

240. Small D (1971) In: Nair P, Kritchevsky D, editors, The Bile Acids: Chemistry, Physiology and Metabolism, New York: Plenum Press. pp. 249–350.

241. Bodansky O (1937) Are the phosphatases of bone, kidney, intestine, and serum identical? Biol Chem 118: 341–362.

242. Persat A, Chambers R, Santiago J (2009) Basic principles of electrolyte chemistry for microfluidic electrokinetics. Part 1: Acid-base equilibria and pH buffers. Lab Chip 9: 2437–2453.

243. Fishman W, Green S, Inglis N (1962) Organ-specific behavior exhibited by rat intestine and liver alkaline phosphatase. Biochim Biophys Acta 62: 363–375.

244. Hofstee B (1955) Alkaline phosphatase 1. Mechanism of action of Zn, Mg, glycine, versene and hydrogen ions. Arch Biochem Biophys 59: 352–365.

245. Wei Y, Wesson P, Kourkine I, Grzybowski B (2010) Measurement of protein-ligand binding constants from reaction-diffusion concentration profiles. Anal Chem 82: 8780–8784.

246. Konzak S, Thies E, Marx A, Mandelkow E, Mandelkow E (2007) Swimming against the tide: mobility of the microtubule-associated protein tau in neurons. J Neurosci 27: 9916–9927.

247. Liu Y, Shi M, Cao R, Zhang Y, Hu Y (2007) Densities and viscosities of the quaternary system mannitol-sorbitol-D-glucose-H_2O and its ternary subsystems at 298.15K*. Chin J Chem Eng 15: 703–709.

Appendix A

BPMAC Synthesis

N-{3-[(4-benzoylphenyl)formamido]propyl}methacrylamide (BPMAC, MW = 350.4 g mol^{-1}) is a bifunctional reagent that allows photoreactive benzophenone groups to be "built-in" to polyacrylamide gels. This is useful for photoactivated attachment of proteins to the gel matrix. Photopolymerization of gel precursor is not advisable if protein attachment is to be performed on chip, as the benzophenone groups will be destroyed by any premature UV exposure (i.e. use the TEMED + APS system to polymerize your gel instead).

- Reagents: dimethylformamide (DMF) as reaction solvent, triethylamine or tetramethylethylenediamine (TEMED, or any other tertiary amine organic base), succinimidyl (NHS) ester of 4-benzoylbenzoic acid (BP-NHS, MW = 323.3, Invitrogen #B1577, 100 mg for $72.00), N-(3-aminopropyl)methacrylamide HCl (APMAC, Polysciences #21200, MW = 178.7, 5g for $105.00, stocks available in lab fridge), **OPTIONAL:** isothiocyanate-functionalized polystyrene beads (Sigma #538604, 5g for $173.50, stocks available).

The conjugation pathway is shown in Figure A.1, and is mostly based on similar reactions reported in [239]. The reactants are incubated together in DMF in the presence of tertiary amine base to form the bifunctional adduct BPMAC. Optionally, the reaction mixture is stripped of remaining APMAC using isothiocyanate-functionalized polymer beads that react with, and thus sequester, any primary amines. After filtration, the DMF phase is dried with the help of acetone in the speedvac, yielding an off-white solid as product. This solid can then be made up in DMSO before addition to aqueous acrylamide precursor solutions. Final concentrations of at least 5 mM can be used in aqueous phase without solubility problems.

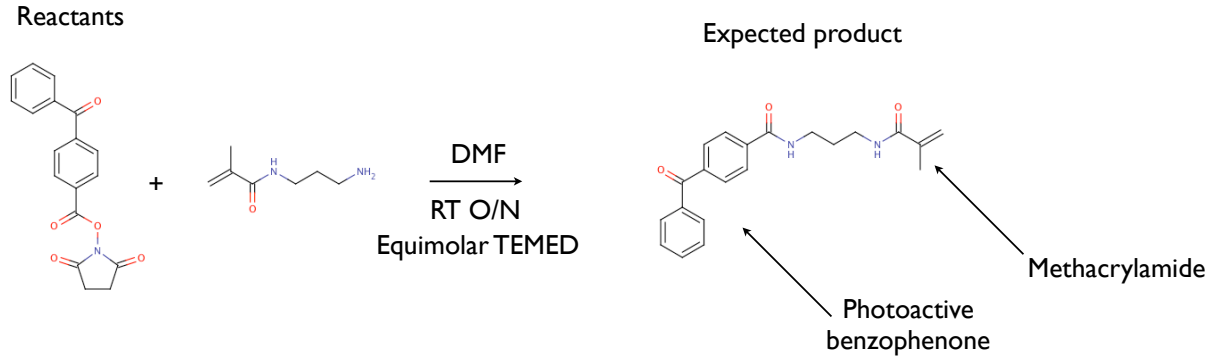

Figure A.1: The organic-phase reaction of BP-NHS with APMAC in DMF in the presence of tertiary amine base.

Step-by-step protocol (note that the reaction is readily scalable to achieve desired product yield):

1. Make up a reaction mixture containing a molar ratio of around 1:1:(1-1.2) parts BP-NHS : APMAC : TEMED or triethylamine. For example, make up separate solutions of BP-NHS and APMAC in DMF by adding 744 μl DMF to 75 μmol of each powder. Mix the two solutions and add 11.1 μl of TEMED (s.g. = 0.78 g ml^{-1}, MW = 116.2). The final reaction volume in this case is 1.5 ml, 50 mM in each of BP-NHS, APMAC and TEMED.

2. Wrap the reaction tube(s) in tin foil and incubate at room temperature on a tube rotator for 5 hrs.

3. A white precipitate may have formed in the tube. Use a 0.2 μm cellulose acetate syringe filter to remove the precipitate.

4. Add around 25 mg of isothiocyanate-functionalized polystyrene beads to the supernatant for every 75 μmol quantity of APMA initially added to the reaction.

5. Incubate at room temperature on a rotator under a piece of tin foil for 3 hrs.

6. Spin the tube at 18,000g for 5 min, remove supernatant using a syringe, and filter into a separate tube using a 0.2 μm syringe filter. Keep the filtered supernatant and discard the first tube with beads.

7. Aliquot the reaction mixture with an equal volume of acetone into 1.5 ml tube(s) and place in the SpeedVac. Spin under vacuum using the "medium" (43 °C) SpeedVac setting until a small amount of oily yellow-brown residue is left in the tube. Add another 1 ml of acetone and dry until a solid white powder remains. The resulting solid is the BPMA conjugate. A 100 mM stock solution in DMSO can be made with vigorous vortexing, aliquot and store in the dark at −20 °C.

Appendix B

Experimental Apparatus

In the integration of separation and reaction (enzyme or antibody probing) assays, we developed a range of related microscale fabrication techniques to build and functionalize microfluidic devices with multi-purposed polyacrylamide materials. Additionally, open-format polyacrylamide matrices were built in conjunction with standard silicon wafers fabricated using SU-8 photolithography for high-throughput single-cell immunoblotting experiments. In this chapter, we summarize general procedures and approaches, with a focus on novel contributions to integrated experimental workflows.

B.1 Assay Substrates

B.1.1 Microfluidic Chips

Several microfluidic chip designs are used here, most commonly of a straight-channel variety wet etched in optical white soda lime glass by Caliper Life Sciences (Hopkinton, MA). Chrome-on-glass chip masks were designed through AutoCAD drafting software and fabricated by Photo Sciences Inc (Torrance, CA). For probed IEF and μWestern blotting assays (Chapters 3, 5, and 6), chips contained four straight-channel devices 10.4 mm in length, each consisting of three parallel channels of 10 μm depth and 70 μm width between two 2 mm diameter access wells providing fluidic interfacing via 10 μl press-fit pipet tips. Electric field was applied via a custom high voltage power supply built in-house.

For μWestern blotting assays in Chapter 6, a higher density 48-lane microchip was also designed and operated with fluidic access directly with 2 μl sample reservoirs via a custom PCB platinum electrode board interfacing with a standard electrophoresis power supply (BioRad PowerPac HV).

B.1.2 Silicon Wafers and Glass Slides for Open Gels

Standard SU-8 on silicon photolithography techniques were used to fabricated micropost arrays for microwell single-cell immunoblotting procedures. Microposts were verified for uniformity across wafers by surface profilometry, which showed <2% error in feature dimensions (diameter and height of microposts) compared to nominal dimensions. Wafers were silanized using dichlorodimethylsilane (DCDMS, 440272, Sigma Aldrich, St. Louis, MO) by vapor deposition in a vacuum chamber. Wafers were placed in the chamber with 2 ml of DCDMS *in vacuo* for 1 hr and rinsed thoroughly with DI water. Methacrylate-functionalized slides were sourced from Arrayit (SMRY3, Sunnyvale, CA), or were fabricated in-house (Appendix B.2.1).

B.2 Gel Fabrication Methods

B.2.1 Microfluidic Devices

Glass microchannels were functionalized with acrylate-terminated self-assembled silane monolayers to ensure attachment of cross linked gels to the microchannel walls, as previously described [23]. For Microfluidic polyacrylamide gels were fabricated via introduction of a gel precursor solution by capillary action. Precursors typically contained 4-35% total acrylamide (%T; % concentrations are w/v unless otherwise noted) with 2.6% of the total as the crosslinker bisacrylamide (2.6%C), buffers, and detergents/solubilizing agents depending on the assay type.

B.2.1.1 Considerations for Design of Gel Buffer Systems

In pore limit electrophoresis of enzymes (PLENZ), 10–35%T gradient gels were used to pseudo-immobilize enzyme analytes prior to in-channel assay. Here, gel precursors contained 75 mM glycine titrated with NaOH to a measured pH of 9.3, with 1% sodium cholate and 1 mM of the reducing agent DTT as solubilizing agents. Sodium cholate is a nondenaturing, anionic detergent with a low aggregation number [240, 241] that solubilizes enzyme analytes, improving loading into PLENZ devices and reducing the tendency for nonspecific adsorption to the gel matrix without compromising full substrate penetration. Glycine buffer was chosen due to its alkaline buffering range ($pK_a \approx 9.8$) to match the pH optimum of intestinal phosphatase analytes while limiting inhibitory effects on their activities [242–244]. The buffer system used for the assay of horseradish peroxidase was similarly tailored for its neutral pH optimum through the use of 25 mM Tris-HCl titrated to pH 7.4 with NaOH.

In IEF, lower percentage gels in the 4-6% range were employed largely to quell electroosmotic flow, and to provide a protein immobilization scaffold without a particular necessity for protein sieving properties. Broad pH range Pharmalyte 3-10 ampholytes were used at 2% titrated to pH 9.9 using NaOH to allow electrophoretic loading of samples into closed microfluidic devices. Detergents/solubilizing agents were 3% CHAPS, 10% sorbitol, and 200 mM sulfobetaine-256 (17236, Sigma Aldrich). Strongly dissociative buffer conditions were necessary for IEF, in general, since protein analytes are prone to non-specific interaction and precipitation at their isoelectric points [7]. For focusing of GFP, a highly soluble protein, the ampholytes were 15% v/v Polybuffer 74 (providing a pH range of 4-7), and Triton X-100 at 0.1% v/v was the only solubilizing agent necessary.

In SDS-PAGE, gels were 7.5%T to provide a balance between effective sieving of species and electrophoretic antibody loading and penetration into gel-patterned microchannels. The gel buffer was 75 mM Tris titrated with HCl to pH 8.8, 0.1% SDS, and 0.1% Triton X-100; similar to standard western blotting, but with the addition of Triton to limit non-specific antibody signal in subsequent probing steps.

B.2.1.2 Gradient Gels for Pore Limit Electrophoresis

Gradient gels for pore limit electrophoresis of enzymes (PLENZ) were generated and polymerized using a protocol modified from [32] (Figure B.1). A 35%T precursor was loaded throughout microchannels and mask-based UV-light initiated fabrication used to produce short plugs of cross linked gel near the termini of each channels.

For each channel, A ∼150 μm-long gel membrane was polymerized approximately three channel widths from one of the two via wells, as defined using a 100 μm × 500 μm slit in a plastic transparency mask (CAD/Art Services, Bandon, OR). For polymerization, the UV-responsive photoinitiator VA-086 (Wako, Richmond, VA) was included in precursor solutions to a concentration of 2 mg ml^{-1} from a 0.1 mg μl^{-1} suspension in deionized water. UV illumination in the 330-375 nm range was provided by the mercury lamp of an IX50 inverted fluorescence microscope (Olympus, Melville, NY) directed through an ND25 filter, UV-permissive filter cube, and 4× objective (UPlan-SApo, N.A. 0.16). Membrane polymerization was achieved with an exposure time of 60 s at a local UV intensity of approximately 20 mW cm^{-2}, as measured by a light meter at the plane of the chip (Mannix UV340 Light Meter, General Tools, New York, NY).

These plugs halted hydrodynamic flow over the lengthy subsequent diffusion step, in which degassed 35%T and 10%T precursors were loading into the wells proximal and distal to the membrane, respectively. Chips were incubated in a dark, humid environment for 20 h to establish a diffusion-generated 10-35% T gradient in gel composition along the channel. Each gradient gel was then polymerized by flood exposing the entire chip (except access wells, which were masked) with UV light for 90 s using an air-cooled 100 W mercury lamp (300-380 nm, UV intensity of ∼10 mW cm^{-2}, B-100AP lamp, UVP, Upland, CA). Completed PLENZ chips were stored at room temperature in gel buffer until use (within 36 h).

B.2.1.3 LAVAgel and PACTgel Materials

N-[3-[(4-benzoylphenyl)formamido]propyl] methacrylamide (BPMAC, $C_{21}H_{22}N_2O_3$, 350.2 g mol^{-1}) monomer was synthesized via reaction of the succinimidyl ester of 4-benzoylbenzoic acid (323.3 g mol-1; B1577, Invitrogen) with N-(3-aminopropyl)methacrylamide hydrochloride (178.7 g mol-1; 21200, Polysciences, Warrington, PA) in the presence of catalytic triethylamine in dimethylformamide, purified and characterized by ^{1}H NMR and mass spectrometry as described in Appendix A. BPMAC was latterly commercially synthesized and purified by PharmAgra Labs (Brevard, NC), to ensure batch-to-batch repeatability. The monomer was added to BPMAC+ LAVAgel/PACTgel precursor solutions at 1.5–5 mM (in the vicinity of 1 mol % with respect to acrylamide) from a 100 mM stock in dimethylsulfoxide (DMSO) to imbue UV-induced protein photocapture functionality [6]. BPMAC- precursors were used in negative control experiments in which protein photocapture was not required, and contained an equivalent volume of DMSO lacking BPMAC.

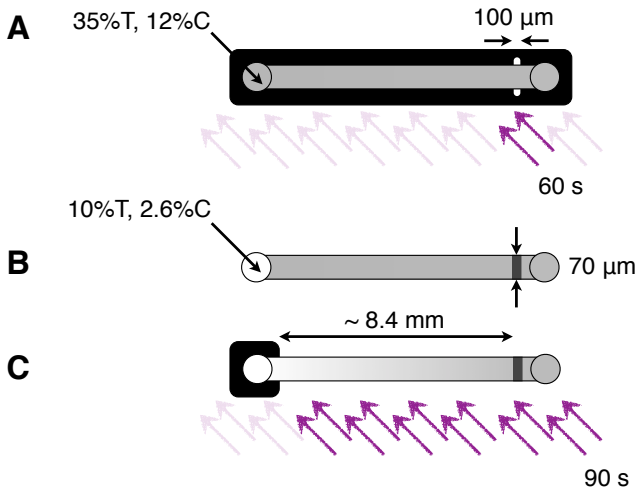

Figure B.1: Fabrication of gradient gels for PLENZ. (A) UV photopatterning of a polyacrylamide membrane at the eventual 35%T end of the device is achieved in 60s using a slit in a black plastic mask. (B) Low percentage acrylamide solution is loaded into the opposite well, beginning the diffusion process. (C) 20 hours later, the pore size gradient is set via a 90s flood illumination under UV.

Photoswitchable LAVAgels (light-activated, volume-accessible gel) and PACTgels (photoactive gel with tunable porosity) differ only in the method of polymerization. LAVAgels are chemically initiated, while PACTgels are photochemically initiated using blue light.

For photopolymerization of PACTgel materials in IEF experiments on GFPs (Chapter 5), the initiators ammonium persulfate (APS, 0.015%, A3678, Sigma), N,N,N',N'-tetramethyl ethylenediamine (TEMED, 0.05% v/v, T9281, Sigma) and riboflavin 5 phosphate (0.0006%, F1392, Sigma) were added just before introduction of degassed precursor to channels. The precursor was polymerized by 6 min flood exposure of chips to 470 nm blue light from a collimated LED source (M470L2, Thorlabs, Newton, NJ) with the chip submerged in gel buffer to prevent gel fouling and to limit hydrodynamic flow during polymerization. The blue light intensity at a 470 nm probe setting was ~2.2 mW cm^{-2} at the chip plane, as measured by a LaserCheck light meter (1098293, Coherent, Santa Clara, CA).

A similar fabrication protocol is used to produce PACTgels for SDS-PAGE, except that discontinuous gel interfaces employed for the transition from ITP to zone electrophoresis are defined using blue light exposure through a plastic transparency mask.

LAVAgels were chemically polymerized, without the ability to control spatial distribution of the patterned polymer, using 0.08% of each of APS and TEMED. Crosslinking of the

precursor begins immediately after adding initiators here, such that rapid precursor loading into microchannels is imperative to avoid channel clogging and to ensure formation of a homogeneous gel. The reaction proceeds over the course of roughly 1 hour, with visible gelation occurring in the 10-20 min range depending on gel buffer composition and the presence of inhibitory oxygen species. To prevent gel fouling, microchannels filled with precursor can again be submerged in gel buffer during polymerization, or access wells can be swapped to gel buffer after partial gelation has occurred (∼5-10 mins after the start of polymerization).

B.2.2 Single Cell Immunoblotting Devices

PACTgels were fabricated in the (typically) 30 μm gap between methacrylate-functionalized glass substrates and silanized SU-8 masters. Details of the fabrication procedure are given in Appendix D.

B.3 Apparatus and Imaging

Chip imaging was conducted using an Olympus IX71 inverted fluorescence microscope equipped with an EMCCD camera (iXon3 885, Andor, Belfast, Northern Ireland), motorized stage (Applied Scientific Instrumentation, Eugene, OR) and automated filter cube turret controlled through MetaMorph software (Molecular Devices, Sunnyvale, CA). Illumination was provided by a mercury arc lamp mated to an automated shutter and attenuation system (X-Cite Exacte, Lumen Dynamics, Mississauga, ON, Canada). LAVAgel photoimmobilization of proteins was conducted via spot UV exposure through a 10x objective (Olympus UPlanFl, NA 0.3) and custom UV-longpass filter cube (excitation 300-380 nm, emission >410 nm; XF1001, XF3097, Omega Optical) at ∼269 mW cm^{-2} as measured via a 365 nm probe (UV513AB meter, General Tools, New York, NY). The same cube was used to observe GFP under UV illumination along with fluorescent pI marker peptides, and channel positions were manually scored (gradient drift between focused-state marker and GFP isoform imaging steps was assumed to be negligible). Green and red fluorescence channels were imaged at 10x using Omega Optical filter cubes optimized for GFP (XF100–3, excitation 445–495 nm at ∼89 mW cm^{-2} for a 470 nm probe setting, emission 508–583 nm) and DsRed2 (XF111–2, excitation 525–555 nm, emission >575 nm). Whole channel imaging at 10x magnification was conducted via stitching of adjacent, overlapping CCD images with 4×4 pixel binning in ImageJ (NIH, Bethesda, MD) to produce full gel channel images and electropherograms as previously described [76]. Imaging scans required ∼20 s to complete. Real-time single-point imaging of GFP isoform dynamics was conducted in burst acquisition mode.

Transformation of fluorescence data via linear fits to pI markers and associated data processing, including correction for constant cathodic isoform drift velocities in dynamic focusing

experiments was performed using MATLAB scripts written in-house (MathWorks, Natick, MA). Least-squares fitting of kinetic data was performed using gnuplot software.

Single-cell immunoblotting slides were imaged by tiled wide field fluorescence microscopy, or using a GenePix 4300A fluorescence microarray scanner, with PMTs manually balanced for optimal bleedthrough characteristics.

B.4 Assay Operation

B.4.1 Probed IEF

B.4.1.1 PSA Assays

After gelation, LAVAgel access wells were filled with gel buffer. Samples (30 μL) were made in loading buffer and titrated to pH 9.9 with 1.5 μL 1M NaOH just prior to introduction at loading wells (3 μL per well). Sample injection was performed at 200 V cm^{-1} for 3 min. Catholyte and anolyte buffers were used to wash opposite wells twice; wells were subsequently filled. Focusing was conducted simultaneously for the four devices in each chip (i.e., all well pairs), at 50 V cm^{-1} for 4 min; 100 V cm^{-1}, 5 min; 200 V cm^{-1}, 5 min. Three-minute 300 V cm^{-1} focusing, imaging, and flood UV exposure steps were conducted individually for each device in series. Imaging of pI markers via 50 ms exposures was preceded by any green and/or red channel scans required. Following marker imaging, the chip was moved into position beneath the lightguide tip under motorized stage control. Under stopped electric field, 2 $\times$ 5 s flood UV exposures were applied in neighboring spots ($\sim$5 mm apart along the channel axis) to ensure uniform UV dosage. The final focusing, imaging, and flood exposure steps were repeated for the other devices on the same chip. Refocusing and imaging was conducted as necessary prior to simultaneous washout of all devices. Access wells were washed and filled with glycine washout/probe buffer consisting of 25 mM Tris, 192 mM Glycine pH 8.3, 0.1% v/v Triton X-100 and 3% v/v DMSO. Mobilization and washout of pH gradients to the anodic wells was achieved via a 20 min electrophoretic step. Labeled antibody probes were diluted in washout/probe buffer, loaded, and removed from LAVAgels in 20-min electrophoretic steps; wells were washed with buffer as required to prevent undesired cross-reaction of 1° and 2° probes in access wells. Probe loading and washout were conducted in opposite directions to minimize nonspecific signal remaining after washout. Final green and/or red scans were performed as necessary with 400 ms image exposure time. In the case of kinetic studies of LAVAgel immobilization, GFP was electrophoretically loaded at 200 V cm^{-1} as a homogeneous stream in untitrated loading buffer (pH 6.5). UV exposure dosage applied via the microscope mercury lamp was tightly controlled via the mechanical excitation shutter. Twenty-minute GFP washout was performed by replacing sample with fresh untitrated loading buffer before application of 200 V cm^{-1} field in the opposite direction to loading for 20 min.

B.4.1.2 GFP Photophysics Assays

After precursor gelation, LAVAgel access wells were flushed and replaced with gel buffer consisting of precursor lacking monomers and initiators. Samples were made in gel buffer and introduced at loading wells (∼3 μl per well). Sample injection was performed at 200 V cm^{-1} for 3 minutes. Opposing wells were briefly washed with catholyte (20 mM lysine, 20 mM arginine pH 10.1) and anolyte (70 mM phosphoric acid) and subsequently filled. Focusing was conducted at 200 V cm^{-1} for 2 min followed by 400 V cm^{-1} for 1 min (focusing typically completed to equilibrium in 3 minutes or less). Imaging and UV photocapture steps (where applicable) were conducted individually for each device in series. UV photocapture was conducted under stopped electric field for 15 s. Access wells were washed and filled with pH gradient washout/probe buffer. Mobilization and washout of pH gradients to the anodic wells was achieved via a 20 min electrophoretic step. Fluorescently labeled anti-GFP antibody was diluted in probe buffer, loaded, and removed from LAVAgels in 20 min electrophoretic steps. Probe loading and washout were conducted in opposite directions to minimize non-specific signal remaining after washout. Finally, gels were scanned for captured GFP and antibody fluorescence.

B.4.2 μWestern Blotting

Samples were combined with a fluorescent molecular mass marker mixture in SDS-PAGE sample buffer (50 mM Tris titrated to pH 6.8 with HCl, 2% SDS, 40 mM DTT), heated at 90°C for 3 min, and loaded immediately after cooling to room temperature. Sample loading was performed electrophoretically at 100 V cm^{-1} for 5–30 s. The sample was removed and the injection well filled with SDS run buffer containing glycine as a trailing ion for transient ITP (25 mM Tris, 192 mM glycine, pH 8.3, 0.1% SDS, 0.1% Triton X-100, 3% DMSO). Sample injection was performed under constant-current conditions of 0.7 μA per well pair, producing a voltage ramp during SDS-PAGE from 50 to 350 V cm^{-1} over a 60 s separation time. SDS-PAGE was imaged in real time via a 4× widefield fluorescence microscope objective, voltage stopped, and UV applied via the objective at ∼40 mW cm^{-2} for 45 s directly after separation was complete. Whole-channel green fluorescence imaging for marker proteins was conducted under 10× magnification, before electrophoretic washing of the PACTgel to remove uncaptured protein, 1 min each with SDS run buffer and plain run buffer lacking SDS (25 mM Tris, 192 mM glycine, pH 8.3, 0.1% Triton X-100, 3% DMSO) at 150 V cm^{-1}. Primary antibody probes were introduced in successive steps of electrophoretic loading and washout from the PACTgel, 20 min for each step at 150 V cm^{-1}. Secondary antibodies were loaded and washed out for 10 min per step. Antibodies were 100 nM each in plain run buffer (mixed in a cocktail for multiplexed antigen detection) with 2 μM BSA for blocking purposes (no separate gel-blocking step is necessary).

For HIV serum assays, primary antibody solution was replaced with 1:100 diluted serum in plain run buffer. All other steps were performed as described. Final green and red fluores-

cence channel imaging was performed for marker proteins and probe readout, respectively.

B.4.3 Single Cell Immunoblotting

Details of cell settling, lysis, protein separation, capture, and immunoprobing are provided in Appendix D.

B.5 Cleaning and Recycling of Microfluidic Chips

Removal of the LAVAgel matrix after use was achieved by overnight incubation of the chip in a 2:1 solution of 70% perchloric acid and 30% hydrogen peroxide heated to 75°C, allowing efficient recycling of glass chips.

Appendix C

Determination of Free-Solution and In-Gel Diffusivities

The diffusion coefficient for GFP in 4%T, 2.6%C polyacrylamide gel was determined by defocusing to be 2.05×10^{-7} cm^2 s^{-1} (Figure 3.6A). The diffusion coefficient for a given protein in a polyacrylamide matrix can be estimated via an adjusted Stokes-Einstein diffusivity [245, 246]:

$$r_H = 0.595(M_W)^{0.427} \tag{C.1}$$

$$D = \frac{k_B T}{6\pi\mu r_H} e^{-k_c r_H \phi^{0.75}} \tag{C.2}$$

r_H is the protein hydrodynamic radius, M_W the protein molecular weight in kDa, k_B is Boltzmann's constant, T temperature, μ the viscosity of the medium ($\mu \sim 1.26 \times 10^{-3}$ Pa.s for a 10% sorbitol solution [247]), $k_c = 0.45$ $\mathring{A}^{-1}$, ϕ the polymer volume fraction.

This relationship gives a diffusivity of GFP in 4%T, 2.6%C polyacrylamide gel of $\sim 2.5 \times 10^{-7}$ cm^2 s^{-1}, which is within 20% of the value measured by defocusing (2.05×10^{-7} cm^2 s^{-1}). Thus, the diffusivity for a probe antibody can be confidently estimated by similar means to be $\sim 4.5 \times 10^{-8}$ cm^2 s^{-1} in the gel and $\sim 3.4 \times 10^{-7}$ cm^2 s^{-1} in free solution.

Appendix D

Single-Cell Immunoblotting Protocol

This protocol describes fabrication and experimental procedure for single-cell immunoblotting using a perforated polyacrylamide sheet on a 1″ x 3″ microscope slide chip. Materials and equipment required:

- Methacrylate-functionalized glass slides from ArrayIt (product no. SMRY3).
- Optional: 8×2 well gasketed hybridization cassette from Arrayit (product no. AHC1×16).
- ThorLabs collimated blue 470 nm LED light source (M470L2-C1) with driver (LEDD1B) and 15V power supply (TPS001).
- Small trays for slide incubation. These can be fashioned from e.g. the bases of cell culture bottles.
- Standard gel electrophoresis power supply, e.g. BioRad PowerPac HV. A caliper-type HVPS will not generate enough current (> 50 mA required to run the full chip).
- Hamamatsu UV spot light source.
- Fluorescence microscope for separations and readout imaging.

Reagents — all percentages are w/v unless otherwise noted:

PACTgel precursor — Photoactive protein capture gel with tunable porosity. Reagents are listed in suggested order of addition:

H_2O	317 μl	
BioRad 1.5 M Tris HCl *p*H 8.8	25 μl	*75 mM final*
30%T, 2.6%C acrylamide stock (37.5:1)	117 μl	*7%T, 2.7%C*
100 mM BPMAC in DMSO	15 μl	*3 mM, 3% DMSO*
Degas before adding remaining reagents		
5% SDS	10 μl	*0.1%*
5% Triton X-100	10 μl	*0.1%*
0.1% Riboflavin 5' phosphate	3 μl	*0.0006%*
10% ammonium persulfate (APS)	0.75 μl	*0.015%*
10% v/v Tetramethylethylenediamine (TEMED)	2.5 μl	*0.05%*
	0.5 ml	

Pulse gel precursor twice by gentle vortexing to *just* mix, avoiding introduction of oxygen.

RIPA-like Lysis/EP buffer:

H_2O	to 100 ml	
10X BioRad Tris-Glycine pH 8.3	5 ml	*0.5X*
SDS	500 mg	*0.5%*
Triton X-100	100 μl	*0.1% v/v*
Sodium Deoxycholate	250 mg	*0.25%*
	100 ml	

Harsh stripping buffer (if required):

H_2O	86.5 ml	
0.5 M BioRad Tris HCl pH 6.8	12.5 ml	*62.5 mM*
SDS	2.5 g	*2.5%*
β-mercaptoethanol	1 ml	*1%*
	100 ml	

Stripping buffer should be prepared in the fume hood due to the unpleasant odor of β-mercaptoethanol.

Protocol (optional stopping points are indicated by "**STOP**"):

1. **Gel Fabrication**
   (a) Begin with a silicon wafer fabricated with the desired post geometries in SU-8.
   (b) Silanize the wafer *in vacuo* next to a small petri dish containing 2 ml of dichlorodimethylsilane (DCDMS) for 60 min. Rinse the wafer briefly with water and dry carefully using a nitrogen stream.
   (c) Place a methacrylate-functionalized glass slide onto the wafer over the post structures, treated side down.
   (d) Make PACTgel precursor solution and degas.
   (e) Add detergents and initiators to PACTgel precursor, mix, and inject steadily from one of the short sides of the slide, after fully wetting the edge to prevent bubble entrainment.
   (f) After loading, press gently on the slide to squeeze excess precursor from the gap and to ensure that the posts on the wafer are in contact with the slide.
   (g) Direct the blue LED downwards and at an angle to illuminate the entire slide from above. Illuminate for 7.5 min at a local intensity of $\sim$470 lux.
   (h) Let polymerization continue for 10-15 more minutes on the bench top, with the LED off.

(i) Drizzle 2 ml PBS along the edges of the slide with a 1 ml pipetor. This fluid will make lifting the slide from the wafer easier.

(j) Carefully lift the slide from one of the short edges using a sharp razor blade to lever the slide from the silicon wafer.

(k) Check well integrity using a microscope and immerse in PBS, gel side up, until settling cells. **STOP**

2. **Cell Settling**

(a) Resuspend cells in PBS and count, optimal well filling occurs in the neighborhood of 1–3$\times 10^6$ cells/ml.

(b) Remove slide from PBS bath, remove excess liquid by draining to a corner, place slide on a large dry petri dish. Apply 1-1.5 ml cell solution and incubate for 5-10 minutes. Check settling periodically using a microscope.

(c) Tip petri dish at a 10-20° angle and remove cell solution from lower edge using a pipet or gentle vacuum.

(d) Wash slide gently by applying 1 ml aliquots (2-3 should be sufficient) to the elevated edge and removing from the lower edge with gentle vacuum. Check slide surface for stray cells and proceed when slide is relatively clean.

(e) Apply 1 ml PBS to one edge of the flat slide so that it spreads over around half of the slide, apply a clean plain slide to the top by lowering from one edge. The PBS should spread evenly between the gap as the slide is lowered, and excess will run from the edges.

(f) Use slight pressure, pick up the slide sandwich and wipe away excess PBS.

(g) Image whole slide under bright field using 4× magnification, 1×1 binning to allow later counting of well occupancy.

(h) Slide the top slide away from the device slowly to remove it.

Move quite quickly through the following steps to prevent the slide from drying out.

3. **Lysis & Separation**

(a) Place cell slide in open, dry electrophoresis dish with platinum electrodes running the length of each edge of the slide, using vaseline at short edges to temporarily adhere slide to the dish.

(b) Set dish on a clear-bottomed stage on the microscope.

(c) After focusing on a fluorescent cell, rapidly pour 10 ml lysis/EP buffer over the entire slide and against the electrodes.

(d) Observe cell lysis (∼10 s), then immediately apply 200–250V and observe fluorescent protein migration.

(e) Stop field and immediately apply UV light via the Hamamatsu supply at a distance of ∼75 mm for ∼45 s to capture bands, power should be in the neighborhood of 40 mW cm^{-2}.

(f) Remove slide from EP dish and place in a 40 ml conical with PBS and store at 4°C until probing (can be done up to a week or more after separation and capture). **STOP**

4. **Immunoblotting**

(a) Antibodies should be applied at high concentration to combat exclusion from the polyacrylamide layer (∼10X dilution, or around 0.6 μM) in TBS (100 mM tris pH 7.5 + 150 mM NaCl) containing 0.1% Tween (TBST) and 2% BSA.

(b) After prepping antibody cocktails, spin them at 20,000g for 10 min to remove large aggregates.

(c) Incubate antibodies with slide against a plain glass wafer in the gap formed by 60 μm SU-8 shims (∼140 μl antibody solution) or standard lab tape; or using the ArrayIt microarray hybridization cassette (∼40-50 μl antibody solution per cassette well) if multiple cocktails are to be used. Incubation times of around 1 hr are sufficient.

(d) Wash slide between probings in a bath of TBST (no BSA) for 30 min.

(e) Remove slide from TBST, rinse briefly in DI water, and spin in the microscope slide centrifuge for 30 s.

(f) Use a strong nitrogen stream to fully dry the gel.

(g) Image chip by tiled exposures on fluorescence microscope or using a microarray scanner.

5. **Stripping**

Antibodies can be stripped from probed slides by incubation in a "harsh" buffer under mild heating, and the slides are then available for reprobing for other targets of interest.

(a) Make stripping buffer in the fume hood and incubate in a glass container on a hotplate to give a solution temperature of 50°C measured using a thermometer. Typically this will require a hotplate temperature of around 110°C.

(b) Introduce slide to be stripped to the bath after rehydrating in PBS for 10 min.

(c) Incubate slide in the stripping buffer for around 2 hrs, be sure to cover the container with foil to ensure the correct temperature is maintained.

(d) Remove slide and wash twice in PBS for 5-10 min each wash.

(e) Slide is ready for reprobing.